



# On Mechanistic Explanation of the Shape of the Universal Curve of Earthquake Recurrence Time Distributions

Mariusz BIAŁECKI

Institute of Geophysics, Polish Academy of Sciences, Warszawa, Poland  
e-mail: bialecki@igf.edu.pl

## Abstract

This paper outlines an idea for an explanation of a mechanism underlying the shape of the universal curve of the Earthquake Recurrence Time Distributions. The proposed simple stochastic cellular automaton model is reproducing the gamma distribution fit with the proper value of parameter  $\gamma$  characterizing the Earth's seismicity and also imitates a deviation from the fit at short interevent times, as observed in real data.

Thus the model suggests an explanation of the universal pattern of rescaled Earthquake Recurrence Time Distributions in terms of combinatorial rules for accumulation and abrupt release of seismic energy.

**Key words:** stochastic cellular automaton, earthquake recurrence time, avalanches, toy model of earthquakes, Markov chains.

## 1. INTRODUCTION

Analyzing seismic catalogs, Corral (2004) has determined that the probability densities of the waiting times between earthquakes for different spatial areas and magnitude ranges can be described by a unique universal distribution if the time is rescaled with the mean rate of occurrence.

---

Ownership: Institute of Geophysics, Polish Academy of Sciences;

© 2015 Białecki. This is an open access article distributed under the Creative Commons Attribution-NonCommercial-NoDerivs license,

<http://creativecommons.org/licenses/by-nc-nd/3.0/>.

To unify diverse observations, the spatiotemporal analysis was carried out as follows. Seismicity is considered as a result of a dynamical process, whose collective properties are largely independent of the physics of individual earthquakes. Following Bak *et al.* (2002), events are neither separated into different kinds (foreshocks, mainshocks, aftershocks) nor the crust is divided into provinces with different tectonic properties. Then, a region of the Earth is selected, as well as temporal period and a minimum magnitude  $M_c$  (for conditions and other details, see Corral (2004, 2007)). Events in this space-time-magnitude window are considered as a point process in time (disregarding the magnitude and the spatial degrees of freedom) and are characterized only by their occurrence time  $t_i$ , with  $i = 1 \dots N(M_c)$ . Then the recurrence (or waiting) time  $\tau_i$  is defined by  $\tau_i = t_i - t_{i-1}$ .

The entire Earth has been analyzed by this method and it appears that different regions' probability densities of waiting times, rescaled by the mean seismic rate, as a function of the rescaled recurrence time, collapse onto a single curve  $f$  (Corral 2004):

$$D(\tau; M_c) = R(M_c)f(R(M_c)\tau), \quad (1)$$

where mean seismic rate  $R(M_c)$  is given by  $R(M_c) = N(M_c)/T$  (here  $T$  is a total time into consideration), and recurrence-time probability density  $D(\tau; M_c)$  is defined as  $D(\tau; M_c) = \text{Prob}[\tau < \text{recurrence time} < \tau + d\tau]/\tau$ . The so-called scaling function  $f$  admits a fit in the form of a generalized gamma distribution

$$f^{fit}(\theta) = C\theta^{\gamma-1} \exp\left(-\frac{\theta^\delta}{\beta}\right), \quad (2)$$

where  $\gamma = 0.67 \pm 0.005$ ,  $\beta = 1.58 \pm 0.15$ ,  $\delta = 0.98 \pm 0.05$ ,  $C = 0.5 \pm 0.1$ , and  $\theta = R\tau$  is dimensionless recurrence time. The value of  $\delta$  can be approximated to 1. The present characterization of the stochastic spatiotemporal occurrence of earthquakes by means of a unique law would indicate the existence of universal mechanisms in the earthquake-generation process (Corral 2004).

This paper outlines an idea for explanation of a possible mechanism underlying the shape of the universal curve in terms of a mechanistic model, namely a cellular automaton model called Random Domino Automaton (RDA). The simple rules for evolution of the model, being a slowly driven system, rely on accumulation and abrupt release of energy only, which well fits the above-described procedure of neglecting individual properties of earthquakes as well as diversified tectonic conditions. We show that RDA reproduces the shape of the "rescaled" distribution of recurrence times.

As can be seen from the original work (Corral 2004) as well as from further studies (Marekova 2012), results obtained from various earthquake catalogs show a deviation from the gamma distribution at the short interevent times.

This holds from worldwide to local scales and for quite different tectonic environments. It is remarkable that the presented toy model reproduces also this deviation. Thus the model suggests an explanation of the universal pattern of rescaled Earthquake Recurrence Time Distributions in terms of its combinatorial rules for accumulation and release of seismic energy.

Note, that we present a preliminary results – here we are not covering the realistic range of earthquake energies. So far, some insight into the origin of the gamma distribution as well as examination the recurrence statistics of a range of cellular automaton earthquake models are presented in Weatherley (2006). It is shown there that only one model, the Olami-Feder-Christensen automaton, has recurrence statistics consistent with regional seismicity for a certain range of conservation parameters of that model.

An explanation of the earthquake recurrence times in terms of probability distributions is presented by Saichev and Sornette (2006, 2013).

## 2. RANDOM DOMINO AUTOMATON

The Random Domino Automaton (RDA) was introduced as a toy model of earthquakes (Białecki and Czechowski 2010, 2013, 2014; Białecki 2015), but can be also regarded as an extension of the well-known 1-D forest-fire model proposed by Drossel and Schwabl (1992). As a field of application of RDA we have already studied its relation to Ito equation (Czechowski and Białecki 2012a,b) and to integer sequences (Białecki 2012). We point out also other cellular automata models (Tejedor *et al.* 2009, 2010) giving an insight into diverse specific aspects of seismicity.

The RDA is characterized as follows:

- space is 1-dimensional and consists of  $N$  cells; periodic boundary conditions are assumed;
- cell may be empty or occupied by a single ball;
- time is discrete and in each time step an incoming ball hits one arbitrarily chosen cell (the same probability for each one). The balls are interpreted as energy portions.

The state of the automaton changes according to the following rule:

- if the chosen cell is empty, it becomes occupied with probability  $\nu$ ; with probability  $(1 - \nu)$  the incoming ball is rebounded and the state remains unchanged;
- if the chosen cell is occupied, the incoming ball provokes an avalanche with probability  $\mu$  (it removes balls from hit cell and from all adjacent cells); with probability  $(1 - \mu)$  the incoming ball is rebounded and the state remains unchanged.

The parameter  $\nu$  is assumed to be constant but the parameter  $\mu = \mu_i$  is allowed to be a function of size  $i$  of the hit cluster. This extension with respect

to Drossel-Schwabl model leads to substantial novel properties of the automaton. Note that only the ratio of these parameters,  $\mu_i/\nu$ , affects properties of the automaton – changing of  $\mu$  and  $\nu$  proportionally corresponds to a rescaling of time unit.

The remarkable feature of the RDA is the explicit one-to-one relation between details of the dynamical rules of the automaton (represented by rebound parameters  $\mu_i/\nu$ ) and the produced stationary distribution  $n_i$  of clusters of size  $i$ , which implies distribution of avalanches  $w_i$ . It shows how to reconstruct details of the “macroscopic” behavior of the system from simple rules of “microscopic” dynamics.

Various sizes  $N$  of RDA can be considered in order to explain the shape of the universal curve of Scaling Law. It appears that the results for quite a small size  $N = 5$  are enough to explain the idea and allow to keep the reasoning concise and detailed. RDA for a bigger size of the lattice behaves similar, and the overall picture remains the same, as results from explanations given below.

RDA is also a Markov chain (Białeckı 2015). It is convenient to define states  $i$  up to translational equivalence. Thus, in the example for  $N = 5$ , instead of  $2^5$ , there are 8 states only – see Table 1. Such a space of states is irreducible, aperiodic and recurrent. Transition matrix  $\mathbf{p}$ , where  $[\mathbf{p}]_{ij}$  = probability of transition  $i \rightarrow j$ , for  $N = 5$  is of the form

$$\frac{1}{5} \begin{pmatrix} 5-5\nu & 5\nu & 0 & 0 & 0 & 0 & 0 & 0 \\ \mu_1 & 5-\mu_1-4\nu & 2\nu & 2\nu & 0 & 0 & 0 & 0 \\ 2\mu_2 & 0 & 5-2\mu_2-3\nu & 0 & 2\nu & \nu & 0 & 0 \\ 0 & 2\mu_1 & 0 & 5-2\mu_1-3\nu & \nu & 2\nu & 0 & 0 \\ 3\mu_3 & 0 & 0 & 0 & 5-3\mu_3-2\nu & 0 & 2\nu & 0 \\ 0 & 2\mu_2 & \mu_1 & 0 & 0 & 5-2\mu_2-\mu_1-2\nu & 2\nu & 0 \\ 4\mu_4 & 0 & 0 & 0 & 0 & 0 & 5-4\mu_4-\nu & \nu \\ 5\mu_5 & 0 & 0 & 0 & 0 & 0 & 0 & 5-5\mu_5 \end{pmatrix}$$

Table 1

States of RDA for the size of the lattice  $N = 5$

State label	Example	Multiplicity
1	$\leftrightarrow         \leftrightarrow$	1
2	$\leftrightarrow         \bullet   \leftrightarrow$	5
3	$\leftrightarrow       \bullet \bullet   \leftrightarrow$	5
4	$\leftrightarrow     \bullet   \bullet   \leftrightarrow$	5
5	$\leftrightarrow     \bullet \bullet \bullet   \leftrightarrow$	5
6	$\leftrightarrow   \bullet   \bullet \bullet   \leftrightarrow$	5
7	$\leftrightarrow   \bullet \bullet \bullet \bullet   \leftrightarrow$	5
8	$\leftrightarrow \bullet \bullet \bullet \bullet \bullet   \leftrightarrow$	1

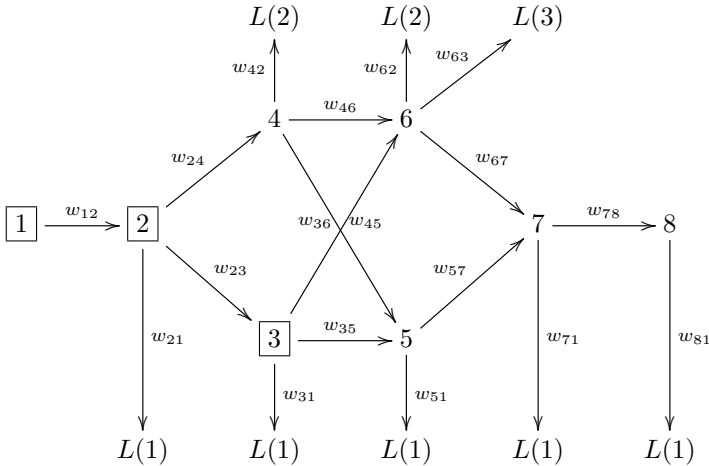


Fig. 1. A state diagram for RDA of size  $N = 5$ . Arrows with respective weights indicate possible transitions; those with avalanches are ended with symbol “L”. A state is boxed, if it is possible to get it directly after an avalanche.

Stationary distribution is given by

$$v \cdot \mathbf{p} = v . \tag{3}$$

The evolution of the system is represented in Fig. 1. Arrows between states  $i$  and  $j$ , with respective weights  $w_{ij}$ , indicate possible transitions. A symbol  $L(j)$  depicts an avalanche to state  $j$ . The density of the system is growing from left side (state 1 has density  $\rho = 0$ ) to right side (up to density  $\rho = 1$  for state 8).

The expected time between two consecutive avalanches  $T_{av}$  may be expressed by various formulas (Bialecki 2015). For example

$$T_{av} = \frac{\langle w \rangle + 1}{1 - P_r} , \tag{4}$$

where  $\langle w \rangle$  is the average avalanche size and  $P_r$  is the probability that the incoming ball is rebounded both from empty or occupied cell.

The probabilities  $v_i$  of states  $i$  obtained from condition 3 allow determining the distribution of frequency  $f_i$  of avalanche of size  $i$ , if rebound parameters  $\mu_i/\nu$  are given. There exists also a procedure of obtaining approximate values of rebound parameters  $\mu_i/\nu$ , which produce requested distribution of avalanches (Bialecki 2013). The approximation comes from nonexistence of exact equations for (stationary) distribution of clusters  $n_i$  for sizes bigger than

4 (see Białeckı 2015). We have used this procedure to obtain values of  $\mu_i/\nu$  that give noncumulative inverse-power distribution of avalanches presented in Table 2, *i.e.*, in the form consistent with Gutenberg-Richter law. The exact value of power (here 2.1) does not affect results of the construction substantially.

Table 2

Approximate values of rebound parameters  $\mu_i$   
and respective avalanche distribution  $w_i$

$i$	1	2	3	4	5
$\mu_i$	0.999060	0.388232	0.284504	0.097650	0.045810
$w_i$	0.413247	0.102851	0.042587	0.022351	0.014306

**Note:** The parameter  $\nu = 0.25$ .

### 3. DISTRIBUTION OF WAITING TIMES

To calculate the distribution of waiting times, each path starting from a state reached after an avalanche and ending with an avalanche is considered. There are 42 such paths for size  $N = 5$ . Each path is assigned its respective probabilities that a total passage time is equal to 1, 2, . . . time steps.

Respective weights  $S_k$  describing how often the system starts from initial state  $k$  are given by

$$S_k = \frac{\sum_{i>k} v_i p_{ik}}{\sum_k \sum_{i>k} v_i p_{ik}} . \tag{5}$$

For  $N = 5$  initial states are 1, 2 and 3.

The expected time of stay in a state  $k$  is

$$t_{av}(k) = \sum_i p_{kk}^{(i-1)} (1 - p_{kk}) \cdot i = (1 - p_{kk})^{-1} . \tag{6}$$

The probability of stay in given state  $k$  for a time equal to  $i$  time steps is given by

$$T_i^k = p_{kk}^{(i-1)} (1 - p_{kk}) , \tag{7}$$

and all possible values are aggregated in a vector  $T^k$  with  $i$ -th component equal to  $T_i^k$ . For a path through two consecutive states,  $k$  and  $l$ , the respective probability of time of stay in both of them equal to  $j$  time steps is defined by

$$T_j^{kl} = (T^k \star T^l)_j = \sum_{n=1}^{j-1} T_n^k T_{n-j}^l . \tag{8}$$

For a path through three states,  $k, l$  and  $m$  we have  $T^{klm} = (T^k \star T^l) \star T^m$ , and so on for longer paths.

The probability rates  $w_{ij}$  for transition  $i \rightarrow j$ , where  $i \neq j$ , are just normalized probabilities  $p_{ij}$ , namely

$$w_{ij} = \frac{p_{ij}}{\sum_{j \neq i} p_{ij}} . \tag{9}$$

Thus for a path  $i_1, i_2, \dots, i_{k-1}, i_k$  there is assigned a combined weight

$$W^{i_1 i_2 \dots i_{k-1} i_k} = S_{i_1} \cdot w_{i_1 i_2} \cdot \dots \cdot w_{i_{k-1} i_k} , \tag{10}$$

as well as combined weighted time vector

$$\Omega^{i_1 i_2 \dots i_k} = W^{i_1 i_2 \dots i_k} \cdot T^{i_1 i_2 \dots i_k} . \tag{11}$$

The  $i$  th component of the vector  $\Omega^{i_1 i_2 \dots i_k}$  gives a contribution to waiting time equal to  $i$  coming from a path  $i_1, i_2, \dots, i_k$ . Summing up those vectors for all possible paths we end with a distribution of waiting times. One can obtain also a distribution related to avalanches of chosen size. For example, if such sum is made for paths related to avalanches of size 2, 3, 4, and 5 only, a distribution of waiting times related to avalanches of size bigger than 1 is obtained.

Rebound parameters presented in Table 2 were chosen in order to obtain noncumulative distribution of avalanches in the form consistent with Gutenberg-Richter law. The exact value of power (here 2.1) does not affect results of the construction substantially.

The system has average density  $\rho = 0.273885$ , average avalanche size  $\langle w \rangle = 1.52458$  and average time between avalanches  $T_{av} = 21.2027$ . The parameter  $P_r = 0.880932$  shows that most of incoming balls are rebounded. Expected times of staying in all states are presented in Table 3. The great majority of avalanches leads to an empty state ( $S_1 = 0.755449$ ), roughly every fifth avalanche leads to state 2 ( $S_2 = 0.205253$ ), and roughly every twenty fifth to state 3 ( $S_3 = 0.0392984$ ).

Table 3

Approximate expected stay times in states  
for the size of the lattice  $N = 5$

State	1	2	3	4	5	6	7	8
$t_{av}$	4.0	2.5	3.3	1.8	3.7	2.2	7.8	21.8

Figure 2 presents obtained distributions of waiting times up to 300 time steps. The upper curve is for avalanches of all sizes, the next is for avalanches

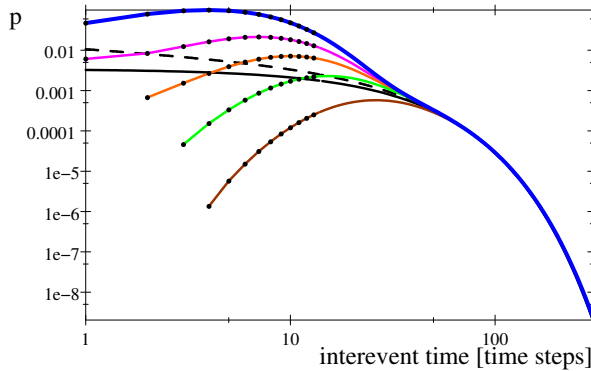


Fig. 2. A plot of distributions of interevent times for RDA with  $N = 5$ . The upper line is for avalanches of all sizes, the curve below is for avalanches of size bigger than 1, the next is for sizes bigger than 2, and so on. The lowest curve counts only avalanches of size 5. The dashed line is a plot of fitted gamma distribution  $ay^{(\gamma-1)}e^{-\frac{y}{b}}$ ; the solid line below is a plot of fitted exponential curve  $a'e^{-\frac{y}{b'}}$ . For large interevent times all these curves overlap.

of size bigger than 1, and so on. The lowest curve counts avalanches of size 5 only.

The dashed line is a fitted gamma distribution  $ay^{(\gamma-1)}e^{-\frac{y}{b}}$ , where  $\gamma = 0.67$ ,  $b = 22.4$ , and  $c = 0.011$ . This fit is done for points with time coordinate from 60 ( $\chi^2 = 5.5346 \cdot 10^{-11}$ ). Values of the parameters  $b$  and  $c$  can be rescaled, depending on their relation to physical quantities (time, number of earthquakes). The parameter  $\gamma$  is a fixed parameter, with exactly the same value which characterizes Earth's seismicity. The solid line below is a plot of fitted exponential curve  $a'e^{-\frac{y}{b'}}$ .

Thus, the exponential part of the universal curve comes from distributions of biggest avalanches. In the presented example the biggest  $t_{av}$  is for the state 8 containing single cluster of size 5 (see Table 3). Thus its contribution to the overall waiting time distribution dominates for bigger times (compare formulas 6 and 7). Also state 7 containing single cluster of size 4 contributes, but it is decaying more rapidly.

The other part of the universal curve, comes from contributions of avalanches of smaller sizes. Its shape is a result of composition of many possible paths of the evolution, as depicted in Fig. 1. For bigger sizes  $N$  there are much more possible paths (*i.e.*, 1554 for  $N = 7$ ) through states containing many clusters with comparable times  $t_{av}$ . Their composition flatten the curve. Moreover, calculation shows that this effect produces a surplus (comparing to the gamma fit) for small waiting times, which is evident in real earthquakes data

(Corral 2004, Marekova 2012). The size of the surplus can be reduced by omitting of a contribution of smallest avalanches (also not recorded in real data).

Note that due to the incompleteness of the seismic catalogs in the short-time scale, real data are usually not displayed on plots for very short time intervals. Thus, the obtained theoretical curve, shown in Fig. 1, may be similarly cut for small times. If it is done for time, say, smaller than 10, it reflects the shape of real data.

#### 4. CONCLUSIONS

Thus, the presented model suggests that the origin of a universal curve is of combinatorial nature of accumulation and abrupt release of energy according to the rules depending on some parameters defining probabilities dependent on size of energy portions, as described above.

We would like to underline some limitations of the presented model resulting from its simplicity. Saichev and Sornette (2006) pointed out the importance of the mechanism of triggering of earthquakes by other earthquakes in understanding of distributions of inter-event times. Such mechanism is absent in the presented model, and we intend to introduce it. Another important issue is the comparison features of waiting time distribution in case of rescaled and not rescaled, and the appropriate scaling is another challenge for the model. Moreover, in the recent study Matcharashvili *et al.* (2015) investigated the relative ratio of correlated and uncorrelated waiting times, and they found that the ratio is similar for different catalogues. We send interested reader to this paper for a detailed discussion of properties of distributions of waiting times.

All this strongly suggests the need of extensions of the presented results in order to explain mechanistically the universal distribution of inter-event time for earthquakes.

**Acknowledgment.** This work was partially supported by National Science Centre, project 2012/05/B/ST10/00598. This work was partially supported within statutory activities No. 3841/E-41/S/2015 of the Ministry of Science and Higher Education of Poland.

#### References

- Bak, P., K. Christensen, L. Danon, and T. Scanlon (2002), Unified scaling law for earthquakes, *Phys. Rev. Lett.* **88**, 17, 178501, DOI: 10.1103/PhysRevLett.88.178501.
- Bialecki, M. (2012), Motzkin numbers out of Random Domino Automaton, *Phys. Lett. A* **376**, 45, 3098-3100, DOI: 10.1016/j.physleta.2012.09.022.

- Białeckı, M. (2013), From statistics of avalanches to microscopic dynamics parameters in a toy model of earthquakes, *Acta Geophys.*, **61**, 6, 1677-1689, DOI: 10.2478/s11600-013-0111-7.
- Białeckı, M. (2015), Properties of a finite stochastic cellular automaton toy model of earthquakes, *Acta Geophys.* **63**, 4, 923-956, DOI: 10.1515/acgeo-2015-0030.
- Białeckı, M., and Z. Czechowski (2010), On a simple stochastic cellular automaton with avalanches: simulation and analytical results. **In:** V. De Rubeis, Z. Czechowski, and R. Teisseyre (eds.), *Synchronization and Triggering: From Fracture to Earthquake Processes*, GeoPlanet – Earth and Planetary Sciences, Springer, Berlin Heidelberg, 63-75, DOI: 10.1007/978-3-642-12300-9\_5.
- Białeckı, M., and Z. Czechowski (2013), On one-to-one dependence of rebound parameters on statistics of clusters: exponential and inverse-power distributions out of Random Domino Automaton, *J. Phys. Soc. Jpn.* **82**, 1, 014003, DOI: 10.7566/JPSJ.82.014003.
- Białeckı, M., and Z. Czechowski (2014), Random Domino Automaton: Modeling macroscopic properties by means of microscopic rules. **In:** R. Bialik, M. Majdański, and M. Moskalik (eds.), *Achievements, History and Challenges in Geophysics*, GeoPlanet: Earth and Planetary Sciences, Springer Intern. Publ., Cham, 223-241, DOI: 10.1007/978-3-319-07599-0\_13.
- Corral, A. (2004), Long-term clustering, scaling, and universality in the temporal occurrence of earthquakes, *Phys. Rev. Lett.* **92**, 10, 108501, DOI: 10.1103/PhysRevLett.92.108501.
- Corral, A. (2007), Statistical features of earthquake temporal occurrence. **In:** P. Bhattacharyya and B.K. Chkrabarti (eds.), *Modelling Critical and Catastrophic Phenomena in Geoscience*, Lecture Notes in Physics, Vol. 705, Springer, Berlin Heidelberg, 191-221, DOI: 10.1007/3-540-35375-5\_8.
- Czechowski, Z., and M. Białeckı (2012a), Three-level description of the domino cellular automaton, *J. Phys. A: Math. Theor.* **45**, 15, 155101, DOI: 10.1088/1751-8113/45/15/155101.
- Czechowski, Z., and M. Białeckı (2012b), Ito equations out of domino cellular automaton with efficiency parameters, *Acta Geophys.* **60**, 3, 846-857, DOI: 10.2478/s11600-012-0021-0.
- Drossel, B., and F. Schwabl (1992), Self-organized critical forest-fire model, *Phys. Rev. Lett.* **69**, 11, 1629-1632, DOI: 10.1103/PhysRevLett.69.1629.
- Marekova, E. (2012), Testing a scaling law for the earthquake recurrence time distributions, *Acta Geophys.* **60**, 3, 858-873, DOI: 10.2478/s11600-012-0007-y.
- Matcharashvili, T., T. Chelidze, and N. Zhukova (2015), Assessment of the relative ratio of correlated and uncorrelated waiting times in the Southern California earthquakes catalogue, *Physica A* **433**, 291-303, DOI: 10.1016/j.physa.2015.03.060.

- 
- Saichev, A., and D. Sornette (2006), “Universal” distribution of inter-earthquake times explained, *Phys. Rev. Lett.* **97**, 7, 078501, DOI: 10.1103/PhysRevLett.97.078501.
- Saichev, A., and D. Sornette (2013), Fertility heterogeneity as a mechanism for power law distributions of recurrence times, *Phys. Rev. E* **87**, 2, 022815, DOI: 10.1103/PhysRevE.87.022815.
- Tejedor, A., J.B. Gomez, and A.F. Pacheco (2009), Earthquake size-frequency statistics in a forest-fire model of individual faults, *Phys. Rev. E* **79**, 4, 046102, DOI: 10.1103/PhysRevE.79.046102.
- Tejedor, A., J.B. Gomez, and A.F. Pacheco (2010), Hierarchical model for disturbed seismicity, *Phys. Rev. E* **82**, 1, 016118, DOI: 10.1103/PhysRevE.82.016118.
- Weatherley, D. (2006), Recurrence interval statistics of cellular automaton seismicity models, *Pure Appl. Geophys.* **163**, 9, 1933-1947, DOI: 10.1007/s00024-006-0105-3.

Received 20 March 2015

Received in revised form 13 July 2015

Accepted 11 August 2015

# Deep Geoelectrical Structure of the Central and Western Ukraine

Igor M. LOGVINOV

Institute of Geophysics, National Academy of Sciences of Ukraine, Kiev, Ukraine  
e-mail: [anna\\_log@ukr.net](mailto:anna_log@ukr.net)

## Abstract

The results of deep induction sounding in Ukraine made in the twenty-first century with the participation of the author have been summarized, including also a number of data obtained in the previous decades. The apparent resistivity and magnetic transfer function on the territories of western Ukraine and eastern Poland have been analyzed. The articulation of these data with the regional magnetic variation soundings allowed taking into account the influence of a static shift of areal interpretation of magnetotelluric resistivity results, which increased the reliability of interpretation. The analysis of induction sounding performed with 1D, 2D, and 3D inversions of magnetic transfer functions allowed localizing the crustal anomalies. The results are discussed.

**Key words:** crust and mantle conductivity, East Carpathians, East European Plate.

## 1. INTRODUCTION

Geoelectric survey in Ukraine is actively underway since the 1970s. The main results made in the twentieth century were summarized by Rokityansky (1982), Bondarenko *et al.* (1972), Rokityansky *et al.* (1976), Dyakonova *et al.* (1986). The results of most of these studies were obtained from interpretation of thousands of magnetotelluric sounding (MTS) in the period range from 0.1 to 900 s made by industrial organizations of Ukraine (Ingerov *et al.*

1999). Results of regional soundings of the mantle down to a depth of about 1000 km have been relatively recently obtained, using data from three geomagnetic observatories of Ukraine.

The basis for this work was the geoelectric study conducted in the past 15 years, with a number of magnetotelluric stations (Jankowski *et al.* 1984, Rakhlin *et al.* 2005) of the Institute of Geophysics of the National Academy of Sciences of Ukraine (IGF NANU). In addition, observations were carried out in the framework of two international projects: Central Europe Mantle geoElectrical Structure (CEMES), which was initiated by the Institute of Geophysics (IGF) of the Polish Academy of Sciences in 2001 (Semenov *et al.* 2008) and joint Polish–Ukrainian observations made in 2006–2007 in Poland and Ukraine. Additionally, this work includes part of the short period MTS results obtained by exploration organizations (Ingerov *et al.* 1999). Results of MTS with periods of more than 40 minutes were considered as deep MT soundings (DMTS) and analyzed together with the results of the regional magnetovariation soundings (MVS).

The area of research covers the south-western edge of the East European Platform (EEP) and the eastern part of the Carpathians (Fig. 1). Interpretation was carried out using 1D, 2D, and quasi-3D inversions. Studies in separate sub-regions were published by Gordienko *et al.* (2005, 2006, 2011, 2012). The paper summarizes the results of all deep geoelectric structures in the Western and Central Ukraine.

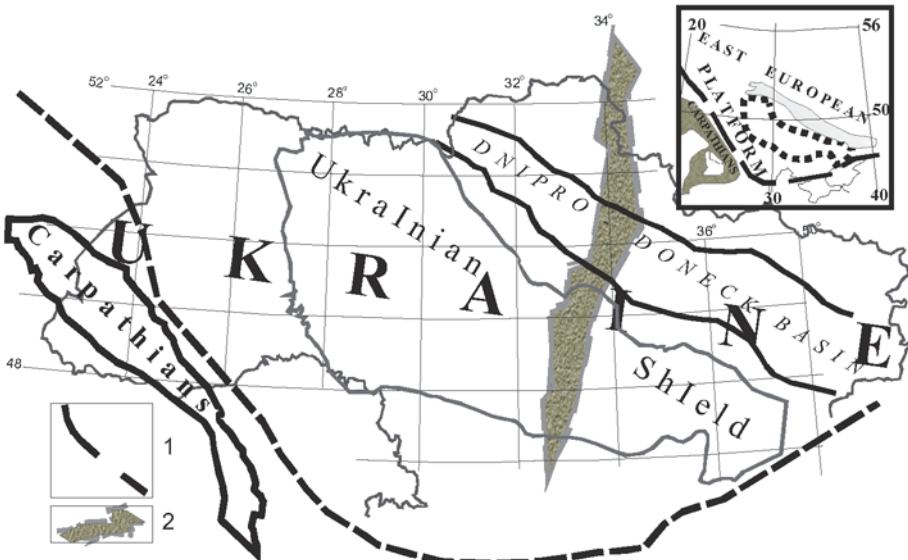


Fig. 1. Major tectonic units of the EEP and Carpathian: 1 – the EEP border, 2 – the Ingulets–Krivoy Rog–Krupetskyi suture zone.



(GMVS) method (Ladanivskyy *et al.* 2010) fills data gaps in the specified range of periods.

Data processing of the observed variations of magnetotelluric fields was carried out using the usual boundary conditions on the Earth's surface according to the formulae:

$$E_x(\omega, \mathbf{r}) = Z_{xx}(\omega)B_x(\omega) + Z_{xy}(\omega)B_y(\omega) ,$$

$$E_y(\omega, \mathbf{r}) = Z_{yx}(\omega)B_x(\omega) + Z_{yy}(\omega)B_y(\omega) ,$$

$$B_z(\omega, \mathbf{r}) = W_{zx}(\omega, \mathbf{r})B_x(\omega, \mathbf{r}) + W_{zy}(\omega, \mathbf{r})B_y(\omega, \mathbf{r}) ,$$

where  $E(\omega, \mathbf{r})$  and  $B(\omega, \mathbf{r})$  are complex Fourier amplitudes of orthogonal horizontal components of the electric  $\mathbf{E}(t)$  and magnetic fields  $\mathbf{B}(t)$ ,  $\omega$  is the angular frequency,  $\mathbf{r}$  is the radius vector on a plane surface of the Earth,  $Z(\omega, \mathbf{r})$  is the impedance, and  $W_z(\omega, \mathbf{r})$  is the the magnetic transfer function. A more complicated theory was suggested by Schmucker (Schmucker 2003) and Shuman (Shuman and Kulik 2002).

Several types of processing algorithms based on the spectral analysis (Egbert and Booker 1986, Egbert 1997, Semenov 1998, Ladanivskyy 2003) and on the analysis of time domain convolution functions (Wieladek and Ernst 1977) were applied to the collected data. Finally, the impedance and magnetic transfer function data were estimated in the period range of 10-10<sup>4</sup> s. Partly, the processing was carried out using the remote reference method. The impedance polar diagrams analysis allowed the detection of main directions of regional structures. Results of the data processing (apparent resistivity, phases of the impedance, magnetic transfer function) formed the data bank used for the solution of 1D, 2D, and quasi-3D modeling and inversion problems.

### 3. 1D INVERSIONS

The methodological basis for present inversion studies was elaborated in the frames of the CEMES international project (Semenov *et al.* 2008). The dense DMTS network allows us to refine the electrical conductivity structure of the crust and mantle on the territory of Ukraine and adjacent narrow strip of Poland. Inverted complex apparent resistivity data were obtained by the extension of DMTS data with regional MVS responses from Ukrainian geomagnetic observatories. The MVS results for the geomagnetic observatory KIV were taken as a reference for EEP sites, while results from observatories LVV and HRB extend data from the Carpathians (Semenov 1998, Semenov and Jóźwiak 2006). Apparent resistivities obtained by different methods displayed a good agreement in phases, while their amplitudes were often distorted by the shift effect. This effect was assumed to be

frequency independent due to the small conductance level of EEP sediments in Ukraine. Thus, the amplitude curves of DMTS apparent resistivity were shifted to MVS levels before their joint 1D inversions by the OCCAM (Constable *et al.* 1987) and D+ (Parker and Whaler 1981) methods.

The total conductance  $S$  beneath the Ukrainian part of EEP increases slowly and monotonically from the surface to a depth of  $\sim 600$  km (the bottom of the upper mantle) and then rapidly from  $\sim 30$  kS at this depth to  $\sim 300$  kS at the depth of 800 km (the center of the mid-mantle). The  $S$  error for the upper mantle with sediments is estimated at 20% level. The main contribution for such a big error comes from the depth interval of 200-400 km, which is the most difficult zone to analyze the Earth's conductivity. This observation is also true for new experimental data giving minimal error bars at the same level (Logvinov 2002). Complex apparent resistivity estimates for Ukrainian sites were recently calculated in this period range using a new approach (Ladanivskyy *et al.* 2010). No regional conductive layers at depths of 150-500 km were detected, as distinct from the western TESZ region where the presence of a well-conductive layer at "asthenospheric" depths was found (Jóźwiak 2013).

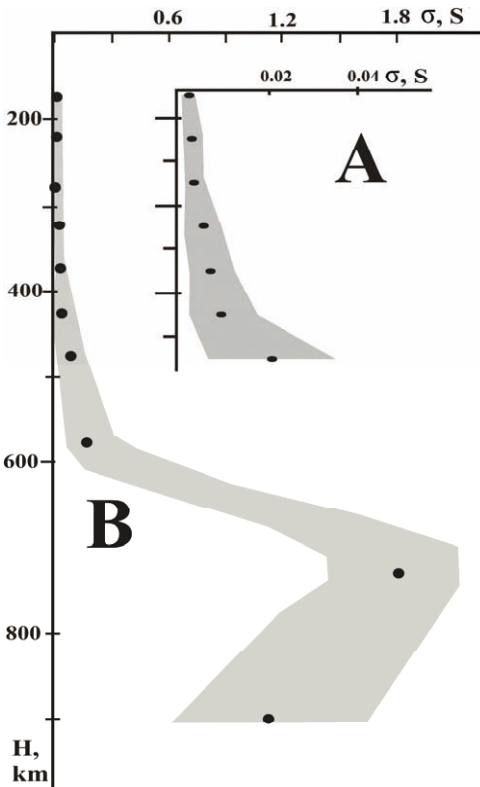


Fig. 3. Averaged conductivity distributions for the southwestern EEP part at depths of 150-500 km (A) and 150-900 km (B); bands display mean square errors.

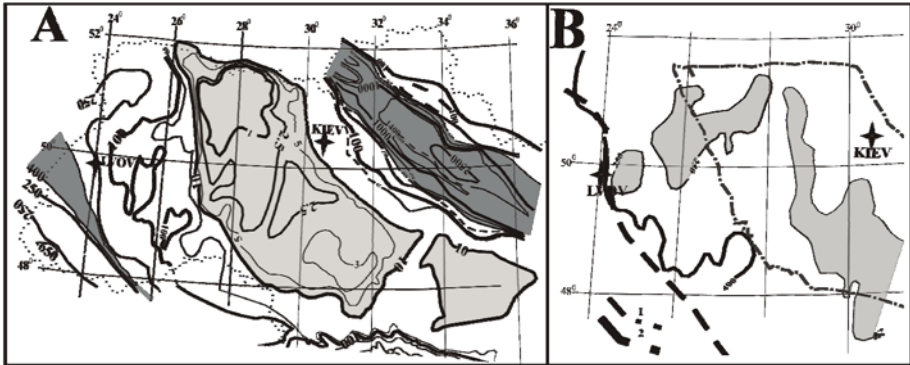


Fig. 4. Conductance maps (in S) for sediments (A) and the crust (B); 1 – the Ukrainian Shield border, 2 – the EEP border.

The averaged conductivity distribution for soundings at 93 sites was estimated from the total conductance  $S$ :  $\sigma = \text{grad } S$ . Conductivity increases slowly and monotonically till the depths of 400-450 km (Fig. 3A) and then sharply at depths greater than 600 km (Fig. 3B). The maximal conductivity is observed at  $\sim 700$  km and a layer with lower conductivity appears at a greater depth of 800-1000 km. A similar distribution of  $\text{grad } S$  with depth was obtained for the Polish EEP part (Semenov and Jóźwiak 2005). This result does not contradict with the results obtained previously (Semenov and Jóźwiak 1999).

Two strong crustal conductivity anomalies, namely, the Carpathian and the Kirovograd, are well known in Ukraine. The condition of horizontal medium homogeneity is not true in these areas and therefore the 1D inversion was not used here.

The sedimentary and, partly, crustal conductancies were additionally estimated using both the data obtained from DC resistivity soundings and 1D inversion at  $\sim 200$  MT prospecting sites (with the period range of 1-3600 s). The resulting conductance maps for the crust (Logvinov 2012) and sediments (Ingerov *et al.* 1999, Logvinov 2012) are presented in Fig. 4. The crustal conductance exceeds the level of 250 S only in areas close to the EEP border (Fig. 4B).

The Moho boundary is situated in the studied region at depths of 40-50 km according to seismic data (Gordienko *et al.* 2005, 2012). For the average depth of the crust, the value of 45 km was accepted.

#### 4. 2D INVERSIONS

The analysis of experimental data at all the profiles shown in Fig. 2 was made using 2D inversion code REBOCC (Siripunvaraporn and Egbert

2000). In this study the misfit between modelled and experimental data was considered satisfactory at the levels of 0.1 for magnetic transfer function,  $10^\circ$  for the impedance phase, and 30% for the apparent resistivity. The goal of the REBOCC inversion was to find the minimum norm model at these misfit levels. To estimate the integral conductivity of local structures the parameter  $G$  (Rokityansky 1982) was used:

$$G_i = Q_i / \rho_i ,$$

where  $Q_i$  is the cross-section area of the conductive object (in  $\text{m}^2$ ), and  $\rho_i$  is its resistivity (in Ohm-m). In case of complex multi-segment structures the overall  $G = \sum G_i$ .

Inversion starting models account for the information known from drilling and seismic surveys, mainly, the thickness of sediments. The “normal” section for the Ukrainian EEP part was based on 1D inversion results obtained at the observatory KIV, while in the Carpathian region the 1D model for the observatory LVV was used (Semenov *et al.* 2008).

Inverted experimental data included impedance estimates for TM and TE modes and magnetic transfer functions. Data at 10-30 sites and 10-13 periods in the period range of 4-3600 s were selected at different profiles. First calculations were carried out separately for TE, TM impedances, and magnetic transfer functions (named below as TP). At the final inversion stage the model with the smallest RMS for these separate mode solutions was chosen as the starting for the joint TE + TM + TP inversion.

The description of the main features of the Carpathian anomaly of conductivity (CrAC) derived from 2D inversion models for all profiles shown in Fig. 2 (CaI-CaVII) is summarized in Table 1. The comparison of these models with the tectonics of the Carpathians indicates that CrAC is located between the Magura thrust and Pieniny Klippen Belt (Fig. 1). The depth to the top of CrAC decreases to the east of the CaIII profile from 8 to 5 km. The integral CrAC conductivity is reduced in the same direction. The width of this anomaly changes between 33 and 45 km.

The modeling along CaI and CaII has revealed a sharp difference in parameters of CrAC in the Tatra Mountains and Eastern Carpathians: the width is reduced at least twice and the depth to its top is increased. The conductance of the anomaly is much smaller in the Tatra Mts (CaI and CaII) than in the Eastern Carpathians (CaIII-CaVII).

The Kirovograd conductivity anomaly (KrAC) is covered with profile soundings on its whole length, from the coast of the Black Sea to the northern border of Ukraine (Fig. 2, KiI-KiVI). Its boundaries correlate with faults forming the Ingulets–Krivoy Rog–Krupetsk suture zone (Fig. 1). The KrAC modelling results can be presented in the form of two separated objects, A

Table 1

Features of the Carpathian and the Kirovograd conductivity anomalies

Profiles	Depth of the top [km]	Width [km]	$G \times 10^7$ [S·m]	Note
Carpathian conductivity anomaly				
CaI	18	18	7.2	*
CaII	18	15	8.2	
CaIII	8	33	52	
CaIV	8	45	38	
CaV	7	42	45	
CaVI	6	33	24	
CaVII	5	42	14	
Kirovograd conductivity anomaly				
KiI	28/7	18/16	5/8	The numerator options object A, denominator – B
KiII	16/21	16/15	6/8.4	
KiIII	21/12	24/9	8.3/0.3	
KiIV	12/10	18/5	5/0.01	
KiV	30/20	7/7	8/4.2	
KiVI	46/15	5/10	3/0.04	

\*)For the first time, 2D modelling of modular values of magnetic transition functions (TP) was performed (Zhdanov *et al.* 1986) along the international Geotraverse II (Fig. 2, CaV). Comparison of the inversion results with the previous model shows good agreement between the geometrical parameters of the two models for the main object, which caused abnormal behavior of TP data along the profile. For example, from the inversion the value of  $G$  is  $4.5 \times 10^8$  S·m, while previous value of  $G$  is  $4.8 \times 10^8$  S·m. Parameters of the object beneath the Carpathians and the Carpathian Foredeep much differ. According to the inversion results, the main part of the object occurs deeper, and the value of  $G$  is 2 times less than in the previous model. The resulting differences are within error limits, as postulated by the authors (Zhdanov *et al.* 1986).

and B. Table 1 shows their main characteristics at only those profiles which had relatively dense magnetic transfer function estimates, because MT responses were not available at all profiles. Object A has much higher  $G$  values than object B.

The joint 2D inversion of TE+TM+TP data was carried out along meridian profiles (Fig. 2c) where TE mode corresponds to northern direction of electric field. The inversion models were obtained for data at periods of 16-2500 s. Each profile contained ~20 observation sites. 2D inversion results

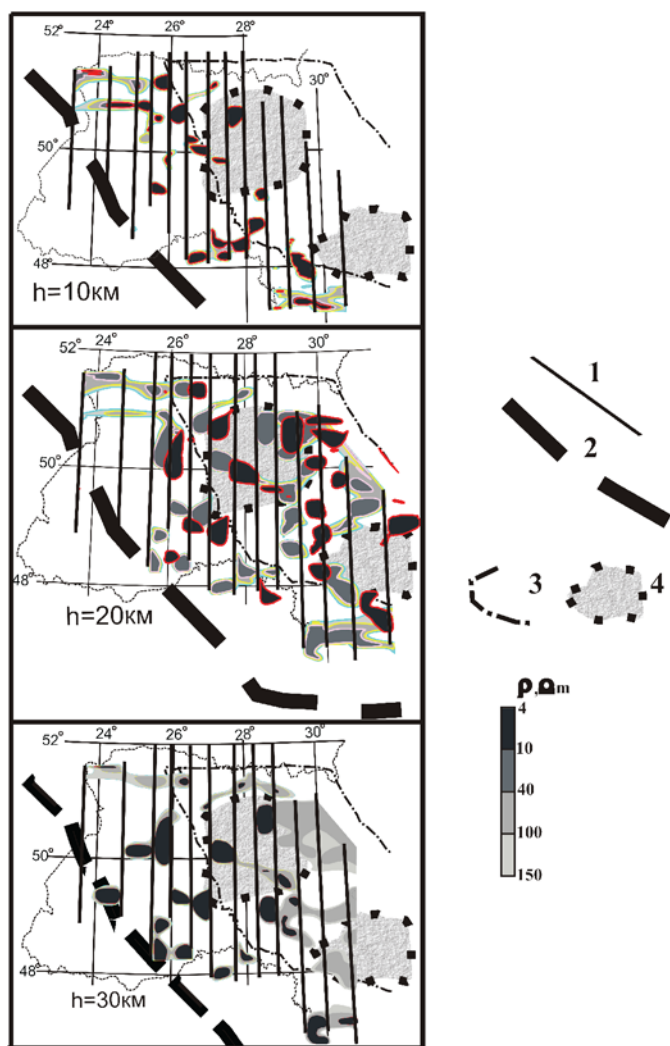


Fig. 5. Contours of crustal conductive objects at the southwestern EEP margin derived from 2D inversion; 1 – inversion profiles, 2 and 3 – borders of the EEP and the Ukrainian Shield, 4 – graphitization areas (Yatsenko 1996).

show that the investigated area hosts a number of local conductive objects. Top edges of some of them lie in the granite layer, but most of the objects are seen at depth of at least of 20 km (Fig. 5). Many conductive objects at such a depth are spatially correlated with areas of graphitization (Fig. 5).

## 5. QUASI-3D INVERSION

The models of the Carpathian and the Kirovograd conductivity anomalies obtained from 2D inversion were used as pilot conductivity distributions for a subsequent quasi-3D modelling (Kovacikova 2001). In the thin sheet ap-

proximation, the anomaly source is replaced by a thin sheet with the anomalous conductance  $S$  at a specified depth in the layered normal section. Equivalent currents within the thin sheet are calculated using a Price equation and the magnetic field at the ground surface can be calculated gradually from the related boundary conditions.

The collected magnetic transfer functions  $W_{zx}(\omega, \mathbf{r})$  and  $W_{zy}(\omega, \mathbf{r})$  for the period range of 400-6000 s at the territory of Czech Republic, Slovakia, Poland, Hungary, and Ukraine made it possible to trace the Carpathian conductivity anomaly (Kovacikova *et al.* 2010, Gordienko *et al.* 2011, 2012). The parameters of the layered medium below the sedimentary cover ( $>4$  km) were taken according to the 1D model for observatory LVV (Semenov *et al.* 2008). A thin sheet was located at a depth of 10 km to estimate the conductivity distribution in this layer (Kovacikova *et al.* 2010). Figure 6 shows the results of such analysis in the Ukrainian Carpathians and the adjacent part of Slovakia.

The magnetic transfer functions for the period range of 40-6000 s were also obtained for the region of the Kirovograd conductivity anomaly (Fig. 6). The complexity in the construction of this quasi-3D model follows from the fact that the anomaly crosses large sedimentary structure of the Dnieper-Donets Basin (Fig. 6). The sedimentary conductance at depths of 0-2 km was taken according to the data shown in Fig. 4. The parameters of layered medium below the sedimentary cover were taken according to 1D model for

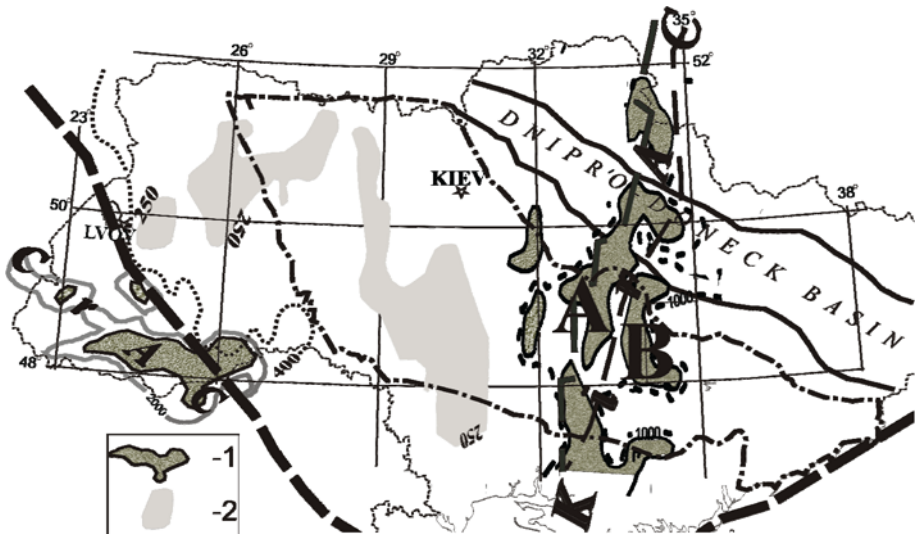


Fig. 6. The crustal conductance in Ukraine according to quasi-3D and 1D inversion of the MTS impedances; conductance values are shown over 4000 S (1) and less than 250 S (2); other notations in Fig. 1.

observatory KIV (Semenov *et al.* 2008). The thin sheet in the inversion was located at a depth from 12 to 20 km (Gordienko *et al.* 2005, 2006).

In recent years the new research has traced the Kirovograd anomaly from Ukraine into SW Russia in the frames of the international project KIROVOGRAD (Varentsov *et al.* 2012). The detailed description of the results of this project studying the geoelectrical structure of the western slope of the Voronezh Massive in Russia and Ukraine by means of the advanced simultaneous deep EM sounding array with natural field excitation and geological and geophysical analysis of the nature of the revealed crustal conducting anomalies has been given by Varentsov *et al.* (2012, 2013). Geoelectrical sections along the series of profiles and maps of sedimentary and crustal conductance obtained from 2D+ and quasi-3D data interpretations are shown in the cited papers. The main advantage of these studies was the use of horizontal MV inter-station responses at the stage of quasi-3D inversion with the two-sheet conductance estimation separated for subsurface and deep crustal distributions (Varentsov *et al.* 2012, 2013).

## 6. CONCLUSION AND DISCUSSION

The distribution of the sedimentary conductance was estimated at for territory of Ukraine and was used to build a world map of the sedimentary conductance (Vozar *et al.* 2006). These estimates are reaching 1000 S and more in the deep sedimentary basins only. The crustal conductance is less than 250 S for most parts of Ukraine. Two regional crustal anomalies exist there, and numerous additional local objects of low resistance were discovered. Most of them do not form large homogeneous areas in Ukraine. The greatest number of such objects is located in the range of 20-30 km in the Ukrainian Shield.

The obtained characteristics of the geoelectric crustal structure confirm the existence of two regional conductivity anomalies, namely, the Carpathian and the Kirovograd ones (Fig. 6). The modelling showed that the Carpathian conductivity anomaly in the Ukrainian Carpathians is located between the Pieniny Klippen Belt and the Magura thrust zone.

The anomalous behavior of MT fields in the region of Kirovograd conductivity anomaly can be explained by the existence of two conductive objects. These objects appear in 2D inversion, as well as in quasi-3D inversion, and spatially correspond to the location of the boundary fault zones that delineate the Ingulets–Krivoy Rog–Krupetsk suture zone. The strongest anomaly of the integral conductivity of object A is confined to the western fault zone and is located in the depth range of 18-40 km (Logvinov 2012).

The spatial distribution of the integral conductivity was obtained in Ukraine for the depth interval from the surface to 900 km. The same distribution was obtained at the Polish part of the EEP (Semenov and Jóźwiak

2005) and in Eurasia (Semenov and Jóźwiak 1999). The most conductive part of the mantle is situated at depths of 600-900 km. Conductivity distribution at the upper mantle depths may be presented as a layer with a gradual increase of conductivity with depth. The distribution of the mantle's apparent resistivity obtained for such a model was chosen as a reference for the correction of shift-effect in the MTS results.

We note that the new data and conclusions about the deep structure of the western part of Ukraine substantially complement the available concepts based primarily on the results of seismic and gravity-magnetic survey.

**Acknowledgments.** I am thankful to V.Yu. Semenov for simulating the work and for discussions.

#### References

- Ádám, A., T. Ernst, J. Jankowski, W. Jóźwiak, M. Hvozدارa, L. Szarka, V. Wesztergom, I. Logvinov, and S. Kulik (1997), Electromagnetic induction profile (PREPAN95) from the East European Platform (EEP) to the Pannonian Basin, *Acta Geod. Geophys. Hung.* **32**, 1-2, 203-223, DOI: 10.1007/BF03325488.
- Bondarenko, A.P., A.I. Bilinsky, and F.I. Sedova (1972), *Geoelectromagnetic Variations in the Soviet Carpathians*, Naukova Dumka, Kiev, 116 pp. (in Russian).
- Constable, S.C., R.L. Parker, and C.G. Constable (1987), Occam's inversion: A practical algorithm for generating smooth models from electromagnetic sounding data, *Geophysics* **52**, 3, 289-300, DOI: 10.1190/1.1442303.
- Dyakonova, A.G., A.I. Ingerov, and I.I. Rokityansky (1986), *Electromagnetic Soundings on the Eastern European Platform and in the Ural*, Naukova Dumka, Kiev (in Russian).
- Egbert, G.D. (1997), Robust multiple-station magnetotelluric data processing, *Geophys. J. Int.* **130**, 2, 475-496, DOI: 10.1111/j.1365-246X.1997.tb05663.x.
- Egbert, G.D., and J.R. Booker (1986), Robust estimation of geomagnetic transfer functions, *Geophys. J. Int.* **87**, 1, 173-194, DOI: 10.1111/j.1365-246X.1986.tb04552.x.
- Gordienko, V.V., I.V. Gordienko, O.V. Zavgorodnyaya, S. Kovachikova, I.M. Logvinov, V.N. Tarasov, and O.V. Usenko (2005), *Ukrainian Shield (Geophysics, Deep Processes)*, Korvin Press, Kiev (in Russian).
- Gordienko, V.V., I.V. Gordienko, O.V. Zavgorodnyaya, S. Kovachikova, I.M. Logvinov, J. Pek, V.N. Tarasov, and O.V. Usenko (2006), *Dnepr-Donetsk Basin (Geophysics, Deep Processes)*, Korvin Press, Kiev, 143 pp. (in Russian).

- Gordienko, V.V., I.V. Gordienko, O.V. Zavgorodnyaya, S. Kovachikova, I.M. Logvinov, V.N. Tarasov, and O.V. Usenko (2011), *Ukrainian Carpathians (Geophysics, Deep Processes)*, Logos, Kiev (in Russian).
- Gordienko, V.V., I.V. Gordienko, O.V. Zavgorodnyaya, S. Kovachikova, I.M. Logvinov, and V.N. Tarasov (2012), *Volyno-Podolian Plate (Geophysics, Deep Processes)*, Naukova Dumka, Kiev (in Russian).
- Ingerov, A.I., I.I. Rokityansky, and V.I. Tregubenko (1999), Forty years of MTS studies in the Ukraine, *Earth Planets Space* **51**, 10, 1127-1133, DOI: 10.1186/BF03351586.
- Jankowski, J., J. Marianiuk, A. Ruta, C. Sucksdorff, and M. Kivinen (1984), Long-term stability of a torque-balance variometer with photoelectric converters in observatory practice, *Geophys. Surv.* **6**, 3-4, 367-380, DOI: 10.1007/978-94-009-5283-6\_17.
- Jóźwiak, W. (2013), Electromagnetic study of lithospheric structure in the marginal zone of East European Craton in NW Poland, *Acta Geophys.* **61**, 5, 1101-1129, DOI: 10.2478/s11600-013-0127-z.
- Kovacikova, S. (2001), Modelling of the geomagnetic induction anomaly sources over the eastern margin of the Bohemian Massif and its contact with the West Carpathians, Ph.D. Thesis, Univerzita Karlova, Praha, Czech Republic, 95 pp.
- Kovacikova, S., W. Jóźwiak, I. Logvinov, K. Nowożyński, J. Pek, B. Ladanivskyy, and V. Tarasov (2010), Database of geomagnetic induction vectors across the Carpathians and modelling of the regional conductivity distribution. **In:** *19th Congress of the Carpathian–Balkan Geological Association, 23-26 September, Thessaloniki, Greece.*
- Ladanivskyy, B.T. (2003), The algorithm of data processing MTS. **In:** *Abstracts Fifth Geophysical Readings of V.V. Fedinskogo, 27 February – 1 March 2003, Moscow, Russia*, 134-135 (in Russian).
- Ladanivskyy, B.T., V.Yu. Semenov, and I.M. Logvinov (2010), Magnetovariational sounding method of Earth's mantle at period band  $10^4$ - $10^5$  s, *Geophys. J.* **32**, 3, 50-59 (in Russian).
- Logvinov, I.M. (2002), Applying the horizontal spatial gradient method for the deep conductivity estimations in the Ukraine, *Acta Geophys. Pol.* **50**, 4, 567-573.
- Logvinov, I.M. (2012), Geoelectrical parameters of the crust and mantle south-west of the East-European platform and Carpathians, Ph.D. Thesis, Subbotin Institute of Geophysics, National Academy of Sciences of Ukraine, Kiev, Ukraine, 306 pp. (in Russian).
- Parker, R.L., and K.A. Whaler (1981), Numerical methods for establishing solutions to the inverse problem of electromagnetic induction, *J. Geophys. Res.* **86**, B10, 9574-9584, DOI: 10.1029/JB086iB10p09574.
- Rakhlin, L., L. Guleuk, E. Nakalov, and O. Kuznecov (2005), Magnetotelluric station GEOMAG-02. **In:** *New Geophysical Technology Forecasting and Monitoring of the Geological Environment*, Lviv, 22-23 (in Russian).

- Rokityansky, I.I. (1982), *Geoelectromagnetic Investigation of the Earth's Crust and Mantle*, Springer Verlag, Berlin Heidelberg, DOI: 10.1007/978-3-642-61801-7.
- Rokityansky, I.I., S.N. Kulik, I.M. Logvinov, and V.N. Shuman (1976), Deep magnetovariational studies in Ukraine. **In:** A. Ádám (ed.), *Geoelectric and Geothermal Studies*, KAPG Geophysical Monograph, Hungarian Academy of Sciences, Budapest, 634-639.
- Schmucker, U. (2003), Horizontal spatial gradient sounding and geomagnetic depth sounding in the period range of daily variations. **In:** *Protokoll über das 20. Kolloquium Elektromagnetische Tiefenforschung, 29.09-3.10.2003, Königstein, Germany*, 228-237.
- Semenov, V.Yu. (1998), Regional conductivity structures of the Earth's mantle, *Publ. Inst. Geophys. Pol. Acad. Sc.* **C-65**, 302, 122 pp.
- Semenov, V.Yu., and W. Józwiak (1999), Model of the geoelectrical structure of the mid- and lower mantle in the Europe – Asia region, *Geophys. J. Int.* **138**, 2, 549-552, DOI: 10.1046/j.1365-246X.1999.00888.x.
- Semenov, V.Yu., and W. Józwiak (2005), Estimation of the upper mantle electric conductance at the Polish Margin of the East European Platform, *Izv. – Phys. Solid Earth* **41**, 4, 326-332.
- Semenov, V.Yu., and W. Józwiak (2006), Lateral variations of the mid-mantle conductance beneath Europe, *Tectonophysics* **416**, 1-4, 279-288, DOI: 10.1016/j.tecto.2005.11.017.
- Semenov, V.Yu., S.N. Kulik, and I.M. Logvinov (1998), Estimations of the geoelectrical structure of the mantle in Ukraine, *Dokl. Nat. Acad. Sc.* **10**, 134-137.
- Semenov, V.Yu., J. Pek, A. Ádám, W. Józwiak, B. Ladanyvskyy, I.M. Logvinov, P. Pushkarev, J. Vozar, and Experimental Team of CEMES Project (2008), Electrical structure of the upper mantle beneath Central Europe: Results of the CEMES project, *Acta Geophys.* **56**, 4, 957-981, DOI: 10.2478/s11600-008-0058-2.
- Shuman, V., and S. Kulik (2002), The fundamental relations of impedance type in general theories of the electromagnetic induction studies, *Acta Geophys. Pol.* **50**, 4, 607-618.
- Siripunvaraporn, W., and G. Egbert (2000), An efficient data-subspace inversion method for 2-D magnetotelluric data, *Geophysics.* **65**, 3, 791-803, DOI: 10.1190/1.1444778.
- Varentsov, Iv.M., S. Kovacikova, V.A. Kulikov, I.M. Logvinov, V.I. Tregubenko, A.G. Yakovlev, and Workgroup KIROVOGRAD (2012), Simultaneous magnetotelluric and magnetovariational soundings in the western slope Voronezh massif, *Geophys. J.* **34**, 4, 90-107 (in Russian).
- Varentsov, I.M., V.V. Gordienko, I.V. Gordienko, O.V. Zavgorodnyaya, S. Kovachikova, I.M. Logvinov, V.N. Tarasov, and V.I. Tregubenko (2013), *The Slope of the Voronezh Crystalline Massif (Geophysics, Deep processes)*, Logos, Kiev (in Russian).

- Vojar, J., V.Yu. Semenov, A.V. Kuvshinov, and C. Manoj (2006), Updating the map of Earth's surface conductance, *Eos Trans. AGU* **87**, 33, 326-331, DOI: 10.1029/2006EO/33004.
- Wieladek, R., and T. Ernst (1977), Application of the method of least squares to determining impulse responses and transfer functions, *Publ. Inst. Geophys. Pol. Acad. Sc.* **G-1**, 110.
- Yatsenko, V.G. (1996), Structural and morphological and genetic types of graphite on an example of deposits of the Ukrainian shield, Ph.D. Thesis, Institute of Geology, Academy of Sciences of Ukraine, Kiev, Ukraine, 253 pp. (in Russian).
- Zhdanov, M.S., N.G. Golubev, I.M. Varentsov, L.M. Abramova, V.S. Shneer, M.N. Berdichevsky, O.N. Zhdanova, V.V. Gordienko, S.N. Kulik, and A.I. Bilinsky (1986), 2-D model fitting of a geomagnetic anomaly in the Soviet Carpathians, *Ann. Geophys. B* **4**, 3, 335-342.

Received 28 January 2014

Received in revised form 3 November 2014

Accepted 18 November 2014



## Prediction of the Shear Wave Velocity from Compressional Wave Velocity for Gachsaran Formation

Saeed PARVIZI<sup>1</sup>, Riyaz KHARRAT<sup>1</sup>, Mohammad R. ASEF<sup>2</sup>,  
Bijan JAHANGIRY<sup>3</sup>, and Abdolnabi HASHEMI<sup>1</sup>

<sup>1</sup>Petroleum University of Technology, Department of Petroleum Engineering,  
Ahwaz, Iran; e-mail: saeed.parvizi68@gmail.com

<sup>2</sup>Kharazmi University, Faculty of Earth Sciences, Department of Applied Geology,  
Tehran, Iran

<sup>3</sup>National Iranian South Oil Company, Department of Drilling Engineering,  
Ahwaz, Iran

### Abstract

Shear and compressional wave velocities, coupled with other petrophysical data, are very important for hydrocarbon reservoir characterization. *In situ* shear wave velocity ( $V_s$ ) is measured by some sonic logging tools. Shear velocity coupled with compressional velocity is vitally important in determining geomechanical parameters, identifying the lithology, mud weight design, hydraulic fracturing, geophysical studies such as VSP, *etc.* In this paper, a correlation between compressional and shear wave velocity is obtained for Gachsaran formation in Maroon oil field. Real data were used to examine the accuracy of the prediction equation. Moreover, the genetic algorithm was used to obtain the optimal value for constants of the suggested equation. Furthermore, artificial neural network was used to inspect the reliability of this method. These investigations verify the notion that the suggested equation could be considered as an efficient, fast, and cost-effective method for predicting  $V_s$  from  $V_p$ .

**Key words:** compressional wave velocity, shear wave velocity, sonic log, DSI log, MATLAB software.

## 1. INTRODUCTION

Compressional and shear velocities ( $V_p$  and  $V_s$ , respectively) are important in seismic inversion and petrophysical evaluation of formations, especially for analysis of reservoir geomechanical properties. For estimating the geomechanical parameters such as Young's modulus, Poisson's ratio, and Lamé parameters, both  $V_p$  and  $V_s$  plus density are needed. Accordingly, knowing  $V_p$ ,  $V_s$ , and density, other elastic parameters of a rock formation can be calculated in terms of the acoustic wave velocities (Liu *et al.* 2012).

$$\mu = \rho V_s^2, \quad (1)$$

$$E = \frac{\rho V_s^2 (3V_p^2 - 4V_s^2)}{(V_p^2 - V_s^2)}, \quad (2)$$

$$\lambda = \rho V_p^2 - 2\rho V_s^2, \quad (3)$$

$$K = \rho V_p^2 - \frac{4}{3}\rho V_s^2, \quad (4)$$

$$\nu = \frac{(V_p^2 - 2V_s^2)}{2(V_p^2 - V_s^2)}. \quad (5)$$

According to the acoustic wave propagation theory, the  $P$ -wave ( $V_p$ ) and  $S$ -wave ( $V_s$ ) velocities can be expressed as:

$$V_p = \sqrt{\frac{\lambda + 2\mu}{\rho}}, \quad (6)$$

$$V_s = \sqrt{\frac{\mu}{\rho}}. \quad (7)$$

The above-mentioned geomechanical parameters are useful in estimating maximum and minimum horizontal stresses, mud weight design, *etc.* Therefore, rock mechanical properties can be estimated using some sonic log providing  $P$ - and  $S$ -wave velocity information such as dipole sonic log and so on. However, very often  $S$ -wave velocity is not recorded in the field all the time due to the cost constrains and lack of technology. Therefore, prediction of the  $S$ -wave velocity is an interesting objective for researchers (Farrokhrouz and Asef 2010). Alternatively, if sonic tools to measure  $V_s$  are not available, we may use a prediction equation for estimating shear wave velocity based on compressional wave velocity obtained from monopole sonic log (Liu *et al.* 2012). Almost all such equations are empirical (Asef

and Farrokhrouz 2010). Castagna *et al.* (1985) suggested Eq. 8, that is, a linear equation based on laboratory data for water-saturated elastic silicate rocks.

$$V_s = 0.862V_p - 1.172 . \tag{8}$$

Han (1986) used an extensive experimental dataset of sandstone with wide ranges of porosity and clay content variation to obtain the equation

$$V_s = 0.794V_p - 0.787 . \tag{9}$$

Brocher (2005) developed a relation between elastic wave velocity in the Earth’s crust and developed Eq. 10 indicating a nonlinear relationship between  $V_p$  and  $V_s$ .

$$V_s = 0.7858 - 1.2344V_p + 0.7949V_p^2 - 0.1238V_p^3 + 0.0064V_p^4 , \quad 1.5 < V_p < 8 , \tag{10}$$

where  $V_s$  and  $V_p$  are in km/s. It is noticed that each of the above empirical equations was developed for a specific field and a specific lithology. Nevertheless, if they are used at Iranian fields, they may result in erroneous predictions. Figures 1 to 3 illustrate the accuracy of the said correlations in Gachsaran formation.

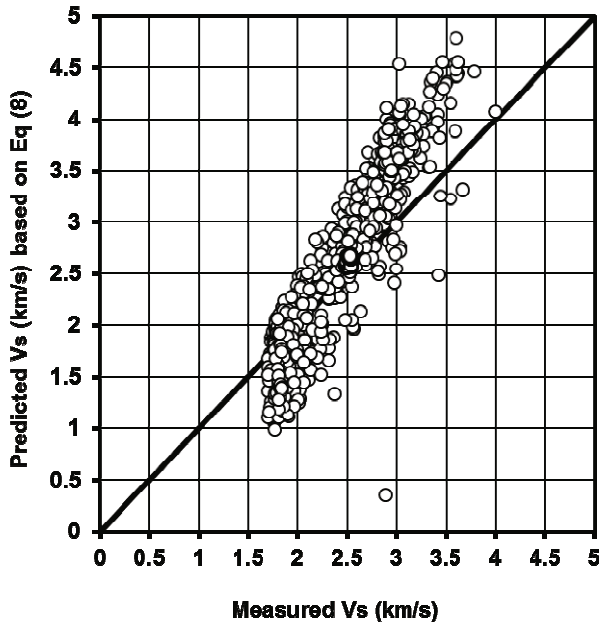


Fig. 1. Calculated  $V_s$  versus measured values using Eq. 8.

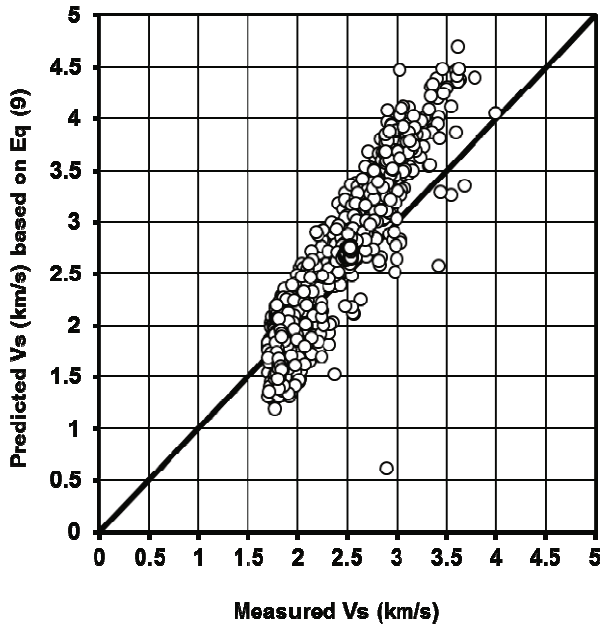


Fig. 2. Calculated  $V_s$  versus measured values using Eq. 9.

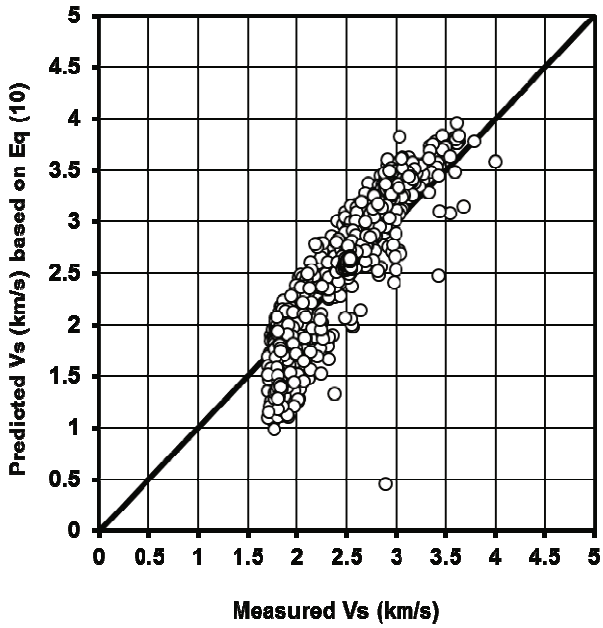


Fig. 3. Calculated  $V_s$  versus measured values using Eq. 10.

Therefore, the present study was conducted to develop a reliable model for predicting shear wave velocity in a rock, based on compressional wave velocity in Maroon oil field. For this purpose, we utilized different regression models to obtain the most appropriate approach. We compared real field measurements of  $V_s$  with predicted values. Furthermore, we applied a neural network model to examine the accuracy and reliability of the suggested approach.

## 2. GEOLOGICAL SETTINGS OF THE STUDIED FIELDS

In this research we used data from Maroon oil field in Ahwaz, Southeast Iran. The main objective of this study was predicting shear wave velocity based on  $P$ -wave data. As it is obvious from petrophysical logs and geological studies, Gachsaran formation in Maroon oil field consist of seven members as presented in Table 1 (Memari 2013).

Table 1

Lithology of the studied formations

Formation	Lithology	Density
Gachsaran 7	made up of mainly anhydrite and some grey marl and limestone	$2.58 < \text{density} < 3.02$
Gachsaran 6	mainly anhydrite, salt, red and gray marl layers	$2.46 < \text{density} < 2.9$
Gachsaran 5	mainly anhydrite, salt, red and gray marl layers	$2.22 < \text{density} < 2.85$
Gachsaran 4	mainly anhydrite, salt and gray marl layers	$2.5 < \text{density} < 2.97$
Gachsaran 3	thick anhydrites with subordinate salt in the lower half, and alternating anhydrites, thin limestones and marls in the upper half	$2.46 < \text{density} < 2.94$
Gachsaran 2	thick salt units with intervening anhydrite and thin limestones	$2.53 < \text{density} < 2.92$
Gachsaran 1 (Cap Rock)	mainly anhydrite and gray marl and minor layers of limestone	$2.69 < \text{density} < 2.71$

The dipole shear sonic imager (DSI) combines monopole and dipole sonic acquisition capabilities for the reliable acoustic measurement of compressional, shear and Stoneley slowness. This is a Schlumberger company tool. DSI log for Gachsaran formation in Maroon field was run. Therefore,  $V_s$  and  $V_p$  were obtained directly from this log.

### 3. DATA ANALYSIS

Regression analysis was carried out to estimate and model the relationship between a response variable and one or more predictors. An empirical equation is not a perfect relationship. In general, all observation points for a statistical relationship do not fall directly on the prediction curve. Meanwhile, there are many regression models to define the best fit between two parameters, such as: linear, polynomial, exponential, *etc.* (Rawlings *et al.* 1998). Therefore, in the first step we obtained well log readings of  $V_s$  and  $V_p$  for 4000 points from 2984 to 3617 m depth at the studied well. Randomly, we picked 1/4 of data points (1000 points) as “additional validating data” for further investigation, and we used 3/4 of data points (3000 points) as “modeling data” for developing prediction equation.

TableCurve software package and MATLAB Curve Fitting Toolbox were used to carry out all regression analyses (linear, polynomial, exponential...). Therefore, the mutual relationship between  $V_p$  and  $V_s$  was studied. The value of  $R^2$  and adjusted  $R^2$  ( $R^2$  adjusted for the number of independent variables in the model) are presented in Table 2.  $R^2$  is the *r*-square defined as:

$$R^2 = 1 - \frac{\sum_i (y_i - f_i)^2}{\sum_i (y_i - \bar{y})^2} \quad (11)$$

A data set has values  $y_i$  which have an associated modeled value  $f_i$  (sometimes called the predicted values) and  $\bar{y}$  is the mean of the observed data. A very good fit yields value of 1, whereas a poor fit results in a value near 0. Adjusted  $R^2$  is defined as:

$$R_{\text{adj}}^2 = 1 - \frac{\frac{\sum_i (y_i - f_i)^2}{n-d-1}}{\frac{\sum_i (y_i - \bar{y})^2}{n-1}}, \quad (12)$$

where  $n$  is the number of points in the data set. Adjusted  $R^2$  is especially important in this research because if unnecessary variables are included,  $R^2$  can be misleadingly high. As it is observed in Table 2, in case of Eq. 19 the value of  $R^2$  increased and RMSE reduced significantly. Also, it should be clarified that  $R^2$  and adjusted  $R^2$  are in reasonable agreement with each other in case of Eq. 19 which implies contribution of  $V_p$  to the prediction equation. Figure 4 illustrates the scatter of data points against prediction curve for Eq. 19. The accuracy of Eq. 19 is further clarified when measured values are plotted against predicted values in Fig. 5. It seems that the exponential model (Eq. 19) is the best for Gachsaran formation. The results of these

analyses are listed in Table 2. The Root Mean Squared Error (RMSE) in all models was estimated as:

$$RMSE = \sqrt{\frac{\sum_{i=1}^n (Vs(\text{observed})_i - Vs(\text{predicted})_i)^2}{n}} \quad (13)$$

Table 2

Prediction equations and impact parameters for Gachsaran formation

Equation name	Model summary			Equation	
	$R^2$	$R^2_{adj}$	RMSE	Statistical criteria	
Linear	0.8885	0.8885	0.16	$V_s = 0.4078 - 0.4614V_p$	(14)
4th order	0.8835	0.8832	0.1481	$V_s = 14.38 - 12.04V_p + 4.061V_p^2 - 0.5692V_p^3 + 0.02913V_p^4$	(15)
Power	0.8868	0.8868	0.1612	$V_s = 0.7144V_p^{0.8308}$	(16)
Logarithmic	0.9014	0.9013	0.1506	$V_s = 15.64 - 36.72\ln(V_p) + 34.2(\ln(V_p))^2 + 13.27(\ln(V_p))^3 - 1.926(\ln(V_p))^4$	(17)
Inverse	0.8187	0.8186	0.2041	$V_s = 4.226 - \frac{7.465}{V_p}, 1.767 \leq V_p$	(18)
Exponential	0.8946	0.8945	0.1555	$V_s = 1.532 + \frac{1.8790389}{1 + e^{\left(\frac{V_p - 4.4767345}{0.839419}\right)}}$	(19)
S-curve	0.863	0.8629	0.1774	$V_s = e^{\left(1.7 - \frac{3.454}{V_p}\right)}$	(20)

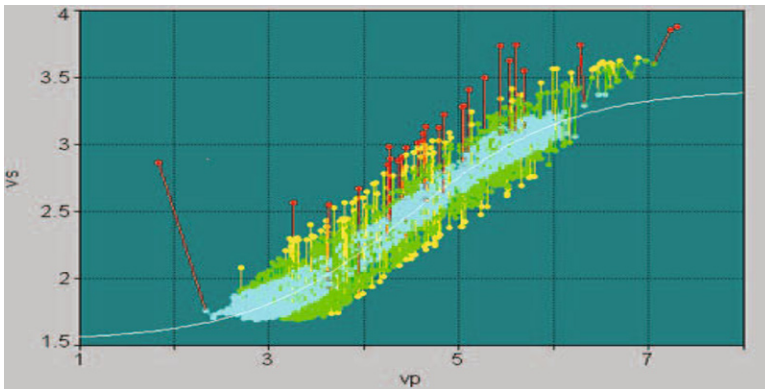


Fig. 4. The main plot of Eq. 19.

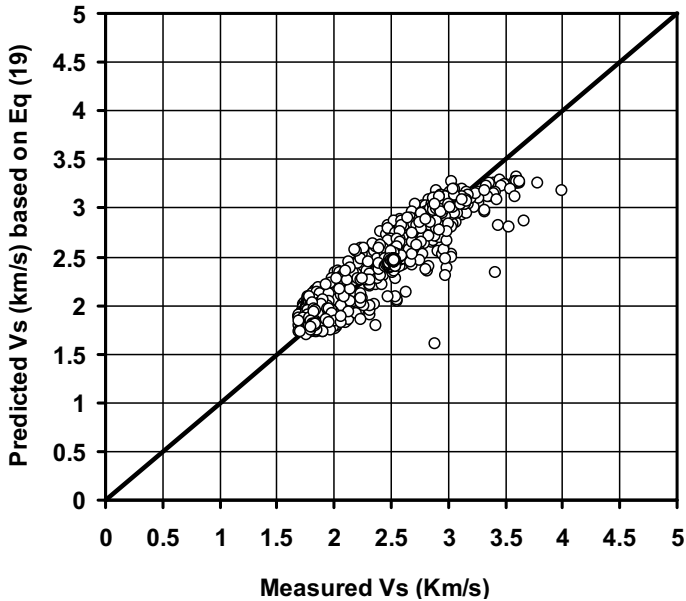


Fig. 5. Measure  $V_s$  versus values calculated based on Eq. 19.

#### 4. GENETIC ALGORITHM OPTIMIZATION

Genetic Algorithm (GA) is mostly used for solving optimization problems based on principles of evolution. GA is essentially an iterative, population based, parallel global search algorithm. Solution to the problem is shown by each individual in the population and the population of individuals is kept at each generation. A fitness value is given to any individual to clue the search. Individuals with superior fitness values are selected and undergo genetic transformation by genetic operators such as crossover and mutation. The crossover operator randomly selects two individuals as parents and exchanges part of their structure to produce two new individuals. The mutation operator just randomly selects one individual from the parent population and changes its internal demonstration and puts it in the child population. For improving the search performance, both of the operator rates should be intentionally adjusted. The newly produced child population becomes the parent population for the subsequent generation and undergoes the same process until a stopping criterion has been satisfied.

For the present study, MATLAB Genetic Algorithm Toolbox for optimization was used to search optimal values of correlation constants for Eq. 19. The performance of GA is generally affected by the size of the initial population, the number of generations, and GA parameters including selection rate, mutation rate, and crossover rate. Therefore, the best fitness of the end

population was evaluated under different sizes of initial population and generations as well as different selection rate, mutation rate, and crossover rate. The best fitness was obtained when the initial population of 2000, number of generations of 200, selection rate of 0.08, mutation rate of 0.05, and crossover rate of 0.6 were obtained by trial and error. The optimum constants are shown in Eq. 21.

$$V_s = 1.68 + \frac{1.56}{1 + \text{EXP}\left(\frac{-V_p - 4.46}{0.63}\right)} \tag{21}$$

**5. VERIFICATION ANALYSIS**

At this step,  $V_s$  is predicted using author’s equation (Eq. 21) as well as Eqs. 8-10 without any change of constants in these three equations. RMSE is calculated for identifying the accuracy of each equation and comparing the results of correlations with real value. The results are shown in Table 3. In this table it is clearly observed that RMSE for Eq. 21 is reasonably less than that for other equations.

Table 3  
RMSE for different prediction equations

Correlation name	Equation no.	Calculated RMSE
Authors	21	0.1741655
Castagna <i>et al.</i> (1985)	8	0.469219
Han (1986)	9	0.458684
Brocher (2005)	10	0.336383

**6. NEURAL NETWORK MODEL**

MATLAB Neural Network Toolbox was used to examine the accuracy of Eq. 21. In the first step, a network including 3000 points (out of 4000) was generated; we called it the “modeling data”, while 1000 points were the unseen data. We did not use 1000 points to generate neural network model to avoid overtraining. Instead, we used these 1000 points as “additional validating data”. We considered  $V_p$  data as input and  $V_s$  data as output. This is because the objective of this research was predicting  $V_s$  based on  $V_p$ . Accordingly, “modeling data” (containing 3000 points) were divided into 3 parts: 70% for training (2100 points), 15% for validation (450 points), and 15% for testing (450 points). We know that the number of the hidden neurons affects the accuracy of the result. In order to obtain the best results, we

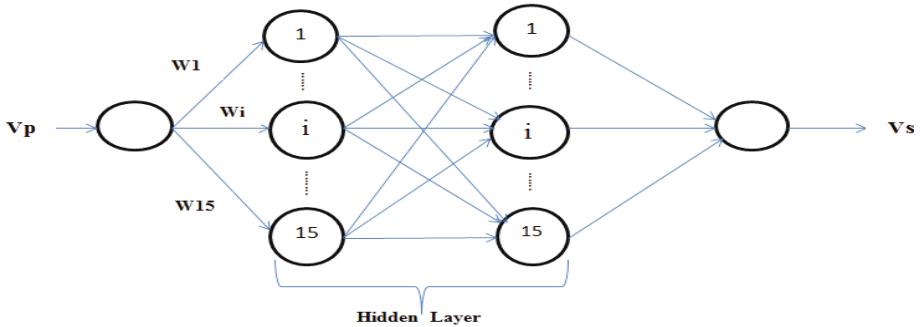


Fig. 6. The architecture of the network developed for  $V_s$  prediction.

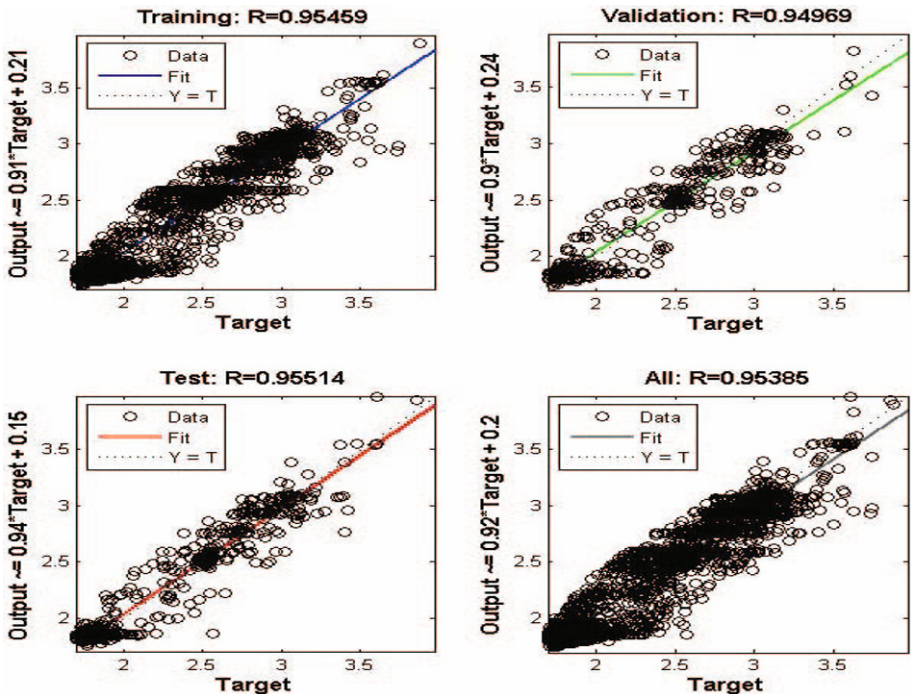


Fig. 7. Establishment of ANN for predicting  $V_s$  using neural network fitting.

examined different number of hidden neurons. Finally, the best results were obtained by 30 hidden neurons (two hidden layers with 15 hidden unite in each). Figure 6 represents a simple drawing of the structure of the network made to predict  $V_s$ .

Figure 7 illustrates four steps of the network generation and their fitness values. This figure shows that the correlation coefficient for tested data is 0.95514, which indicates that reliable results can be obtained.

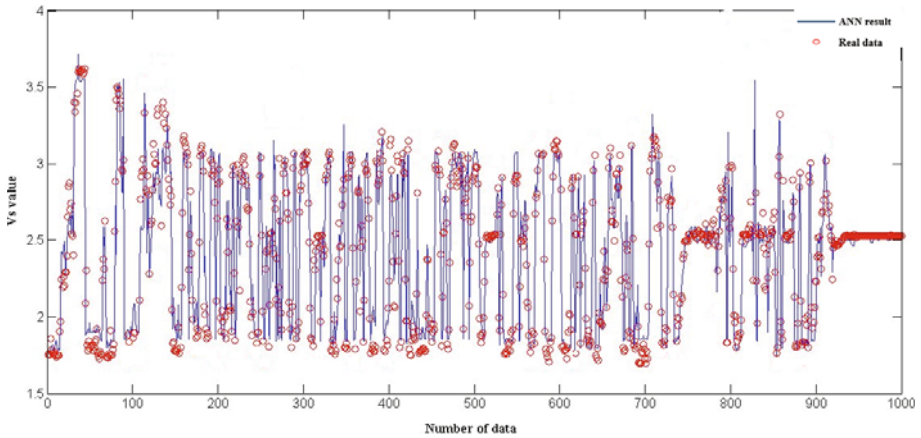


Fig. 8. Performance of ANN for predicting  $V_s$  using “additional validating data”.

In the next step, the established network model was employed for predicting  $V_s$  using “additional validating data” (1000 points of unseen data). Then the results of the network was compared with real value of the  $V_s$ . Figure 8 illustrates the comparison of the  $V_s$  value predicted by Artificial Neural Network (ANN) against real values. RMSE and  $R^2$  were equal to 0.1573 and 0.8985, respectively, which indicates a fairly good prediction.

### 7. DETERMINING THE ACCURACY OF EQUATION 21 IN OTHER WELLS

In the last step of this research, reliability of Eq. 21 was further examined in other wells. Well B at Maroon reservoir has monopole sonic log in Gachsaran formation and only  $V_p$  can be obtained from this log. Both Eq. 21 and

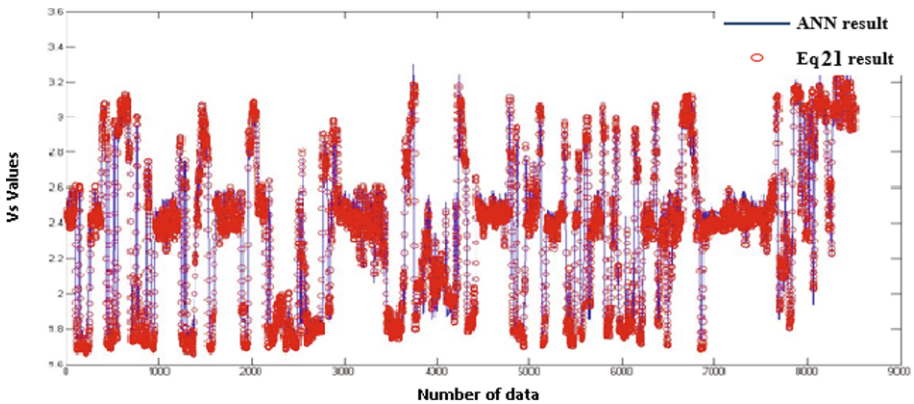


Fig. 9. Prediction of  $V_s$  from  $V_p$  using ANN/Eq. 21 in well B in Maroon reservoir.

the established ANN were used to predict shear wave velocity for Gachsaran formation in well B. A statistical correlation assessment was carried out to compare predicted shear wave velocity based on these two approaches (Eq. 21 and ANN). RMSE and  $R^2$  were equal to 0.464 and 0.987, respectively. This indicated that predictions of  $V_s$  from  $V_p$  based on these two methodologies are very similar. The result is shown in Fig. 9. However, Eq. 21 is preferred because it is simpler.

## 8. CONCLUSIONS

We demonstrated that the shear wave velocity can be predicted from the compressional wave velocity. We suggested an equation that can efficiently minimize the errors and is more accurate than the three previous equations, namely Castagna *et al.* (1985), Han (1986), and Brocher (2005) ones. The suggested equation is reliable to predict shear wave velocity for anhydrite, salt, marl, and limestone formations. Genetic algorithm was used to obtain the optimal value for constants of the suggested equation. Accordingly, both the ANN model and the suggested equation could successfully predict  $V_s$ . The suggested correlations for predicting the shear velocity in Gachsaran formation is reliable enough to be used in a case monopole log is at hand and  $V/S$  data are not available due to the cost constrains, lack of technology or old cased wells.

**Acknowledgement.** Authors would like to appreciate the National Iranian Oil Company (NIOC) for providing data and support.

### *Nomenclature*

DSI Log	– Dipole Shear Sonic imager
MDA	– Monopole-Dipole Array
VSP	– Vertical Seismic Profiling
$V_s$	– Shear wave velocity [km/s]
$V_p$	– Compressional wave velocity [km/s]
$E$	– Young's modulus
$\nu$	– Poisson ratio
$k$	– Bulk modulus
$\lambda$	– Lamé parameter
$\mu$	– Shear modulus
$R^2$	– Square error
$R^2_{\text{adj}}$	– Adjusted Square Error
RMSE	– Root Mean Square Error
ANN	– Artificial Neural Networks

## References

- Asef, M.R., and M. Farrokhrouz (2010), Methods and parameters for estimation of wave velocity in rock. **In:** *19th Int. Geophysical Congress and Exhibition, 23-26 November 2010, Turkey, Ankara*, DOI: 10.13140/2.1.5072.5440.
- Brocher, T.M. (2005), Empirical relations between elastic wavespeeds and density in the Earth's crust, *Bull. Seismol. Soc. Am.* **95**, 6, 2081-2092, DOI: 10.1785/0120050077.
- Castagna, J.P., M.L. Batzle, and R.L. Eastwood (1985), Relationships between compressional-wave and shear-wave velocities in elastic silicate rocks, *Geophysics* **50**, 4, 571-581, DOI: 10.1190/1.1441933.
- Farrokhrouz, M., and M.R. Asef (2010), Dominant parameters for estimation of shear wave velocity. **In:** *19th Int. Geophysical Congress and Exhibition, 23-26 November 2010, Turkey, Ankara*.
- Han, D.H. (1986), Effects of porosity and clay content on acoustic properties of sandstones and unconsolidated sediments, Ph.D. Thesis, Stanford University, Department of Geophysics, Stanford, USA.
- Liu, Y., Z. Chen, and K. Hu (2012), Shear velocity prediction and its rock mechanic implications. **In:** *Conf. GeoConvention 2012: Vision, 14-18 May 2012, Calgary, Canada*, 5 pp.
- Memari, A. (2013), Evaluation of surface subsidence in one of Iran's oil fields using INSAR technique, *Am. J. Oil Chem. Technol.* **1**, 4, 9-17.
- Rawlings, J.O., S.G. Pantula, and D.A. Dickey (1998), *Applied Regression Analysis: A Research Tool*, 2nd ed., Springer Texts in Statistics, Springer, New York.

Received 6 July 2014

Received in revised form 10 October 2014

Accepted 15 October 2014

# Modeling Electrical Field Distribution in Layered Geological Rock Formations with a Borehole Using the Coulomb Charges Method

Adam CICHY and Andrzej OSSOWSKI

AGH University of Science and Technology,  
Department of Geology, Geophysics and Environmental Protection,  
Kraków, Poland; e-mails: [cichy@agh.edu.pl](mailto:cichy@agh.edu.pl), [ossowski@geol.agh.edu.pl](mailto:ossowski@geol.agh.edu.pl)

## Abstract

The Coulomb charges method is used to model apparent resistivity measurements carried out in layered geological formations with a borehole using various devices. It is characterized by a high level of effectiveness and accuracy. The results are compared with the theoretical solutions for a homogenous medium with the borehole and invaded zone for point current source lateral devices. The relative error was less than 2% for different values of the range of the invaded zone and resistivity of invaded and true resistivity of formation.

**Key words:** Coulomb charges method, apparent resistivity, lateral device, normal device.

## 1. INTRODUCTION

Modeling borehole geophysical tools which measure the apparent resistivity is very important in order to determine the true resistivity of a rock formation. Currently, the finite element method is mainly used for this purpose (Tan *et al.* 2011). Calculations using this method are time-consuming and require powerful computers. For such a type of modeling, the Coulomb charges method can be used (Alpin 1964, Alpin *et al.* 1985). The algorithm

proposed in this paper has been modified from algorithms published previously and shows a high degree of effectiveness and accuracy. It is also much less time-consuming and calculations can be carried out on an ordinary PC.

**2. THEORETICAL BASIS**

The Coulomb charges method (Alpin 1964, Alpin *et al.* 1985) can be used to solve the first kind of boundary problem for the Laplace equation with internal boundary conditions by reducing it to the Fredholm integral equations of the second kind. The algorithm presented here assumes a rock formation model consisting of horizontal homogenous layers with a vertical borehole as well as vertical cylindrical coaxial homogenous layers with diameters reflecting the ranges of invaded zones. Horizontal and vertical layers can be of different thickness and resistivity. The idea of the Coulomb charges method is as follows (Alpin 1964, Alpin *et al.* 1985):

At the boundary between two conducting media with different resistivity, the normal component of current density vector is continuous. At each point “p” laying on the surface separating two media we have the following relation:

$$\frac{1}{R^i} \cdot E_n^i(p) = \frac{1}{R^{i+1}} \cdot E_n^{i+1}(p) , \tag{1}$$

where  $R^i$  and  $R^{i+1}$  are the resistivities of two homogenous media with numbers  $i$  and  $i + 1$ ; and  $E_n^i(p)$  and  $E_n^{i+1}(p)$  are the normal components of the electrical field at point “p”.

The normal component of the electrical field,  $E_n$ , can be explained by the presence of surface charge density  $\sigma(p)$ . The dependence between the surface charge density and normal components of electrical field at point “p” is expressed by the following relation:

$$E_n^{i+1}(p) - E_n^i(p) = \frac{\sigma(p)}{\epsilon_0} , \tag{2}$$

where  $\epsilon_0$  is the permittivity of vacuum.

Transforming Eqs. 1 and 2 we obtain the following relation (Alpin 1964, Alpin *et al.* 1985):

$$\sigma(p) = 2\epsilon_0 K(p) E_n^{av}(p) , \tag{3}$$

where  $K(p) = \frac{R^{i+1} - R^i}{R^{i+1} + R^i}$  is the reflectivity, and  $E_n^{av}(p) = \frac{E_n^i(p) + E_n^{i+1}(p)}{2}$  is the average of normal components of the electrical field at point “p”.

The average of normal components  $E_n^{av}(p)$  in Eq. 3 is the sum of normal components of the electrical fields coming from primary sources,  $E_n^{sr}(p)$ , charges induced on horizontal boundaries between layers,  $E_n^h(p)$ , charges induced on cylindrical boundaries,  $E_n^c(p)$ , and charges coming from cylindrical electrodes of the device,  $E_n^s(p)$ , calculated at point “p”.

Thus we have:

$$E_n^{av}(p) = E_n^{sr}(p) + E_n^h(p) + E_n^c(p) + E_n^s(p) . \tag{4}$$

Individual normal components can be calculated in the following way

$$E_n^{sr}(p) = \frac{1}{4\pi} \frac{I_A R_m (\bar{L}_{Ap}, \bar{n})}{L_{Ap}^3} , \tag{5}$$

$$E_n^h(p) = \frac{1}{4\pi\epsilon_0} \int_{\Omega^h} \frac{\sigma^h(q) \cdot (\bar{L}_{qp}, \bar{n})}{L_{qp}^3} d\Omega^h , \tag{6}$$

$$E_n^c(p) = \frac{1}{4\pi\epsilon_0} \int_{\Omega^c} \frac{\sigma^c(q) \cdot (\bar{L}_{qp}, \bar{n})}{L_{qp}^3} d\Omega^c , \tag{7}$$

$$E_n^s(p) = \frac{1}{4\pi\epsilon_0} \int_{\Omega^s} \frac{\sigma^s(q) \cdot (\bar{L}_{qp}, \bar{n})}{L_{qp}^3} d\Omega^s , \tag{8}$$

where  $\bar{L}_{qp}$  is the distance vector between points “p” and “q” (Fig. 1);  $\bar{L}_{Ap}$  is the distance vector between points “A” and “p” (Fig. 1);  $\bar{n}$  is the normal unit

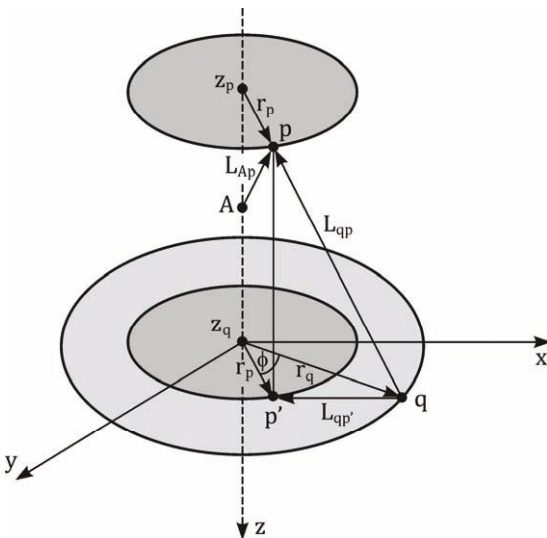


Fig. 1. Diagram of symbols.

vector to the boundary between two media;  $(*,*)$  are scalar products;  $\sigma^h(p)$ ,  $\sigma^c(p)$ , and  $\sigma^s(p)$  are charge densities on the horizontal and cylindrical boundaries and the cylindrical surfaces of the electrodes of the device;  $I_A$  is current strength of the point source located at point A; and  $R_m$  is the borehole mud resistivity at point A.

Integration is held for all boundary surfaces, *i.e.*, the horizontal  $\Omega^h$ , the cylindrical  $\Omega^c$ , and the device  $\Omega^s$ .

Putting Eqs. 6-8 into Eq. 3 we obtain Fredholm's equation of the second kind (Alpin *et al.* 1985):

$$\sigma(p) - \lambda \int_{\Omega^q} N(p,q)\sigma(q) d\Omega^q = f(p) , \tag{9}$$

where

$$N(p,q) = \frac{K(p)(\bar{L}_{qp}, \bar{n}_p)}{L_{qp}^3} , \tag{10}$$

$$f(p) = 2\varepsilon_0 K(p) E^{sr}(p) , \tag{11}$$

$$\lambda = \frac{1}{2\pi} . \tag{12}$$

After taking into account the meanings of symbols from Fig. 1, relation 3 in cylindrical coordinate system assumes the following forms:

□ for charge density on cylindrical boundaries:

$$\begin{aligned} \sigma_{n,s}^c(p) = \frac{K_n^c(p)}{2\pi} & \left\{ \frac{I_A R_m (r_n - r_A)}{\left[ (r_n + r_A)^2 + (z_{np} - z_A)^2 \right]^{3/2}} + \right. \\ & + \sum_I r_I \int_{z_I^c}^{z_{I+1}^c} \int_0^{2\pi} \frac{(r_n - r_I \cos \varphi)}{\left[ r_n^2 + r_I^2 + (z_{np} - z)^2 - 2r_n r_I \cos \varphi \right]^{3/2}} \sigma_I^c(z) dz d\varphi + \\ & + \sum_m \int_{r_m}^\infty \int_0^{2\pi} \frac{(r_n - r \cos \varphi)}{\left[ r_n^2 + r^2 + (z_{np} - z_m)^2 - 2r_n r \cos \varphi \right]^{3/2}} \sigma_m^h(r) r dr d\varphi + \\ & + \sum_s r_s \int_{z_s^c}^{z_{s+1}^c} \int_0^{2\pi} \frac{(r_n - r_s \cos \varphi)}{\left[ r_n^2 + r_s^2 + (z_{np} - z)^2 - 2r_n r_s \cos \varphi \right]^{3/2}} \sigma_s^c(z) dz d\varphi + \\ & \left. + \sum_s \frac{I_s}{2\pi h_s} \int_{z_s^c}^{z_{s+1}^c} \int_0^{2\pi} \frac{r_n - r_s \cos \varphi}{\left[ r_n^2 + r_s^2 + (z_{np} - z)^2 - 2r_n r_s \cos \varphi \right]^{3/2}} \right\} , \tag{13} \end{aligned}$$

□ for charge density on horizontal boundaries:

$$\begin{aligned}
 \sigma_m^h(\mathbf{p}) = \frac{K_m^h(\mathbf{p})}{2\pi} & \left\{ \frac{I_A R_A (z_m - z_A)}{\left[ (r_{mp} + r_A)^2 + (z_m - z_A)^2 \right]^{3/2}} + \right. \\
 & + \sum_l r_l \int_{z_l^c}^{z_{l+1}^c} \int_0^{2\pi} \frac{z_m - z}{\left[ r_{mp}^2 + r_l^2 + (z_m - z)^2 - 2r_{mp} r_l \cos \varphi \right]^{3/2}} \sigma_l^c(z) dz d\varphi + \\
 & + \sum_k (z_m - z_k) \int_{r_k}^{\infty} \int_0^{2\pi} \frac{1}{\left[ r_{mp}^2 + r^2 + (z_m - z_k)^2 - 2r r_{mp} \cos \varphi \right]^{3/2}} \sigma_k^h(r) r dr d\varphi + \\
 & + \sum_s r_s \int_{z_s^c}^{z_{s+1}^c} \int_0^{2\pi} \frac{z_m - z}{\left[ r_{mp}^2 + r_s^2 + (z_m - z)^2 - 2r_{mp} r_s \cos \varphi \right]^{3/2}} \sigma_s^c(z) dz d\varphi + \\
 & \left. + \sum_s \frac{I_s}{2\pi h_s} \int_{z_s^c}^{z_{s+1}^c} \int_0^{2\pi} \frac{z_m - z}{\left[ r_{mp}^2 + r_s^2 + (z_m - z)^2 - 2r_{mp} r_s \cos \varphi \right]^{3/2}} dz d\varphi \right\}, \quad (14)
 \end{aligned}$$

where  $\sigma_n^c(\mathbf{p})$ ,  $\sigma_l^c(z)$ ,  $\sigma_s^c(z)$ , and  $\sigma_m^h(\mathbf{r})$  are charge densities on cylindrical boundaries of numbers  $n$ ,  $l$ ,  $s$ ,  $m$  at points “p”, “r”, “z” and on horizontal boundaries of numbers  $m$  at points “r”;  $n$  – number of cylindrical boundaries;  $s$  – number of the cylinders of the device;  $m$  – number of horizontal boundaries;  $K_n^c(\mathbf{p})$ ,  $K_s^c(\mathbf{p})$ , and  $K_m^h(\mathbf{p})$  are reflectivities at point “p” on the cylindrical boundaries of numbers  $n$  and  $s$  and on the horizontal boundary of number  $m$ ;  $I_A$  and  $I_s$  are strength of current flowing from electrode A and the cylindrical electrode of the device of number  $s$ ;  $R_m$  – resistivity of the mud,  $r_A$  – radial distance of point electrode A from the borehole centre;  $z_A$  – z-coordinate of point electrode A;  $r_n$ ,  $r_l$ , and  $r_s$  are radial distances of cylindrical boundaries of numbers  $n$  and  $l$  and cylindrical electrode of the device of number  $s$ ;  $z_1^c$  and  $z_{l+1}^c$  – z-coordinate of the start and the end of the  $l$ -th cylindrical boundary;  $z_s^c$  and  $z_{s+1}^c$  – z-coordinate of the start and the end of the  $s$ -th cylindrical electrode of the device;  $z_{np}$  – z-coordinate of the point “p” laying on the cylindrical boundary of number  $n$ ;  $r_{mp}$  – radial distance of the point “p” laying on the horizontal boundary of number  $m$ ;  $r_m$  – radial distance of the start of the horizontal boundary of number  $m$ ;  $z_m$  – z-coordinate of the horizontal boundary of number  $m$ ; and  $h_s$  – the length of the  $s$ -th cylinder of the device.

The above integral equations were solved in a numerical way. The unknown functions of charge densities were expanded into Taylor’s series up to the second order. The first and second derivatives were calculated using

approximations of the finite differences. The coefficients for numerical quadratures were calculated in an analytical way, integrating kernels of integrals with elements of Taylor's series expansion. Some integrals could not be calculated in an analytical way. There were integrals of the following type:

$$L_1 = \int_0^{\pi/2} \left[ \ln \left| 1 - k^2 \sin^2 \varphi + a \right| \right] d\varphi , \tag{15}$$

$$L_2 = \int_0^{\pi/2} \left[ \sin^2 \varphi \ln \left| 1 - k^2 \sin^2 \varphi + a \right| \right] d\varphi \tag{16}$$

for  $k^2 < 1$ .

In those cases they were calculated numerically using the 32-point Gaussian quadrature.

After reordering the above equations, we obtain a system of linear equations with unknown charge densities of elementary cylinders and rings (Eq. 17).

$$\sum_{k=1}^{n^h} \sum_{j=1}^{n_k^h} a_{i,j}^h \cdot \sigma_j^h + \sum_{k=1}^{n^c} \sum_{j=1}^{n_k^c} a_{i,j}^c \cdot \sigma_j^c + \sum_{k=1}^{n^s} \sum_{j=1}^{n_k^s} a_{i,j}^s \cdot \sigma_j^s = f_i , \tag{17}$$

where  $i = 1, 2, 3, \dots, N$ ;  $N = \sum_{k=1}^{n^h} n_k^h + \sum_{k=1}^{n^c} n_k^c + \sum_{k=1}^{n^s} n_k^s$  is the total number of all elementary cylinders and rings;  $\sigma_i^{h,c,s}$  is the charge density of the  $i$ -th elementary cylinder ( $c$ ), ring ( $h$ ), and cylinder of the electrode of the device ( $s$ );  $a_{i,j}^h$  are quadrature coefficients for horizontal boundaries;  $a_{i,j}^c$  are quadrature coefficients for cylindrical boundaries;  $a_{i,j}^s$  are quadrature coefficients for cylindrical electrodes of the device;  $n^h$  number of horizontal boundaries;  $n_k^h$  is the number of elementary rings on the  $k$ -th horizontal boundary;  $n^c$  is the number of cylindrical boundaries;  $n_k^c$  is the number of elementary cylinders on the  $k$ -th cylindrical boundary;  $n^s$  is the number of cylindrical electrodes of the device;  $n_k^s$  is the number of elementary cylinders on the  $k$ -th cylindrical electrode of the device; and  $f_i$  is the charge density on the  $i$ -th element due to primary sources.

Figure 2 shows the division of the cylindrical boundary into elementary cylinders of height equal to  $h$  as well as the division of the horizontal boundary for elementary coaxial rings of width initially equal to  $h$  and next increasing in a geometric progression. Unknowns in the system of linear equations (Eq. 17) are charge densities on elementary cylinders on cylindrical boundaries and cylindrical electrodes of the device as well as on elementary rings on horizontal boundaries.

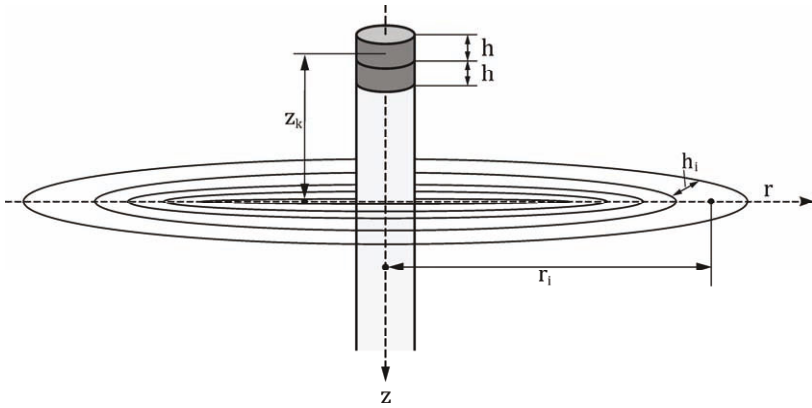


Fig. 2. Diagram of the division of cylindrical and horizontal boundaries for elementary cylinders and rings.

After putting in order, the system of linear equations (Eq. 17) can be written in the matrix form:

$$A\sigma = f, \quad (18)$$

where  $A$  is the matrix of coefficients,  $\sigma$  is the vector of unknowns, *i.e.*, charge densities on all elementary cylinders and rings, and  $f$  is the vector of free terms.

This system of linear equations was solved using the Gauss elimination method.

The potential  $V(r_0, z_0)$  at any point  $r_0, z_0$  coming from the point source and charges of elementary cylinders and rings is calculated in the following way:

$$\begin{aligned}
 V(r_0, z_0) = & \frac{1}{4\pi} \frac{I_A R_m (z_0 - z_A)}{\left[ (r_0 + r_A)^2 + (z_0 - z_A)^2 \right]^{1/2}} + \\
 & \frac{1}{4\pi\epsilon_0} \left\{ \sum_l r_l \int_{z_l^c}^{z_{l+1}^c} \int_0^{2\pi} \frac{1}{\left[ r_0^2 + r_l^2 + (z_0 - z)^2 - 2r_0 r_l \cos \varphi \right]^{1/2}} \sigma_l^c(z) dz d\varphi + \right. \\
 & + \sum_k \int_{r_k}^{\infty} \int_0^{2\pi} \frac{1}{\left[ r_0^2 + r^2 + (z_0 - z_k)^2 - 2r r_0 \cos \varphi \right]^{1/2}} \sigma_k^h(r) r dr d\varphi + \\
 & \left. + \sum_s r_s \int_{z_s^c}^{z_{s+1}^c} \int_0^{2\pi} \frac{1}{\left[ r_0^2 + r_s^2 + (z_0 - z)^2 - 2r_0 r_s \cos \varphi \right]^{1/2}} \sigma_s^c(z) dz d\varphi \right\}. \quad (19)
 \end{aligned}$$

The meaning of symbols is the same as in Eq. 14.

The apparent resistivity  $R_a(r=0, z_0)$  measured by probe in the middle of the borehole at the point of  $z$ -coordinate equal to  $z_0$  is given by the following expression:

$$R_a(0, z_0) = KN \frac{V(0, z_0)}{I_A}, \quad (20)$$

where  $KN = 4\pi L$  is the device coefficient for electric normal probe,  $L$  is the length of the device, *i.e.*, the distance between the source and the measuring electrode of the device,  $z_0$  is the  $z$ -coordinate of the source electrode A, and  $I_A$  is the current strength flowing out from the source electrode.

In case of a lateral device, the apparent resistivity is given by the following expression:

$$R_a(0, z_0) = KL \frac{|\Delta V|}{I_A} = \frac{|V(0, M) - V(0, N)|}{I_A}. \quad (21)$$

In this case  $KL$  has the form:

$$KL = 4\pi \frac{AM \cdot AN}{MN}, \quad (22)$$

where AM and AN are distances between source electrode A and measuring electrodes M and N, respectively;  $z_0$  is the middle of points M and N;  $V(0, M)$  is the potential at the point (0, M);  $V(0, N)$  is the potential at the point (0, N).

### 3. COMPARING RESULTS OBTAINED USING THE METHOD OF COULOMB CHARGES WITH ANALYTICAL SOLUTIONS

In order to test the accuracy and effectiveness of the Coulomb charges method, the apparent resistivity of a point current source lateral device was calculated. The rock formation was vertically homogeneous containing a borehole, the invaded zone, and the virgin zone. The scheme of this model is presented in Fig. 3.

At the axis of the borehole, at point A, there is the source with current strength  $I_A$ . This source and the charges induced at two cylindrical boundaries generate potential difference  $V_M - V_N$  between points M and N of  $z$ -coordinates  $z_M$  and  $z_N$ . At the point (0,  $z_0$ ), where  $z_0$  is the  $z$ -coordinate of the middle between points M and N, we can calculate the apparent resistivity  $R_a(0, z_0)$  according to Eq. 21. Analytical solutions for such a model were presented by Dachnov (1967).

Inside the cylinder of length  $L_{\text{cyl}}$  there are two cylindrical boundaries with radii  $r_i$  and  $r_s$ , respectively, separating the mud from the invaded zone and the invaded zone from the virgin zone. Resistivities of the mud, invaded

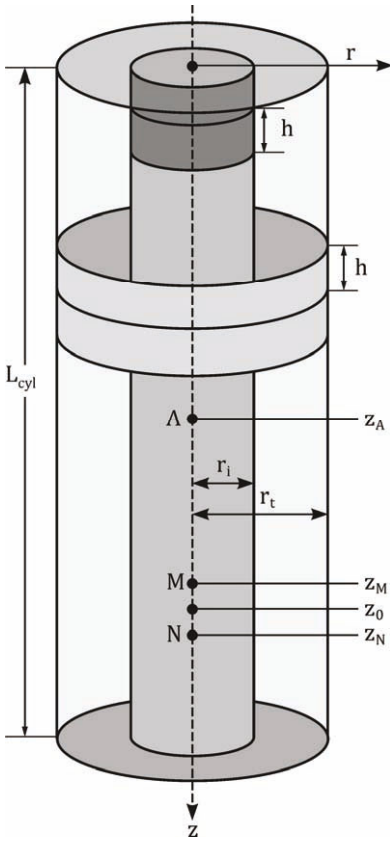


Fig. 3. Model of the rock formation.

zone and virgin zone are  $R_m$ ,  $R^i$ , and  $R^{i+1}$ , respectively. Each of these cylinders with length  $L_{cyl}$  was divided into  $N$  elementary cylinders with height  $h$ , where  $N = L_{cyl}/h$ . Thus, the number of elementary cylinders on which the source of the current generates charge density is equal to  $2N$ . These charge densities are obtained by solving the system of linear equations (Eq. 18).

We calculate the potential  $V(0, z_M)$  at point M in the following way:

$$V_M = V(0, z_M) = \frac{1}{4\pi} \frac{I_A R_m}{|z_M - z_A|} + \frac{1}{2\epsilon_0} \left[ r_i \sum_{j=1}^N \sigma_j \int_{z_j - \frac{h}{2}}^{z_j + \frac{h}{2}} \frac{dz}{[r_i^2 + (z - z_M)^2]^{1/2}} + r_t \sum_{k=1}^N \sigma_k \int_{z_k - \frac{h}{2}}^{z_k + \frac{h}{2}} \frac{dz}{[r_t^2 + (z - z_M)^2]^{1/2}} \right], \quad (23)$$

where  $\sigma_j$  are charge densities of elementary cylinders on the boundary between mud and the invaded zone,  $z_j$  are  $z$ -coordinates of the middle of the  $j$ -th elementary cylinder on the boundary between mud and the invaded

zone,  $\sigma_k$  are charge densities of elementary cylinders on the boundary between the invaded zone and the virgin zone,  $z_k$  are  $z$ -coordinates of the middle of the  $k$ -th elementary cylinder on the boundary between the invaded zone and the virgin zone.

The meaning of the other symbols is explained in Fig. 3 or was mentioned earlier.

In the same way we calculate the potential  $V(0, z_N)$  at point N.

Using Eq. 21 the apparent resistivity  $R_a(0, z_0)$  was calculated for different values of parameters  $R_i/R_m, R_t/R_m,$  and  $D/d$ , where  $d = 2r_i$  is the diameter of the borehole,  $D = 2r_t$  is the diameter of the invaded zone.

Calculations were carried out for different values of the parameter  $L/d$ , where  $L = |z_A - z_0|$  is the distance from the source electrode to the middle point of M and N measuring electrodes.

Calculations were made for  $d = 0.2$  m,  $h = 0.05$  m,  $L_{cyl} = 50$  m and MN distance equal to 0.01 m.

For such values, the number of unknowns in the system of linear equations (Eq. 18) was equal to 2000. The relative error for all the results presented below for different values of parameters  $R_i/R_m, R_t/R_m,$  and  $D/d$  was less than 2%.

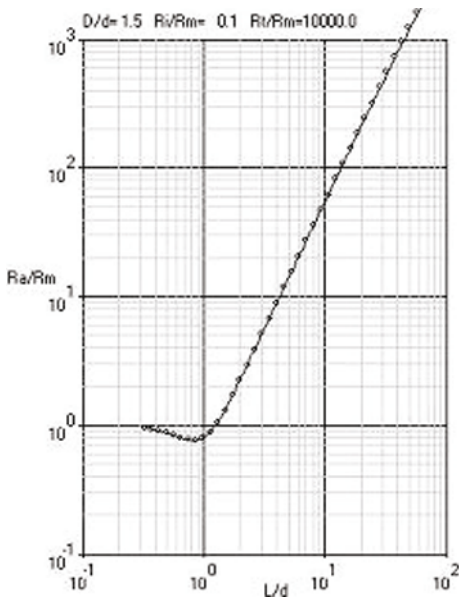


Fig. 4. Comparison of numerical results with analytical solutions for  $D/d = 1.5, R_i/R_m = 0.1, R_t/R_m = 10\ 000$ .

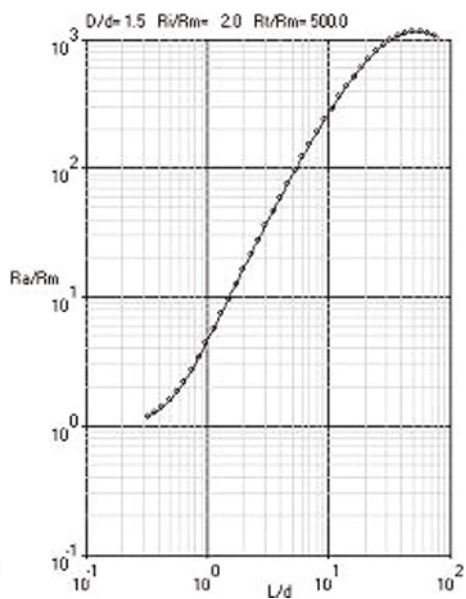


Fig. 5. Comparison of numerical results with analytical solutions for  $D/d = 1.5, R_i/R_m = 2, R_t/R_m = 500$ .

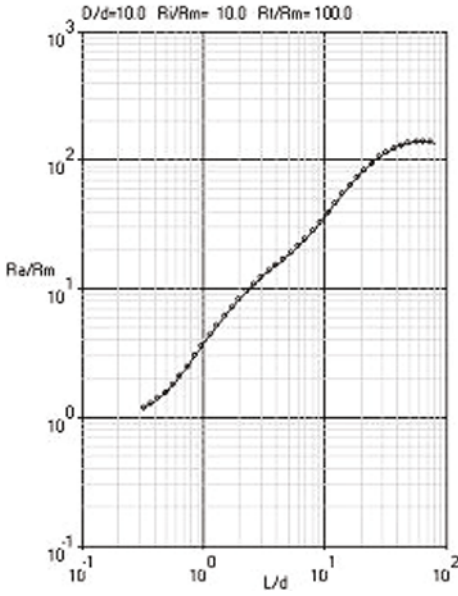


Fig. 6. Comparison of numerical results with analytical solutions for  $D/d = 10$   $R_i/R_m = 10$   $R_t/R_m = 100$ .

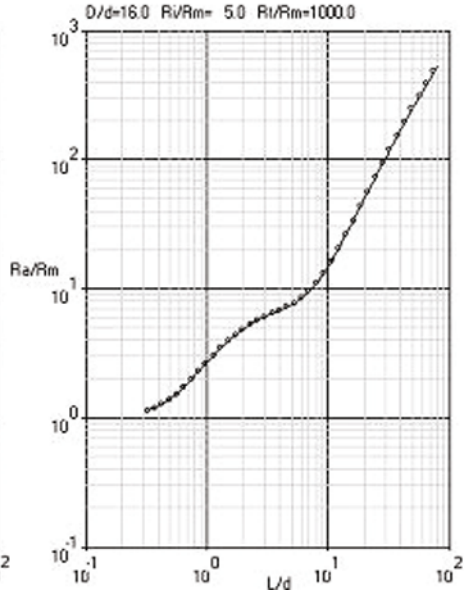


Fig. 7. Comparison of numerical results with analytical solutions for  $D/d = 16$   $R_i/R_m = 5$   $R_t/R_m = 1000$ .

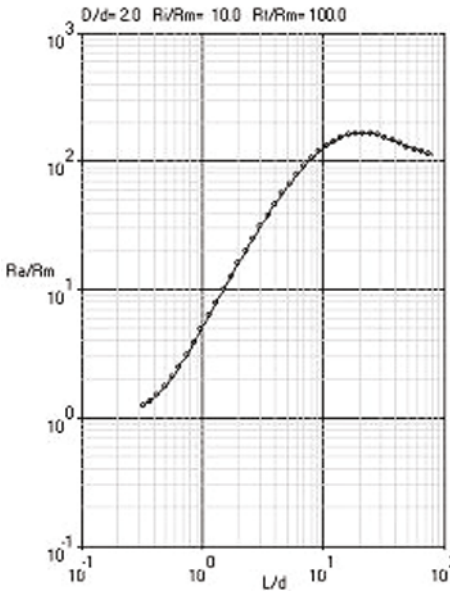


Fig. 8. Comparison of numerical results with analytical solutions for  $D/d = 2$   $R_i/R_m = 10$   $R_t/R_m = 100$ .

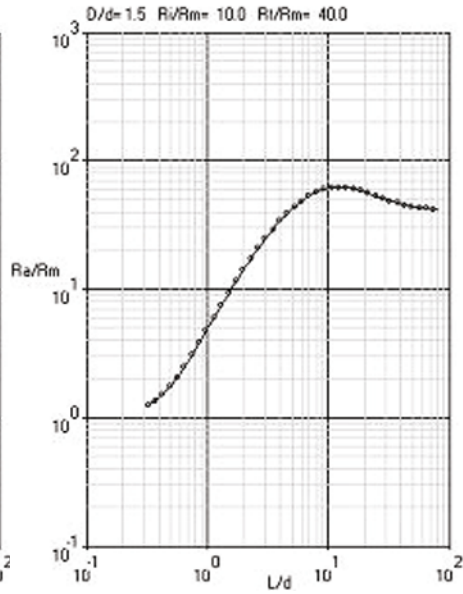


Fig. 9. Comparison of numerical results with analytical solutions for  $D/d = 1.5$   $R_i/R_m = 10$   $R_t/R_m = 40$ .

Increasing the length of the cylinder  $L_{\text{cyl}}$  and decreasing the height of the elementary cylinder  $h$  improved the accuracy of calculations (the relative error was less than 1%) but significantly increased the number of unknowns and, of course, the time of calculations.

The results using Coulomb charges method (points) in comparison with analytical solutions (continuous line; Dachnov 1967) for several chosen values of parameters  $R_i/R_m$ ,  $R_t/R_m$ , and  $D/d$ , are presented in Figs. 4 to 9.

#### 4. CONCLUSIONS

The Coulomb charges method presented in this paper can be used for modeling measurements of apparent resistivity carried out in a borehole with the invaded zone in multilayered rock formations. The method is effective because it does not require calculations with the use of powerful computers. A comparison of the results of calculations with analytical solutions shows that the method is also accurate. It can be successfully used for modeling measurements of apparent resistivity with the use of a more complicated construction, for instance of laterolog type.

#### References

- Alpin, L.M. (1964), Some theoretical methods for solving direct resistivity logging problem, *Izv. AN SSSR Ser. Geophys.* **2**, 236-238 (in Russian).
- Alpin, L.M., D.S. Dajev, and A.D. Karinskij (1985), *The Theory of Alternating Fields for Exploratory Geophysics*, Nedra, Moskva (in Russian).
- Dachnov, V.N. (1967), *Electric and Magnetic Methods for Logging*, Nedra, Moskva (in Russian).
- Tan, M.-J., J. Gao, X.-C. Wang, and S.-Y. Zhang (2011), Numerical simulation of the dual laterolog for carbonate cave reservoirs and response characteristics, *Appl. Geophys.* **8**, 1, 79-85, DOI: 10.1007/s11770-011-0268-2.

Received 18 June 2014

Received in revised form 29 September 2014

Accepted 3 October 2014



## EMD Method Applied to Identification of Logging Sequence Strata

Ni ZHAO <sup>1,2</sup> and Rui LI<sup>1</sup>

<sup>1</sup>State Key Laboratory of Oil and Gas Reservoir Geology and Exploitation (CDUT), Chengdu, China

<sup>2</sup>Xi'an Technological University, Computer Science and Engineering College, Xi'an, China; e-mail: zhaoni369@126.com (corresponding author)

### Abstract

In this work, we compare Fourier transform, wavelet transform, and empirical mode decomposition (EMD), and point out that EMD method decomposes complex signal into a series of component functions through curves of local mean value. Each of Intrinsic Mode Functions (IMFs – component functions) contains all the information on the original signal. Therefore, it is more suitable for the interface identification of logging sequence strata.

Well logging data reflect rich geological information and belong to non-linear and non-stationary signals and EMD method can deal with non-stationary and non-linear signals very well. By selecting sensitive parameters combination that reflects the regional geological structure and lithology, the combined parameter can be decomposed through EMD method to study the correlation and the physical meaning of each intrinsic mode function. Meanwhile, it identifies the stratigraphy and cycle sequence perfectly and provides an effective signal treatment method for sequence interface.

**Key words:** empirical mode decomposition (EMD), intrinsic mode function (IMF), logging data processing, sequence stratigraphy.

## 1. INTRODUCTION

Sequence stratigraphy is a branch of stratigraphy, and it studies chronostratigraphic framework based on erosion surface or comparable integrated surface, inner stratum of sedimentary sequence, and petrographic distribution pattern which is in a cycle type in time and internally linked by formation. Sequence partition and interface identification are the foundation to study sequence stratigraphy. Generally, outcrop data, core data, logging data, and seismic data are adopted for the partition and identification of sequence stratigraphy. The logging data contains rich geologic information. When the information from outcrop and core is not enough and seismic resolution is limited, logging data becomes more important during the partition of sequence stratigraphy (Van Wagoner *et al.* 1990).

As the theory of high resolution sequence stratigraphy puts forward, various methods such as wavelet analysis, Hilbert–Huang transform (HHT) are applied into strata partition. Hilbert–Huang transform is an arithmetic method, based on Hilbert spectrum. It includes empirical mode decomposition and Hilbert Spectrum Analysis. Empirical mode decomposition, EMD method for short, calculates local mean curve for instable signals, which decomposes the complex signal to a series of component functions for instantaneous frequency with obvious physical meaning. This method is very useful to deal with non-stationary and non-linear processes (Huang *et al.* 1998, 1999; Wu and Huang 2004). In this study, the EMD method is applied into logging data processing. It serves as an effective method for identifying sequence interface in logging.

## 2. EMPIRICAL MODE DECOMPOSITION (EMD) METHOD

### 2.1 Theoretical basis of EMD method

EMD is a kind of transform method, in which analysis should be adaptable to the nature of the data. Its essential is to obtain signal's intrinsic fluctuating mode by using the characteristic temporal scale of signal (Li *et al.* 2010). Compared with wavelet transform and Fourier transform, the EMD transform is ideally suitable for handling data from non-stationary and non-linear processes. EMD method can decompose any complicated data into a small number of intrinsic mode function components, IMFs, which represent the basic characteristics of the data. As it is adaptable and the decomposition is based on the local characteristics of the data, the IMFs usually are mono-component oscillatory modes. Specifically, this method is based on the following hypothesis:

- (i) A signal shall have a maximum value and a minimum value;
- (ii) The characteristic temporal scale shall be defined by the time interval of extreme points.

### 2.2 Decomposing procedure of EMD method

Effective algorithm procedure of EMD of a signal  $x(t)$  is presented in Fig. 1.

Intrinsic mode functions (IMFs) have to satisfy the following two conditions:

- (i) in the whole data set, the number of extreme values and the number of zero crossings must be either equal or differ at most by one;
- (ii) at any point the mean value of the envelope defined by the local maxima and the envelope defined by the local minima is zero (de Lima *et al.* 2006).

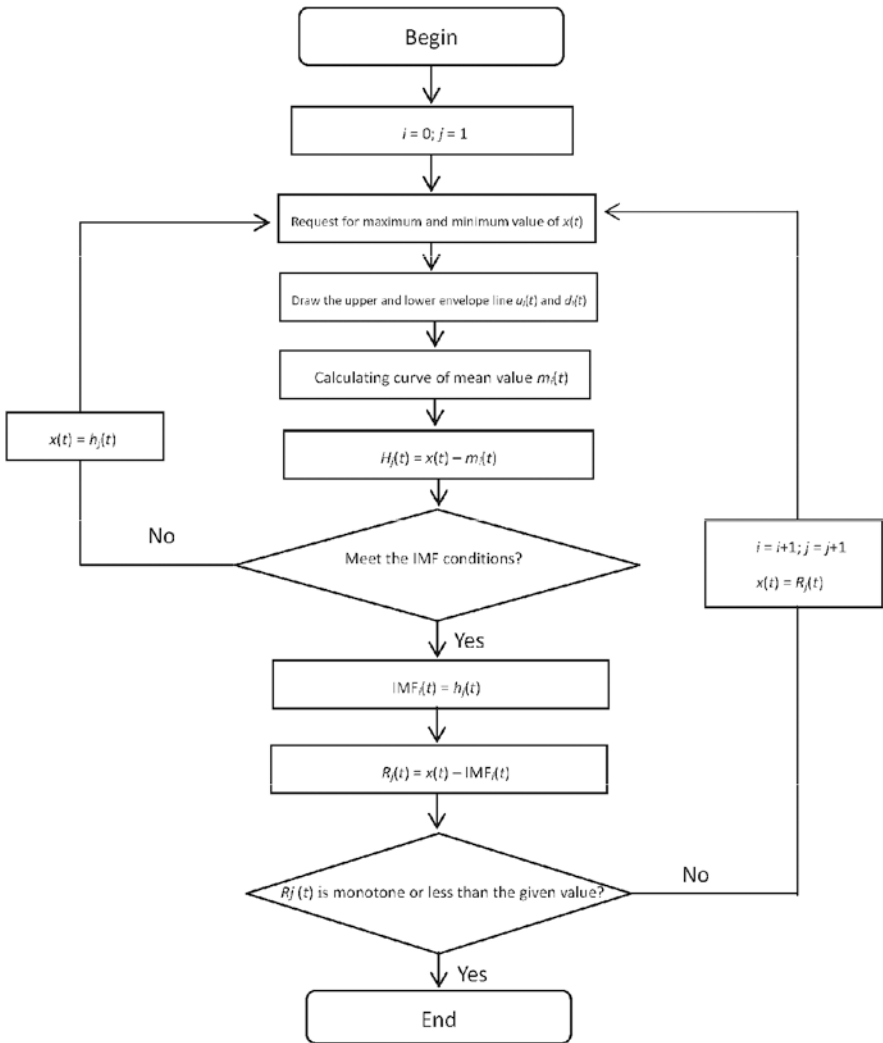


Fig. 1. Decomposing procedure of EMD.

The first condition guarantees that the maximum value of datum of local part is positive and minimum value is negative; the second condition eliminates the instantaneous frequency vibration caused by nonsymmetrical waveform (Huang *et al.* 1998).

For a given signal  $x(t)$ , EMD ends up with a representation of the form:

$$x(t) = \sum_{i=1}^n \text{IMF}_i(t) + R(t) . \quad (1)$$

In Eq. 1,  $R(t)$  stands for a residual trend and the intrinsic mode functions  $\{\text{IMF}_i(t), i = 1, \dots, n\}$  are the modulating wave of frequency-amplitude modulation constrained by zero-mean value (Flandrin *et al.* 2004).

As depicted in Fig. 1, when the first IMF has been calculated successfully, it is separated from the original signal and produced a residual. This residual is considered as a new signal to be computed again. It was repeated until the residual no longer contains any oscillations (Bowman and Lees 2013).

The process shows that the starting point of EMD is to consider signals at the level of their local oscillations. EMD method is used to decompose original signal into a series of intrinsic mode functions (IMFs) from high frequency to low frequency as well as a residual trend item, namely  $\text{IMF}_i(t)$  and  $R(t)$ , respectively. Once this decomposition (EMD) is achieved, details are considered as effective and consisting of all local feature.

In practice, the EMD sifting process was multi-scale, adaptable, and based solely on the data, so we can find an appropriate scale that may reveal important information embedded in the original signal.

### 2.3 Advantages of EMD

Fourier transform and wavelet analysis are the common methods in logging signal analysis. Now, EMD method is compared with them:

Fourier transform is the foundation for analyzing signal frequency spectrum. It decomposes an original signal into weighted sum of several sine signals, of which each sine signal aims at one fixed frequency and amplitude value. It is suitable for analyzing stable signal that does not change with time (Wu and Huang 2004). Logging data is instable signal-in-space. Through Fourier transform, frequency signal can be obtained. It has a maximum resolution in the frequency domain but it does not contain depth information, so you may find the maximum frequency but you cannot confirm its depth.

Wavelet transform is the extension of Fourier transform. It can adjust the size of window automatically according to the frequency (Wawrzyniak 2010). Meanwhile, it has more resolving and analytic functions. Discrete wavelet decomposition produces low frequency signal and high frequency signal generated from two complementary filters (Akansu *et al.* 2010). In

application, low frequency part is regarded as the most important part. The limitation of wavelet transform includes: first, the selection of wavelet function shall influence the accuracy of decomposing, and secondly, each extraction does not contain the complete information. It only represents the part after filtering.

EMD method is the key part of HHT and it is designed specifically for adaptable representation of non-stationary and non-linear signal processes. It can be used to decompose any complicated data into sums of intrinsic mode functions plus a residual (Huang and Wu 2008). EMD provides us with a useful method to find out the underlying processes of non-stationary and non-linear signals and better indicate the physical meaning of local phase change with the instantaneous frequency than any other non-IMF time series. EMD decomposes the whole signal and each component contains whole information that can reflect the characteristics of instantaneous frequency (Zheng and Yang 2007). This is the major advantage of EMD method compared to wavelet transform.

### **3. EMD METHOD APPLICATION IN IDENTIFICATION OF LOGGING SEQUENCE STRATA**

#### **3.1 Parameters selection and processing**

During well logging data collection, various interference factors cannot be avoided, which must influence the resolution of signal. Using a linear combination of sensitive parameters, highly correlated, is an effective method to improve accuracy of logging interpretation. At the beginning of processing well logging signals data should be deeply analyzed and various parameters should be compared. As a result, sensitive parameters reflecting lithological characteristics will be selected. Next, cross-correlation coefficients on the selected sensitive parameters such as spontaneous potential and natural gamma ray, and transit interval time and density, *etc.* will be calculated. Combining various linearly correlated parameters can strengthen stratum characteristics information. Because the noise is generated randomly, stacked signals with good correlation can highlight useful information and decrease the influence of interference factors.

In order to stack groups of data with different units, normalization should be applied and, next, sets of non-dimensional data can be used to form a new analytic parameter.

#### **3.2 Identification method of circle of basic level**

##### **3.2.1 Data processing rule**

EMD decomposes the original signal into intrinsic functions ( $IMF_i$ ) with different frequency and a remaining trend item  $R$ . Each IMF is the mode of a

signal at some characteristic dimension. The component with high frequency reflects the short-term cycle characteristics that is mainly controlled by astronomical factors (such as long eccentricity, precession cycle), while the component with low frequency reflects the middle and long term stable cycle characteristics that is controlled by long term structure formation process (such as regional tectonic movement, the tectonic of stress field transformation, and tectonic episodic intensity change).  $R$  refers to the data trend or zero drift of instruments (Zhang and Nie 2011).

Based on this rule, correlation of intrinsic mode function  $IMF_i$  obtained after EMD can be determined as follows:

(i) calculate the correlation coefficient of every  $IMF_i$  and its original signal. Commonly, those  $IMF_i$ s which have good correlation with the original signal are the best signal components reflecting stable sedimentary environment;

(ii) analyze the correlation between different  $IMF_i$ s and combine those  $IMF_i$ s with good correlation. This is because that good correlation reveals that they have consistent variation style. Combining them can reduce interference factors and strengthen signals that reflect the geological characteristics; therefore, it can improve the accuracy of bed boundary identification.

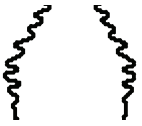
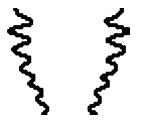
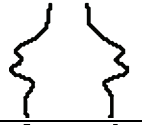
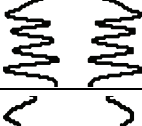
### 3.2.2 EMD response characteristics

After the well logging signal is decomposed using EMD method, the time-frequency characteristics of original well logging signals can be obtained from different dimensions, which can reflect different sedimentary cycle grades. If the correlation with all kinds of sequence interfaces can be identified, then it can be deemed as the standard to divide the sequence of well logging.

When the river reaches balance under the dynamics, suppose the balanced profile as a potential energy surface, called the base level. The land surface or sedimentary boundary will develop towards the base level through sedimentary or erosion action to reach a new balance. Such a circling process is called sequence formation cycle (Zheng *et al.* 2000, 2001). This kind of cycle of sequence stratum is reflected in well logging data as rhythmicity of mineral grains granularity and lithology. It is reflected as different amplitude and frequency characteristics in well logging curve. Yet, the break points of a curve are often the sequence interfaces (Serra and Abbott 1982). Based on this, it is useful to make the mirror image on response characteristics of EMD curve of well logging parameters reflecting all kinds of sedimentary environment and summarize five basic types (Table 1). Most well logging curves of different sedimentary environments are the combination or variants of these five basic types.

Table 1

Basic types of sedimentary environment  
that is corresponding to EMD curve of well logging

Curve type		Indicating type	Analysis of curve type
Gradually-varied type		Top	Poorly sorted. To the top, amplitude becomes less gradually and the curve turns into zigzag shape, which shows normal graded bed sequence.
		Bottom	Poorly sorted. To the bottom, amplitude becomes less gradually and the curve turns into zigzag shape, which shows reverse grain size order.
Abrupt change type		Top	Well sorted. An abrupt change at the top. Stacked upward-fining cycle.
		Bottom	Well sorted. An abrupt change at the bottom. Stacked downward-fining cycle.
Fluctuating type		Top	Granularity turns from coarser below to finer and the amplitude becomes less drastically. It belongs to typical transgression and shows positive grain size order.
		Bottom	Granularity turns from finer below to coarser and the amplitude becomes bigger drastically. It belongs to typical regression and shows reverse grain size order.
Thin inter-bedding type		Inter-bedding	Multi-lithology alternately appears and changes quickly. It often can be seen in thin inter-bedding.
Block combination type		Simplex lithology	The lithology is simplex, so the grain size of sediment changes are small and stable.

#### 4. PRACTICAL EXAMPLE

EDM method was applied for the X well logging data, Xujia River Group, middle section of West Sichuan Depression, Sichuan Basin. The sequence stratum was divided by using EMD and the cycle of base level was identified.

#### 4.1 Analysis on parameter combination

Natural gamma ray (GR) log is a common logging method to measure intensity of natural gamma ray in rock along the well bore. Rocks contain different amounts of radioactive elements and constantly emit radiation. GR curve reflects the granularity, sorting and clay minerals content, which can be used to judge lithology, compare stratum, and estimate the shale content. Commonly, gamma ray readings in sandstone and clay-stone are low and high, respectively. Yet, when sandstone has radioactive minerals such as mica or zircon or others, the reading of gamma ray will be influenced directly.

Spontaneous potential (SP) log is an effective logging method for analyzing geological profile in borehole, which can be used to measure shaft spontaneous potential changes in an open hole. SP curve is often used to divide the sandy-shaly profile into sandstone and shale lithology, compare the stratum, define the interface position of filtering layer, calculate the content of shale of the stratum, and spread the sedimentary face to study, *etc.*

The presented analysis indicated that these two well logging data (GR and SP) are the sensitive parameters that are suitable for sequence division of the study area. At the same time, their curves indication have consistent rule: at the profile of sandstone and shale section well, the value of these two curves is low at sandstone while the value is high at shale. So, these parameters can be combined.

Correlation coefficient between natural gamma ray and spontaneous potentials parameters was equal to 0.44, which indicated that correlation was sufficient. Normalization treatment on natural gamma ray and spontaneous potentials curves was done to eliminate the influence of units and select linear normalization formula:

$$y = \frac{x - Min}{Max - Min} \quad (2)$$

In Eq. 2,  $x$  refers to current parameter value,  $Max$  and  $Min$  are  $x$ 's maximum and minimum value, respectively, and  $y$  is the value after  $x$  normalization.

With this expression the normalized values of GR, namely GR' (Eq. 3) and SP' (Eq. 4), were calculated:

$$GR' = \frac{GR - GR_{Min}}{GR_{Max} - GR_{Min}} \quad (3)$$

$$SP' = \frac{SP - SP_{Min}}{SP_{Max} - SP_{Min}} \quad (4)$$

Mean values of the normalized parameters (GR' and SP') were combined to form a new parameter marked GR\_SP:

$$GR\_SP = \frac{GR' + SP'}{2} . \quad (5)$$

Analyzing the correlation of GR\_SP and natural gamma ray (GR) and spontaneous potentials (SP), there was found the correlation coefficient of GR\_SP and GR equal to 0.94, and the correlation coefficient of GR\_SP and SP equal to 0.73. This shows that the new parameter had higher correlation with natural gamma ray and spontaneous potentials. It can replace the original parameters.

## 4.2 Cycle identification and stratigraphic division

Following the EMD decomposition process presented in Fig. 1 a program with MATLAB was prepared. Adopting EMD on GR\_SP data of X well, Xujia River Group, middle section of West Sichuan Depression, Sichuan Basin, the intrinsic mode functions IMF were obtained (Fig. 2).

IMF1-IMF4 reflected strong vibrations of the signal (Fig. 2). Yet, the positions of high amplitude value were different. This showed the influence of noise on high frequency component. As the frequency of all IMF signals declined, the stable transform trend in signal became stronger and stronger.

A different intrinsic mode function component can be obtained through the decomposition of EMD. Superposing the decomposed components, the original signal may be reproduced. Using such characteristics, we repeated the reverse accumulation of the intrinsic mode functions IMF1-IMF9 and trend item *R* of each stages of GR\_SP in Fig. 2, namely, the combination from the component with low frequency to high frequency (Fig. 3).

IMF9, IMF7, IMF6 or IMF5 acted importantly in original sequence (Fig. 3). The changes of original sequence were mainly caused by the oscillation of these four functions. They all had consistent change pattern. This pattern reflected the characteristics of stable sedimentary environment of the stratum.

Specifically, the wave scope of IMF5, IMF6, and IMF7 covered several meters to tens of meters and the wave width of IMF9 is over one hundred meters. The cycles with different base levels commonly are divided according to time distribution. In practical layers, the thickness of short-term cycle is of several meters to dozens of meters. The middle term cycle is dozens of meters to nearly one hundred meters and the long term cycles are nearly one hundred meters to several hundred meters. Therefore, IMF5, IMF6, and IMF7 reflects the short-term circle characteristics, while IMF9 the middle and long term characteristics.

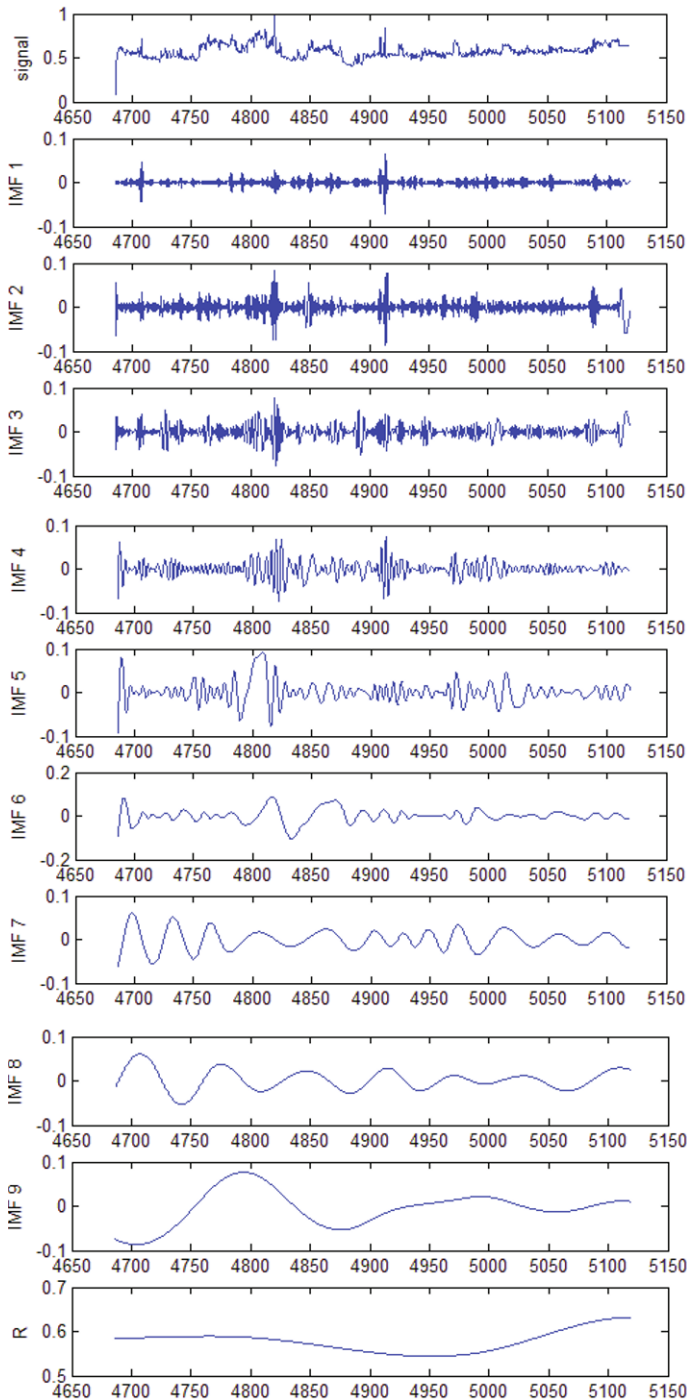


Fig. 2. EMD diagram of GR\_SP (IMFs 1-9 are the empirical mode decompositions (EMD) of the signal which is the new combined parameter between GR and SP).  $R$  represents the final residual which showed the data trend.

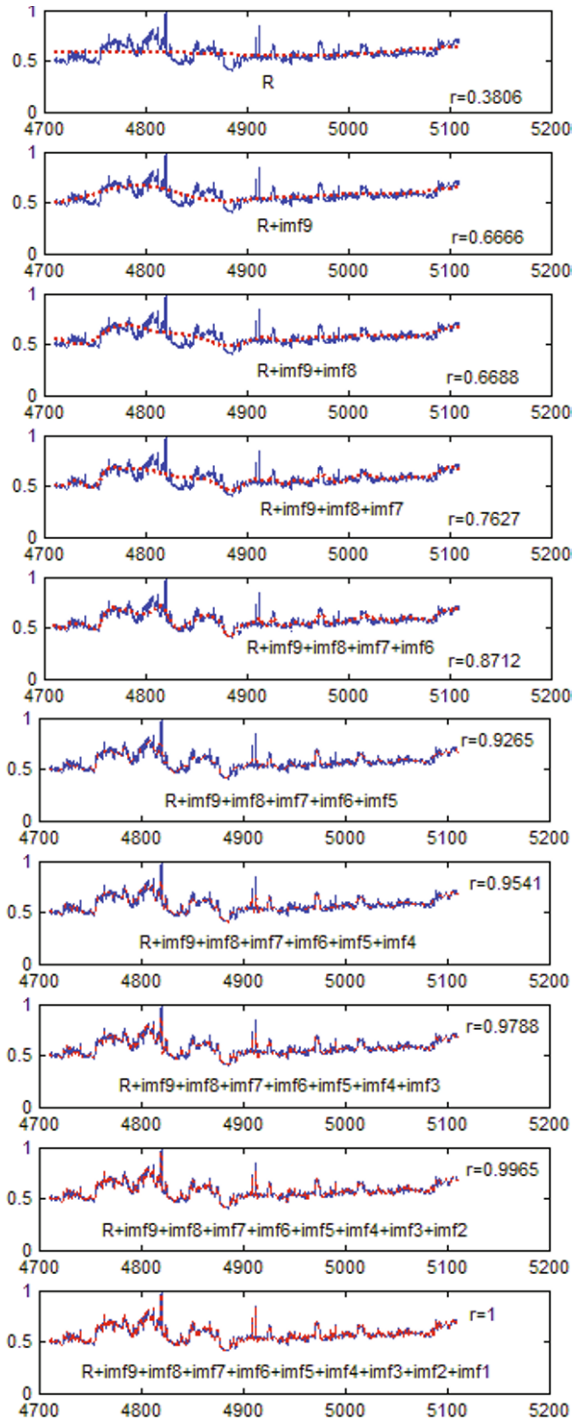


Fig. 3. Reconstruction of GR\_SP components by using IMF (GS\_SP – solid line, reproduced sequence – broken line,  $r$  – correlation coefficient of reproduced sequence with GR\_SP).



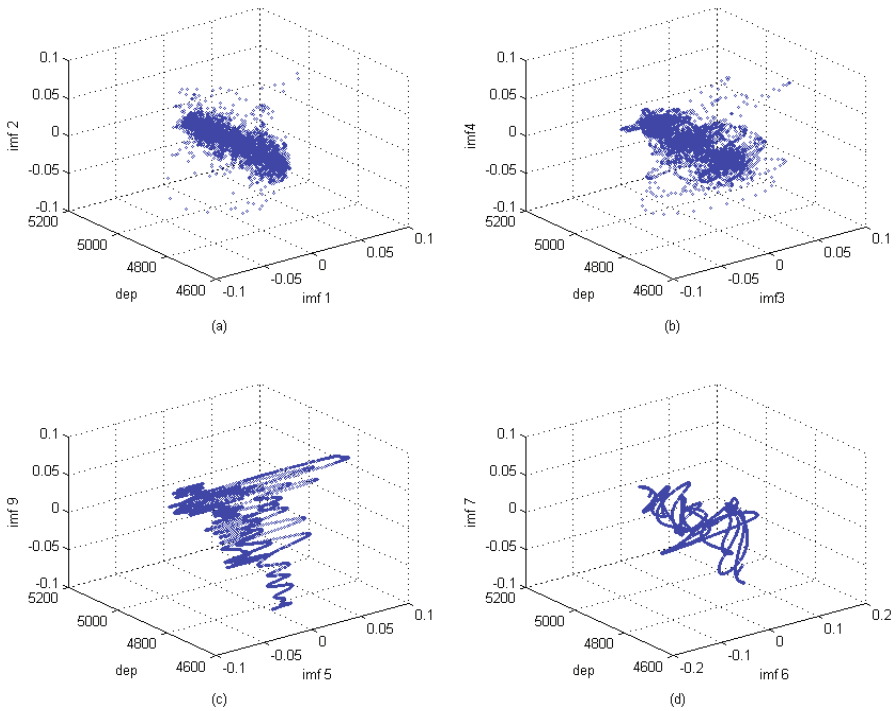


Fig. 4. IMF components scatter plot.

IMF1-IMF2 and IMF3-IMF4 with less correlation to GS\_SP were selected as one group and IMF5-IMF9 and IMF6-IMF7 with better correlation to GS\_SP were selected as the other group, the scatter diagrams were made in depth domain (Fig. 4). The scatter diagram for the combination of IMF1 and IMF2 as well as IMF3 and IMF4 were disorderly. They all had poor correlation with GR\_SP. Furthermore, the correlation coefficients in Table 3 were comparatively low. So, the combination of IMF5 and IMF9 as well as IMF6 and IMF7 not only revealed better correlation, they also had higher correlation coefficients values. Their scatter diagrams were smooth curves, which showed their rules.

In order to further the explanation of the discussed problem, the periodic functions and non-periodic functions with lower correlation coefficients as well as random sequences were selected, respectively (Figs. 5a-c) (Bogle *et al.* 1994, Hoste and Zirbel 2006).

In the first plot in each group in Figs. 5a-c there are presented two original signals;  $r$  is the correlation coefficient. In the second plot of each group in Figs. 5a-c there is the overlapped signal of those two original signals given in the first figure. In the third plot there is the scatter diagram of those two original signals.

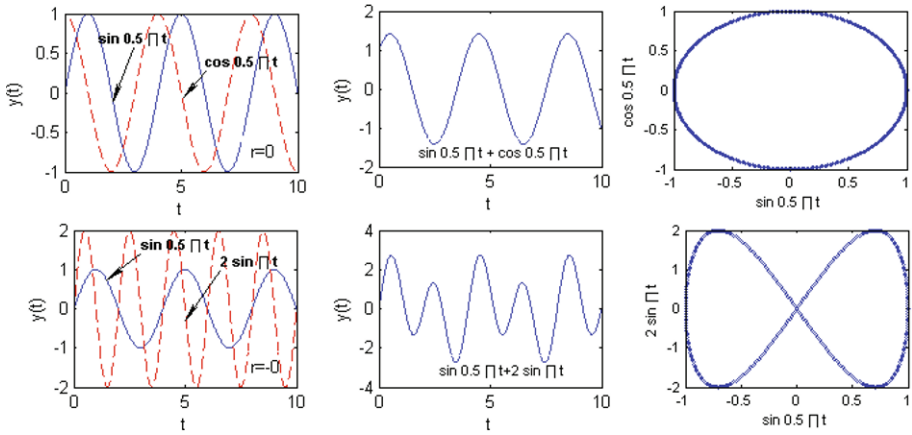


Fig. 5a. Scatter diagram of two groups of non-linear correlation periodic functions.

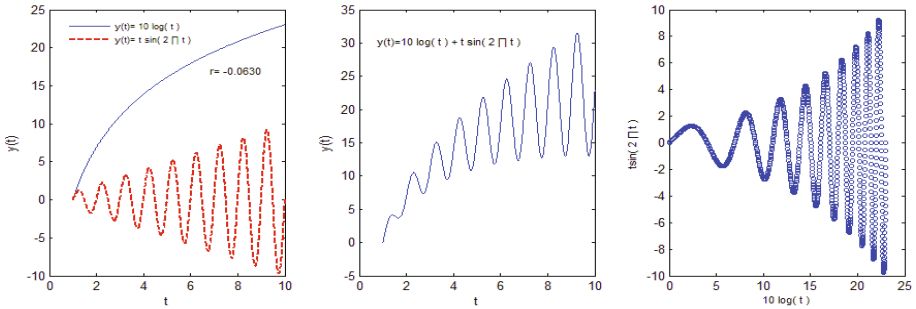


Fig. 5b. Scatter diagram of non-linear correlation and non-periodic functions.

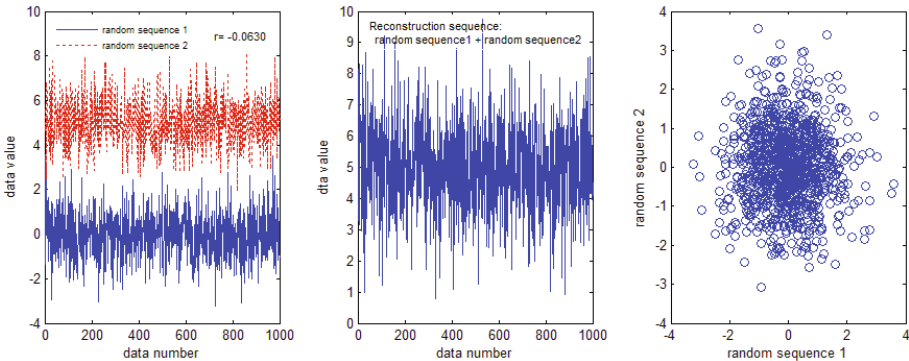


Fig. 5c. Scatter diagram of random sequences for non-linear correlation.

In Fig. 5a there is an example of periodic function adopted to make the scatter diagram of functions with same frequency and different phases as well as the functions with same phase and different frequency. The curves of

two periodic functions of non-linear correlation still had periodicity after overlapping. Then, their scatter diagrams were stable closed curves. In Fig. 5b the presented examples belong to non-periodic functions of non-linear correlation. After combination they are still non-periodic functions and their scatter diagrams are the curves that will never close. In Fig. 5c there are random sequences of non-linear correlation; when they are combined, they still belong to non-periodic random sequence and their scatter diagrams are disordered.

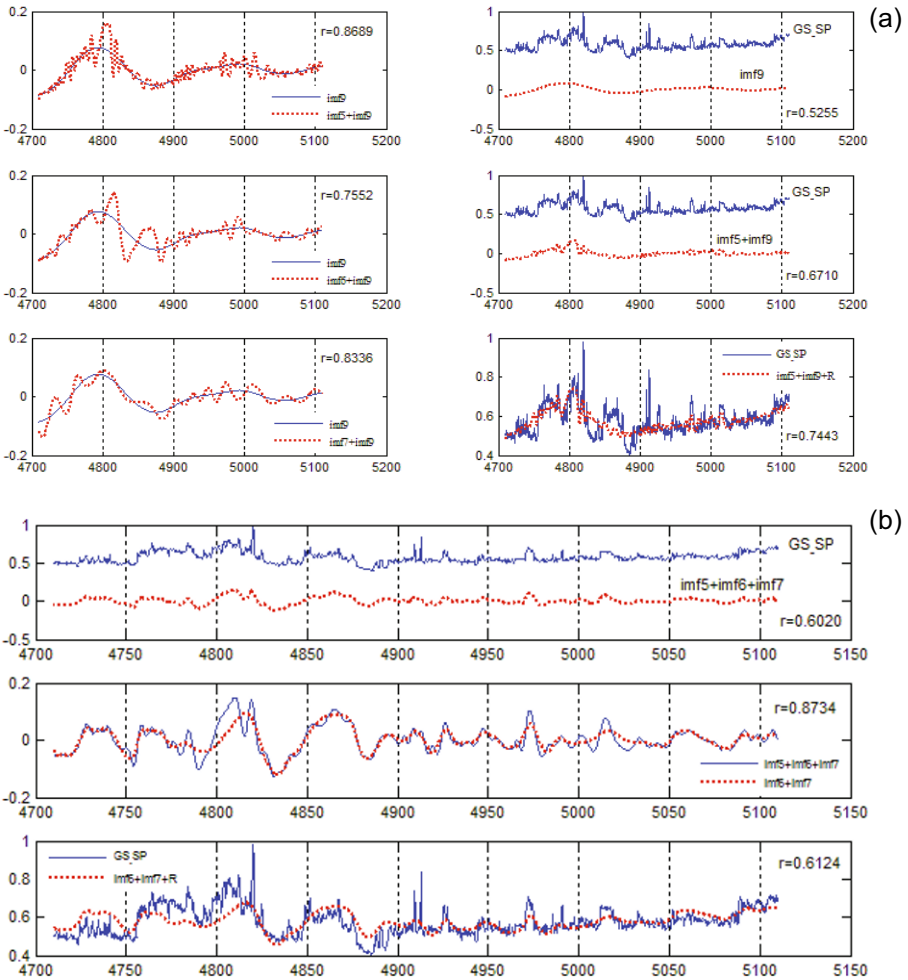


Fig. 6. Comparison of low frequency signals combination: (a) comparison with the related signal of IMF5+IMF9, and (b) comparison with the related signal of IMF6+IMF7;  $r$  – correlation coefficient.

The scatter diagrams of IMF5 and IMF9, IMF6 and IMF7 are smooth curves (Fig. 4c and d). Figure 4c has the correlative characteristics of piecewise curve and they have no obvious closed diagram while Fig. 4d has many staged closed diagrams in the scatter diagram. According to sedimentology, the stratum in different periods may have different sedimentation rules while the stratum in the same period may have similar characteristics; these conform to the rules reflected by scatter diagram. Accordingly, the combination of IMF5 and IMF9 is suitable for researching sedimentation rules of the stratum in middle or long-term and the combination of IMF6 and IMF7 is suitable for researching the short term sedimentation rules of the stratum.

In Fig. 6, from the correlation of combined signals we can further prove that the overlapped sequences of IMF5 and IMF9 as well as IMF6 and IMF7 can best reveal the rules of long-term cycles and the short-term cycle.

Besides, the combined sequence of IMF5+IMF9 has higher correlativity with IMF9 of low frequency component, which obviously improves the correlativity of IMF9 and GS\_SP due to participation of IMF5. Similarly, IMF6+IMF7 not only well reflect the rule of IMF5+IMF6+IMF7, but also have good correlation with GS\_SP.

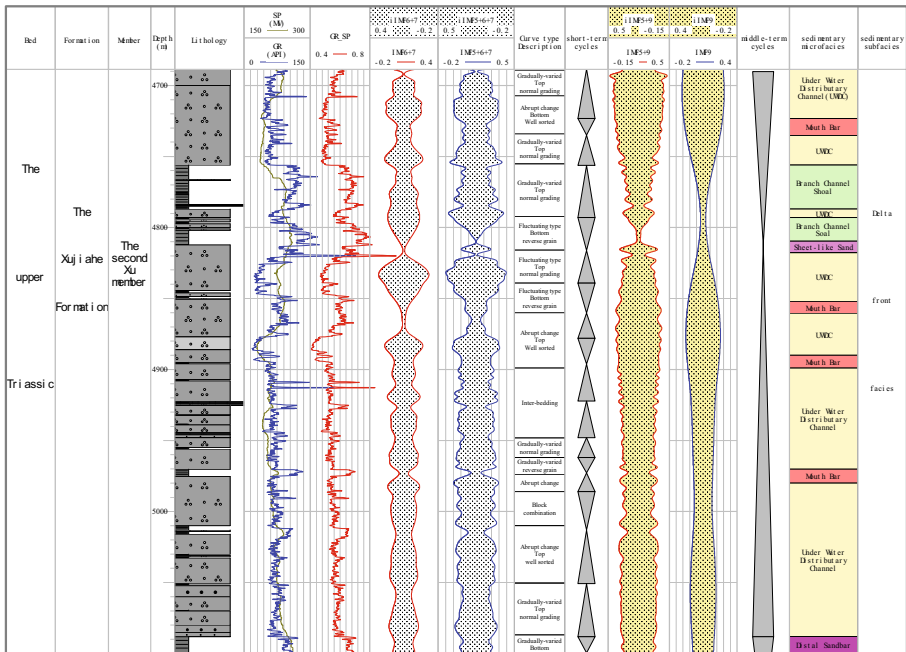


Fig. 7. Plots illustrating identification of short and middle-term cycle sequence stratum of X well using EMD method.

Further analysis showed that combining the decomposition signals under EMD resulted in strengthening of intrinsic information reflecting stratum characteristics and declined the influence of noise interference. The compared result defined that in the all combined signals of IMFs, only those which have good correlation index between each other and also have good correlation index with the original signal can better reveal the cycle characteristics of stratum. In Fig. 7 the results of EDM analysis are presented.

GR\_SP was a new combined parameter between natural gamma ray and spontaneous potential. IMFs were the results of empirical mode decomposition (EMD) of GR\_SP. The IMF6+7 denoted IMF6 plus IMF7 and IMF5+9 denoted IMF5 plus IMF9. Both iIMF6+7 and iIMF5+9 represented their mirror image, respectively. Therefore, IMF5+6+7 and iIMF5+6+7, IMF9 and iIMF9 have the same rule as before.

These combined curves not only contained changes of the lithology, but also revealed the trend in cycle of sequence stratum. In order to identify short and middle-term cycle sequence stratum effectively, we should refer to Table 1 (discussed in Section 3.2.2); we analyzed the classification of these curves and found out the normal graded bed sequence and reverse grading.

## 5. DISCUSSION

X well is located at Xiaoquan-Fenggu Structure Belt, middle section of West Sichuan Depression, Sichuan Basin. In Fig. 7 there are shown the characteristics of base level cycle of the stratum, the second section of Xujia River group. Its lithology includes mainly fine and middle grained sandstone and shale, belonging to delta front sub-facies. The combined signals with different frequencies were analyzed after EMD of curve characteristics according to Table 1. Short-term or long-term cycle characteristics were obviously identified and the sedimentary micro-facies were presented as follows:

**Under water distributary channel:** its lithology includes grey fine-grained to middle coarse particle sandstone. It represents the characteristics of cycle of positive graded bedding. It belongs to cross bedding, inclined bedding, and plot bedding. The scour and fill structure can be seen.

**Mouth bar:** its lithology chiefly is well sorted silt or fine sand and filled with cross-bedded sandstone, which has the characteristics of reverse grain size order cyclic-sequence.

**Branch channel shoal:** its lithology chiefly includes clay and contains less fine sand or silt. It is horizontally bedding.

**Sheet-like sand:** its lithology is separated into sorted fine sand or silt. It is cross-bedding and has the characteristics of reverse grain size order cyclic-sequence.

**Distal sandbar:** it is located at the farther part before estuary dam and its lithology mainly is silt and filled with cross-bedded sandstone, which has the characteristics of reverse grain size order cyclic-sequence.

## 6. CONCLUSIONS

□ Logging indices reflected the physical property characteristics of stratum's lithology, formation, sequence, and reservoir rocks. Sensitive indices were selected to improve the accuracy of logging interpretation.

□ Spontaneous potential and natural gamma ray were the sensitive indices reflecting geological formation and lithology. The mathematical methods were adopted for selecting new parameters and combining them. The new parameters strengthened the intrinsic characteristics and improved the results of partition.

□ EMD is an innovative time-frequency analysis method; not only does it guarantee the inherent characteristics in non-linear and non-stationary processes after the decomposition of signal, but also avoids the limitation of windowed Fourier Transform being constrained by time window and wavelet transform influenced by basis function. It can accurately describe the time-varying characteristics of signals. In fact, every  $IMF_i$  may has a physical meaning (*i.e.*, it may be related to geological phenomena.), and, as already highlighted, an important issue in practical application is how to judge the existence of this meaning in each  $IMF_i$ . This calls for further study and discussion.

□ EMD method was adopted for various combined logging indices; a discussion on relativity of mode functions and a search for the valued combinations are presented. Creating  $IMF_i$  combined signal helps to obtain abnormal dots (*e.g.*, mutations in different sedimentary layer interface) and better identify the cycle of stratigraphic base level.

## References

- Akansu, A.N., W.A. Serdijn, and I.W. Selesnick (2010), Emerging applications of wavelets: A review, *Phys. Comm.* **3**, 1, 1-18, DOI: 10.1016/j.phycom.2009.07.001.
- Bogle, M.G.V., J.E. Hearst, V.F.R. Jones, and L. Stoilov (1994), Lissajous knots, *J. Knot Theor. Ramif.* **3**, 2, 121-140, DOI: 10.1142/S0218216594000095.
- Bowman, D.C., and J.M. Lees (2013), The Hilbert–Huang transform: A high resolution spectral method for nonlinear and nonstationary time series, *Seismol. Res. Lett.* **84**, 6, 1074-1080, DOI: 10.1785/0220130025.

- de Lima, E.R., A.O. Andrade, J.L. Pons, P. Kyberd, and S.J. Nasuto (2006), Empirical mode decomposition: a novel technique for the study of tremor time series, *Med. Biol. Eng. Comput.* **44**, 7, 569-582, DOI: 10.1007/s11517-006-0065-x.
- Flandrin, P., G. Rilling, and P. Gonçalves (2004), Empirical mode decomposition as a filter bank, *IEEE Signal Process. Lett.* **11**, 2, 112-114, DOI: 10.1109/LSP.2003.821662.
- Hoste, J., and L. Zirbel (2006), Lissajous knots and knots with Lissajous projections, arXiv: math/0605632 [math.GT], 1-17.
- Huang, N.E., and Z. Wu (2008), A review on Hilbert–Huang transform: Method and its applications to geophysical studies, *Rev. Geophys.* **46**, 2, RG2006, DOI: 10.1029/2007RG000228.
- Huang, N.E., Z. Shen, S.R. Long, M.C. Wu, H.H. Shih, Q. Zheng, N.C. Yen, C.C. Tung, and H.H. Liu (1998), The empirical mode decomposition and the Hilbert spectrum for nonlinear and non-stationary time series analysis, *Proc. R. Soc. Lond. A.* **454**, 1971, 903-995, DOI: 10.1098/rspa.1998.0193.
- Huang, N.E., Z. Shen, and S.R. Long (1999), A new view of nonlinear water waves: the Hilbert spectrum, *Ann. Rev. Fluid Mech.* **31**, 417-457, DOI: 10.1146/annurev.fluid.31.1.417.
- Li, Y.-J., X.-Y. Hu, and Z.-X. He (2010), Application situation and prospects of Hilbert-Huang transform in geophysics, *Chin. J. Eng. Geophys.* **7**, 5, 537-543, (in Chinese).
- Serra, O., and H.T. Abbott (1982), The contribution of logging data to sedimentology and stratigraphy, *Soc. Petrol. Eng. J.* **22**, 1, 117-131, DOI: 10.2118/9270-PA.
- van Wagoner, J.C., R.M. Mitchum, K.M. Campion, and V.D. Rahmanian (1990), *Siliciclastic Sequence Stratigraphy in Well Logs, Cores, and Outcrops: Concepts for High-Resolution Correlation of Time and Facies*, AAPG Methods in Exploration Series, No. 7, The American Association of Petroleum Geologists, Tulsa, USA.
- Wawrzyniak, K. (2010), Application of time-frequency transforms to processing of full waveforms from acoustic logs, *Acta Geophys.* **58**, 1, 49-82, DOI: 10.2478/s11600-009-0043-4.
- Wu, Z., and N.E. Huang (2004), A study of the characteristics of white noise using the empirical mode decomposition method, *Proc. R. Soc. Lond. A* **460**, 2046, 1597-1611, DOI: 10.1098/rspa.2003.1221.
- Zhang, T., and C.-Y. Nie (2011), Information extraction of acoustic logging for oil layers based on EMD time-frequency analysis, *J. Changchun Univ.* **21**, 8, 15-18 (in Chinese).
- Zheng, R.-C., S.-M. Yin, and J. Peng (2000), Sedimentary dynamic analysis of sequence structure and stacking pattern of base-level cycle, *Acta Sediment. Sin.* **18**, 3, 369-375 (in Chinese).

- 
- Zheng, R.-C., J. Peng, and C.-R. Wu (2001), Grade division of base-level cycles of terrigenous basin and its implications, *Acta Sediment. Sin.* **19**, 2, 249-255 (in Chinese).
- Zheng, T.-X., and L.-H. Yang (2007), Discussion and improvement on empirical mode decomposition algorithm, *Acta Scient. Nat. Univ. Sunyatseni* **46**, 1, 1-6 (in Chinese).

Received 28 March 2014

Received in revised form 6 October 2014

Accepted 15 October 2014



# Short-term Tests of Potassium dIdD Vector Magnetometer

Eugen VUJIĆ

Faculty of Geodesy, University of Zagreb, Zagreb, Croatia  
e-mail: eugvujic@gfz.hr

## Abstract

In this paper the results of short-term tests of a suspended Potassium dIdD vector magnetometer are presented. The instrument was installed on a stable pillar during May 2012 near Milton (Ontario, Canada). The aim was to investigate primarily the bias current stability and the noise level of the instrument (for measured components less than 10 pT in a root-mean-square sense). A brief description of the measurement principles and a review of formulae used for field component calculations are given. The errors of components, which arise from assumptions on dIdD orientation as well as from the total field time variations during a measurement cycle, are estimated and discussed, both for real and simulated data. Finally, the accuracy of the instrument was estimated, and the maximal theoretical accuracies of components were better than 60 pT at mid-latitudes.

**Key words:** Potassium dIdD vector magnetometer, magnetometer calibration, error calculation.

## 1. INTRODUCTION

The temporal variations of the geomagnetic field are continuously recorded at geomagnetic observatories and periodically at variometer stations. The most common instruments are triaxial fluxgate instruments, which are relative instruments and have to be calibrated periodically by measurements of

the absolute instruments, such as D/I Fluxgate and (Overhauser effect) proton magnetometers. However, in remote areas and over the oceans there is a need for automation of absolute measurements (Newitt *et al.* 1996, Auster H.U. *et al.* 2007 and references therein).

During the recent twelve years, substantial efforts were made in developing the automated absolute instruments. The automation of D/I Fluxgate was presented in Van Loo and Rasson (2007). The method of performing the absolute measurements without the theodolite, and using a scalar magnetometer and a three axis fluxgate magnetometer rotating about two defined axes is presented in Auster and Auster (2003), and further developed in Auster H.U. *et al.* (2007). The basic idea is that the calibration of the magnetometer and the determination of the field in direction of the rotation axis can be done with the same procedure. The calibration principle by using a scalar magnetometer is given, *e.g.*, in Pang *et al.* (2013). A processor controlled proton magnetometer design and its application for an automated absolute measurement is presented in Auster V. *et al.* (2007).

There is also a class of magnetometers which measure field components by a scalar sensor equipped with coil systems (Jankowski and Sucksdorff 1996, Auster H.U. *et al.* 2007 and references therein). In this class are the dIdD vector magnetometers. The deflected Inclination deflected Declination (dIdD) method of measuring was first proposed by Alldredge (1960), using a proton precession sensor, and by Alldredge and Saldukas (1964), using an optically pumped rubidium sensor. The development of suspended Overhauser effect dIdD, which uses the Overhauser effect magnetometer sensor inside the two orthogonal bias coils, was briefly described in Hegymegi *et al.* (2004). The temperature characteristics of this instrument were given in Csontos *et al.* (2007).

The first three-component magnetometer using a scalar potassium sensor was presented in Alexandrov *et al.* (2004). During recent years, the Potassium dIdD was developed, with a potassium magnetometer sensor inside the bias coils. The first example of usage of this instrument was given in Hrvoic *et al.* (2009), and it was used as the variometer during very sensitive (1 fT/m) SuperGradiometer installation in Oaxaca State (Mexico). The dIdD vector magnetometers are actually semi-absolute instruments, *i.e.*, once the calibration parameters are known, the absolute measurements can be derived (Heilig 2007). These instruments are also automatically operated, so after their initial calibration they represent the automated absolute magnetometers. Still, under temperature and humidity uncontrolled conditions, it is advisable to make the occasional re-calibrations (Csontos *et al.* 2012).

The aims of this work are listed hereafter. The prime objectives of measurements performed with Potassium dIdD, which are presented here, were to test the bias coils fields' stability and instrumental noise levels. Fur-

ther, the geomagnetic components deviations due to the dIdD orientation errors are estimated, both for real and simulated data, which were derived for quiet and disturbed conditions at locations of four observatories in western hemisphere, in equatorial, mid-latitude, auroral, and polar regions, respectively. Also, the influence of assumptions on calibration of real data is presented. The errors of components due to the total field time variations during measurements were estimated, both for real and simulated data (at four observatories), for different sampling rates and geomagnetic activity levels. Moreover, the instrumental accuracy of measured components was obtained, and also the maximal theoretical accuracies as functions of the bias fields at locations of four observatories. Finally, the estimations of the calibration parameters' accuracies, which are necessary for the instrumental long-term stability up to 5 nT, were derived.

## 2. A BRIEF REVIEW OF THE USED MAGNETOMETER

### 2.1 Theory of instrument operation

Alkali vapor optically pumped magnetometers use gaseous alkali metals, such as potassium. A vapour cell containing gaseous metal is exposed by light of a specific wavelength. Let us consider, *e.g.*, three energy levels of atoms (two ground states, 1 and 2, with energy levels  $E_1$  and  $E_2$ , and excited state 3, with energy level  $E_3$ , with assumption that  $E_1 < E_2 \ll E_3$ ). The frequency of light is specifically selected and circularly polarized, to excite atoms from level 2 to 3. The atoms at level 3 spontaneously decay to both energy levels 1 and 2. Eventually the level 1 is fully populated and level 2 is depleted. Further, RF (radio frequency) power is applied to the cell to move atoms from level 1 back to level 2. The frequency of the RF field required to repopulate level 2 varies with the local magnetic field over a sensor, and is actually the Larmor frequency. The light intensity becomes modulated by the RF, and by detecting its modulation and measuring the frequency one can obtain a value of the local magnetic field (Alexandrov and Bonch-Bruevich 1992, Hrvoic and Newitt 2011). The block diagram of potassium magnetometer and its explanation is given, *e.g.*, in Alexandrov and Bonch-Bruevich (1992).

The suspended Potassium dIdD (P-dIdD) consists of a potassium magnetometer sensor centered inside two orthogonal spherical coil systems (Fig. 1a, attained at <http://www.gemsys.ca>). Coils are eventually aligned to be approximately perpendicular to the local geomagnetic field direction in the horizontal and geomagnetic meridian planes, respectively. High level of orthogonality of the two bias coils can be achieved experimentally by monitoring their mutual induction. Each measurement cycle consists of five sequences: bias currents in both directions are applied to both coil system, the



Fig. 1a. The suspended P-dIdD on a pillar. The outer spherical bias coils (D-coils) can be seen.

four biased total fields along with the unbiased total field are measured in a cycle (Schott *et al.* 2001, Heilig 2007, Hrvoic and Newitt 2011). The mechanical design of suspended P-dIdD is the same as for suspended Overhauser effect dIdD (Hegymegi *et al.* 2004), with potassium magnetometer sensor inside the bias coils instead of Overhauser effect proton magnetometer sensor.

A duration of one sequence (a sequence time) is five times shorter than sampling interval (a cycle time). These sequences are denoted as  $D_p$ ,  $D_m$ ,  $F$ ,  $I_p$ , and  $I_m$  (Fig. 1b).  $D_p$  is a local field over sensor when D-coils bias field is towards the magnetic east,  $D_m$  when this bias field is in opposite direction,  $F$  is a local field without any bias,  $I_p$  is a field when I-coils bias field is towards the Earth's surface, and  $I_m$  is a field over sensor when this bias field is in opposite direction (Heilig 2007, Hrvoic and Newitt 2011). Switching from one bias to another requires a delay for transients to die out, but the time required is so short that either instrument can be considered approximately continuous (this time interval is about 80  $\mu\text{s}$  for D-coils, and about 60  $\mu\text{s}$  for I-coils). As with most optically pumped magnetometers, the P-dIdD sensor should be properly oriented with respect to the direction of magnetic field. The ideal angle between sensor axis and magnetic field is  $45^\circ \pm 35^\circ$  or  $135^\circ \pm 35^\circ$ . Beyond these limits, the Larmor signal will be weakened and eventually faded away; these dependencies are known from Dehmelt (1957), and Bell and Bloom (1957) experiments.

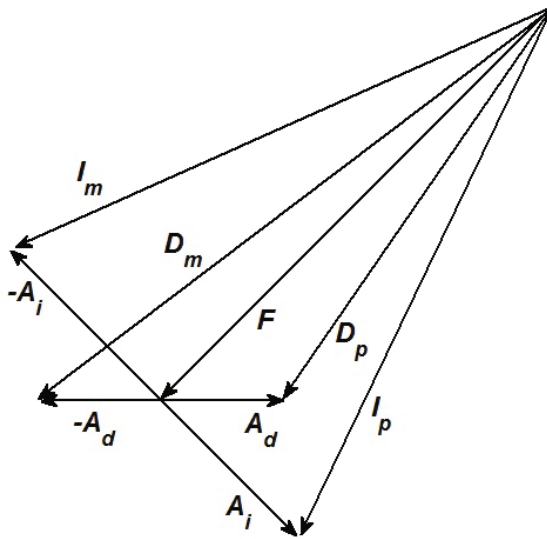


Fig. 1b. Measurement principle of P-dIdD:  $D_p$ ,  $D_m$ ,  $F$  (the local total field),  $I_p$  and  $I_m$  are measured components;  $A_d$  and  $A_i$  are D-coils and I-coils bias fields, respectively.

## 2.2 Calculation of the geomagnetic field components

In this analysis two coordinate reference frames will be used. The first one is orthogonal right-handed  $XYZ$ -frame, with positive  $X$ -axis in direction of geographic north, positive  $Y$ -axis in direction of geographic east, and  $Z$ -axis in direction of local vertical and is positive downward (Campbell 2003). The second one is SDI-frame (dIdD reference frame, not necessarily orthogonal), and it is always defined by the orientation of the bias coils axes. The two axes (D and I) are parallel to D- and I-coils axes, respectively, and the third axis (S) is defined to be perpendicular to both coils axes. It is defined that the dIdD is aligned when the D-axis is horizontal and D- and I-axes are orthogonal, and oriented when both axes are perpendicular to the local geomagnetic field vector. In case when the bias coils are not oriented but are aligned,  $D_0$  will be an angle between D-coil plane and a local geographic meridian, while  $I_0$  will be an angle between I-coil plane and horizontal plane (Schott and Leroy 2001, Heilig 2007). The D- and I-coil bias magnetic fields are  $A_d = [(D_p^2 + D_m^2 - 2F^2)/2]^{0.5}$  and  $A_i = [(I_p^2 + I_m^2 - 2F^2)/2]^{0.5}$ , respectively. The total field components in SDI-frame are (Schott *et al.* 2001):  $B_D = (D_p^2 - D_m^2)/4A_d$ ,  $B_I = (I_p^2 - I_m^2)/4A_i$  and  $B_S = (F^2 - B_D^2 - B_I^2)^{0.5}$ .

Let us consider a real case when dIdD is not aligned and oriented. The formalism given in Heilig (2007) is used. The orthogonality error between D- and I-axes is  $\varepsilon_O$ , and this error can be removed by using the transfor-

mations of total field components from non-orthogonal to orthogonal SDI-frame (the one where SDI-axes form a right-handed coordinate system, denoted by '), which are given by:

$$\begin{pmatrix} B'_D \\ B'_I \end{pmatrix} = \begin{pmatrix} 1/\cos \varepsilon_o & -\tan \varepsilon_o \\ 0 & 1 \end{pmatrix} \begin{pmatrix} B_D \\ B_I \end{pmatrix}, \quad (1)$$

$$B'_S = \left[ F^2 - (B_D^2 + B_I^2 - 2B_D B_I \sin \varepsilon_o) / \cos^2 \varepsilon_o \right]^{0.5}.$$

The next step is to set a D-coil axis horizontal. This can be achieved if the orthogonal SDI-frame is rotated by angle  $\theta$  about its S-axis in clockwise direction, when looking towards the origin. The matrix of that rotation is  $\Theta$ . Now one has perfectly aligned, but not oriented dIdD. One has to make two additional rotations to obtain XYZ-frame. The first is a rotation of SDI-frame about D-axis by angle  $I_0$ , in a counterclockwise direction when looking towards the origin. This makes S-axis horizontal, I-axis vertical, the corresponding rotation matrix is  $\mathbf{I}$ . The last rotation is about I-axis by angle  $D_0$  in a clockwise direction when looking towards the origin, and a rotation matrix is  $\mathbf{D}$ . Finally one has that SDI-frame coincides with XYZ-frame. Now the field components in XYZ-frame can be expressed with those in SDI-frame (Heilig 2007):

$$\begin{pmatrix} X \\ Y \\ Z \end{pmatrix} = \mathbf{D} \mathbf{I} \Theta \begin{pmatrix} B'_S \\ B'_D \\ B'_I \end{pmatrix}. \quad (2)$$

### 3. MEASUREMENTS AND dIdD CALIBRATION

The suspended P-dIdD was installed at an artificial noise-free location (Fig. 2) near town Milton (Ontario, Canada), on a nonmagnetic stable pillar, where the horizontal and vertical total field gradients are in the range of 1-2 nT/m, and covered by a shelter. The differences between measured biased fields after dIdD installation were  $D_p - D_m < 2$  nT and  $I_p - I_m < 2$  nT. The instrument operated in the period 11-15 May 2012, and powered from AC power supply. The instrument has 0.1 pT resolution and was sampling at 1 Hz sampling rate (*i.e.*, the duration of one measurement sequence was 0.2 s). Since the total field modulus during measurement sequence was not constant, the stage duration must be much longer than the atomic transition relaxation times, which are of the order of 30 ns (Happer 1972), to avoid transient effects. The aim of these measurements was to test dIdD data acquisition software, the bias field current source stability, and instrumental noise level.

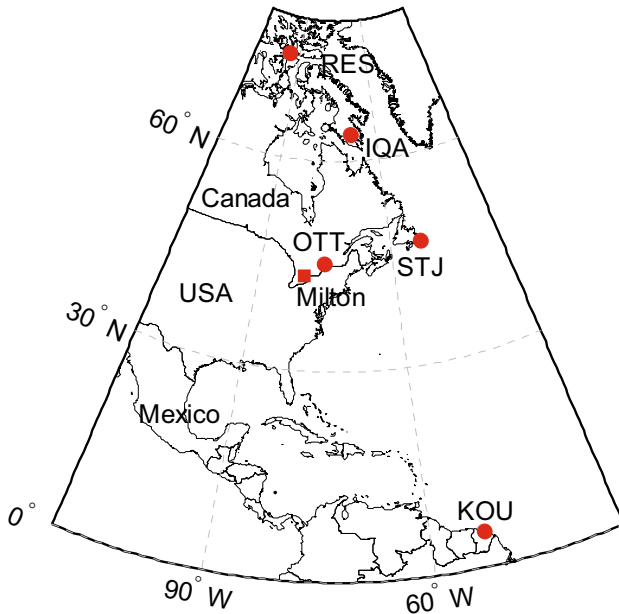


Fig. 2. The location of Milton (square), Ottawa observatory (OTT), and the observatories (RES, IQA, STJ, and KOU) used for the estimation of virtual dIdD errors and accuracies.

The absolute measurements of declination, inclination (both with D/I Fluxgate), and total field intensity (with Overhauser effect proton magnetometer) were performed on 11 May, after the dIdD setup (installed on 10 May 2012), on a tripod some 20 m away from dIdD pillar. For  $D$  and  $I$  measurements a null-method was used (Newitt *et al.* 1996). Two high precision GPS receivers in differential mode were used for the determination of the azimuth of the reference mark (Gu *et al.* 2006). One GPS was used as a reference mark, about 120 m away from the DI tripod (due to practical reasons), and a second GPS receiver was set on the tripod. The reference azimuth error was estimated to be less than  $8''$ .

After dIdD setup and absolute measurements, one can make a dIdD vector calibration (Heilig 2007), *i.e.*, to derive the angles  $D_0$ ,  $I_0$ ,  $\theta$ , and  $\varepsilon_0$  (see Section 2.2). The calibration was derived under the assumption that the time variations of geomagnetic field components are the same at dIdD and absolute instrument, and that the differences in  $X$ ,  $Y$ , and  $Z$  components between these two sites are known (non zero-gradient field). These site differences can be estimated by absolute measurements taken on both sites. The total field difference between dIdD and absolute instruments' site was 3.5 nT. The following condition for the geomagnetic field components was applied:

$$\sum_i (E_{i(\text{abs})} - E_{i(\text{dIdD})}) = \sum_i \Delta E_i, \quad (3)$$

where  $E = X, Y$  or  $Z$ , subscript “abs” is for absolute measurements and dIdD for P-dIdD measurements (their one-minute averages), and  $\Delta E$  is a difference between absolute and dIdD sites. Considering summation index  $i$ , there are seven options: if  $i = 3$ , then one has summation  $X + Y + Z$ ; if  $i = 2$ , one may have  $X + Y$ ,  $X + Z$  or  $Y + Z$ ; and if  $i = 1$ , one will have only condition for  $X, Y$  or  $Z$ . It was found numerically for what values of parameters  $D_0, I_0, \theta$ , and  $\varepsilon_0$  the condition 3 is fulfilled, within 0.01 nT, for all of the seven options simultaneously. The estimated uncertainties are ( $D_0, I_0, \theta$ , and  $\varepsilon_0$ ):  $\pm 0.0008^\circ, \pm 0.0003^\circ, \pm 0.024^\circ$ , and  $\pm 0.0168^\circ$ . One-minute averages were determined by using the Gaussian low-pass filter (St-Louis 2004).

## 4. DATA ANALYSIS AND DISCUSSION

### 4.1 The bias fields stability

Generally, for calculation of field components it is assumed that the bias currents are stable during one measurement cycle, *i.e.*, one can presume that  $A_d$  and  $-A_d$  are antiparallel and have the same amplitude, and also for  $\pm A_i$ . This is not true in practice since current source could produce fluctuations within one cycle. One has to consider the so-called hypothesis of symmetrical polarization (Marsal *et al.* 2007), *i.e.*, to verify an assumption about the same amplitude of bias fields during one cycle, respectively. The aim was to search for anomalous and asymmetrical polarizations, and a formalism proposed in Marsal *et al.* (2007) for both bias fields was applied and adjusted for the used cycle time.

First one has to find anomalous polarizations, and that means to find the sudden spikes in bias field time series. After that, one has to find asymmetrical polarization in each cycle, which provides information about the symmetrical hypothesis of bias field. The spikes in both polarisations (in a given cycle) indicate an erroneous value. In this case, percentage of the erroneous values (*i.e.*, seconds) during five days was 0.0028% (2.4 per day), with 5 mA bias coils' current. These stability tests' results are about twice better than those when noncalibrated P-dIdD was operated in 2011 for two months on the same pillar, with 6 mA bias coils' current. Also, the standard deviations of first differences for  $A_d$  and  $A_i$  were 3 and 1 pT, respectively.

Figure 3 shows the hourly mean air temperature (attained at <http://climate.weatheroffice.gc.ca/climateData>) from Weather Station Guelph Turfgrass ( $\varphi = 43.55^\circ \text{N}$ ,  $\lambda = 80.05^\circ \text{W}$ ), which is some 18 km SW away from measurement site, and the hourly mean values of D- and I-coils bias fields during five days. In both cases, the negative linear correlations were derived, and they are very high,  $-0.9315$  and  $-0.9335$  for D- and I-coils bias

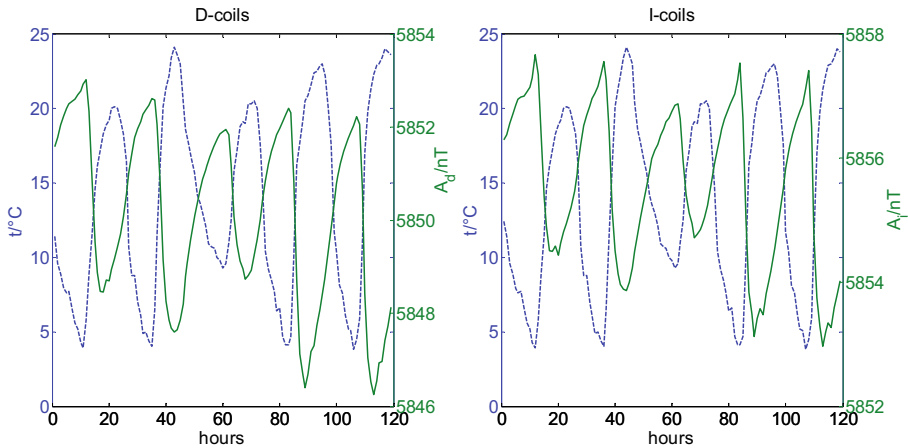


Fig. 3. Hourly mean air temperature at Weather Station Guelph Turfgrass (blue) and hourly mean values of D- and I-coils bias fields (green). D-coils bias field is in the interval from 01:00 on 11 May to 00:00 on 16 May 2012, and I-coils bias field is from 00:00 on 11 May to 23:00 on 15 May 2012. Temperature is in the interval from 00:00 on 11 May to 23:00 on 15 May 2012 (all in UTC).

field, respectively. The clear temperature dependence of the bias fields was also reported by Marsal *et al.* (2007), but for more controlled observatory conditions, for different bias coil design and for a dIdD that uses proton magnetometer sensor. They have obtained that for temperature variations of 1 °C the bias field variations were about 1 nT, although for differently designed dIdD. In this case, there were about 0.33 nT (outer, D-coils) and about 0.23 nT (inner, I-coils) changes for 1 °C external temperature variations. These “thermal coefficients” are only their effective values, because dependences of the bias fields on ambient temperature are not linear, and the corresponding temperature differences at Milton and Guelph station are (probably) not the same.

#### 4.2 Components deviations due to the dIdD orientation errors

After dIdD calibration it is possible to estimate the errors arising from the the instrument misorientation, *i.e.*, due to different values of  $D_0$ ,  $I_0$ ,  $\theta$ , and  $\varepsilon_0$  taken to calculate the geomagnetic components. The results for maximal errors are given in Table 1, and they are based on all one-minute averages. The first row gives the errors of components when there are two cases: in the first one the values for  $D_0$ ,  $I_0$ ,  $\theta$ , and  $\varepsilon_0$  derived as a results of instrument calibration were used, and in the second the values for  $D_0$  and  $I_0$  (*i.e.*,  $D'_0$  and  $I'_0$ ) were used, and they originated from assumption that during calibration there is  $\theta = 0$  and  $\varepsilon_0 = 0$ . In the second row are the errors when there are also

two cases: in the first one the values for  $D_0$ ,  $I_0$ ,  $\theta$ , and  $\varepsilon_O$  obtained from instrument calibration were used, and in the second one  $D_0$ ,  $I_0$ ,  $\theta$ , and  $\varepsilon_O$  (i.e.,  $D_{0a}$ ,  $I_{0a}$ ,  $\theta_a$ , and  $\varepsilon_{0a}$ ) were derived under the assumption that  $X$ ,  $Y$ , and  $Z$  components are the same at absolute instrument and dIdD sites during calibration (zero-gradient field).

Table 1

The maximal absolute errors of calculated geomagnetic components, but with different assumptions about the dIdD orientation (see text for details)

P-dIdD errors	Max $ \Delta X $ [nT]	Max $ \Delta Y $ [nT]	Max $ \Delta Z $ [nT]
$D_0$ $I_0$ $\theta$ $\varepsilon_O$ $D'_0$ $I'_0$ 0 0	0.4	0.4	0.1
$D_0$ $I_0$ $\theta$ $\varepsilon_O$ $D_{0a}$ $I_{0a}$ $\theta_a$ $\varepsilon_{0a}$	0.5	0.6	0.2

In Figure 4 there are shown the maximal absolute errors, when only one calibration parameter has been changed by  $-0.1^\circ$  to  $0.1^\circ$ , and the others were constant. In a case of  $X$  component,  $\Delta I_0$  has the largest and  $\Delta \varepsilon_O$  the smallest influence, and the errors due to  $\Delta I_0$  and  $\Delta D_0$  are much larger than due to  $\Delta \varepsilon_O$  and  $\Delta \theta$ . Considering  $Y$  component errors,  $\Delta D_0$  has the largest and  $\Delta \theta$  the smallest influence, and the errors due to  $\Delta D_0$  and  $\Delta I_0$  are much larger than due to  $\Delta \varepsilon_O$  and  $\Delta \theta$ . Finally, in the case of  $Z$  component,  $\Delta I_0$  has much larger influence than the other three parameters (their errors are less than 0.04 nT).

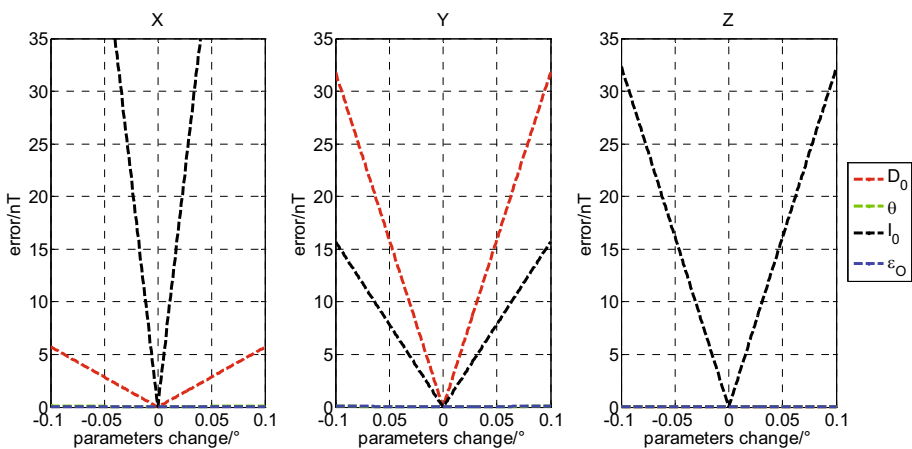


Fig. 4. The maximal absolute errors of  $X$ ,  $Y$ , and  $Z$  components when only one calibration parameter has been changed by  $-0.1^\circ$  to  $0.1^\circ$ , and the others were constant.

It is also possible to estimate these errors by putting a virtual dIdD in some observatory, since there the variations of  $X$ ,  $Y$ , and  $Z$  are known. This has been done for the following observatories (Fig. 2): Resolute (RES, polar cap region), Iqaluit (IQA, auroral oval region), St John's (STJ, mid-latitude region), and Kourou (KOU, equatorial region), during very disturbed days (severe geomagnetic storms from 29 to 31 October 2003) and very quiet geomagnetic conditions, respectively. The quiet daily variations were derived from SQ1 Model (Campbell 2003) for 30 October 2003. The dIdD parameters were taken under circumstances that dIdD is approximately oriented to the estimated quiet-night (QN) field, but with some realistic  $\theta$  and  $\varepsilon_O$  values, *i.e.*,  $D_0 = D_{QN}$ ,  $I_0 = I_{QN}$ ,  $\theta = 0.5^\circ$ , and  $\varepsilon_O = 0.1^\circ$ . The following procedure was used: from corrections and rotations given in Section 2.2 it is possible to calculate bias fields in  $XYZ$ -frame, and then using  $X$ ,  $Y$ ,  $Z$ , and  $F$  one can calculate the angles between bias fields and total field vectors, respectively. After that, one can obtain  $D_p$ ,  $D_m$ ,  $F$ ,  $I_p$ , and  $I_m$ .

Table 2

The maximal absolute errors of  $X$ ,  $Y$ , and  $Z$  components (one-minute values) when only one calibration parameter has been changed by  $-0.1^\circ$  to  $0.1^\circ$ , and the others were constant

Errors [nT]		Quiet				Disturbed			
		$D_0$	$I_0$	$\theta$	$\varepsilon_O$	$D_0$	$I_0$	$\theta$	$\varepsilon_O$
RES	$X$	1.7	85.6	0.02	0.02	4.4	87.1	2.7	1.3
	$Y$	2.7	54.1	0.03	0.03	3.8	55.0	3.9	2.1
	$Z$	0.0005	3.3	0.001	0.0005	0.0005	4.5	0.1	0.09
IQA	$X$	8.4	83.1	0.02	0.02	13.6	84.8	5.0	3.3
	$Y$	13.0	53.8	0.03	0.03	14.4	54.9	8.0	5.1
	$Z$	0.0005	15.5	0.003	0.0005	0.0005	16.4	1.1	0.3
STJ	$X$	12.0	78.6	0.03	0.007	13.6	79.5	1.4	0.7
	$Y$	31.7	29.8	0.02	0.02	33.4	30.1	1.9	1.8
	$Z$	0.0005	33.9	0.01	0.0006	0.0005	35.9	0.6	0.02
KOU	$X$	14.8	16.1	0.01	0.01	15.1	16.3	0.08	0.1
	$Y$	46.7	5.1	0.03	0.03	46.9	5.2	0.5	0.4
	$Z$	0.00005	49.0	0.02	0.0003	0.00005	49.2	0.3	0.004

**Note:** The errors are estimated for solar quiet variation and severe geomagnetic storm, respectively, for a virtual dIdD in four observatories: RES, IQA, OTT, and KOU.

In Table 2 are maximal absolute errors (in nT) of  $X$ ,  $Y$ , and  $Z$  components (one-minute values) when only one calibration parameter has been changed by  $-0.1^\circ$  to  $0.1^\circ$ , and the others were constant. It can be noticed that the errors due to  $D_0$  and  $I_0$  changes are higher for disturbed conditions, but not so

relatively drastically as in the cases of  $\theta$  and  $\varepsilon_O$  changes, especially for IQA. For RES and IQA the errors are largest for  $I_0$  changes, and smallest for  $\varepsilon_O$  changes, but for RES during very disturbed conditions the errors in  $X$  and  $Y$ , respectively, become comparable in the cases of  $D_0$  and  $\theta$  changes. The result for STJ shows a similar manner as that previously derived for Milton. For KOU observatory, in the cases of  $X$  and  $Y$  the errors due to  $I_0$  and  $D_0$  changes are much larger than those due to  $\varepsilon_O$  and  $\theta$  changes; they are slightly larger for  $I_0$  changes in  $X$ , but for  $Y$  component  $D_0$  has a largest influence; in the case of  $Z$ ,  $I_0$  has much larger influence than the other three parameters. The parameter  $D_0$  has negligible influence on  $Z$ ; on  $Y$  it has the largest influence, increasing from polar toward equatorial regions, and also for  $X$  component. The parameter  $I_0$  has an increasing influence on  $X$  and  $Y$  (higher for  $X$ ) from equatorial toward polar regions, and increasing on  $Z$  from polar toward equatorial regions.

### 4.3 Errors due to time variations of the total field

The total field vector has its time variations during one measurement cycle (Schott *et al.* 2001, Marsal *et al.* 2007), and this fact was neglected in Section 2.2. The components  $D_p$ ,  $D_m$ ,  $F$ ,  $I_p$ , and  $I_m$  are measured at the time instants  $t_1$ ,  $t_2$ ,  $t_3$ ,  $t_4$ , and  $t_5$ , respectively. The idea is that all measurements have to be reduced to the time instant  $t_3$ . The assignments  $D_p(t_1) = D_{p1}$ ,  $F(t_3) = F_3$ ,  $I_m(t_5) = I_{m5}$  are used. In this approach, the only approximation is that the amplitudes of  $A_d$  and  $A_i$  are constant over a single measurement cycle, *i.e.*, that both polarizations are symmetrical, and it is assumed that the bias fields are homogenous over the sensor size. We have  $D_{p3} = A_d + F_3 = A_d + F_1 + \Delta F_{13} = D_{p1} + \Delta F_{13}$ ,  $D_{m3} = D_{m2} + \Delta F_{23}$ ,  $I_{p3} = I_{p4} - \Delta F_{34}$  and  $I_{m3} = I_{m5} - \Delta F_{35}$ , where  $\Delta F_{jk}$  denotes the total field changes from instant  $t_j$  to instant  $t_k$ . From these equations one can derive that  $D_{p3}$ ,  $D_{m3}$ ,  $I_{p3}$ , and  $I_{m3}$  are functions of  $D_{p1}$ ,  $D_{m2}$ ,  $I_{p4}$ ,  $I_{m5}$ ,  $F_3$ ,  $\Delta F_{ij}$ ,  $A_d$ , and  $A_i$  (Schott *et al.* 2001), respectively, *e.g.*,  $D_{p3} = [D_{p1}^2 + 2\Delta F_{13} \cdot (A_d + F_3) - |\Delta F_{13}|^2]^{0.5}$  and  $I_{m3} = [I_{m5}^2 - 2\Delta F_{35} \cdot (-A_i + F_3) - |\Delta F_{35}|^2]^{0.5}$ .

These equations for  $D_{p3}$ ,  $D_{m3}$ ,  $I_{p3}$ , and  $I_{m3}$  can be inserted into equations for  $B_{D3}$ ,  $B_{I3}$ ,  $B_{S3}$ ,  $A_d$ , and  $A_i$  (see Section 2.2), to obtain a square nonlinear system of equations with the unknowns ( $B_{D3}$ ,  $B_{I3}$ ,  $B_{S3}$ ,  $A_d$ ,  $A_i$ ), and solved numerically for each measurement cycle. In above equations  $\Delta F_{jk}$  have to be known from nearby triaxial variometer (Schott *et al.* 2001), which has to operate on a sampling rate higher or equal than dIdD sequence time. Since both conditions were not satisfied in the case of a Milton data, this method was tested on a virtual dIdD placed inside observatories RES, IQA, STJ, and KOU.

Using the procedure from Section 4.2 one can derive  $D_{p1}$ ,  $D_{m2}$ ,  $F_3$ ,  $I_{p4}$ , and  $I_{m5}$  from  $X$ ,  $Y$ , and  $Z$ , with the minimal sequence time ( $\tau$ ) of 1 s, *i.e.*, cycle time of 5 s. This analysis was used in three cases: using the one-second variations registered at Milton, using a one-second observatories data on quiet day (6 December 2012) and on disturbed days (geomagnetic storm on 23/24 April 2012), respectively; the geomagnetic activity attained by using Ottawa Observatory  $K$  index (<http://geomag.nrcan.gc.ca>). Also, the highest global activity indices on 23 April 2012 were  $Kp = 6^-$ ,  $Ap = 26$  nT and  $Dst = -95$  nT, and on 24 April 2012 they were  $Kp = 7^-$ ,  $Ap = 41$  nT and  $Dst = -108$  nT ( $Kp$  and  $Ap$  attained at <http://www.gfz-potsdam.de>;  $Dst$  attained at <http://swdcwww.kugi.kyoto-u.ac.jp>).

In Table 3a there are displayed the estimated maximal absolute errors of one-second Milton data, due to the differences of  $D_{p1}$ ,  $D_{m2}$ ,  $I_{p4}$ , and  $I_{m5}$ , and corresponding values reduced to  $t_3$ , respectively. The reduced values were estimated from measured one ( $\tau = 0.2$  s) by adding: (a) constant values with random sign ( $+\Delta$  or  $-\Delta$ ); and (b) random values with given amplitude ( $\pm\Delta$ ). The errors are largest for  $Y$  and smallest for  $Z$  component, and increase linearly with amplitude of differences; they are larger for case (a), and the presented values are averages over random 2000 cases, respectively.

In sequel, Table 3b shows the mean absolute errors of geomagnetic components for observatories RES, IQA, STJ, and KOU, during quiet and disturbed conditions, respectively. These errors are larger during disturbed conditions, and then are largest in  $Y$  and smallest in  $Z$  component for RES, IQA and STJ, while for KOU are smallest in  $X$ , and about the same in  $Y$  and  $Z$ . Also, they increase with sequence time, but it is not so obvious for KOU. These errors are largest for IQA and smallest for KOU during disturbed conditions. During quiet conditions, the errors are largest for STJ (possibly due

Table 3a

The estimated  $X$ ,  $Y$ , and  $Z$  maximal absolute errors of Milton data due to the differences of  $D_{p1}$ ,  $D_{m2}$ ,  $I_{p4}$ , and  $I_{m5}$ , and corresponding values reduced to  $t_3$ , respectively

Errors	Constant			Random		
	$X$ [nT]	$Y$ [nT]	$Z$ [nT]	$X$ [nT]	$Y$ [nT]	$Z$ [nT]
0.004	0.04	0.04	0.01	0.04	0.04	0.01
0.02	0.21	0.22	0.06	0.20	0.21	0.06
0.1	1.04	1.09	0.32	1.00	1.05	0.32
0.5	5.20	5.4	1.6	5.0	5.2	1.6
2.5	26.0	27.2	8.1	24.9	26.2	7.9

Table 3b

The mean absolute errors of  $X$ ,  $Y$ , and  $Z$  components due to the total field variation during measurement cycle (with sequence times 1 to 4 s), for four observatories (RES, IQA, STJ, and KOU) during quiet and disturbed conditions, respectively

Errors [nT]	Quiet			Disturbed		
$\tau/s$	$X$	$Y$	$Z$	$X$	$Y$	$Z$
RES						
1	0.12	0.12	0.005	0.23	0.39	0.013
2	0.12	0.22	0.007	0.48	0.68	0.026
3	0.14	0.24	0.007	0.65	0.98	0.036
4	0.18	0.21	0.009	0.81	1.29	0.046
0.2	0.010	0.014	0.001	0.043	0.066	0.002
IQA						
1	0.08	0.14	0.02	0.54	1.39	0.17
2	0.13	0.26	0.03	1.14	2.73	0.34
3	0.18	0.38	0.05	1.79	4.02	0.50
4	0.23	0.49	0.06	2.54	5.25	0.67
0.2	0.012	0.025	0.003	0.12	0.27	0.034
STJ						
1	0.32	0.34	0.13	0.41	0.48	0.18
2	0.32	0.35	0.13	0.52	0.66	0.24
3	0.37	0.36	0.15	0.68	0.86	0.33
4	0.36	0.39	0.15	0.84	1.07	0.40
0.2	0.023	0.025	0.010	0.046	0.058	0.022
KOU						
1	0.03	0.08	0.06	0.03	0.08	0.07
2	0.05	0.09	0.11	0.06	0.15	0.11
3	0.06	0.13	0.11	0.05	0.13	0.16
4	0.04	0.10	0.10	0.05	0.15	0.17
0.2	0.003	0.007	0.007	0.003	0.009	0.010

**Note:** The estimated errors for  $\tau = 0.2$  s are derived from errors for sequence times 1 to 4 s.

to the ocean coast effect) and smallest for KOU. They are then largest in  $Y$  and smallest in  $Z$  component for RES, IQA, and STJ, while for KOU are largest in  $Y$  and smallest in  $X$ . They also increase with sequence time, but not so obvious as for disturbed conditions (except for IQA). The very rough errors estimates for  $\tau = 0.2$  s are based on the errors for sequence times 1 to 4 s (linear dependence of errors on sequence times).

#### 4.4 The instrumental accuracy

To the noise level of dIdD, beside a thermal noise of sensor and a noise of electronic circuits connected to the sensor, there contributes a noise from the bias fields' current source. They produce additional fluctuations in measured components  $D_p$ ,  $D_m$ ,  $I_p$ , and  $I_m$ . For their root-mean-square (rms) noise levels estimation, a single instrument analysis was used, and it works well when the geomagnetic field is in a quiet, undisturbed conditions. The first differences between successive one-second data of particular component were computed, and then the root-mean-square errors of successive five-minute moving averages were derived. The minimal values of these errors during quiet intervals were the corresponding noise levels (Worthington *et al.* 2009). This method was approved by applying it to the data derived by adding a white noise of known amplitudes on quiet time variations (from SQ1 Model), and it was found that this gives quite reasonable estimates of noise levels (noise amplitudes). In Table 4 the estimates for measured components in Milton are given.

Table 4

The estimated rms noise levels of measured components, for P-dIdD in Milton

rms noise level	$M_{Dp}$ [pT]	$M_{Dm}$ [pT]	$M_F$ [pT]	$M_{Ip}$ [pT]	$M_{Im}$ [pT]	Mean [pT]
P-dIdD	9	9	6	9	9	8±1

**Note:** These values are the mean over five days, when  $K_{OT} \leq 1$ .

By using the data from Table 4 one can estimate the maximal (short-term) theoretical accuracies of calculated components, and they were for  $X$ ,  $Y$ ,  $H$  (horizontal field), and  $Z$ , respectively: 56, 59, 56, and 21 pT. The mean field values were taken as the averages of geomagnetic components over five days. One can also estimate that the bias fields accuracies for Milton data are  $\pm 0.08$  nT. The relative error of assumption that both bias fields are equal is about 0.09%, and in this case the mean bias field is 5853 nT (5 mA bias current).

Additionally, the Overhauser effect dIdD was operated at 1 Hz sampling rate with 11960 nT mean bias field, in the interval 16-20 May 2012, on the nonmagnetic pillar some 20 m away from P-dIdD pillar, due to the similar reasons as P-dIdD. The mean estimated rms noise level of measured components was  $144 \pm 9$  pT, and the estimated maximal theoretical accuracies of  $X$ ,  $Y$ , and  $Z$  were 426, 484, and 195 pT, respectively.

The next figure shows the maximal theoretical accuracies of calculated components as functions of the bias fields, when  $A_i = A_d = 4000$ -8000 nT.

The shown results are the estimations for RES, IQA, STJ, and KOU. The values for geomagnetic elements were derived from IGRF-11 Model ([http://www.geomag.us/online\\_calculators.html](http://www.geomag.us/online_calculators.html)) on the middle of May 2012. The calibration parameter values were:  $D_0 = D_{IGRF}$ ,  $I_0 = I_{IGRF}$ ,  $\theta = 0.5^\circ$  and  $\varepsilon_0 = 0.1^\circ$ . From Fig. 5 one can notice that the estimated maximal theoretical accuracies increase with increasing bias fields, and depend on geomagnetic coordinates. The  $X$  and  $Y$  components accuracies increase with decreasing geomagnetic latitude, *i.e.*, both are higher in equatorial than in polar cap region, and for the same bias field are smaller for  $Y$  component. In the case of

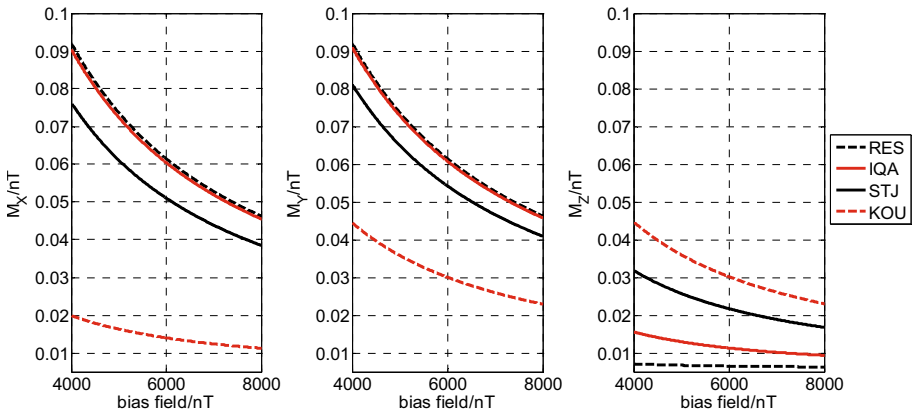


Fig. 5. The estimated maximal theoretical accuracies of directional components for the four observatories (RES, IQA, STJ, and KOU), as the functions of bias field, for May 2012.

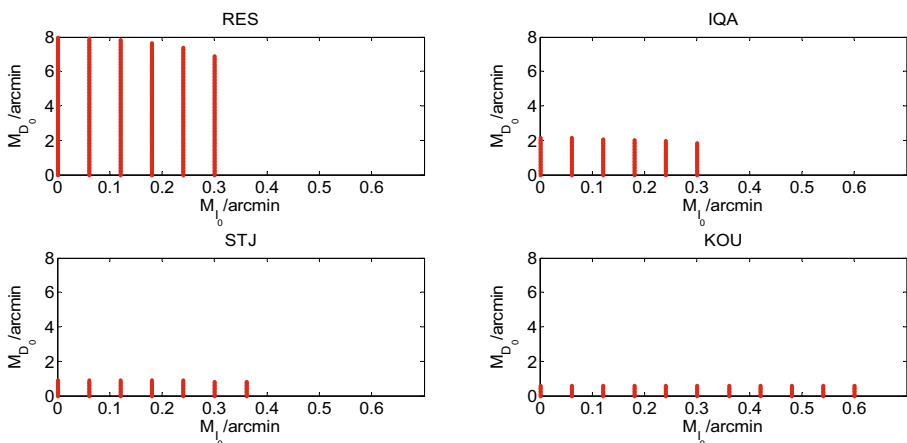


Fig. 6. The long-term  $D_0$  and  $I_0$  accuracies, *i.e.*,  $(M_{I_0}, M_{D_0})$  pairs, when  $M_\theta = 0.5^\circ$  and  $M_{\varepsilon_0} = 0.2^\circ$ , needed to achieve the  $X$ ,  $Y$ , and  $Z$  accuracies higher than 5 nT, for RES, IQA, STJ, and KOU observatories, respectively.

the  $Z$  component accuracies, they are highest in the polar cap region (almost constant with respect to the bias field) and smallest in the equatorial region.

The long term accuracies will depend, beside on measured components' accuracies, on long-term accuracies of  $D_0$ ,  $I_0$ ,  $\theta$ , and  $\varepsilon_0$ . These parameters could be time-dependent during humidity and temperature uncontrolled conditions. The long-term accuracies estimation was made under the same assumptions about the mean components and calibration parameters values, as the maximal accuracies. By using some characteristic one-year accuracies under controlled conditions (Heilig 2007), it is possible to estimate the long-term accuracies. In this case study, the values of  $M_\theta = 0.5^\circ$  and  $M_{\varepsilon_0} = 0.2^\circ$  were taken, and the pairs of  $(M_{I_0}, M_{D_0})$  values were found, so that the long-term accuracies of  $X$ ,  $Y$ , and  $Z$  were higher than 5 nT. The results for RES, IQA, STJ, and KOU are shown in Fig. 6, where each dot represents  $(M_{I_0}, M_{D_0})$  pair.

## 5. CONCLUSIONS

During the presented short-term tests, dIdD has operated with 1 Hz sampling rate during five days on a stable nonmagnetic pillar. After instrument setup and calibration, attention was focused on stability tests, considering the bias fields and the instrumental noise level. It was estimated that the D- and I-coils bias fields are quite stable when considering their current source fluctuations, and confirmed that there is a negative correlation between the bias fields and the surrounding air temperature. One can presume that this is due to the small temperature changes of bias coils dimensions. The calculated components' correlations with the nearest observatory (Ottawa) were high.

The errors due to the instrument orientation assumptions (with deviations up to  $0.1^\circ$ ) were estimated to be the most sensitive on the calibration parameter  $I_0$  in the case of  $X$ ,  $Y$ , and  $Z$  components for polar (up to 87 nT) and auroral observatory (up to 85 nT); and  $X$  and  $Z$  components for mid-latitude and equatorial observatory (up to 80 and 49 nT, respectively). Parameter  $D_0$  had the highest influence on  $Y$  component at mid-latitude and equatorial observatory (up to 33 and 47 nT, respectively). The parameters  $\theta$  and  $\varepsilon_0$  had very small influence, but the errors due to them were relatively severely increased during disturbed conditions (up to 8 and 5 nT for  $Y$  component in auroral region, respectively). The orientation errors in Milton were less than 1 nT. The errors due to the total field time variations during dIdD measurement cycle, based on synthetic and real data from four observatories and Milton, were estimated for different cycle times and during different geomagnetic conditions. It was estimated that these errors are generally larger for longer cycle time and during disturbed conditions (up to 5 nT for  $Y$  component in auroral region at 20 s cycle time).

On the basis of measured components' noise level (better than 10 pT in rms sense) one can estimate the geomagnetic components maximal theoretical accuracies, and they depend also on the position of measurement site on the Earth. In this case study it was estimated that the highest short-term accuracies for horizontal components will be in equatorial regions (better than 20 pT in  $X$  and 40 pT in  $Y$ ), and for vertical component in polar region (better than 10 pT). Also it was estimated that the long-term geomagnetic components' accuracies will depend dominantly on  $D_0$  and  $I_0$  accuracies, with lowest  $D_0$  and highest  $I_0$  accuracies in polar region, and *vice versa* in equatorial regions.

The mechanical design of P-dIdD is the same as for the Overhauser effect dIdD, but at the same sampling rate of 1 Hz the P-dIdD has about 18 times better measured components' accuracy, and about 7-9 times better the maximal theoretical accuracies of  $X$ ,  $Y$ , and  $Z$  components (at mid-latitudes). All the results in this study considering Potassium dIdD at 1 Hz sampling rate could indicate that it can be suitable for, *e.g.*, the geomagnetic observatories, repeat station, directional drilling surveys, and could be also used in some ionospheric or magnetospheric studies.

**Acknowledgments.** The author is deeply grateful to Dr. I. Hrvoic for providing him training at GEM System Inc., and for providing Potassium dIdD for this study. The staff of GEM System Inc. participating in the field work are kindly acknowledged. The author thanks the national institutes that support geomagnetic observatories and Intermagnet for promoting high standards of magnetic observatory practice ([www.intermagnet.org](http://www.intermagnet.org)). The Ottawa Geomagnetic Observatory and the Weather Station Guelph Turfgrass are kindly acknowledged for providing the data. The author would like to thank Dr. M. Brkić (Zagreb) and M.Sc. B. Heilig (Tihany) for valuable comments on the manuscript. The Associate Editor Dr. M. Zarroca and two anonymous reviewers are acknowledged for their constructive comments that improved the manuscript.

## References

- Alexandrov, E.B., and V.A. Bonch-Bruevich (1992), Optically pumped atomic magnetometers after three decades, *Opt. Eng.* **31**, 4, 711-717, DOI: 10.1117/12.56132.
- Alexandrov, E.B., M.V. Balabas, V.N. Kulyasov, A.E. Ivanov, A.S. Pazgalev, J.L. Rasson, A.K. Vershovski, and N.N. Yakobson (2004), Three-compo-

- ment variometer based on a scalar potassium sensor, *Meas. Sci. Technol.* **15**, 5, 918-922, DOI: 10.1088/0957-0233/15/5/020.
- Allredge, L.R. (1960), A proposed automatic standard magnetic observatory, *J. Geophys. Res.* **65**, 11, 3777-3786, DOI: 10.1029/JZ065i011p03777.
- Allredge, L.R., and I. Saldukas (1964), An automatic standard magnetic observatory, *J. Geophys. Res.* **69**, 10, 1963-1970, DOI: 10.1029/JZ069i010p01963.
- Auster, H.U., and V. Auster (2003), A new method for performing an absolute measurement of the geomagnetic field, *Meas. Sci. Technol.* **14**, 7, 1013-1017, DOI: 10.1088/0957-0233/14/7/315.
- Auster, H.U., M. Manda, A. Hemshorn, E. Pulz, and M. Korte (2007), Automation of absolute measurement of the geomagnetic field, *Earth Planets Space* **59**, 9, 1007-1014, DOI: 10.1186/BF03352041.
- Auster, V., O. Hillenmaier, R. Kroth, and M. Wiedemann (2007), Advanced proton magnetometer design and its application for absolute measurement, *Publs. Inst. Geophys. Pol. Acad. Sc.* **C-99**, 398, 60-68.
- Bell, W.E., and A.L. Bloom (1957), Optical detection of magnetic resonance in alkali metal vapor, *Phys. Rev.* **107**, 6, 1559-1565, DOI: 10.1103/PhysRev.107.1559.
- Campbell, W.H. (2003), *Introduction to Geomagnetic Fields*, 2nd ed., Cambridge University Press, Cambridge.
- Csontos, A., L. Hegymegi, and B. Heilig (2007), Temperature tests on modern magnetometers, *Publs. Inst. Geophys. Pol. Acad. Sc.* **C-99**, 398, 171-177.
- Csontos, A., D. Šugar, M. Brkić, P. Kovács, and L. Hegymegi (2012), How to control a temporary DIDD based observatory in the field? *Ann. Geophys.* **55**, 6, 1085-1094, DOI: 10.4401/ag-5447.
- Dehmelt, H.G. (1957), Modulation of a light beam by precessing absorbing atoms, *Phys. Rev.* **105**, 6, 1924-1925, DOI: 10.1103/PhysRev.105.1924.
- Gu, Z., Z. Zhan, J. Gao, T. Yao, and W. Han (2006), Application of GPS in geomagnetic survey, *Earth Planets Space* **58**, 6, 723-729, DOI: 10.1186/BF03351974.
- Happer, W. (1972), Optical pumping, *Rev. Mod. Phys.* **44**, 2, 169-249, DOI: 10.1103/RevModPhys.44.169.
- Hegymegi, L., B. Heilig, and A. Csontos (2004), New suspended dIdD magnetometer for observatory (and field?) use. **In:** *Proc. 11th IAGA Workshop on Geomagnetic Observatory Instruments, Data Acquisition and Processing, 9-17 November 2004, Kakioka and Tsukuba, Japan*, 28-33.
- Heilig, B. (2007), Intercalibration of dIdD and Fluxgate Magnetometers, *Publs. Inst. Geophys. Pol. Acad. Sc.* **C-99**, 398, 144-151.
- Hrvoic, I., and L.R. Newitt (2011), Instruments and methodologies for measurement of the Earth's magnetic field. **In:** M. Manda and M. Korte (eds.), *Geomagnetic Observations and Models*, IAGA Special Sopron Book Series,

- Vol. 5, Springer-Verlag, Berlin Heidelberg, 105-126, DOI: 10.1007/978-90-481-9858-0\_5.
- Hrvoic, I., G. Cifuentes-Nava, E. Cabral-Cano, E. Hernandez, M. Wilson, and F. Lopez (2009), New magnetic observatory installation in Oaxaca, Mexico. **In:** *Proc. 13th IAGA Workshop on Geomagnetic Observatory Instruments, Data Acquisition and Processing, 9-18 June 2008, Boulder and Golden, CO, USA*.
- Jankowski, J., and C. Sucksdorff (1996), *Guide for Magnetic Measurements and Observatory Practice*, International Association of Geomagnetism and Aeronomy, Warszawa, Poland, 235 pp.
- Marsal, S., J.M. Torta, and J.C. Riddick (2007), An assessment of the BGS  $\delta D\delta I$  vector magnetometer, *Publs. Inst. Geophys. Pol. Acad. Sc. C-99*, 398, 158-165.
- Newitt, L.R., C.E. Barton, and J. Bitterly (1996), *Guide for Magnetic Repeat Station Surveys*, International Association of Geomagnetism and Aeronomy, Warszawa, Poland.
- Pang, H., J. Li, D. Chen, M. Pan, S. Luo, Q. Zhang, and F. Luo (2013), Calibration of three-axis fluxgate magnetometers with nonlinear least square method, *Measurement* **46**, 4, 1600-1606, DOI: 10.1016/j.measurement.2012.11.001.
- Schott, J.J., and P. Leroy (2001), Orientation of the DIDD magnetometer, *Contrib. Geophys. Geod.* **31**, 1, 43-50.
- Schott, J.J., V. Boulard, A. Pérès, and J.M. Cantin (2001), Magnetic component measurements with the DIDD, *Contrib. Geophys. Geod.* **31**, 1, 35-42.
- St-Louis, B. (ed.), (2004), Intermagnet technical reference manual: Version 4.2, <http://www.intermagnet.org>.
- van Loo, S.A., and J.L. Rasson (2007), Presentation of the prototype of an automated DIFlux, *Publs. Inst. Geophys. Pol. Acad. Sc. C-99*, 398, 77-86.
- Worthington, E.W., E.A. Sauter, and J.J. Love (2009), Analysis of USGS one-second data. **In:** *Proc. 13th IAGA Workshop on Geomagnetic Observatory Instruments, Data Acquisition and Processing, 9-18 June 2008, Boulder and Golden, CO, USA*.

Received 22 April 2014

Received in revised form 1 September 2014

Accepted 3 October 2014



## Evaluating Electrical Anisotropy Parameters in Miocene Formations in the Cierpisz Deposit

Maria BAŁA and Adam CICHY

AGH University of Science and Technology, Department of Geology,  
Geophysics and Environmental Protection, Kraków, Poland;  
e-mails: bala@geol.agh.edu.pl, cichy@agh.edu.pl (corresponding author)

### Abstract

The electrical anisotropy of rocks is generally an effect of alternating layers of thin-bedded sandstones and shales with clear lamination.

Thin-bedded rock sequences can be treated as an anisotropic medium described by two resistivities: horizontally to the bedding  $R_H$  and vertically to the bedding  $R_V$ . Such sequences have fairly low resistivity and, as a result of poor vertical resolution of conventional electric tools, one can sometimes fail to distinguish them from the adjoining shales.

This paper presents the possibility of calculating the anisotropy parameters based on resistivity logs recorded with a laterolog tool (DLL) and an induction tool HRAI. We have also performed an analysis of the ambiguity of the results and attempts to assess the water saturation (SW) generating cross-plots based on calculated resistivities,  $R_H$  and  $R_V$ .

It is very important to correctly evaluate the resistivity of sandstone interbeds when calculating water saturation (SW) and hydrocarbon saturation (SG), in formulating an integrated quantitative interpretation of anisotropic formations.

**Key words:** electrical anisotropy, dual laterolog tools, induction device HRAI, horizontal resistivity, vertical resistivity.

## 1. INTRODUCTION

The objective of this paper is an attempt to evaluate three electrical anisotropy parameters, namely: horizontal resistivity ( $R_H$ ) vertical resistivity ( $R_V$ ), and the anisotropy coefficient ( $\lambda$ ). This can be achieved by measurements carried out using different electrical tools, namely an induction tool with high vertical resolution, HRAI, and dual laterolog tools, LLS and LLD. It is known from the theory that apparent resistivity measured using an induction device, HRAI, provides information on horizontal resistivity ( $R_H$ ) while a controlled device LLD records apparent resistivity, which is a result of the influence of both horizontal  $R_H$  and vertical  $R_V$  resistivities (Bała 2011). The problem of electrical anisotropy of rocks and its influence on the resistivity measured in boreholes using electrical tools has been dealt with by a number of researchers for many years (Kunz and Moran 1958, Zajkowskij *et al.* 1965, Dachnov 1967, Chemali *et al.* 1987, Klein 1993, Bittar and Rodney 1994, Klein *et al.* 1995, Hagiwara 1996, Yang 2001, Anderson *et al.* 2002, 2008; Faivre *et al.* 2002, Tabanou *et al.* 2002, Rosthal *et al.* 2003). The author of this paper has recently been engaged in an evaluation of electric anisotropy of sandy-shale Miocene rocks, based on resistivity logs recorded using laterolog tools and induction tools in boreholes (Bała 2009, 2011).

The electrical anisotropy of rocks may be caused by a number of factors, but the most important ones include alternating layers of thin-bedded sandstones and shales with a clear lamination. Anisotropy in the microscopic scale is caused by the internal arrangement of grains of different size, which are elongated in one direction, or by different pore sizes.

In Miocene formations of the Carpathian Foredeep one can observe the alternating thin layers of sandstone, mudstone, and clay. Thin-bedded rock sequences can be treated as an anisotropic medium described by two resistivities: horizontally to the bedding ( $R_H$ ) and vertically to the bedding ( $R_V$ ).

Such sequences have fairly low resistivity and, as a result of the poor vertical resolution of conventional electric tools, one can fail to distinguish them from the adjoining shales. Mollison *et al.* (2001) called this a pay zone with low resistivity contrast. An example of such deposits are turbidites from a Miocene basin plain and submarine fans that are very important to hydrocarbon accumulation. Those deposits contain thin beds of sandy-shaly-mudstone heteroliths from the Lower and Middle Sarmatian (Myśliwiec 2004).

Based on well logging data analysis, well C-3 in the Cierpisz structure was chosen for testing, logging was carried out in order to evaluate electrical anisotropy, DLL and HRAI.

## 2. GEOLOGICAL SETTING

The Cierpisz gas deposit is located in sand-shale Sarmatian sediments in the southern part of the Carpathian Foredeep, near the great gas deposit of Czarna Sędziszowska (Fig. 1).

The detailed study of SED dipmeter logs permitted the evaluation of structures and dip angles in well C-3.

In shallow sections of the well there occur regular layered alternating series of shales, mudstones, and sandstones, which have been deposited in a low-energy environment. The deposits lie almost horizontally or are dipping at a small angle to the north.

The underlying transgressive series of sandstones and mudstones are also dipping at small angles in the same direction.

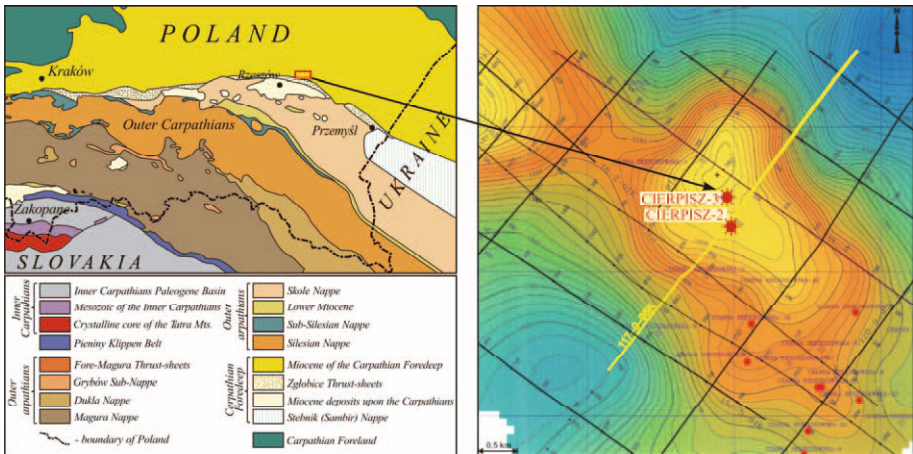


Fig. 1: right: Location of the Cierpisz-3 well in the structural map of 9th gas horizon of the Cierpisz gas deposit (Syrek-Moryc 2006); left: Schematic map of Carpathians and Carpathian Foredeep: 1 – northern range of Miocene formations, 2 – northern border of the Carpathians, and 3 – boundaries of tectonic units of the Outer Carpathians (Karnkowski 1999).

## 3. ANISOTROPY OF THE ELECTRICAL PROPERTIES OF ROCKS

Most of sedimentary rocks have anisotropic properties. The electric current flows easily along the bedding rather than perpendicular to it.

In a uniform and anisotropic medium, the potential of the electric field ( $U$ ) at an arbitrary point of the medium, decreases inversely proportionally to the distance ( $r$ ) from the source of the direct current, with an intensity of  $I$ .

$$U = \frac{I \cdot R_{av}}{4\pi \cdot r \cdot \sqrt{1 + (\lambda^2 - 1) \cdot \cos^2 \alpha}}, \quad (1)$$

where

$$\lambda^2 = R_V / R_H \quad (2)$$

is the anisotropy coefficient,

$$R_{av} = \sqrt{R_V \cdot R_H} \quad (3)$$

is the geometric mean,  $R_V$  is the electric resistivity measured vertically to the bedding,  $R_H$  is the electric resistivity measured horizontally to the bedding, and  $\alpha$  is the angle between the layer dip and the vertical to measurement direction.

For given values of  $R_{av}$  and  $\lambda$ , the potential depends on the direction (angle  $\alpha$ ) along which one studies how the  $U$  changes depend on  $r$ .

Having assumed that the borehole diameter and drilling mud are neglected (no borehole) in a uniform and anisotropic medium, the measured resistivity ( $R_a$ ) does not depend on type and size of the tool (lateral or normal tool) (e.g., Dachnov 1967, Kunz and Moran 1958).

$$R_a = \frac{\lambda \cdot R_H}{\sqrt{1 + (\lambda^2 - 1) \cdot \cos^2 \alpha}} \quad (4)$$

For the case of  $\alpha = 0^\circ$

$$R_a^{(v)} = \frac{\lambda \cdot R_h}{\lambda} = R_h \quad (4a)$$

and for the case of  $\alpha = 90^\circ$

$$R_a^{(h)} = \lambda \cdot R_h \quad (4b)$$

thus

$$R_a^{(h)} > R_a^{(v)} \quad (4c)$$

This means that the apparent resistivity  $R_a^{(v)}$  measured normal to the strike direction is less than  $R_a^{(h)}$  measured along the strike direction, although it is known that the true resistivity of an anisotropic formation, normal to its stratification  $R_v$ , is greater than parallel to the plane of stratification  $R_h$ . This phenomenon is called "the paradox of anisotropy".

However, due to the presence of the borehole and of the tool, the real measured values differ from the theoretical ones (Moran and Gianzero 1979).

In our case, the paradox of anisotropy does not appear due to the big diameter of the borehole (0.216 m) and the presence of mud.

Based on dipmeter measurements in well C-3 one can observe that the dips in layers in the reservoir zones do not exceed  $1\text{-}3^\circ$ . Also, the small inclination of a borehole does not have any great impact in terms of a proper evaluation of electrical anisotropy parameters.

This confirms that a given methodology may be used to interpret  $R_H$  and  $R_V$  in the C-3 well.

### 3.1 Modelling of distribution of $R_H$ and $R_V$ with depth

An attempt was made to model the resistivity depth distributions of  $R_H$  and  $R_V$  for the assumed “synthetic” model, composed of a dozen layers with varying thickness and resistivity (Fig. 2). The model was constructed based

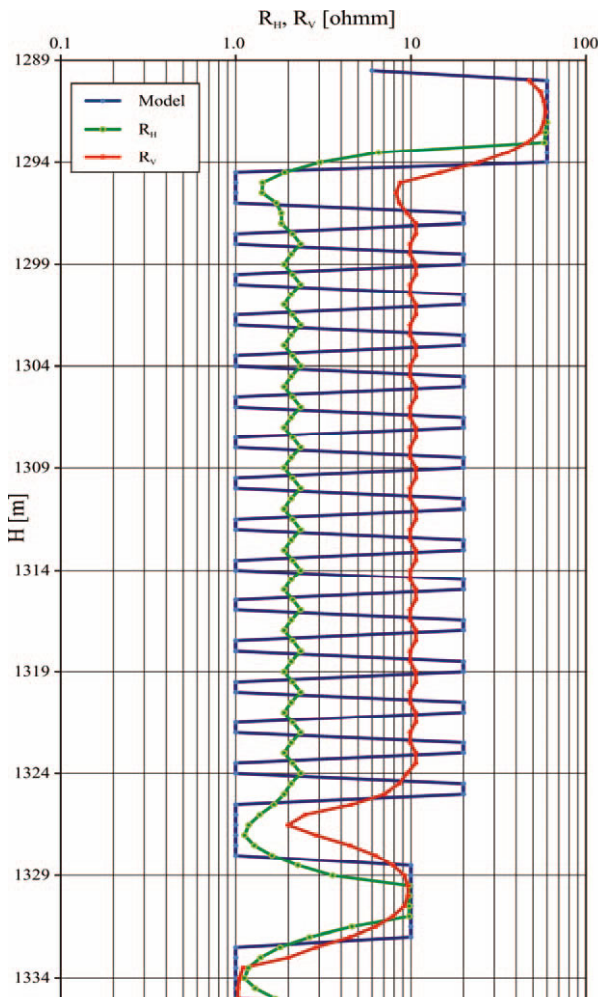


Fig. 2. Resistivities  $R_H$  and  $R_V$  as a function of depth for the assumed model.

on apparent resistivity logs from a depth interval of 1290.0 to 1338.0 m. In addition to single layers with the thickness ranging from 2.0 to 5.0 m and resistivity  $R_t$  ranging from 10 to 60 ohmm, it was assumed that there was an anisotropic series built of higher-resistivity sandstone interbeddings ( $R_{\text{sand}} = 20$  ohmm) and low-resistivity shale interbeddings ( $R_{\text{sh}} = 1$  ohmm). The thickness of each layer was taken as  $h = 0.5$  m.

The calculations were performed using the following formula (Tabonou *et al.* 2002, Quirein *et al.* 2012):

$$R_V(z) = \int_{-H/2}^{H/2} R_t(z') F_H(z-z') dz' , \quad (5)$$

$$\frac{1}{R_H(z)} = \int_{-H/2}^{H/2} \frac{F_H(z-z')}{R_t(z')} dz' , \quad (6)$$

where  $R_t$  is the assumed resistivity of model layers,  $F_H(z-z')$  is the convolution of the log (here of the model) with a constant sampling interval and accepted filter (*e.g.*, Gaussian filter), and  $H$  represents calculation of window size.

The assumed model (blue curve) and calculated horizontal resistivity (green curve) and vertical resistivity (red curve) are shown in Fig. 2. It can be seen that for the complex anisotropic beds, the horizontal resistivity ( $R_H$ ) approaches 2 ohmm, vertical resistivity ( $R_V$ ) approaches 10.29 ohmm, and the anisotropy coefficient  $\lambda = 2.01$ .

These models confirm the observed very low resistivity in zones of thin silty sandstone interbedding in the Miocene.

#### 4. DETERMINATION OF RESISTIVITY $R_H$ AND $R_V$ AND ANISOTROPY COEFFICIENT IN LAYERS OF MIOCENE SHALY SANDSTONES

##### 4.1 Analysis of measured data

Table 1 contains electric logs and measurement intervals in well C-3 and results of tester formation.

The measurements in well C-3 were conducted in 2004 by Geofizyka Kraków with the use of a Halliburton DDL-D logging unit. Due to the good quality of the borehole, the data are of good quality. An exception was HRAI logging, in which a lot of disturbances were observed being a result of anomalous high-conductivity zones. The disturbances were partly eliminated with the use of correction procedures (C-3 Well 2004).

Table 1

## Electric logs in well C-3

Borehole (year of drilling completion)	Electric logs	Measurement interval [m]	Results of tester formation
C-3 (2004)	SP	220-1497	1330-1346 m gas $V = 235 \text{ m}^3/\text{min}$
	DIL + LL3	220-1497	1394-1440 m gas
	SED	220-1497	$V = 129 \text{ m}^3/\text{min}$
	HRAI	220-1499	1450-1455 m gas $V = 54 \text{ m}^3/\text{min}$

## 4.2 Results of calculations in well C-3

Horizontal resistivity ( $R_H$ ) and vertical resistivity ( $R_V$ ) were calculated based on available data recorded with an induction HRAI tool and dual laterolog DLL tool.

After Hagiwara (1996), Faivre *et al.* (2002), Tabanou *et al.* (2002), and Bała (2011), it was assumed that the deep penetration induction tool (3.048 m) with high vertical resolution (0.3048 m) can record resistivities that are comparable to horizontal resistivity for vertical borehole and horizontally layered rock mediums. The authors also suggest that the resistivity measured with a LLD tool is similar to the geometrical mean of resistivity ( $R_{av}$ ), and based on this it is easy to calculate  $R_V$  and  $\lambda$ .

Figures 4 and 5 show HRAI and DLL logs for depth intervals of 910-952 and 1290-1325 m, which included layers partly saturated with gas and formation water with different shale volumes. Paths 2 and 3 present the results of quantitative interpretation made by Geofizyka Kraków in 2004, while path 4 shows selected dipmeter logs (PDD1, PDD2, PDD3), followed by: Dual Laterolog curves (path 5), some HRAI logs after depth correction (path 6), calculated anisotropy parameters  $R_H$ ,  $R_V$  (path 7), and the anisotropy coefficient  $\lambda$  (path 8). Figure 3 presents captions to logs and calculation results.

In studying the logs in Figs. 4 and 5 one can see that the calculated anisotropy coefficient is highly variable. Its value oscillates from 1 to 2.2 and locally exceeds 2.3. At a depth interval of 910-952 m the anisotropy coefficient considerably increases ( $1.2 < \lambda < 2.3$ ). The lithology of that depth interval includes shales intercalated with sandstones and mudstones with a significantly increased porosity (Fig. 4).

At a depth interval of 1290-1325 m one can observe the high variability of  $\lambda$  values while the increased values are usually related with higher shaliness (Fig. 5).

C - 3										
Depth (m)	Lithology	Saturation	Measurements						Resistivity $R_{H1}, R_v$ (OHMM)	Anisotropy Coefficient
			SED		DLL		HRAI			
	Shale	Res. Hydr.	PDD1 (OHMM)	MSFL (OHMM)	HC012 (OHMM)	RH OHMM		LAMBDA		
			0.0 20.0	0.0 10.0	0.0 6.0	0.0 10.0				
	Sandstone	Mov. Hydr.	PDD2 (OHMM)	LLS (OHMM)	HC01 (OHMM)	RV OHMM		LAMB		
			0.0 20.0	0.0 10.0	0.0 6.0	0.0 10.0		0.0 3.0		
		Free Water	PDD3 (OHMM)	LLD (OHMM)	HC03 (OHMM)					
			0.0 20.0	0.0 10.0	0.0 6.0					
		Bound Water			HC06 (OHMM)					
					0.0 6.0					
	VCL	SW			HC09 (OHMM)					
	1.0 0.0	1.0 0.0			0.0 6.0					
	PHI	SX0								
	1.0 0.0	1.0 0.0								

Fig. 3. Headline for Figs. 4 and 5 showing measurements and calculated anisotropy parameters.

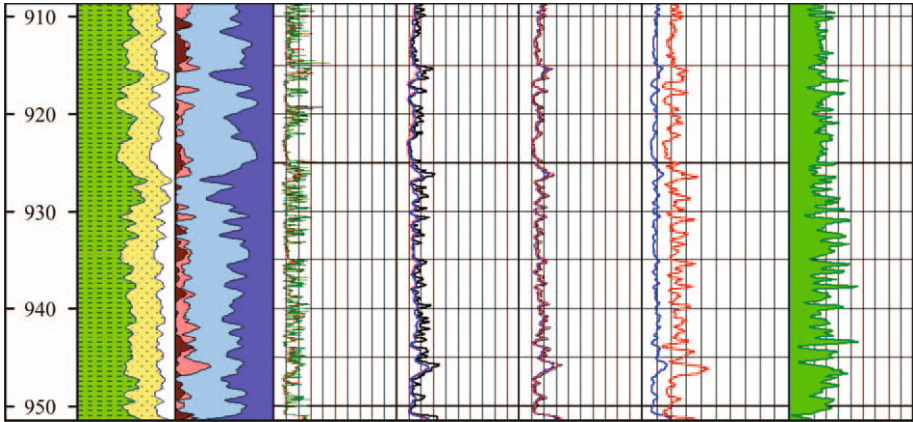


Fig. 4. Well logs and calculation results for depth interval of 910-952 m.

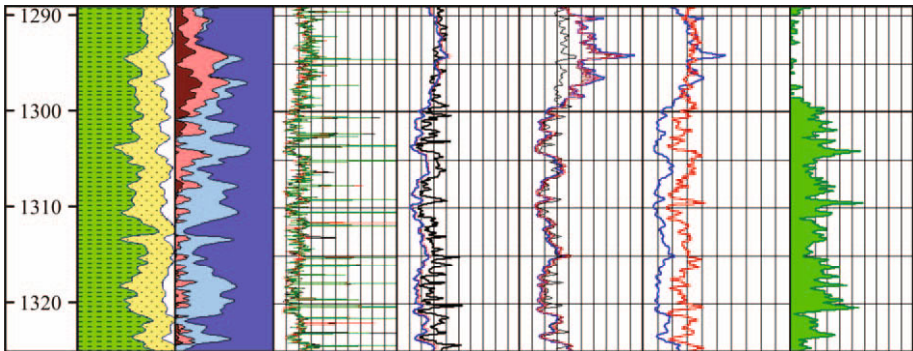


Fig. 5. Well logs and calculation results for depth interval of 1290-1325 m.

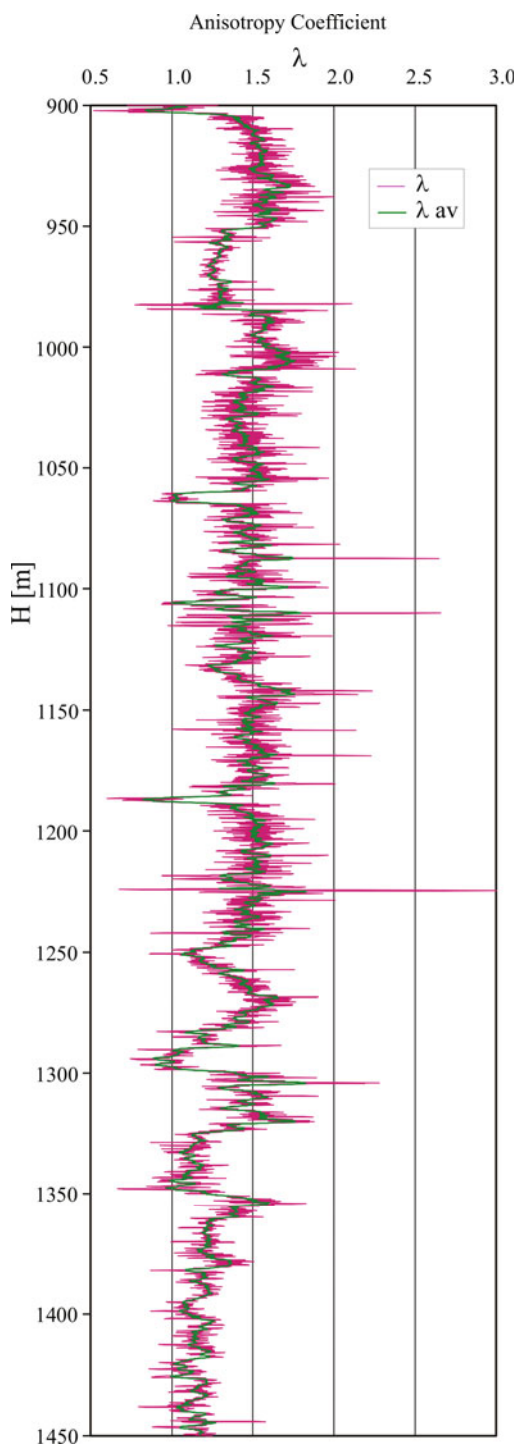


Fig. 6. Anisotropy coefficient *versus* depth for a depth interval of 900-1450 m.  $\lambda$  – value calculated for each measurement point,  $\lambda_{av}$  – value averaged with a 13-point filter.

To better illustrate the changes of  $\lambda$  with depth  $H$ , we present the plot in Fig. 6; the plot shows the values calculated for each measurement point with a step of 0.1 m and the value averaged with a 13-point filter (moving average). The moving average value smoothes the oscillations and eliminates extreme values that can be a result of the misfit of the log depth.

Based on the averaged values of  $\lambda$  we calculated the mean, minimum, and maximum values of the anisotropy coefficient for the whole interval of 900 to 1450 m. The results for selected intervals are given in Table 2.

Table 2

Mean, minimum, and maximum values for the electric anisotropy coefficient (after averaging with a 13-point filter) for selected depth intervals. Well C-3.

Depth interval [m]	Electric anisotropy coefficient $\lambda$			Remarks
	Mean value	Minimum value	Maximum value	
904.0 – 950.0	1.551	1.319	1.735	Shales, medium shaliness, sandstone intercalations, high porosity, anisotropy(?)
1010.0 – 1059.4	1.464	1.310	1.628	Sandstone and shale, anisotropy
1064.5 – 1100.0	1.471	1.158	1.750	Shale and sandstone, anisotropy
1109.5 – 1184.9	1.481	1.220	1.794	Shale with sandstone intercalations, gas saturation, high porosity, anisotropy(?)
1192.0 – 1243.7	1.494	1.292	1.830	Shale with sandstone intercalations, variable gas saturation, anisotropy(?)
1299.5 – 1321.1	1.501	1.232	1.828	Shale with sandstone intercalations, anisotropy

Due to intercalations of the sandstones and shales and increased values of coefficient  $\lambda$  observed in them, some intervals from Table 2 can be regarded as anisotropic layers.

The detailed study of high-resolution logs measured with a SED dipmeter shows that anisotropic layers can occur there.

The table indicates three layers in which we can deal with anisotropy or variable gas saturation, or increasing influence of the mud. These layers are indicated with a question mark “?”.

Studying the calculated anisotropy coefficients one should:

□ Eliminate intervals in which resistivity changes are observed as a result of mud filtrate invading the borehole environment (flushed zone), particularly when the mud has increasing effects on resistivity. There is still the phenomenon of equivalence observed by Kunz and Moran (1958), who indicated that an anisotropic layer with the infinite thickness ( $h \rightarrow \infty$ ) is equivalent to an isotropic, radially inhomogeneous layer whose resistivity varies according to:

$$R_{\text{eq}} = \frac{R_{\text{av}} \cdot r'}{\lambda \cdot r' - (\lambda - 1) \cdot a} \quad \text{for } r > a, \quad (7)$$

and

$$R_{\text{eq}} = R_m \quad \text{for } r' < a \quad \text{and} \quad r' = \frac{r}{a},$$

where  $r$  is the radial component,  $a$  is the borehole radius, and  $R_m$  represents mud resistivity.

When resistivity distributions  $R_{\text{eq}}$  given by Eqs. 7 for  $R_H = 1.5$  ohmm and  $\lambda = 2$  were compared with the  $R_a$  distribution under the assumption of a shallow invaded zone, in the water-bearing layer with increased mud effect (Bała 2011), it was noted that resistivity changes were similar; this may be misleading and suggest the anisotropy in a layer with radially variable resistivity.

□ It was also observed that higher gas saturation and higher porosity caused an increase in  $R_V$  and this in turn resulted in increased values of  $\lambda$  but did not correspond to anisotropic zones (such zones are marked in Table 2 by a question mark “?”).

## 5. ANALYSIS OF AMBIGUITY OF THE RESULTS

### 5.1 Effect of sandstone and shale volume on the anisotropy coefficient

Resistivities  $R_V$  and  $R_H$  for anisotropic formations of a laminar model (Klein 1993, Mollison *et al.* 2001, Bała 2011) can be calculated from the simplified formula:

$$R_V = V_{\text{sand}} \cdot R_{\text{sand}} + V_{\text{sh}} \cdot R_{\text{sh}}, \quad (8)$$

$$R_H = \frac{R_{\text{sand}} \cdot R_{\text{sh}}}{V_{\text{sand}} \cdot R_{\text{sh}} + V_{\text{sh}} \cdot R_{\text{sand}}}, \quad (9)$$

and

$$V_{\text{sand}} + V_{\text{sh}} = 1.$$

It can be seen that the varying proportions of sandy and shale fractions influence the values of resistivities,  $R_H$  and  $R_V$ , and the anisotropy coefficient  $\lambda$ .

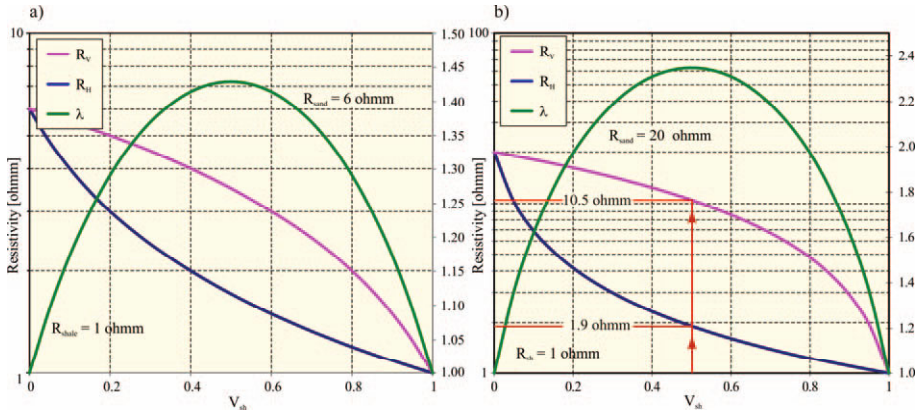


Fig. 7. Resistivity as a function of shale volume. Calculations for: (a)  $R_{sh} = 1$  ohmm,  $R_{sand} = 6$  ohmm; and (b)  $R_{sh} = 1$  ohmm,  $R_{sand} = 20$  ohmm. Laminar model.

Figure 7 presents plots of resistivity *versus* shale volume for a laminar model and  $R_{sh} = 1$  ohmm and  $R_{sand} = 6$  and 20 ohmm, which are most characteristic for the Miocene deposits.

It can be seen that the anisotropy coefficient first grows from 1 (scale on the left) for  $V_{sh}$  rising from 0 to 50% when it attains its maximum: for (a)  $\lambda = 1.43$ , and for (b)  $\lambda = 2.35$ , then it decreases to 1 along with increasing shale volume. It can also be read that for  $V_{sh} = 0.5$  (model (b)) resistivity  $R_v = 10.5$  ohmm and  $R_H = 1.9$  ohmm.

Let us assume that a model of anisotropic formation is composed of 8 sand-shale alternating layers ( $V_{(i)} = 12.5\%$ ) with the same thickness and resistivity:  $R_{sand} = 20$  ohmm, and  $R_{sh} = 1$  ohmm (Fig. 8). Applying Eqs. 8 and 9 for a laminar model we get  $R_v = 10.5$  ohmm and  $R_H = 1.9$  ohmm. These are the same values as obtained from the model (b) (Fig. 7). Hence, that represents a low-resistivity formation. In vertical and slightly inclined wells, a traditional induction tool records the horizontal resistivity  $R_H$  which is strongly dependent on low-resistivity shale interbeds and poorly indicates hydrocarbon saturation.

In their paper, Ferraris and co-authors (Ferraris *et al.* 2007) emphasize that measuring the horizontal and vertical resistivity of anisotropic rocks in vertical or slightly inclined wells, represents a serious problem for conventional induction tools and laterologs. Faivre *et al.* (2002) studied the distributions of current lines from induction tools and laterologs with different electrode configurations and they are of the opinion that laterolog tools respond more to the vertical component. However, when the invaded zone is deep ( $Di > 30$ -50 cm), then the sensitivity to the vertical component is too small to be used for the evaluation of  $R_v$ .

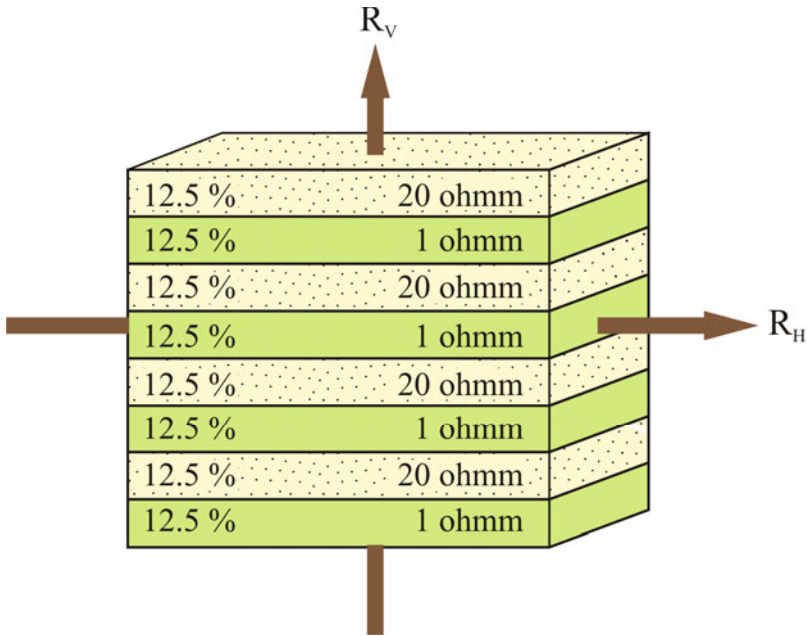


Fig. 8. Model of anisotropic rock consisting of a sequence of eight alternate layers of sand and shale with the same thickness (Bała 2011).

The current lines around deep laterolog tools (LLD) are almost horizontal, although their configuration is rather disturbed in anisotropic media. Faivre *et al.* (2002) concludes that shallow laterolog (LLS) and spherically focused log (SFL) devices are more sensitive to medium's anisotropy, however the mud filtration can decrease or even conceal the anisotropy (Moran and Gianzero 1979).

## 5.2 Estimation of errors

Anderson and Barber (1996) have evaluated that the accuracy of a conventional induction tool (AIT) amounts to 2% of the relative error when the tool measures resistivity of less than 25 ohmm.

In their respective papers, Yin (2000) and Yin and Kurniawan (2008) show that the accuracy of induction tool measurement is  $\pm 0.02$  ohmm for a resistivity range of 1 to 10 ohmm,  $\pm 0.54$  ohmm for resistivity of 25 ohmm, and  $\pm 7.5$  ohmm for resistivity of 100 ohmm.

Starting with the simplest models of series and parallel connections of resistors and transforming Eqs. 8 and 9, one can calculate the resistivity of sand interbedding,  $R_{\text{sand}}$ .

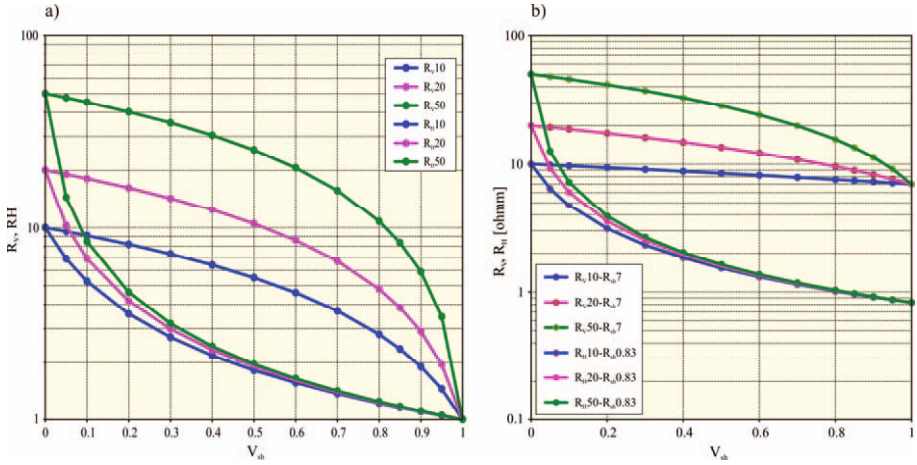


Fig. 9. Resistivity  $R_V$  and  $R_H$  calculations based on a model of series connection and parallel connection of resistors as a function of shale volume. It was assumed that  $R_{sand} = 10, 20, 50$  ohmm, and (a)  $R_{sh} = 1$  ohmm, isotropic shale; and (b) intrinsic anisotropy of shale:  $R_{shH} = 0.83$  ohmm,  $R_{shV} = 7.0$  ohmm.

For series connection:

$$R_{sand} = \frac{R_V - R_{sh} \cdot V_{sh}}{1 - V_{sh}} \quad (10)$$

and for parallel connection:

$$R_{sand} = \frac{R_H \cdot R_{sh} \cdot (1 - V_{sh})}{R_{sh} - R_H \cdot V_{sh}} \quad (11)$$

Figure 9 presents resistivities  $R_V$  and  $R_H$  versus shale volume calculated for both models (series connection and parallel connection), for  $R_{sand} = 10, 20$  and  $50$  ohmm; and (a) isotropic shales with  $R_{sh} = 1$  ohmm (Fig. 9a); and (b) shales with intrinsic anisotropy with resistivity based on logs from well C-3:  $R_{shH} = 0.83$  ohmm and  $R_{shV} = 7.0$  ohmm (Fig. 9b).

Similar calculations as for the model (a) but for the other parameters were presented by Yin and Kurniawan (2008).

It can be observed in the curves that:

- All three values of  $R_H$  overlap for shale volume  $V_{sh} > 50\%$  and this may result in considerable ambiguity in the  $R_{sand}$  calculation if the parallel connection model is solely applied.
- $R_V$  values have good resolution for different  $R_{sand}$  when  $V_{sh}$  ranges from 0 to 95%. Using a series connection model gives a proper evaluation of  $R_{sand}$  which is of considerable importance for further quantitative interpre-

tation of anisotropic formations. This is valid both for isotropic shales and shales with intrinsic anisotropy.

## 6. AN ATTEMPT TO ASSESS WATER SATURATION $S_w$

An attempt to assess water and gas saturation was made using the approach described in the literature (Klein 1993, Minh *et al.* 2007, Bała 2011). The method consists in generating cross-plots based on the calculated resistivities,  $R_H$  and  $R_V$  (Fig. 10). In the cross-plots there are templates characterizing two families of curves:  $R_{sand}$  and  $V_{sh}$ . When the coordinates of the “shale” point were  $R_{shV} = R_{shH} = 1$  ohmm (isotropic shales), a number of points interpreted for a depth interval of 1065 to 1100 m in well C-3 did not fall within the range of these  $R_{sand}$  and  $V_{sh}$  values (Fig. 10a). This may indicate the intrinsic anisotropy of shales. After the shale point had been shifted to  $R_{shV} = 7.0$  ohmm and  $R_{shH} = 0.83$  ohmm, all points were within the “grid template” for  $R_{sand}$  and  $V_{sh}$  (Fig. 10b).

The resistivity of sandstone layers ( $R_{sand}$ ) and shale volume ( $V_{sh}$ ) were calculated. The resistivity of water-bearing zone ( $R_o$ ) can be also read from the cross-plot (Fig. 10b) at line  $R_V = R_H$  (which runs at an angle of  $45^\circ$ ). The line linking  $R_o$  with the shale point delimits the area  $S_w = 1$  from the area  $S_w < 1$ , which is on the right of the  $R_o$  line. This mirrors the assumption that all sandstone beds have a similar porosity.

Water saturation and hydrocarbon saturation for selected levels with electric anisotropy were calculated with the use of commonly known

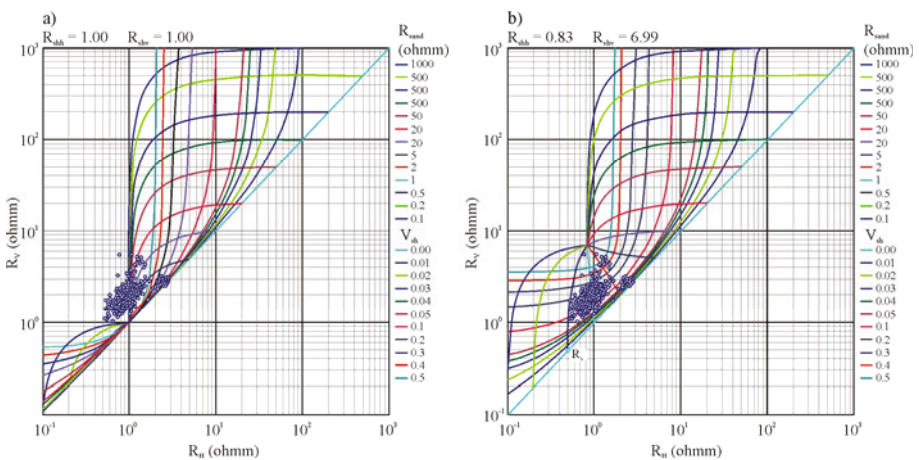


Fig. 10. Cross-plots  $R_H = f(R_V)$  for Miocene formations in the Cierpisz-3 well at a depth interval of 1065-1100 m with templates showing values for  $R_{sand}$  and  $V_{sh}$ : (a) isotropic shales, and (b) intrinsic anisotropy of shales.

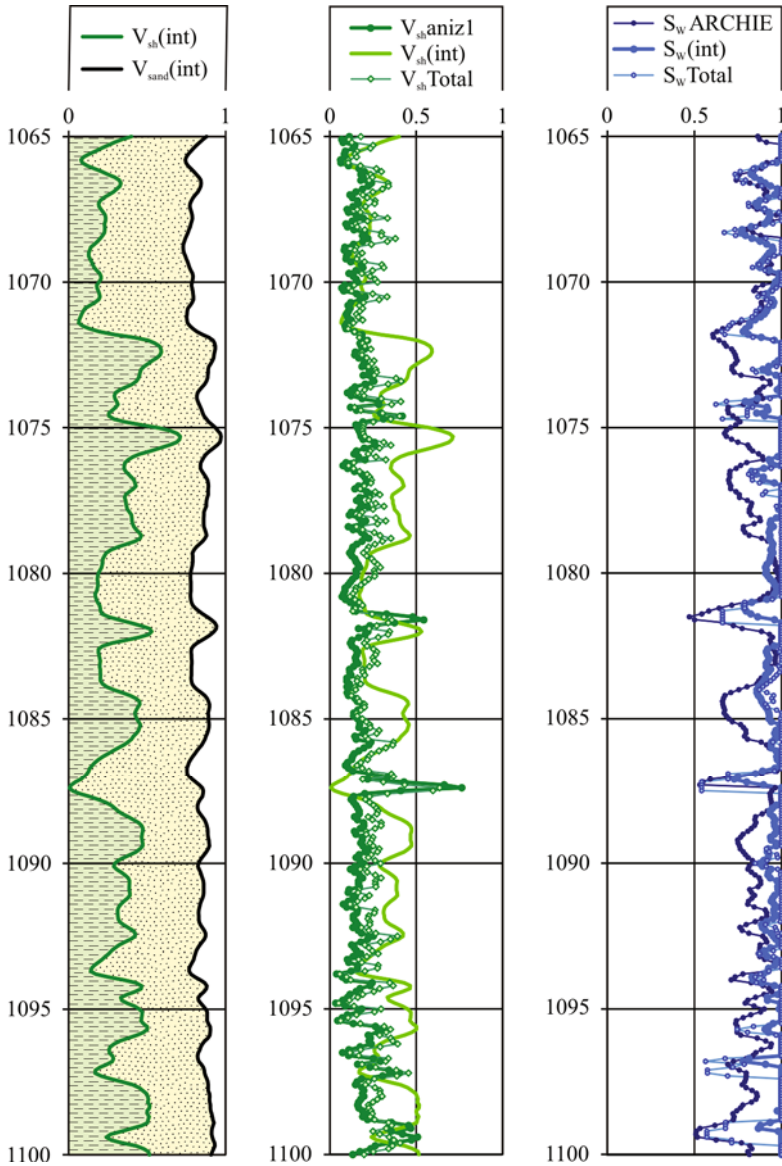


Fig. 11.  $V_{sh}$  and  $S_w$  calculated by applying the anisotropic procedure and routine quantitative interpretation made by Geofizyka Kraków:  $V_{sh}(int)$ ,  $S_w(int)$ .

Archie's, Simandoux's, Total, Indonesian, and Waxman-Smits' equations. They are included in the procedure that was based on the above-described cross-plots (Fig. 10). From the  $R_{sand}$  and  $V_{sh}$  values determined from the cross-plots and the suitably shifted shale point and known (or assumed) po-

rosity value, data sets containing calculated water saturation,  $S_W$ , were generated.

In this way, the saturation level ( $S_W$ ARCH1) and ( $S_W$ TOT) was calculated for the whole depth interval of 1065-1100 m and was then compared with routine interpretations ( $S_W$ (int)) made by Geofizyka Kraków (C-3 Well 2004). The results are shown in Fig. 11. The results are generally compatible although discrepancies can be observed over some intervals.

Though it slightly deforms the “grid template”, shifting the shale point towards lower values of  $R_{shH}$  has a minimal impact on the calculated values of  $R_{sand}$  and  $V_{sh}$ , while decreasing  $R_{shV}$  causes a significant decrease in  $S_W$  and increase in  $V_{sh}$ . Thus, as a result of an improper choice of the shale point one can get a reading that is either too high or too low  $S_W$  ( $S_G$ ).

Therefore, points in the “grid template” should be carefully studied before choosing the point of intrinsic anisotropy of shales.

The presented method is based on cross-plots and gives an initial evaluation of water and gas saturation based on calculated values of  $R_H$  and  $R_V$  and estimated  $R_{sand}$  and  $V_{sh}$ .

The method is independent of results of an integrated interpretation of well logging data and allows saturation in anisotropic levels to be roughly evaluated.

## 7. CONCLUSIONS AND DISCUSSION

Anisotropy parameters were calculated based on resistivity logs recorded with a laterolog tool (DLL) and induction tool HRAI, in Miocene formations in well C-3.

It can be observed that the calculated electric anisotropy coefficient is highly variable and ranges from 1 to 2.2, while only locally does it exceed 2.3. The increase in the anisotropy coefficient value usually corresponds to zones with a higher shale volume that are interbedded with sandstones and mudstones.

The examination of calculated electric anisotropy coefficients should include the following elements:

- Elimination of intervals with resistivity changes near the well due to infiltration of the mud filtrate that can result in possible equivalence.
- A detailed study of high-resolution logs recorded with a dipmeter SED that can prove the possible presence of anisotropic levels.
- Higher gas saturation and higher porosity cause an increase in  $R_V$  which results in greater values of  $\lambda$  but does not correspond to the anisotropic zones.
- It is very important to correctly evaluate the resistivity of sandstone interbeds when calculating water saturation ( $S_W$ ) and hydrocarbon saturation

( $S_G$ ), in the course of an integrated quantitative interpretation of anisotropic formations.

- Calculation of resistivities  $R_H$  and  $R_V$ , as a function of depth for the assumed models, gives a better understanding of the effects of anisotropy on the resistivity measured.
- Evaluation of water and hydrocarbon saturation based on cross-plots created on the basis of calculated horizontal resistivity  $R_H$  and vertical resistivity  $R_V$ , can provide early information on saturation in anisotropic parts of a deposit.

This method is independent of the results of a comprehensive interpretation of well logging data and allows one to estimate the hydrocarbons and water saturation level of the anisotropic zones.

**Acknowledgements.** The paper is part of research project NN525 363537 led by Prof. M. Bała (in 2009-2012) and research project NN307 294439 (2010-2013) financed by The National Science Center, Poland led by Prof. J. Jarzyna (2010-2013).

## References

- Anderson, B., and T. Barber (1996), Induction logging, Schlumberger, <http://www.hub.slb.com/index.cfm?id=id8880>.
- Anderson, B.I., T.D. Barber, and T.M. Habashy (2002), Interpretation and inversion of fully triaxial induction data, A sensitivity study. **In:** *Proc SPWLA 43th Ann. Logg. Symp., 2-5 June 2002, Oiso, Japan*, SPWLA-2002-O.
- Anderson, B., T. Barber, R. Bastia, K.R. Saxena, A.K. Tyagi, J.-B. Clavaud, B. Coffin, M. Das, R. Hayden, T. Klimentos, C.C. Minh, and S. Williams (2008), Triaxial induction – A new angle for an old measurement, *Oilfield Rev.: Summer* **20**, 2, 64-84.
- Bała, M. (2009), Study of the effects of anisotropy and shaliness on velocities of longitudinal and shear waves and other elastic parameters of clastic rocks, *Geologia* **35**, 2/1, 559-566 (in Polish, abstract in English).
- Bała, M. (2011), Evaluation of electric parameters of anisotropic sandy-shaly miocene formations on the basis of resistivity logs, *Acta Geophys.* **59**, 5, 954-966, DOI: 10.2478/s11600-011-0033-1.
- Bittar, M.S., and P.F. Rodney (1994), The effects of rock anisotropy on MWD electromagnetic wave resistivity sensors. **In:** *Proc. SPWLA 35th Ann. Logg. Symp., 19-22 June 1994, Tulsa, USA*, SPWLA-1994-PP.
- C-3 Well (2004), Final documentation of C-3 well, Geofizyka, Kraków.

- Chemali, R., S.C. Gianzero, and S.M. Su (1987), The effect of shale anisotropy on focused resistivity devices. **In:** *Proc. SPWLA 28th Ann. Logg. Symp.*, 29 June – 2 July 1987, London, England, SPWLA-1987-H.
- Dachnov, W.N. (1967), *Electric and Magnetic Methods of Logging. Fundament of Theory*, Nedra, Moskwa (in Russian).
- Faivre, O., T. Barber, L. Jammes, and D. Vuhoang (2002), Using array induction and array laterolog data to characterize resistivity anisotropy in vertical wells. **In:** *Proc. SPWLA 43th Ann. Logg. Symp.*, 2-5 June 2002, Oiso, Japan, SPWLA-2002-M.
- Ferraris, P., M.R. Coutinho, A.A.G. Meira, and T. Adams (2007), Campos basin anisotropic turbidities formation evaluation: challenges and proposed solutions. **In:** *Proc. SPWLA 48th Ann. Logg. Symp.*, 3-6 June 2007, Austin, USA, SPWLA-2007-QQ.
- Hagiwara, T. (1996), A new method to determine horizontal-resistivity in anisotropic formations without prior knowledge of relative dip. **In:** *Proc. SPWLA 37th Ann. Logg. Symp.*, 16-19 June 1996, New Orleans, USA, SPWLA-1996-Q.
- Karnkowski, P. (1999), *Oil and Gas Deposits in Poland*, Geosynoptics Society „GEOS”, Kraków, 380 pp.
- Klein, J.D. (1993), Induction log anisotropy corrections, *The Log Analyst* **34**, 2, 18-27.
- Klein, J.D., P.R. Martin, and D.F. Allen (1995), The petrophysics of electrically anisotropic reservoirs. **In:** *Proc SPWLA 36th Ann. Logg. Symp.*, 26-29 June 1995, Paris, France, SPWLA-1995-HH.
- Kunz, K.S., and J.H. Moran (1958), Some effects of formation anisotropy on resistivity measurements in boreholes, *Geophysics* **23**, 4, 770-794, DOI: 10.1190/1.1438527.
- Minh, C.C., J.B. Clavaud, P. Sundararaman, S. Froment, E. Caroli, O. Billon, G. Davis, and R. Fairbairn (2007), Graphical analysis of laminated sand-shale formations in the presence of anisotropic shales. **In:** *Proc. SPWLA 48th Ann. Logg. Symp.*, 3-6 June 2007, Austin, USA, SPWLA-2007-MM.
- Mollison, R.A., O.N. Fannini, B.F. Kriegshauser, L. Yu, G. Ugueto, and J. van Popta (2001), Impact of multicomponent induction technology on a deep-water turbidite sand hydrocarbon saturation evaluation. **In:** *Proc. SPWLA 42th Ann. Logg. Symp.*, 17-20 June 2001, Houston, USA, SPWLA-2001-T.
- Moran, J.H., and S. Gianzero (1979), Effects of formation anisotropy on resistivity-logging measurements, *Geophysics* **44**, 7, 1266-1286, DOI: 10.1190/1.1441006.
- Myśliwiec, M. (2004), The Miocene reservoir rocks of the Carpathian Foredeep, *Geol. Rev.* **52**, 7, 581-592 (in Polish, abstract in English).
- Quirein, J., B. Donderici, D. Torres, E. Murphy, and J. Witkowsky (2012), Evaluation of general resistivity density-based saturation in thin, laminated sand-

- shale sequences. **In:** *AAPG Int. Conf. Exhib. "Asia Pacific Resources: Fueling the Future"*, 16-19 September 2012, Singapore.
- Rosthal, R., T. Barber, S. Bonner, K.-Ch. Chen, S. Davydycheva, G. Hazen, D. Homan, C. Kibbe, R. Schlein, L. Villegas, H. Wang, and F. Zhou (2003), Field test results of an experimental fully-triaxial induction tool. **In:** *Proc. SPWLA 44th Ann. Logg. Symp.*, 22-25 June 2003, Galveston, USA, SPWLA-2003-QQ.
- Syrek-Moryc, C. (2006), The deposit of natural gas Cierpisz as an important point in the issues concerning the future search in the thin strata of Miocene deposits of the Carpathian Foredeep and potential natural gas resources connected with the deposits, *Prace Inst. Nafty i Gazu* **137**, 223-230 (in Polish, abstract in English).
- Tabanou, J.R., P. Cheung, Ch.B. Liu, S. Hansen, J. Lavigne, T. Pickens, T. Borbas, and B. Wendt (2002), Thinly laminated reservoir evaluation in oil-base mud: High resolution versus bulk anisotropy measurement – A comprehensive evaluation. **In:** *Proc. SPWLA 43rd Ann. Logg. Symp.*, 2-5 June 2002, Oiso, Japan, SPWLA-2002-P.
- Yang, W. (2001), Determining resistivity anisotropy by joint lateral and induction logs. **In:** *Proc. SPWLA 42nd Ann. Logg. Symp.*, 17-20 June 2001, Houston, USA, SPWLA-2001-CC.
- Yin, H. (2000), Limitations and error inherent in resistivity log inverse modeling for formation evaluation. **In:** *SEG 70th Ann. Int. Meeting Exp. Abstr.*, 6-11 August 2000, Calgary, Canada, SEG-2000-1798, 1798-1801.
- Yin, H., and B. Kurniawan (2008), Resistivity anisotropy models and multi-component induction measurements: Impact on Sw and uncertainty on Hpv estimation. **In:** *Proc. SPWLA 48th Ann. Logg. Symp.*, 25-28 May 2008, Austin, USA, SPWLA-2008-LLLL.
- Zajkowskij, I.J., D.E. Kowalenko, and A.E. Kulinkowich (1965), Opriedelenie parametrov anizotropowego plasta po kriwym Bokowogo Karotaznogo Zondirowania (BKZ), *Prikl. Geofiz.* **46**, 213-216 (in Russian).

Received 13 February 2014

Received in revised form 12 May 2014

Accepted 4 July 2014



## Estimation of Permeability from NMR Logs Based on Formation Classification Method in Tight Gas Sands

Deng-Feng WEI<sup>1</sup>, Xiao-Peng LIU<sup>2</sup>, Xiao-Xin HU<sup>2</sup>, Rui XU<sup>3</sup>,  
and Ling-Ling ZHU<sup>3</sup>

<sup>1</sup>School of Graduate Student, College of Resources and Environment,  
Southwest Petroleum University, Sichuan, PR China; e-mail: 13101103@qq.com

<sup>2</sup>Geological Exploration and Development Research Institute, Sichuan-Changqing  
Drilling and Exploration Engineering Corporation, CNPC, Sichuan, PR China

<sup>3</sup>Tuha Division of CNPC Well Logging Company Ltd., Xinjiang, PR China

### Abstract

The Schlumberger Doll Research (SDR) model and cross plot of porosity *versus* permeability cannot be directly used in tight gas sands. In this study, the HFU approach is introduced to classify rocks, and determine the involved parameters in the SDR model. Based on the difference of FZI, 87 core samples, drilled from tight gas sandstones reservoirs of E basin in northwest China and applied for laboratory NMR measurements, were classified into three types, and the involved parameters in the SDR model are calibrated separately. Meanwhile, relationships of porosity *versus* permeability are also established. The statistical model is used to calculate consecutive FZI from conventional logs. Field examples illustrate that the calibrated SDR models are applicable in permeability estimation; models established from routine core analyzed results are effective in reservoirs with permeability lower than 0.3 mD, while the unified SDR model is only valid in reservoirs with permeability ranges from 0.1 to 0.3 mD.

**Key words:** tight gas sandstones, permeability, formation classification method, SDR model, nuclear magnetic resonance (NMR) logs.

## 1. INTRODUCTION

Permeability calculation is of great importance in formation evaluation and deliverability prediction (Mao *et al.* 2013). There is no conventional log to be used to directly calculate permeability. Generally, permeability prediction is always relied on a good relationship of core derived porosity and permeability in conventional reservoirs (Salah 2012, Deng *et al.* 2013, Delli and Grozic 2013, Hulea 2013). However, the permeability estimation faces a great challenge in tight gas sands and carbonate formations (Hulea and Nicholls 2012, Xiao *et al.* 2014). The relationship between core derived porosity and permeability cannot be expressed by a single function due to the complicated pore types, structure, and high degree of heterogeneity (Lucia 1995, Xiao and Xiao 2008). In the right panel of Fig. 1, we show a cross plot of core derived porosity and permeability; the core samples were drilled from tight gas sandstone reservoirs in five adjacent wells of E basin in northwest China. The left panel of Fig. 1 displays the micro-resistivity scanning imaging log response obtained from STAR II tool; this figure is acquired from the same interval with the plug samples marked using ellipse in the right panel of this figure. In the E basin, all core derived porosities are measured by using the helium gas injection method, and to acquire fluid permeability for routine core analysis in tight gas sandstones, an instantaneous-pulse permeability test method instead of the conventional steady-state method was applied. By using the instantaneous-pulse permeability test method, the extremely low permeability of 0.000001 mD can also be measured under the experimental conditions of confinement pressure of 10.0~60.0 MPa, and pore pressure of 0.0~15.0 MPa (Yang 2001). In the process of experimental measurement, we simulated the formation conditions. Hence, the measured results are reservoir fluid permeabilities, and no additional corrections (such as stress correction) needed to be made (Gao *et al.* 1991). From Fig. 1, it can be observed that in tight gas sands of E basin, the related function cannot be established to directly calculate permeability from porosity. If the relationship is constrainedly established, inaccurate permeability is obtained. Meanwhile, micro-resistivity scanning imaging log data illustrated that in the target formations of E basin, the intergranular pore is dominant, and only few fractures developed in formations with extreme matrix porosity (the marked area in Fig. 1), which had been verified by Mao *et al.* (2008). Hence, in our target tight gas sands, formations are dominant by matrix permeability. Rezaee *et al.* (2012) and Xiao *et al.* (2014) pointed out that permeability estimation model can be established from mercury injection capillary pressure (MICP) data in tight gas sands, and Hulea and Nicholls (2012) estimated permeability from the total normalized pore-throat radius in heterogeneous carbonate rocks. However, all these models were established

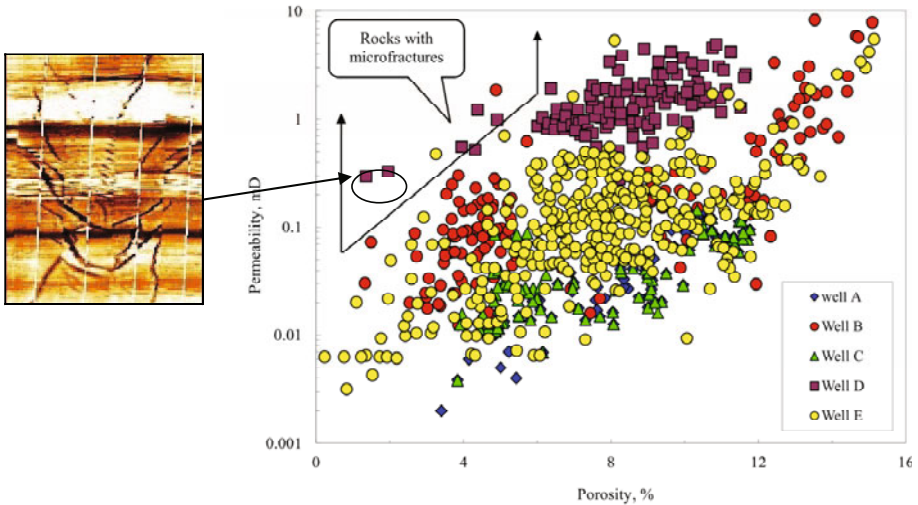


Fig. 1. The cross plot of core derived porosity and permeability for core samples drilled from five adjacent wells in tight gas sands of E basin in northwest China.

based on the laboratory experimental measurements, no cases had been exhibited to introduce how these can be used in field applications, and those intermediate parameters were hardly acquired from conventional or nuclear magnetic resonance (NMR) logs at present. Coates *et al.* (1999) and Dunn *et al.* (2002) pointed out that NMR logs can be used to estimate permeability. In this paper, we will analyze the applicability of NMR logs in tight gas sandstone permeability estimation, and propose appropriate method to calculate permeability from NMR logs.

## 2. PERMEABILITY ESTIMATION FROM NUCLEAR MAGNETIC RESONANCE (NMR) LOGS

### 2.1 Classical permeability prediction models based on NMR logs

Nuclear magnetic resonance (NMR) logs are effective in predicting permeability (Coates *et al.* 1999, Dunn *et al.* 2002). From NMR logs, two proposed models can be used to calculate permeability; they are known as the SDR and Timur–Coates models (Kenyon 1997, Kenyon *et al.* 1988, Coates *et al.* 1999). The SDR and Timur–Coates models are expressed as follows:

$$K = C_1 \times \phi^{m_1} \times T_{2lm}^{n_1}, \quad (1)$$

$$K = \left( \frac{\phi}{C_2} \right)^{m_2} \times \left( \frac{\text{FFI}}{\text{BVI}} \right)^{n_2}, \quad (2)$$

where  $K$  is the permeability (in mD);  $\varphi$  is the total porosity (in %);  $T_{2lm}$  is the logarithmic mean of NMR  $T_2$  spectra (in ms); FFI is the free fluid bulk (in %); BVI is the bulk volume irreducible (in %);  $m_1$ ,  $n_1$ ,  $C_1$ ,  $m_2$ ,  $n_2$ , and  $C_2$  are the statistical model parameters, whose values can be derived from lab NMR experimental data sets of core samples. When not enough core samples are usable,  $m_1$ ,  $n_1$ ,  $C_1$ ,  $m_2$ ,  $n_2$ , and  $C_2$  are assigned to empirical values of 4, 2, 10, 4, 2, and 10, respectively (Mao *et al.* 2013).

## 2.2 Limitations of permeability estimation model in tight sandstone reservoirs

From Eqs. 1 and 2, it can be observed that permeability can be estimated from NMR logs once the values of  $m_1$ ,  $n_1$ ,  $C_1$ ,  $m_2$ ,  $n_2$ , and  $C_2$  are first calibrated and the necessary input parameters of  $\varphi$ ,  $T_{2lm}$ , FFI, and BVI can be precisely obtained.  $\varphi$  and  $T_{2lm}$  can be acquired from NMR logs after the necessary hydrocarbon correction has been made (Xiao *et al.* 2012a, b, c). The values of FFI and BVI can be calculated from NMR logs as follows (Morriss *et al.* 1997):

$$\text{BVI} = \frac{\int_{T_{2\min}}^{T_{2\text{cutoff}}} S(T)dt}{\int_{T_{2\min}}^{T_{2\max}} S(T)dt} \times 100\% , \quad (3)$$

$$\text{FFI} = 100 - \text{BVI} , \quad (4)$$

where  $T_{2\min}$  is the minimum horizontal relaxation time,  $T_{2\max}$  is the maximum horizontal relaxation time,  $T_{2\text{cutoff}}$  is the  $T_2$  cutoff, and the units of them are microsecond.  $S(T)$  is the porosity distribution function, which is associated with the  $T_2$  relaxation time.

Equations 3 and 4 illustrate that if one wants to calculate FFI and BVI from NMR logs,  $T_{2\text{cutoff}}$  must be first determined. The histogram method is always used to determine a fixed  $T_{2\text{cutoff}}$  for calculating FFI and BVI from NMR logs (Xiao *et al.* 2012a, b, c; Mao *et al.* 2013). Field applications illustrate that defining fixed  $T_{2\text{cutoff}}$  to calculate FFI and BVI is not always effective. Figure 2 shows the statistical histogram of  $T_{2\text{cutoff}}$  of 87 core samples, which were drilled from the same tight gas reservoirs as Fig. 1, and the  $T_{2\text{cutoff}}$  were obtained by using the centrifugal displacement method. The principle of obtaining  $T_{2\text{cutoff}}$  with centrifugal displacement method is illustrated in Fig. 3.

From the statistical  $T_{2\text{cutoff}}$  shown in Fig. 2 we can observe that in tight gas sands, not a fixed  $T_{2\text{cutoff}}$  can be acquired to calculate FFI and BVI from NMR measurements in the whole intervals. To calculate accurate FFI and BVI, the optimal method is obtaining variable  $T_{2\text{cutoff}}$  with the depth. How-

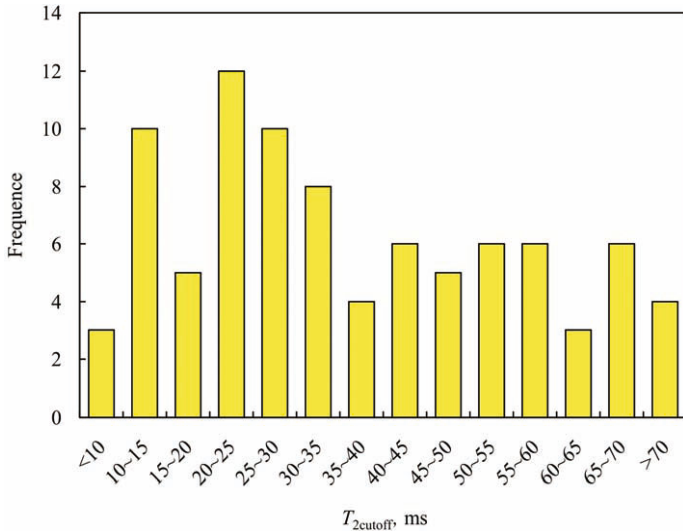


Fig. 2. The statistical histogram of  $T_{2\text{cutoff}}$  for 87 core samples drilled from tight sandstone reservoirs of E basin in northwest China.

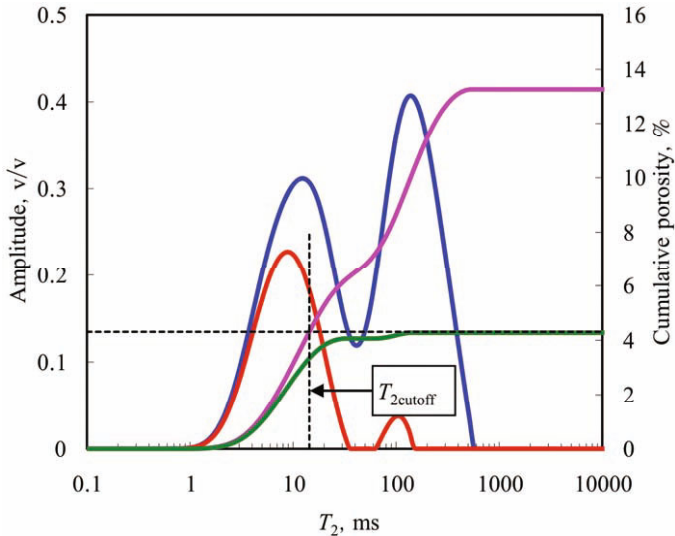


Fig. 3. The principle of obtaining  $T_{2\text{cutoff}}$  from NMR measurement with centrifugal displacement method.

ever, there is no effective method to obtain variable  $T_{2\text{cutoff}}$  at present (Xiao *et al.* 2012a, b, c). This makes a great challenge of calculating permeability by using the Timur–Coates model. Therefore, the SDR model is very popular in permeability estimation in practical applications (Mao *et al.* 2013).

To calculate permeability from NMR logs by using the SDR model, the parameters  $C_1$ ,  $m_1$ , and  $n_1$  needed to be first calibrated. In this study, 87 core samples drilled from tight gas sands in the E basin of northwest China were chosen for laboratory NMR measurements. By using the NMR experimental results, the SDR model was calibrated and expressed as follows:

$$K = 0.00000389 \times \phi^{2.302} \times T_{2lm}^{1.373}, \quad R^2 = 0.682. \quad (5)$$

Figure 4 displays the relationship of core derived porosity and permeability for the same 87 core samples. If we only observe the correlation coefficients listed in Fig. 4 and Eq. 5, we may conclude that permeability can be directly estimated from NMR logs by using the unified SDR model. However, if we observe Fig. 4 in detail, we can find out that the relationship is much worse; although good correlation coefficient exist between them, most of the core samples cannot pass by the regressed trend line, and they are scattered on both sides of the trend line. This means that permeability may be overestimated or underestimated from NMR logs by using the unified calibrated SDR model. To improve the applicability of SDR model in tight gas sands, formation classification method is introduced to classify reservoirs into several types, and the above-mentioned parameters in the SDR model are calibrated in every type of reservoir separately.

The hydraulic flow unit (HFU) approach is used in formation classification. In the next section, we will introduce tight gas sandstone permeability estimation method based on formation classification.

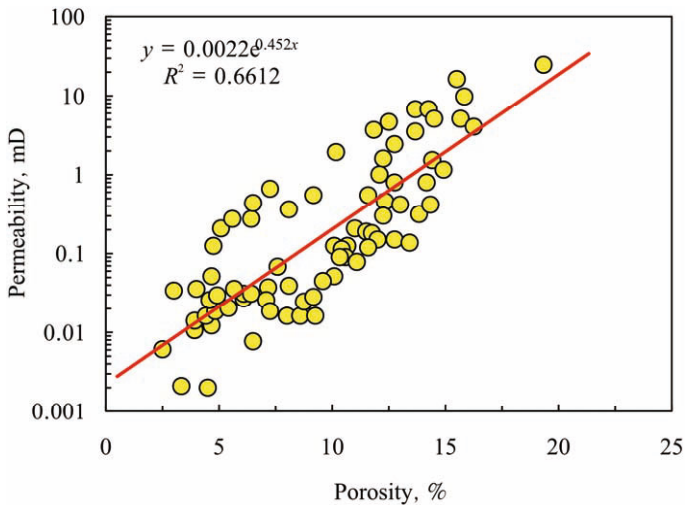


Fig. 4. The cross plot of core derived porosity and permeability for core samples with laboratory NMR measurements.

### 3. PERMEABILITY PREDICTION FROM NMR LOGS BASED ON FORMATION CLASSIFICATION METHOD

#### 3.1 The hydraulic flow unit (HFU) approach

A HFU is a reservoir zone that is continuous laterally and vertically with similar permeability, porosity, and bedding characteristics (Hearn *et al.* 1984). Rocks with similar permeability, porosity, and bedding characteristics often have similar pore throat attributes and therefore belong to the same HFU. The HFU is often used to classify formation, and it is of great help for the evaluation of reservoir classification with strong heterogeneity (D'Windt 2007).

Based on a modified Kozeny–Carman equation and the concept of mean hydraulic radius, Tiab *et al.* (1993) developed a generalized formula of the relationship between porosity and permeability; this formula can be expressed as follows:

$$K = \frac{\phi^3}{(1-\phi)^2} \times \frac{1}{K_T S_{V_{gr}}^2}, \quad (6)$$

where

$$K_T = K_{ps} \tau, \quad (7)$$

and  $S_{V_{gr}}$  is the specific surface area per unit grain volume in  $\text{m}^2/\text{cm}^3$ ,  $K_{ps}$  is the pore shape factor,  $\tau$  is the pore tortuosity, and  $K_T$  is the pore-level effective zoning factor. Though varying among flow units, this parameter is constant within a given unit.

If the unit of permeability is transformed from  $\mu\text{m}^2$  to millidarcy, the following formula can be obtained by dividing both sides of Eq. 6 by porosity and taking the square root of both:

$$0.0314 \times \sqrt{\frac{K}{\phi}} = \frac{\phi}{1-\phi} \times \frac{1}{\sqrt{K_T S_{V_{gr}}}}, \quad (8)$$

where 0.0314 is the conversion coefficient for  $K$  from  $\mu\text{m}^2$  to mD.

There are three important parameters in the HFU theory and they are defined as follows:

(1) Reservoir quality index (RQI): RQI is defined as follows:

$$\text{RQI} = 0.0314 \times \sqrt{\frac{K}{\phi}}; \quad (9)$$

(2) Flow zone indicator (FZI): FZI is defined as:

$$\text{FZI} = \frac{1}{\sqrt{K_T S_{V_{gr}}}}; \quad (10)$$

(3) Normalized porosity ( $\phi_z$ ): Normalized porosity is defined as:

$$\phi_z = \frac{\phi}{1-\phi} . \quad (11)$$

By carrying out some algebraic transformations for Eq. 8, the expression of FZI can be rewritten as follows:

$$\text{FZI} = 0.0314 \times \sqrt{\frac{K}{\phi}} \times \frac{1-\phi}{\phi} . \quad (12)$$

### 3.2 Determination of formation classification criteria

Based on the analysis above section, the boundary of the FZI needed to be first determined to classify formations. If we substitute Eqs. 9 to 11 into 8 and take logarithms on both sides, Eq. 8 can be transformed as follows:

$$\log(\text{RQI}) = \log(\text{FZI}) + \log(\phi_z) . \quad (13)$$

Equation 13 illustrates that for core samples with the same FZI, the relationship of  $\phi_z$  versus RQI in log-log coordinates will be a straight line, and core samples with a different FZI will be on other parallel lines.

To obtain the classification criteria of FZI to classify formation, 87 core samples displayed in Fig. 4 are processed by using of the theory of HFU. The cumulative frequency distribution of FZI and the cross plot of  $\phi_z$  versus RQI for 87 core samples are displayed in Figs. 5 and 6, separately. From

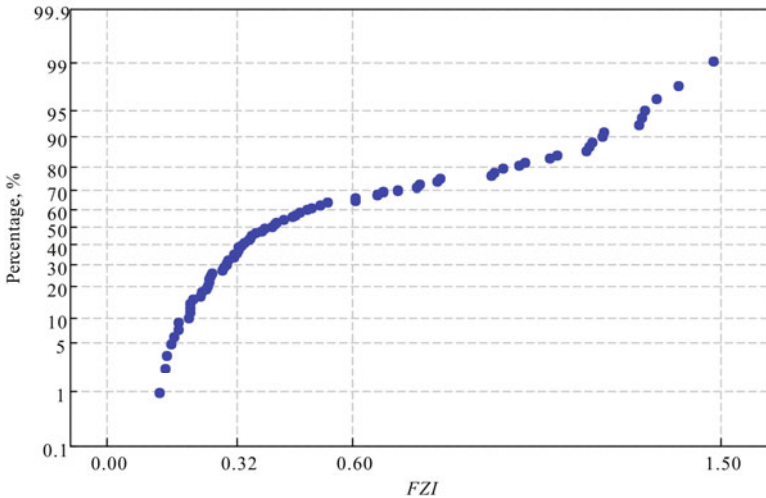


Fig. 5. The cumulative frequency distribution of FZI for 87 core samples in our target tight gas sandstone reservoirs.

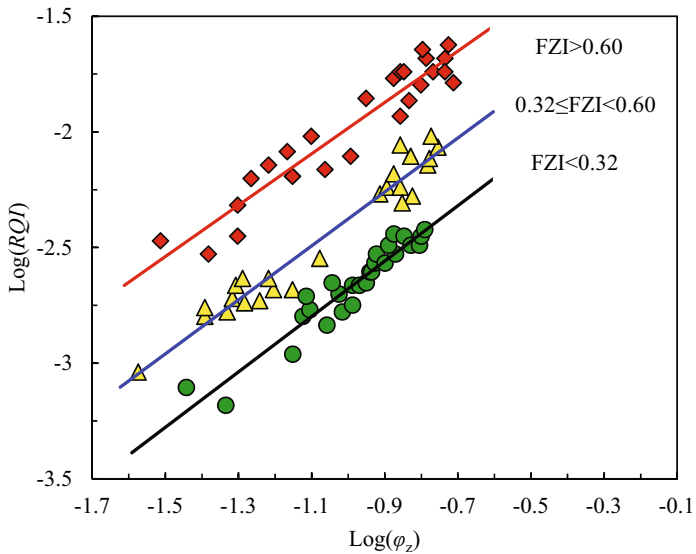


Fig. 6. The cross plot of  $\phi_z$  versus RQI in log-log coordinates for the target core samples.

these two figures, we can conclude that in our target tight gas sandstone reservoirs, the best classification of HFU is for three types; the boundary values of FZI for different types of formations are 0.32 and 0.60. Maybe, the permeability estimation can be a little improved; after formations are classified into many more types, a larger workload will be introduced.

To verify the reasonableness of formation classification based on the difference of FZI, 3 representative core samples, which contain similar porosity but belong to different FZI, were chosen for MICP experimental measurements, and the MICP data were acquired. Figure 7 displayed the MICP curves of these 6 core samples, the pore throat radius distribution and the corresponding NMT  $T_2$  distribution. These core samples are classified into 2 groups based on the difference of porosities. For every group of core samples, the porosities are similar. From Fig. 7 we can observe that for core samples with different FZI, the pore structures are discrepant. Even if they contain similar porosity, the pore type and structure are entirely different. For a core sample with good pore structure, the corresponding FZI is high, and *vice versa*. For two groups of core samples, even if their petrophysical properties are discrepant, the regularities are analogous. Hence, these core samples should be classified, and a permeability estimation model should be established.

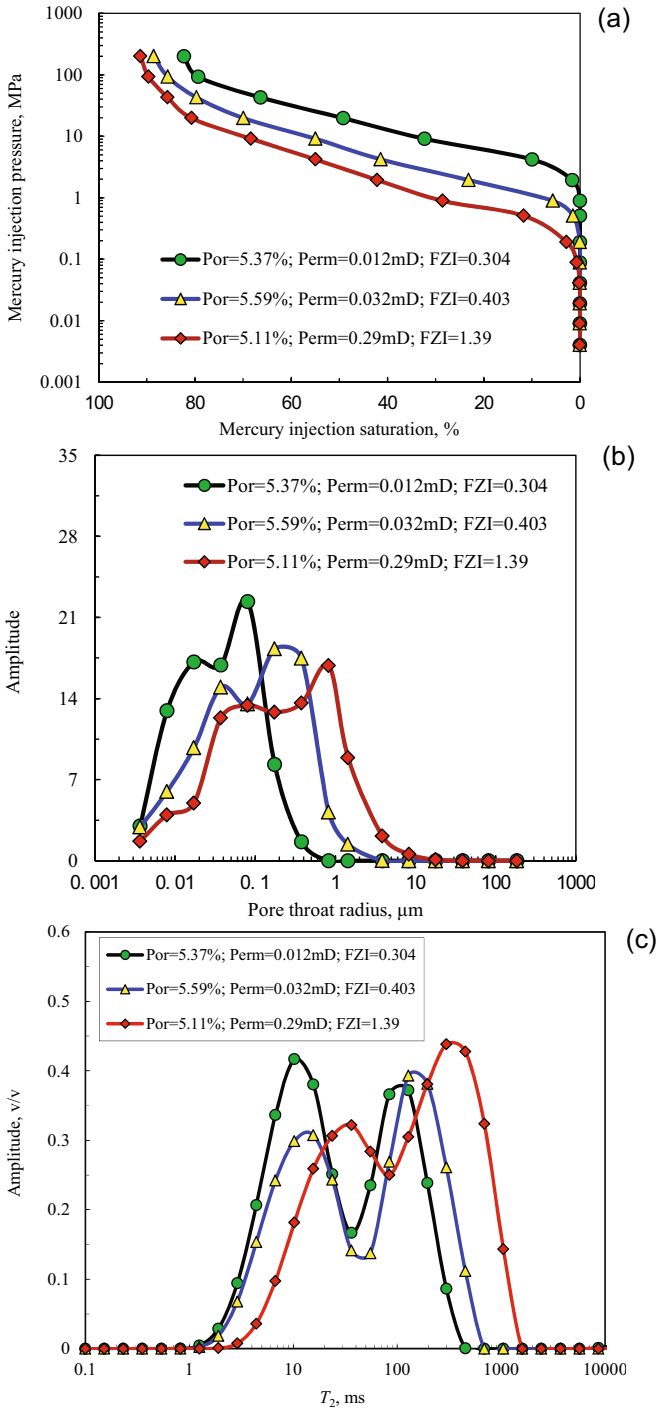


Fig. 7. Caption on next page.

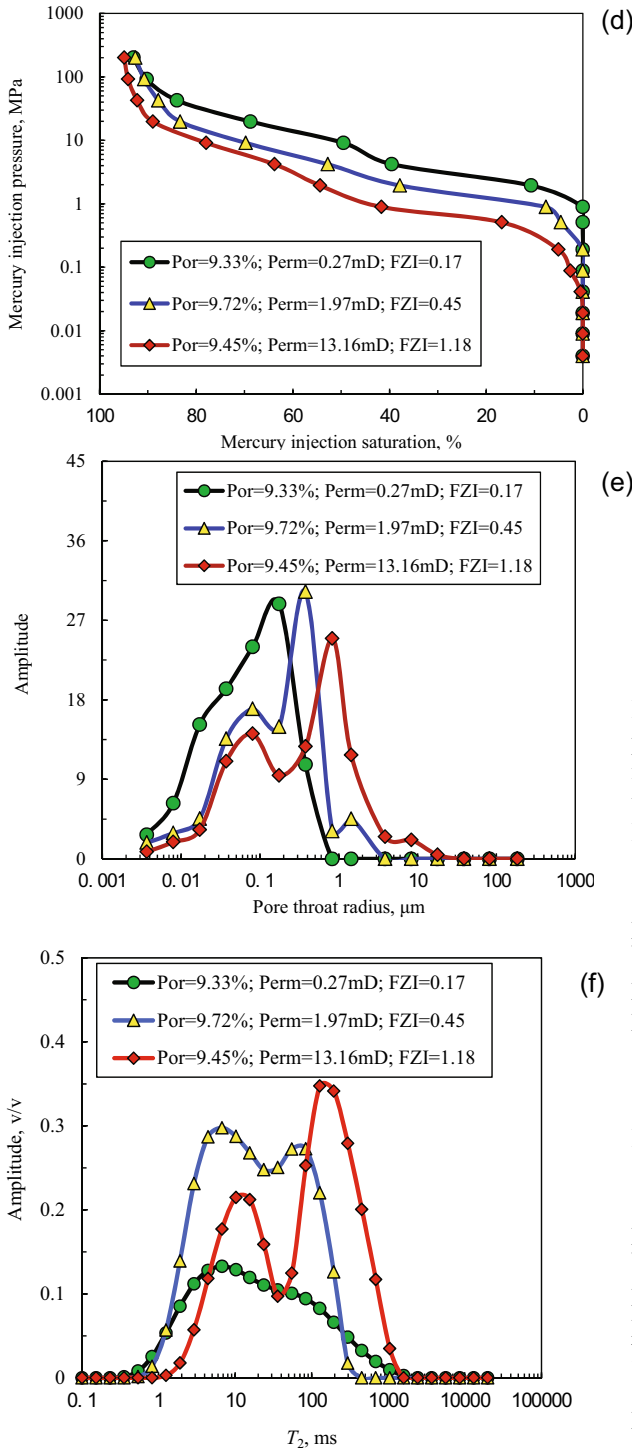


Fig. 7. Comparison of pore structure for 6 representative core samples with different FZI: (a) the MICP curves for 3 core samples with poor physical properties, (b) the pore throat radius distributions for 3 core samples with poor physical properties, (c) the NMR  $T_2$  spectra for 3 core samples with poor physical properties, (d) the MICP curves for 3 core samples with poor physical properties, (e) the pore throat radius distributions for 3 core samples with better physical properties, and (f) the NMR  $T_2$  spectra for 3 core samples with better physical properties.

### 3.3 Calibration of the SDR model

With the same classification criteria of FZI, core samples displayed in Fig. 4 are classified into three types; the laboratory NMR measurements are reused to calibrate the involved parameters in the SDR model by using the multiple regression method. The rock classification criteria of FZI and the corresponding calibrated SDR models are listed in Table 1.

Table 1  
Rock classification criteria of FZI and the corresponding calibrated SDR permeability estimation models in tight sandstone reservoirs of E basin in northwest China

Type of rock	The classification criteria of FZI	Calibrated SDR model	Correlation coefficient ( $R^2$ )
1st type	less than 0.32	$K = 0.0000019 \times \varphi^{4.24} \times T_{2lm}^{0.17}$	0.88
2nd type	between 0.32 and 0.6	$K = 0.000057 \times \varphi^{2.90} \times T_{2lm}^{0.49}$	0.97
3rd type	greater than 0.6	$K = 0.0036 \times \varphi^{4.08} \times T_{2lm}^{0.93}$	0.96

From Table 1 it can be observed that the correlations of permeability with porosity and  $T_{2lm}$  are improved for every type of rocks. The correlation coefficients are high enough, ensuring the applicability of SDR model in tight sandstone permeability prediction.

### 3.4 Establishment of relationships for routine core derived porosity and permeability

To verify the applicability of the theory of HFU in routine core analysis, it is also applied in core samples displayed in Fig. 1. By using the same classification criteria of FZI listed in Table 1, the core samples are reused, and they are also classified into three types. For every type of core samples, we attempt to establish the relationship of core derived porosity and permeability. The correlations of core derived porosity *versus* permeability are displayed

Table 2  
Rock classification criteria of FZI and the corresponding relationships of core derived porosity and permeability those displayed in Fig. 1

Type of rock	The classification criteria of FZI	Calibrated SDR model	Correlation coefficient ( $R^2$ )
1st type	less than 0.32	$K = 0.0017 \times \varphi^{2.70}$	0.87
2nd type	between 0.32 and 0.6	$K = 0.0002 \times \varphi^{3.02}$	0.88
3rd type	greater than 0.6	$K = 0.00007 \times \varphi^{3.00}$	0.82

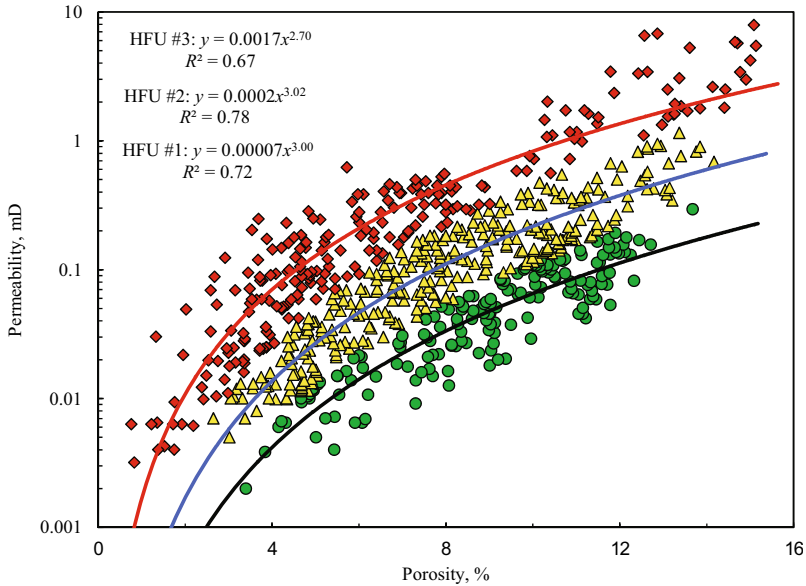


Fig. 8. Cross plots of porosity *versus* permeability for core samples with three different types of HFU.

in Fig. 8, and the corresponding permeability estimation models based on routine core analysis are listed in Table 2. By using the list models, formation permeability can also be estimated from porosity. Analyzing Fig. 8 we can observe that for the first two types of core samples, the regressed trend lines can be used to express the relationship of porosity and permeability, whereas for the third type of core samples, the regressed model will underestimate the permeability in formations with permeability higher than 2.0 mD.

### 3.5 Calculation of FZI from conventional logs

#### 3.5.1 Establishment of FZI prediction model

The above section has illustrated that the SDR model is applicable in tight sandstone permeability estimation once the FZI is introduced to classify rocks. To extend this proposed technique into field applications, consecutive FZI should be first calculated to classify formations. Abbaszadeh *et al.* (1996), D'Windt (2007), and Haghghi *et al.* (2011) pointed out that FZI can be calculated from conventional logs by using the multiple regression method. In this study, the multiple regression method is also applied to calculate FZI. The correlation analysis of obtained FZI from core porosity and permeability by using Eq. 12 and conventional logs illustrates that FZI is

much sensitive to the interval transit time (AC), density (DEN), compensated neutron (CNL), natural gamma (GR), the ratio of deep and shallow lateral resistivity (LLD/LLS), and shale content (VSH) in our target tight gas sands. Hence, these six parameters are chosen to establish the FZI prediction model. In the process of establishing FZI calculation models, only 55 core samples were used, and the other 32 core samples were retained to verify the reliability of the estimated FZI. By using these 55 core samples, the FZI calculation model is calibrated and expressed as follows:

$$\begin{aligned} \text{FZI} = & -0.0033 \times \text{AC} - 0.027 \times \text{CNL} - 0.0094 \times \text{DEN} + 0.0074 \times \text{GR} \\ & + 9.18 \times (\text{LLD/LLS}) - 0.13 \times \text{VSH} - 10.20 \text{ correlation coefficient} = 0.89 \end{aligned} \quad (14)$$

From Eq. 14, it can be observed that good relationship exists between FZI and conventional logs. If it is applied in field applications, consecutive FZI can be calculated from conventional logs.

It is important to note that the parameter of LLD/LLS, which represents the drilling mud invasion characteristics, and thus fluid saturation, has been involved in Eq. 14. Hence, the FZI estimated from Eq. 14 should be heavily affected by the degree of drilling mud invasion and saturation conditions, and the applicability of Eq. 14 should be reduced in formations with significant drilling mud invasion.

Fortunately, in our target tight gas sands, the drilling mud invasion is not obvious due to the poor permeability, the amplitude difference of deep and shallow lateral resistivity is not prominent, and the contribution of LLD/LLS to FZI is not primary. Therefore, Eq. 14 can be well used to estimate FZI in tight gas sands of E basin.

### **3.5.2 Reliability verification for FZI estimation**

To verify the reliability of these FZI estimation models, expressed in Eq. 14, in field applications, it is applied to tight sandstone reservoirs in the E basin to obtain FZIs from conventional logs, and they are compared with laboratory derived results for 32 core samples. Figure 9 shows the cross plot of derived FZI from 32 core samples and predicted results by using Eq. 14. The solid lines in this figure represent the diagonal lines, which clarify the discrepancy of the calculated FZI with that of the core analyzed results. This figure demonstrates that the FZIs estimated by using Eq. 14 and the core derived results locate in the neighborhood of the diagonal lines. This means that the predicted FZIs by using Eq. 14 are acceptable, and Eq. 14 can be applied in field applications to calculate consecutive FZI, and then the permeability estimation formulae listed in Table 1 can be used for accurate permeability prediction.

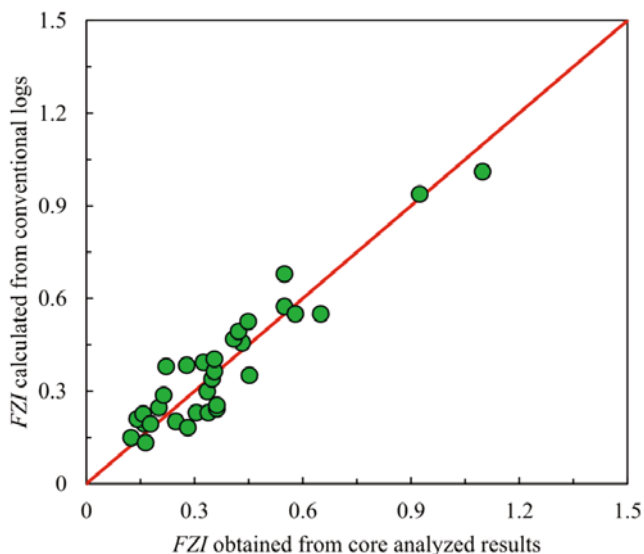


Fig. 9. Comparison of FZI acquired from core samples and calculated from conventional logs.

#### 4. CASE STUDY

Based on the proposed technique, several wells in the E basin of northwest China are processed, and the corresponding tight gas sandstone permeability is estimated. In the process of field applications, we should note that all permeability estimation formulae based on the SDR model are established with laboratory NMR measurements from fully brine saturated core samples. If it is used in field tight gas reservoirs, the effect of diffusion relaxation of natural gas to NMR logs (NMR porosity and  $T_{2lm}$ ) should be considered. In regard to the porosity calculation in tight gas sands, Xiao *et al.* (2012a, b, c) had proposed appropriate model, and it had been verified to be effective in tight gas porosity calculation in the E basin. Hence, it is directly cited in this study to acquire precise porosity. In regard to the gas correction of  $T_{2lm}$ , Xiao *et al.* (2012a, b, c) pointed out that a relationship of between  $T_{2lm}$  acquired from field NMR logs and measured from core samples under fully brine saturated can be established, and it was widely applicative. Based on the method proposed by Xiao *et al.* (2012a, b, c), a relationship is also established to correct the effect of natural gas to NMR  $T_{2lm}$ , as is shown in Fig. 10. From Fig. 10 we can observe that good relationship exists between the  $T_{2lm}$  acquired from field NMR logs and measured from core samples that were fully brine saturated. With this relationship, the effect of natural gas to field NMR  $T_{2lm}$  can be diminished, and, using the corrected NMR parameters, little errors should be introduced in permeability estimation.

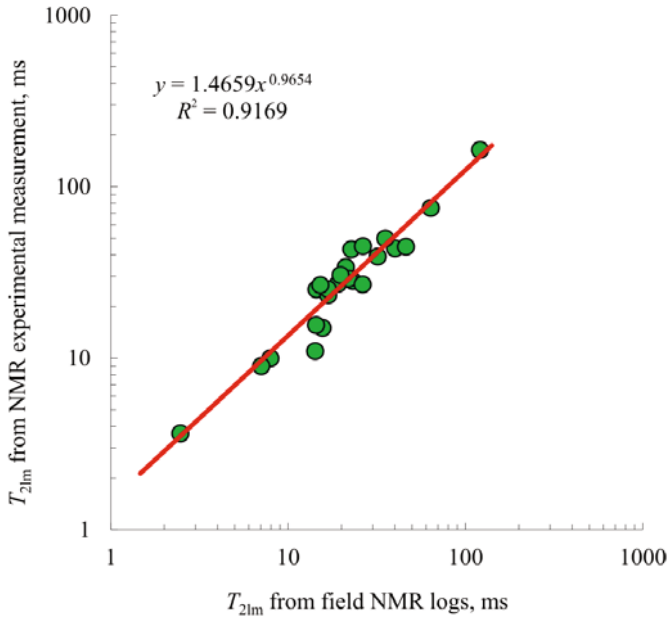


Fig. 10. A relationship between  $T_{2lm}$  acquired from field NMR logs and from core measurement under full brine-saturation in the target tight gas sands of E basin.

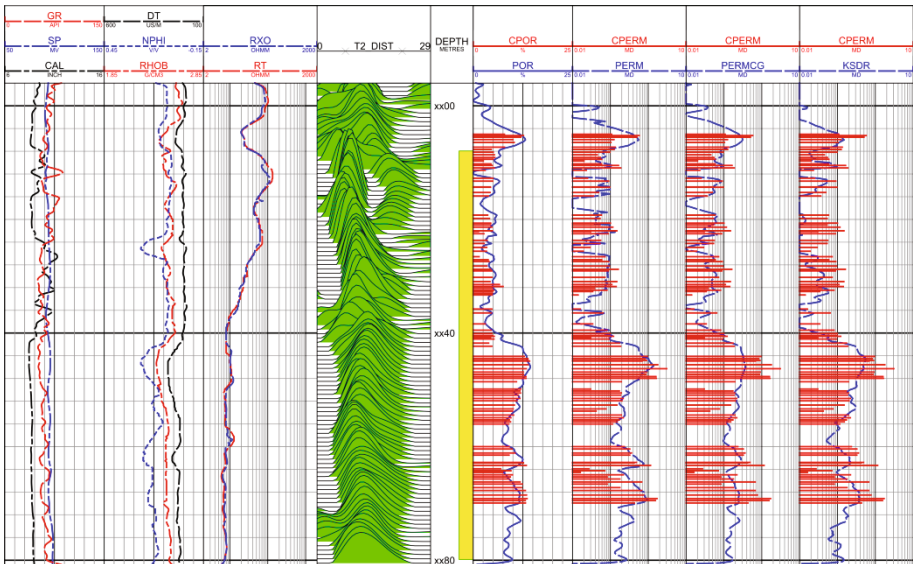


Fig. 11. Comparisons of permeabilities estimated from field NMR logs by using three methods.

Figure 11 shows a field example of estimating permeability in the E basin. In the first track, the displayed curves are gamma ray (GR), spontaneous potential (SP), and borehole diameter (CAL), they are used for effective formation indication. In the second track, we display the curves of density log (DEN), compensated neutron log (CNL), and interval transit time log (AC).

They are used for porosity estimation. RT displayed in the third track is deep lateral resistivity, and RXO is shallow lateral resistivity.  $T_2$  distribution displayed in the fourth track is field NMR  $T_2$  spectrum, which was acquired from the Halliburton's MRIL-C tool, and  $T_{2lm}$  is the logarithmic mean of the NMR  $T_2$  distribution. The fifth track is depth and its unit is meter. In the sixth track of Fig. 11, we display the comparison of routine core derived porosity (CPOR) and NMR derived porosity (POR), and POR is calculated from field NMR and conventional acoustic log using method proposed by Xiao *et al.* (2012a, b, c). This comparison illustrates that the calculated porosity matches the core derived porosity very well, which means that POR is reliable and little error will be brought in when it is applied in permeability estimation. PERM displayed in the seventh track is the formation permeability estimated from field NMR logs by using the proposed technique, and CPERM is the core analyzed permeability. PERMCG displayed in the eighth track is permeability curve obtained by using the models listed in Table 2, and it is directly predicted from porosity after formations are classified into three types by the difference of FZI. KSDR displayed in the last track is permeability estimated from field NMR logs by using the unified SDR model without formation classification. From the comparisons displayed in these three tracks, we can observe that permeabilities can be precisely estimated from field NMR logs once tight gas sandstone reservoirs are classified into three types by using the difference of FZI and the corresponding calibrated SDR models are applied. Models established by using the routine core analyzed results are effective for formations with permeability lower than 0.3 mD, while in formations with permeability higher than 0.3 mD, PERMCG is underestimated. However, formation permeability can only be effectively predicted in the intervals with permeability ranges from 0.1 to 0.3 mD by using the unified SDR model. When formation permeability is higher than 0.3 mD or lower than 0.1 mD, permeability will be underestimated from the unified SDR model. The accuracy of estimated permeability was confirmed by drill stem testing data, in the interval of xx08 to xx80 m (highlighted in Fig. 11),  $3.12 \times 10^4$  m<sup>3</sup>/day of gas production is acquired and the dynamic permeability acquired from well testing in this interval is 0.65 mD. To make the estimated results from different methods can represent the true permeability of the whole test interval they are all normalized by using thickness weighted average method. The results illustrate that per-

meabilities estimated from the calibrated SDR models based on FZI classification, the conventional method by using the models listed in Table 2 and the unified SDR model in the same interval are 0.57, 0.42, and 0.36 mD, separately, while the average core derived permeability in this interval is 0.6 mD. These comparisons adequately show that the technique proposed in this study is much more effective in tight gas sands permeability estimation. Permeability calculated by using calibrated SDR models based on FZI classification is very close to the core derived result and dynamic permeability, whereas permeabilities estimated by using the other two methods are all much underestimated.

## 5. DISCUSSIONS

To intuitively illustrate the improvement of permeability estimation by using the calibrated SDR models based on formation classification method, permeabilities acquired from four different kinds of methods are compared and they are displayed through Figs. 12 to 14, respectively. To carefully analyze the applicability of the models mentioned in this study, core samples with different FZI values are marked with different colour code. The blue lines in these three figures represent the diagonal lines which highlight the discrepancy of predicted permeability with those of core analyzed results.

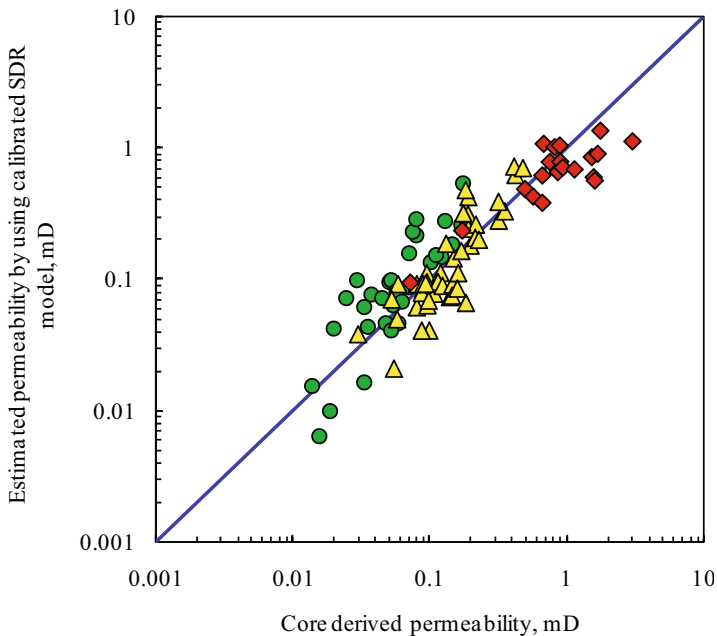


Fig. 12. Cross plot of core derived permeability *versus* estimated permeability by using calibrated SDR models.

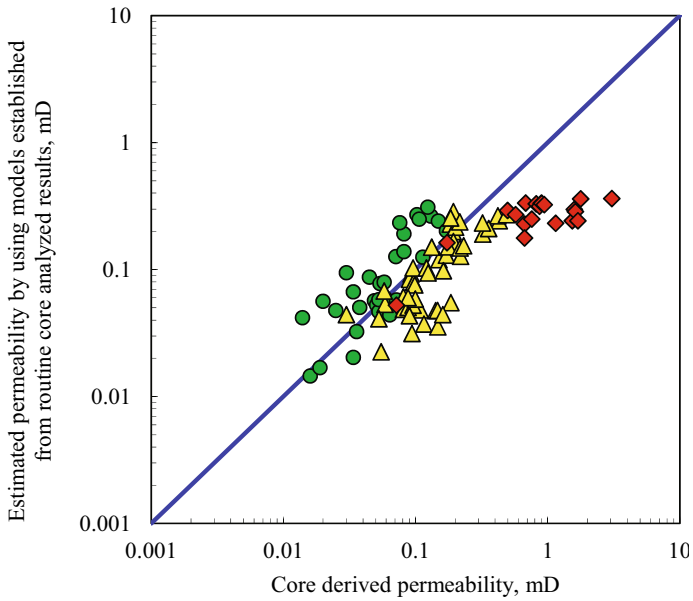


Fig. 13. Cross plot of core derived permeability *versus* estimated permeability by using established models from routine core analyzed results based on FZI classification.

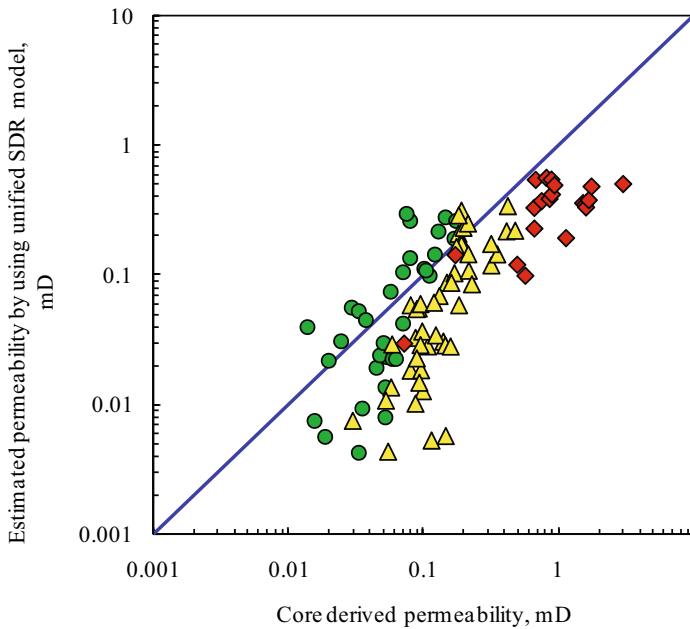


Fig. 14. Cross plot of core derived permeability *versus* estimated permeability by using unified SDR models.

Figure 12 demonstrates that the permeabilities estimated by using the calibrated SDR models based on FZI classification, and the core derived results, are located in the vicinity of the diagonal line for almost all core samples, which indicates that permeabilities obtained from these two methods are approximate. From Fig. 13, however, we can observe that the permeabilities predicted by using the established models from routine core analyzed results based on FZI classification only match the core derived results when permeabilities are lower than 0.3 mD. In this range, the data points are located in the vicinity of the diagonal line, while they are much more divergent than those of the calibrated SDR models. For formations with different type of FZI, the accuracy of permeability estimation is not disparate. For formations with the third type of FZI and permeabilities that are higher than 0.3 mD, these models underestimate the formation permeability. This coincides with the results displayed in Fig. 8.

Figure 14 indicates that the unified SDR model is effective in permeability estimation when formation permeabilities range from 0.1 to 0.3 mD, and the corresponding formations contain the first type of FZI. In the other cases, permeabilities are underestimated. This observation is consistent with those displayed in Fig. 11.

From these comparisons, displayed in Figs. 11 to 14, we can observe that the accuracy of tight gas sandstone permeability estimation is not high enough from NMR logs by using the unified SDR model; once the formations are classified into three types based on the difference of FZI, and the above-mentioned parameters in the SDR model are calibrated separately, the permeability prediction is much improved. Although permeability can be estimated from porosity after formations are classified into three types based on the difference of FZI, and the estimated permeabilities are much more precise than those obtained from unified SDR models, the accuracy needs to be improved for tight gas sands evaluation; the reasons may be that the input parameter used is the logarithmic mean of NMR  $T_2$  spectra except of the porosity in the calibrated SDR models, and the logarithmic mean of NMR  $T_2$  spectra is the response of pore structure. However, the models established from routine core analyzed results only contain univocal porosity, and from Fig. 8 we can also observe that the relevance between core derived porosity and permeability is not high enough, and, especially for the third type of rocks, permeability should be underestimated by using the regressed relationship. Maybe, the permeability can be much more precisely estimated from porosity after formations are classified into many more types, but the processing procedure should be complicated, and many more median errors may be introduced.

## 6. CONCLUSIONS

- The classical Timur–Coates model is poorly applicable in permeability estimation, because it is difficult to accurately obtain the involved parameters of FFI and BVI from NMR logs at present.
- If the SDR model is directly applied in tight gas sandstone permeability prediction with the unified calibrated parameters, precise permeability can only be estimated in the intervals with permeability ranges from 0.1 to 0.3 mD; when formation permeability is higher than 0.3 mD or lower than 0.1 mD, the formation permeability will be underestimated.
- After core samples are classified into three types based on the differences of FZI, the above-mentioned parameters in the SDR model can be calibrated, respectively. Once the same criteria are applied to field applications, formations can be classified and the corresponding SDR models can be used to effectively improve the permeability estimation in tight sandstone reservoirs.

## References

- Abbaszadeh, M., H. Fujii, and F. Fujimoto (1996), Permeability prediction by hydraulic flow units – theory and applications, *SPE Formation Eval.* **11**, 4, 263-271, DOI: 10.2118/30158-PA.
- Coates, G.R., L.Z. Xiao, and M.G. Prammer (1999), *NMR Logging – Principles and Applications*, Gulf Publ. Co., Houston, 256 pp.
- D'Windt, A. (2007), Reservoir zonation and permeability estimation: A Bayesian approach. **In:** *Proc. 48th SPWLA Annual Logging Symposium, 3-6 June 2007, Austin, USA*, paper UUU.
- Delli, M.L., and J.L.H. Grozic (2013), Prediction performance of permeability models in gas-hydrate-bearing sands, *SPE J.* **18**, 2, 274-284, DOI: 10.2118/149508-PA.
- Deng, J.M., X.X. Hu, X.P. Liu, and X.M. Wu (2013), Estimation of porosity and permeability from conventional logs in tight sandstone reservoirs of north Ordos basin. **In:** *SPE Unconventional Gas Conference and Exhibition, 28-30 January 2013, Muscat, Oman*, SPE163953, DOI: 10.2118/163953-MS.
- Dunn, K.-J., D.J. Bergman, and G.A. Latorraca (2002), *Nuclear Magnetic Resonance: Petrophysical And Logging Applications*, Handbook of Geophysical Exploration, Vol. 32, Pergamon, New York, 176 pp.
- Gao, J.B., L.T. Sun, and C.R. Wang (1991), Development of a transient pulse permeameter for tight rocks, *Chin. J. Sci. Instr.* **12**, 4, 365-371 (in Chinese).
- Haghighi, M.B.P., M. Shabaninejad, and K. Afsari (2011), A permeability predictive model based on hydraulic flow unit for one of Iranian carbonate tight gas

- reservoir. **In:** *SPE Middle East Unconventional Gas Conference and Exhibition, 31 January – 2 February 2011, Muscat, Oman*, SPE 142183, DOI: 10.2118/142183-MS.
- Hearn, C.L., W.J. Ebanks Jr., R.S. Tye, and V. Ranganathan (1984), Geological factors influencing reservoir performance of the Hartzog Draw field, Wyoming, *J. Petrol. Technol.* **36**, 8, 1335-1347, DOI: 10.2118/12016-PA.
- Hulea, I.N. (2013), Capillary pressure and permeability prediction in carbonate rocks – New methods for fractures detection and accurate matrix properties prediction. **In:** *SPE Middle East Oil and Gas Show and Conference, 10-13 March 2013, Manama, Bahrain*, SPE164251, DOI: 10.2118/164251-MS.
- Hulea, I.N., and C.A. Nicholls (2012), Carbonate rock characterization and modeling: Capillary pressure and permeability in multimodal rocks – A look beyond sample specific heterogeneity, *AAPG Bull.* **96**, 9, 1627-1642, DOI: 10.1306/02071211124.
- Kenyon, W.E. (1997), Petrophysical principles of applications of NMR logging, *The Log Analyst* **38**, 2, 21-43.
- Kenyon, W.E., P.I. Day, C. Straley, and J.F. Willemsen (1988), A three-part study of NMR longitudinal relaxation properties of water-saturated sandstones, *SPE Formation Eval.* **3**, 3, 622-636, DOI: 10.2118/15643-PA.
- Lucia, F.J. (1995), Rock-fabric/petrophysical classification of carbonate pore space for reservoir characterization, *AAPG Bull.* **79**, 9, 1275-1300.
- Mao, Z.Q., Z.N. Wang, Y. Jin, W.N. Zhou, X.G. Liu, and B. Xie (2008), Study on petrophysical foundation, methodology and techniques of logging reservoir evaluation for Upper Triassic Xujiahe Formation in Sichuan Basin, *Well Log. Technol.* **31**, 3, 203-206.
- Mao, Z.Q., L. Xiao, Z.N. Wang, Y. Jin, X.G. Liu, and B. Xie (2013), Estimation of permeability by integrating nuclear magnetic resonance (NMR) logs with mercury injection capillary pressure (MICP) data in tight gas sands, *Appl. Magn. Reson.* **44**, 4, 449-468, DOI: 10.1007/s00723-012-0384-z.
- Morriss, C., D. Rossini, C. Straley, P. Tutunjian, and H. Vinegar (1997), Core analysis by low-field NMR, *The Log Analyst* **38**, 2, 84-94.
- Rezaee, R., A. Saedi, and B. Clennell (2012), Tight gas sands permeability estimation from mercury injection capillary pressure and nuclear magnetic resonance data, *J. Petrol. Sci. Eng.* **88-89**, 92-99, DOI: 10.1016/j.petrol.2011.12.014.
- Salah, A. (2012), The impact of pore geometry aspects on porosity-permeability relationship – a critical review to evaluate NMR estimated permeability. **In:** *North Africa Technical Conference and Exhibition 2012, 20-22 February 2012, Cairo, Egypt*, 808-818, SPE150887, DOI: 10.2118/150887-MS.
- Tiab, D., D.M. Marschall, and M.H. Altunbay (1993), Method for identifying and characterizing hydraulic units of saturated porous media: tri-kappa zoning process, U.S. Patent No. 5193059 A.

- Xiao, L., Z.Q. Mao, and Y. Jin (2012a), Calculation of irreducible water saturation ( $S_{wirr}$ ) from NMR logs in tight gas sands, *Appl. Magn. Reson.* **42**, 1, 113-125, DOI: 10.1007/s00723-011-0273-x.
- Xiao, L., Z.Q. Mao, G.R. Li, and Y. Jin (2012b), Calculation of porosity from nuclear magnetic resonance and conventional logs in gas-bearing reservoirs, *Acta Geophys.* **60**, 4, 1030-1042, DOI: 10.2478/s11600-012-0015-y.
- Xiao, L., Z.Q. Mao, Z.N. Wang, and Y. Jin (2012c), Application of NMR logs in tight gas reservoirs for formation evaluation: A case study of Sichuan basin in China, *J. Petrol. Sci. Eng.* **81**, 182-195, DOI: 10.1016/j.petrol.2011.12.025.
- Xiao, L., X.P. Liu, C.C. Zou, X.X. Hu, Z.Q. Mao, Y.J. Shi, H.P. Guo, and G.R. Li (2014), Comparative study of models for predicting permeability from nuclear magnetic resonance (NMR) logs in two Chinese tight sandstone reservoirs, *Acta Geophys.* **62**, 1, 116-141, DOI: 10.2478/s11600-013-0165-6.
- Xiao, Z.X., and L. Xiao (2008), Method to calculate reservoir permeability using nuclear magnetic resonance logging and capillary pressure data, *Atom. Ener. Sci. Technol.* **42**, 10, 868-971 (in Chinese).
- Yang, M.S. (2001), Study of optimal work condition about instantaneous-pulse permeability test equipment, *J. Southwest Petrol. Inst.* **23**, 1, 46-48 (in Chinese).

Received 20 January 2014

Received in revised form 8 July 2014

Accepted 14 July 2014

# Estimation of Seismic Site Coefficient and Seismic Microzonation of Imphal City, India, Using the Probabilistic Approach

Kumar PALLAV<sup>1</sup>, S.T.G. RAGHUKANTH<sup>2</sup>,  
and Konjengbam D. SINGH<sup>3</sup>

<sup>1</sup>Department of Civil Engineering, Motilal Nehru National Institute of Technology  
Allahabad, India; e-mail: kumarpallav23@gmail.com

<sup>2</sup>Department of Civil Engineering, Indian Institute of Technology Madras, India;  
e-mail: raghukanth@iitm.ac.in

<sup>3</sup>Department of Civil Engineering, Indian Institute of Technology Guwahati, India;  
e-mail: darun@iitg.ac.in

## Abstract

Seismic site coefficients ( $F_s$ ) for Imphal city have been estimated based on 700 synthetically generated earthquake time histories through stochastic finite fault method, considering various combinations of magnitudes and fault distances that may affect Imphal city. Seismic hazard curves and Uniform Hazard Response Spectra (UHRS) are presented for Imphal city.  $F_s$  have been estimated based on site response analyses through SHAKE-91 for a period range of engineering interest (PGA to 3.0 s), for 5% damping.  $F_s$  were multiplied by UHRS values to obtain surface level spectral acceleration with 2 and 10% probability of exceedance in 50 year (~2500 and ~500 year) return period. Comparison between predicted mean surface level response spectra and IS-1893 code shows that spectral acceleration value is higher for longer periods (*i.e.*, > 1.0 s), for ~500 year return period, and lower for periods shorter than 0.2 s for ~2500 year return period.

**Key words:** seismic site coefficient, seismic microzonation, ground motion.

## 1. INTRODUCTION

Past earthquakes have demonstrated that the local soil plays significant role in the characteristics of ground motions. Building codes have incorporated soil amplification effects by specifying few site categories (soil profile types) and assigning soil/site amplification effects for each site category. According to Martin and Dobry (1994) the site coefficients  $F_a$  specified in the National Hazard Reduction Program (NEHRP) provisions (BSSC 1995) are about the mean values and the site coefficients  $F_v$  are approximately the mean plus one standard deviation values. However, the variations in these site coefficients are not specified. The work carried out by Hwang *et al.*, (1997) specified the site coefficient for site categories given in the 1994 NEHRP provisions (BSSC 1995) using the ground motions expected to occur in the eastern United States. A set of generic site coefficients was derived and summarized similar to NEHRP site coefficients (BSSC 1995), with an added dimension of the Mississippi Embayment deposits thickness to the Paleozoic rock by Park and Hashash (2005). All these site coefficients categorize only the type of soil and do not correlate it with rock-level time histories. In this paper, a simple procedure has been established to compute the seismic site coefficients ( $F_s$ ) due to seismic loading (earthquake time-history) that may be useful for design engineers to obtain the surface level response. The study has been performed for Imphal city (capital of Manipur State, India; Fig. 1) and  $F_s$  with respect to 700 synthetically generated earthquake time-histories have been obtained. These time-histories have been

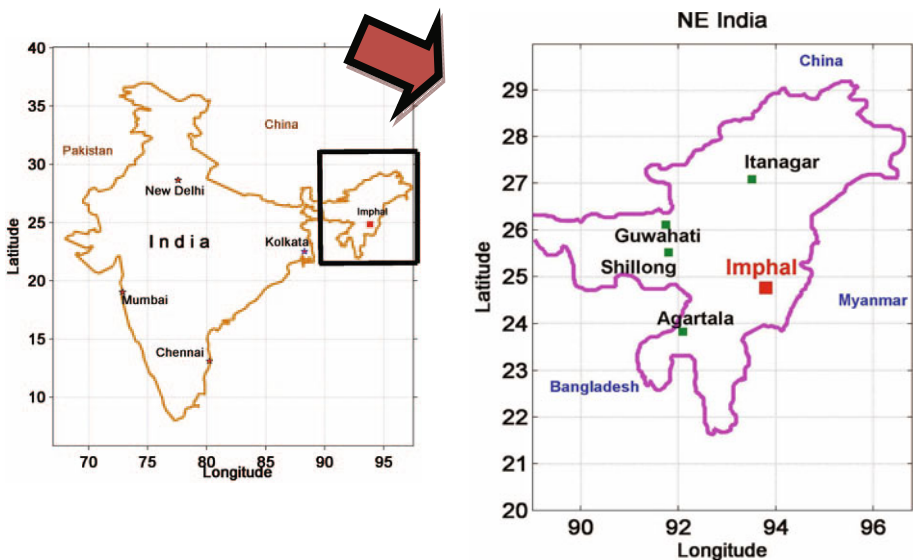


Fig. 1. Location of Imphal city.

generated at a regular interval of magnitude of 0.5 and distance of 20 km, for  $M_w$  magnitudes between 5.0 and 8.5, and 5-200 km distance using finite-fault seismological model (Motazedian and Atkinson 2005) in conjunction with equivalent linear site response analyses (Idriss and Sun 1992) on all 122 borehole locations of Imphal city. Further,  $F_s$  are used to get the surface level response for input rock level motion. Pallav *et al.* (2012) have already performed the probabilistic seismic hazard analysis of Manipur State in which the rock level PGA for Imphal city has been estimated for 2 and 10% probability of exceedence in 50 year (~2500 and ~500 year) return period. Surface level response for Imphal city has been estimated by multiplying the rock level input with  $F_s$ . Further on, seismic microzonation maps at PGA, 0.3 and 1.0 s with ~500 and ~2500 year return period have been prepared for Imphal city and a comparison was made between predicted mean surface level response spectra and the existing Indian Code of Practice (IS-1893 2002).

## 2. ABOUT IMPHAL CITY

Imphal city (24°48'N, 93°56'E), the capital of Manipur state, is one of the oldest cities of North East India; it forms the central part of the oval-shape Imphal valley. The developmental growth of city has been very slow for various political and geographical reasons compared to other capital cities of India. However, in the recent years, an increase in population/population density in and around Imphal city has been observed. According to the 2011 census, Imphal city has a population of 264 986; which is around 10% of the entire state's population. The growth pattern has been considerably influenced by physiographic characteristic of Imphal city. Major growth has taken place in the central area – near Kangla Palace, and towards the south along the highways (NH-39 and NH-150), which is shown in Fig. 2.

In recent time, local government has taken up several important infra-structural building programmes to accommodate increase in population. New buildings, *viz.*, capital buildings, high court, city convention center, *etc.*, are coming up along with some new international projects, like rail link from Manipur to Vietnam, trilateral highways project between India, Myanmar, and Thailand, digital connectivity of optical fiber cable link between Moreh in Manipur and Mandalay in Myanmar (PTI 2010) are in pipeline. As such, due to proximity Indo Burma Range (IBR), Shillong Plateau (SP), and Naga Disang Thrust, vulnerability of Imphal city to damaging earthquakes has increased. In view of this, it is pertinent to understand the near surface soil effect on Imphal city due to earthquake events and model the local site that helps engineers and designers to use the developed parameters, *i.e.*, seismic site coefficients, due to seismic loading in their design.

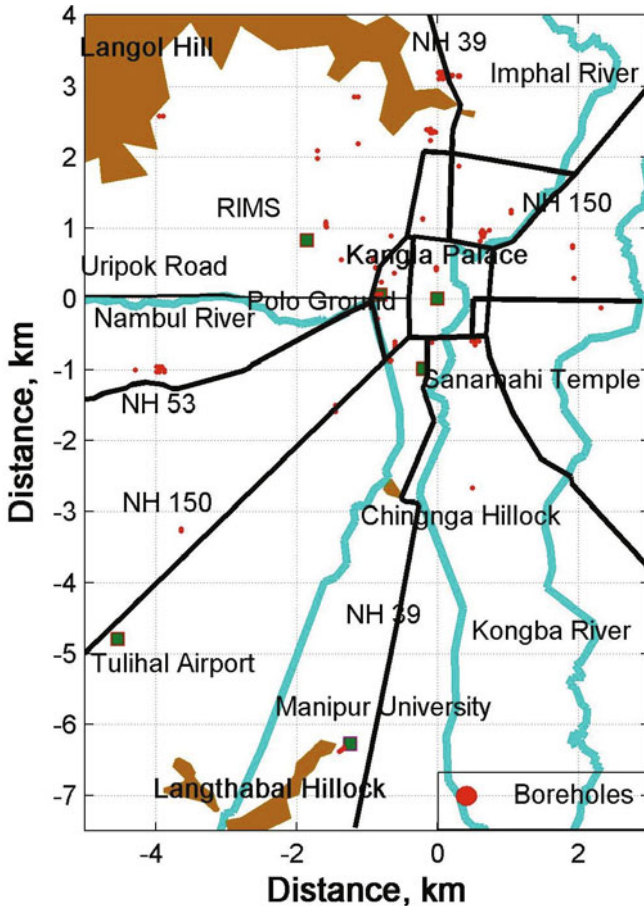


Fig. 2. Imphal city with important places, rivers, and transportation network along with boreholes location (origin (0 km, 0 km) corresponds to latitude of  $24.81^\circ$  and longitude of  $93.94^\circ$ , at Kangla palace).

### 3. SEISMIC SETUP AROUND IMPHAL CITY

In a period of 147 years (1866-2013), North East (NE) India has experienced more than 2200 earthquakes of magnitude  $M_w \geq 4.0$ . These earthquakes, of both crustal as well as subduction zone origin, are close to Imphal ( $< 300$  km). Seismotectonic features in a broad region around Imphal city have been identified and described basing on the seismotectonic atlas of India (GSI 2000). Figure 3 (after Pallav *et al.* 2010, 2012) shows that almost the entire region around Imphal city is surrounded by faults. These faults contribute to tectonic activity in the region, which is mainly due to the interaction between the north-south convergence along the Himalayan boundary,

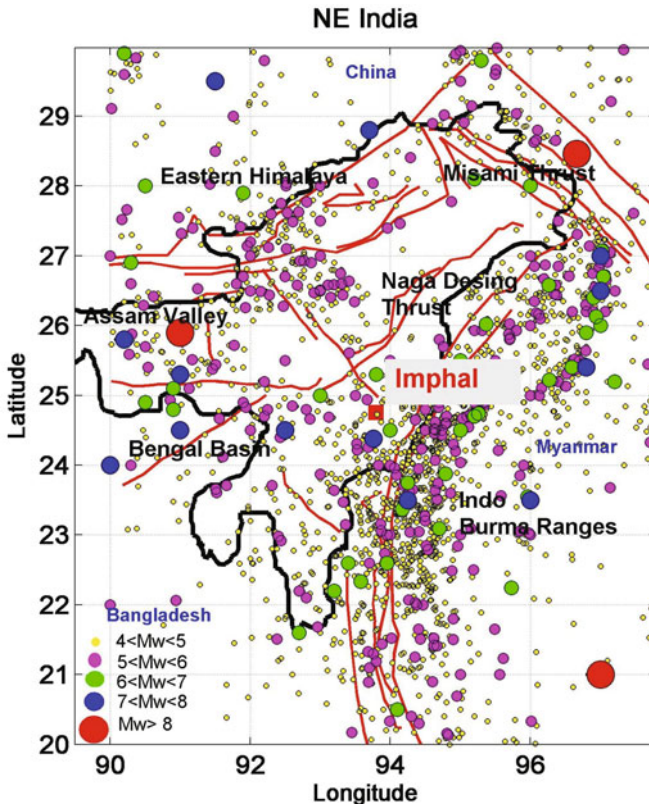


Fig. 3. Seismotectonic setup around Imphal city with seven seismic blocks along with epicenters (1866-2013).

and east-west convergence along the IBR. Based on its seismotectonic features and geology, NE India is broadly divided into seven seismic zones. These are: 1 – Indo-Burma Ranges, IBR; 2 – Eastern Himalaya, EH; 3 – Mishmi Thrust, MT; 4 – Shillong Plateau, SP; 5 – Naga-Disang thrust, ND; 6 – Bengal basin, BB; and 7 – Assam Valley, AV (Goswami and Sarmah 1982, Nandy 2001). The details on seismicity of NE India and damages incurred due to past earthquake in Imphal city/Manipur state were discussed in Raghukanth *et al.* (2009), and Kumar *et al.* (2010, 2012).

#### 4. GEOGRAPHY, GEOLOGY AND LOCAL SOIL CONDITION

##### 4.1 Geography

Imphal valley (also known as Manipur valley) is surrounded by a series of mountain chains, *i.e.*, Patkai hills on the north and north-east and the Manipur hills, Lushai hills, Naga hills, and Chin hills on the south, running from

north to south, forming an integral part of IBR (Laiba 1992, Ibotombi 2000). It has NNW-SSE orientation with a gentle tilting slope towards the south, at 798 m above mean sea level (a.m.s.l.) at the extreme north, and 746 m a.m.s.l. at the south. The structural and tectonic pattern near Imphal valley is transitional between the NE-SW trending pattern of Naga–Patkai hills and the N-S trend of Mizoram and Chin hills (Brunnschweiler 1974). These hills comprise geologically young rock formations due to Tertiary upward displacement of the Himalayas from the shallow bed of the Tethys Sea. The rocks are mainly of Tertiary and Cretaceous sediments with minor igneous and metamorphic rocks. Geomorphologically, the valley area can be categorized into five major units: 1 – moderate to high structural cum Denudational hills, which can be seen as the hills and mountains surrounding the valley, 2 – residual hills composed of hillocks and hills which are scattered in the valley (*e.g.*, Langol and Chingna hills), 3 – piedmont plain features along the foothills, 4 – older alluvial plains of alluvium deposits near foothills of Imphal valley, and 5 – younger alluvial plains having lower elevation than the older alluvial plains and which are mostly flat (Singh 2004). Imphal valley is surrounded by four major river basins, *viz.*, the Barak river basin (Barak valley) to the west, the Manipur river basin in central Manipur, the Yu river basin in the east, and a portion of the Laniye river basin in the north (Haokip 2007). The river basins have the major rivers: Imphal, Iril, Nambul, Sekmai, Chakpi, Thoubal, and Khuga. All these rivers originate from the surrounding hills and deposit their sediment load in the Loktak lake (Laiba 1992) located in Imphal valley.

## 4.2 Geology

Geological information and a detailed geological report on Imphal city are still not available. As per the report published by Manipur Science and Technology Council (MASTEC 2007), Imphal valley is almost flat in nature, filled with fluvio-lacustrine dark grey to black clay, silt, and sand alluvium deposits. The major portion of sediments are clay and mixture of clay and sand, whilst silt and sand forms lensoids and bands within clay. As per the authors' knowledge, the bed rock profile has not been mapped; however, the MASTEC (2007) report suggests that the average thickness of alluvium is at least ~100-150 m. It is suggested that the basement mainly consists of Disang sediments. The extension of the basement faults led to the growth of isolated hillocks, as remnants of horsts. This forms the basis of tectonic beginning and creation of Imphal valley (Ibotombi 2000). However, this is in disparity to the erosional formation of valley, according to which the valley was formed due to filling of river borne sediments in the Loktak lake, the original lake that engulfed the entire valley once. Laiba (1992) as another theory

suggesting the fluvio-lacustrine origin of the valley due subsequent earthquakes in the area.

### 4.3 Local soil condition

Imphal is a city located on the banks of Imphal, Nambul, and Kongba rivers that have left several palaeoseismic channels over which the present human settlement exists. The main constituents of Imphal valley are sands, clays, silts, *etc.* of fluvio-lacustrine origin, whereas ferruginous red soils are found near isolated foothill regions. Alluvial soils occur near the riverbanks. Clayey soils in the valley region are rich in humus. In the low-lying areas of Imphal city, *i.e.*, Lamphelpat, Takyelpat, Prompat, Kakwapat (“pat” means lake), virgin soils as clayey loam, dark clayey, and boggy kind of soils are found (Laiba 1992).

The near surface soil conditions play an important role in soil amplification potential of a site. It is therefore essential to take into account the soil properties of the near surface soil layers to obtain the surface level ground motion. The shear wave velocity profiles and Cone Penetration Test (CPT) data are not readily available for sites in Imphal city. However, Standard Penetration Test (SPT-N) data and soil characteristics are available for several sites, 122 location, of Imphal city. These sites are scattered over an area of about  $11.5 \times 8$  km along the NH-39 and NH-53, as shown in Fig. 2. The SPT-N values have been measured at 1.5 m interval along the depth of boreholes. The boreholes depth ranges from 6 to 20 m for most of the sites. However, for important construction projects, SPT-N has been carried out down to a depth of 30 m. The type of soil deposits in Imphal city comprises of sandy clay, silty clay, and clayey along with organic matters deposited in different layers. They are loose in density due to typical alluvial/fluvial deposits. The SPT-N data shows that even at a depth of 25-30 m below the ground surface the values are low, of the order of 12 to 20, except of few places where they are about 30-40. In addition to the sides of NH-39, NH-53, and NH-150 roads, most of these boreholes are located around the Kangla Palace area that houses several commercial and administrative establishments. Further, the classification of the site categories present in Imphal city has been made based on International Building Code (IBC-2006 2006), in which the average standard penetration resistance ( $\bar{N}$ ) at all the boreholes is computed by the following equation:

$$\bar{N} = \frac{\sum_{i=1}^n d_i}{\sum_{i=1}^n (d_i / N_i)} , \quad (1)$$

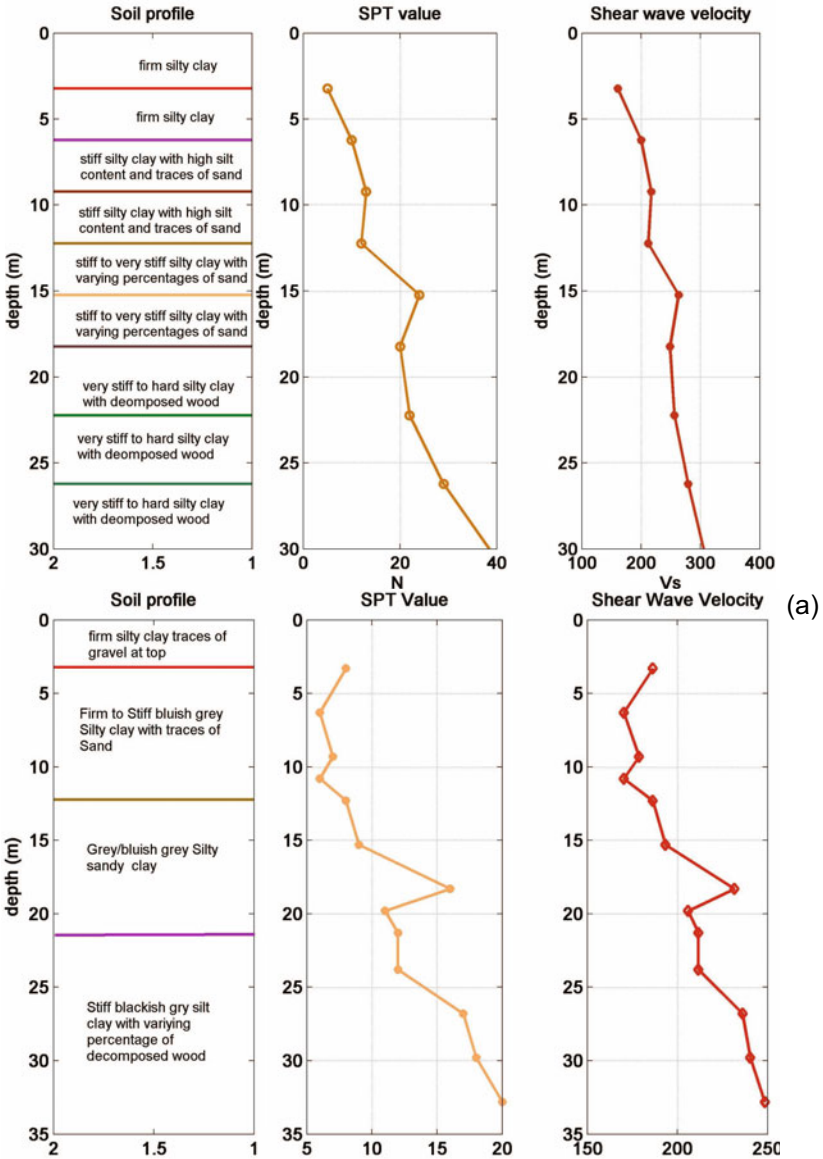


Fig. 4. Typical D (a) and E (b) type soil profile, SPT-N value, and shear (b) velocity.

where  $d_i$  and  $N_i$  are the thickness and SPT-N value of each layer, respectively, and  $n$  is the total number of soil layers. Out of the 122 boreholes in Imphal city which are considered in the present analysis, 114 boreholes are classified as soil class E-type ( $\bar{N} < 15$ ) while remaining 8 boreholes are of

soil class D-type ( $15 < \bar{N} < 50$ ) following the classification concept applied by IBC-2006. A typical D-type and E-type subsurface soil condition and SPT-N value profile are shown in Fig. 4. It may be noted that IBC-2006 requires soil data down to a 30 m depth. In present study, as not all the soil data down to 30 m depth are available for site classification, the mean SPT-N value was estimated from those boreholes for which SPT values were available down to 30 m depth, and it has been used as additional data for the remaining depth down to 30 m.

## 5. DETERMINATION OF ROCK LEVEL ACCELERATION TIME HISTORIES

Due to the unavailability of strong motion records of past earthquakes that caused damages to Imphal city, the synthetic ground motion is simulated by stochastic finite fault model. In this model, features of source and path are modelled as primary system parameters and the effect of near surface soil layers is treated as a secondary modification. The rock level ground motions are simulated by stochastic finite fault approach of Motazedian and Atkinson (2005) which is based on the concept of dynamic corner frequency and pulsing subfaults.

In the present approach, the fault is divided into  $N$  subfaults and they are represented as point sources. The triggering occurs when the rupture front spreads radially from the nucleation point and it reaches their center. The sub-fault acceleration time histories are propagated to the observation point by considering specified distance-duration curves and attenuation model. The Fourier amplitude spectrum of ground motion  $[Y(r, f)]$  due to the  $j$ -th subfault at a site is derived from the point source seismological model, expressed as

$$Y_j(r, f) = \left( \frac{M_0 D_j}{\sum_{j=1}^N D_j} \right) \left( \frac{N(2\pi f)^2 \sum_j \left( \frac{f^2}{1+(f/f_0)^2} \right)^2}{\left( 1+(f/f_{0j}(t))^2 \right) \sum_j \left( \frac{f^2}{1+(f/f_{0j}(t))^2} \right)^2} \right)^{1/2} \left( \frac{\sqrt{2} < R_{\theta\phi} >}{4\pi\rho V_s^3} \right) \left( G e^{-\frac{\pi r_j}{V_s Q}} \right) \left( F(f) e^{-\pi f \kappa_0} \right), \quad (2)$$

where  $M_0$  is the total seismic moment of all the subfaults,  $G$  refers to the geometric attenuation,  $r_j$  is the subfault distance from the site,  $V_s$  is the shear wave velocity, and  $Q$  is the quality factor of the region.  $D_j$  is the average final slip acting on the  $j$ -th subfault,  $f_{0j}(t)$  is the dynamic corner frequency (Motazedian and Atkinson 2005), and  $F(f)$  represents site amplification due to propagation of earthquake waves from the source region toward the surface. The term  $\exp(-\pi f \kappa_0)$  is a high cut filter which takes care of the rapid

spectral decay at high frequencies (Anderson and Hough 1984).  $\langle R_{\theta\phi} \rangle$  is the radiation coefficient averaged over an appropriate range of azimuths and take-off angles and  $\rho$  is the density of the crust at the focal depth. The dynamic corner frequency  $f_{0j}(t)$ , the seismic moment and the stress drop ( $\Delta\sigma$ ) are related through the following equation

$$f_{0j}(t) = 4.9 \times 10^6 (N_R(t))^{-1/3} N^{1/3} V_s \left( \frac{\Delta\sigma}{M_0} \right)^{1/3}, \quad (3)$$

where  $N_R(t)$  is the cumulative number of ruptured subfaults at time  $t$ . The corner frequency at the end of the rupture,  $f_0$ , is obtained by substituting  $N_R(t) = N$  in Eq. 3. Motazedian and Atkinson (2005) introduced the concept of pulsing area where the cumulative number of active subfaults,  $N_R(t)$ , increases with time at the initiation of rupture, to attain a constant magnitude at some fixed percentage of the total rupture area referred to as percentage pulsing area; this accounts for realistic model of earthquake rupture. This parameter (*i.e.*, pulsing area) determines the number of active subfaults during the rupture of  $j$ -th subfault. These numerous subfaults are used in Eq. 3 for computing the dynamic corner frequency. Finite fault seismological model for North East India has been calibrated by Raghukanth and Somala (2009). The range of stress drop, pulsing percentage and the quality factor for Indo-Burma, Shillong Plateau, and Bengal basin tectonic blocks have been derived from the strong motion data of minor and moderate events in NE India. Pallav *et al.* (2012) has studied that Indo Burmes Range and Shillong Plateau are situated closer to Imphal and contribute significantly in seismic hazard. Hence the parameters used to study in the present work are shown in Table 1. The quality factor,  $Q(f)$ , geometric spreading, and distance-dependent

Table 1

Input parameters in the stochastic finite fault seismological model  
(Raghukanth and Somala 2009)

Parameter	Shillong Plateau	Indo-Burma Ranges
Depth to top of the fault [km]	5	60
Stress drop [bars]	50-100	50-100
$Q(f)$	$221f^{0.89}$	$431f^{0.73}$
Site effects [ $F(f)$ ]	Quarter wavelength	Quarter wavelength
Kappa factor	0.03	0.03
Pulsing percentage	25-60	25-60
Rupture velocity	$0.8 \beta$	$0.8 \beta$
Slip distribution	Random field	Random field

duration operators for North East India are taken from Raghukanth and Somala (2009).

Acceleration time histories of length equal to the strong motion duration (Boore and Atkinson 1987) are simulated for each subfault from the point source seismological model of Boore (1983). The simulated acceleration time histories for all the subfaults are summed up with a time delay  $\Delta t_j$  to obtain the ground motion acceleration,  $a(t)$ , from the entire fault as

$$a(t) = \sum_{j=1}^N a_j(t + \Delta t_j) . \quad (4)$$

The ground motion samples obtained are based on a given set of model parameters, which are themselves uncertain. Thus the sample ground motions from a suite of such simulations may still not reflect all the variability observed in real ground motion. To account for this, the slip distribution, stress drop and pulsing percentage are treated as random variables, distributed uniformly about a mean value.

These methods are successfully validated for Imphal city (Raghukanth *et al.* 2009, and Pallav *et al.* 2010). Altogether 700-earthquake time-history has been generated for different combinations of magnitudes ( $M_w$  of 5-8.5) and distances (20-200 km) from the faults under consideration and their mean Peak Ground Acceleration (PGA) distribution is shown in Fig. 5. The mean PGA is relatively low at lower magnitude ( $M_w < 6$ ) or large distance (greater than 90 km).

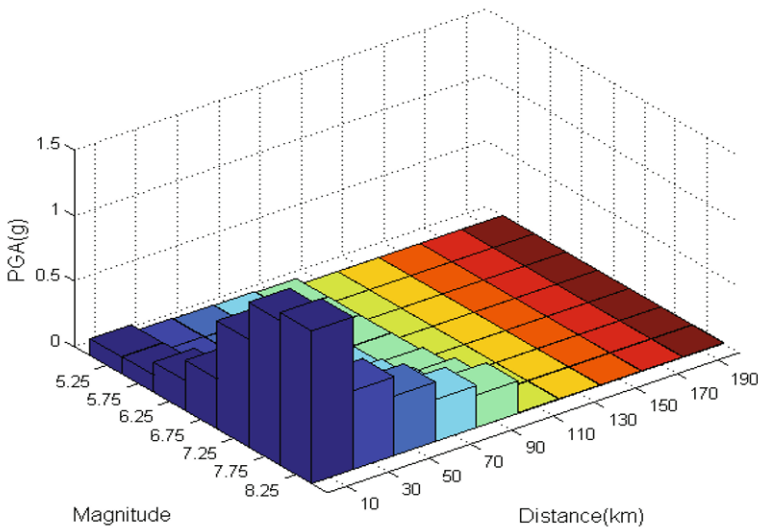


Fig. 5. Mean PGA distribution.

## 6. SOIL AMPLIFICATION

As  $V_s$  (shear-wave velocity) values were not mapped for Imphal city, they have been computed from the  $N$  values using the empirical relation  $V_s = 97 N^{0.314}$  of Imai and Tonouchi (1982), where  $N$  is SPT  $N$  value and  $V_s$  is in m/s. Although there are many equations available for computing  $V_s$ , intention to choose the above equation is its applicability to all types of soil and, moreover, the fact that methods of conducting SPT in Indian and Japanese standards are quite similar. Further, it is assumed that the top soil layer (*i.e.*, alluvial/fluvial deposits) is underlain by rock. Modification of acceleration time history between soft rock and soil site is a non-linear problem in one dimension and hence, for such sites, amplification was already found by the nonlinear site response analysis in Raghukanth *et al.* (2009). The nonlinear behavior of the soil, *i.e.*, reduction of shear modulus and increase of damping ratio with increasing/decreasing shear strain are accounted by using equivalent linear soil properties. For this purpose, shear modulus *versus* shear strain curves and damping ratio *versus* shear strain curves proposed by Vucetic and Dobry (1991) for different types of soil, *i.e.*, clay and sand (Fig. 6a and b) whereas for rock, the curve proposed by Schnabel *et al.* (1972) has been used in the present analysis (Fig. 6c), in which  $G$  and damping ratio is approximated by adopting equivalent linear values. The equivalent linear value of  $G$  is the secant modulus of a first hysteresis loop. Similarly, the equivalent linear value of damping is the energy loss in the first hysteresis loop. The equivalent linear approach considers the variation of  $G$  and damping ratio for different strain values. Equivalent nonlinear site response analysis has been carried out using the software SHAKE-91 of Idriss and Sun (1992). The simulated acceleration time history at rock level from finite fault seismological model for Imphal city has been used as input in SHAKE-91 to generate surface level time histories, in which the vertical propagation of SH waves may be represented by a stack of infinitesimal elements. One-dimensional equation of motion for vertically propagating SH waves can be written as follows:

$$\rho \frac{\partial^2 u}{\partial t^2} = \frac{\partial \sigma_{xz}}{\partial z} . \quad (5)$$

The stress-strain relationship for such a model is given as

$$\tau = G\gamma + \eta \frac{\partial \gamma}{\partial t} . \quad (6)$$

Substituting Eq. 5 into Eq. 6 with  $\tau = \sigma_{xz}$  and  $\gamma = \partial u / \partial z$ , we get

$$\rho \frac{\partial^2 u}{\partial t^2} = G \frac{\partial^2 u}{\partial z^2} + \eta \frac{\partial^3 u}{\partial z^2 \partial t} . \quad (7)$$

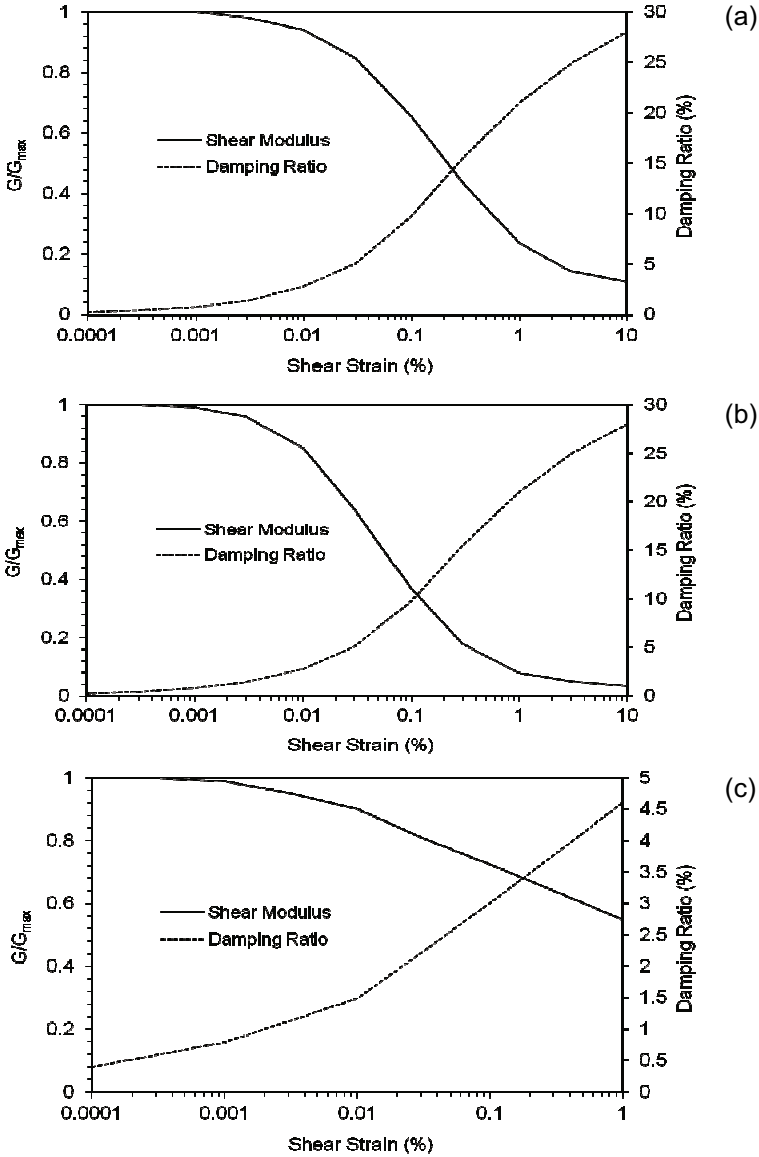


Fig. 6. Modulus reduction curve and damping curves: (a) clay, (b) sand (Vucetic and Dobry 1991), and (c) rock (Schnabel *et al.* 1972).

The solution to the wave equation (Eq. 7) for a harmonic motion of frequency  $\omega$  is given by:

$$u(z,t) = Ee^{i(kz+\omega t)} + Fe^{-i(kz-\omega t)}, \quad (8)$$

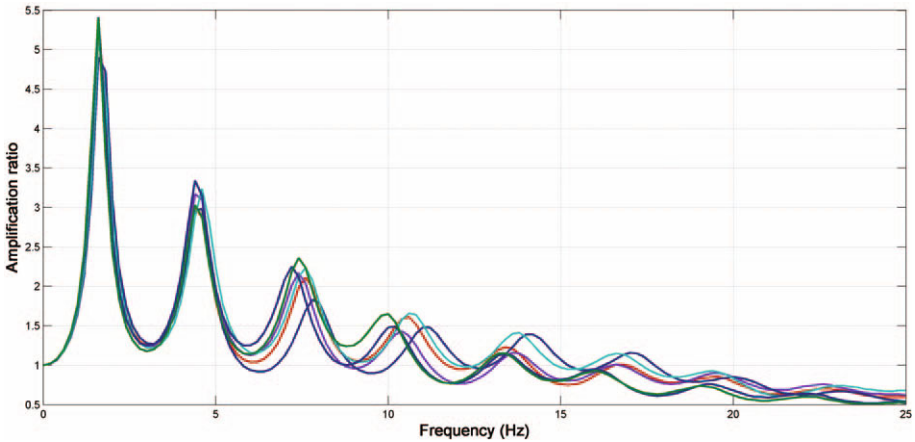


Fig. 7. Frequency response functions of sample of six soil profiles in Imphal city.

where the first term represents the incident wave travelling in the negative  $z$  direction (upwards) and the second term represents the reflected wave travelling in the positive  $z$  direction (downwards).

The frequency response functions (FRF) are defined as the ratio of acceleration at the ground surface, computed through SHAKE-91, to the acceleration at the bedrock level; for 6 sites the soil profiles are shown in Fig. 7. It can be seen that the maximum amplitude occurred in the range of 1-3 Hz, which corresponds to the range of the first natural frequency of the soil deposits, respectively, and the same is observed for almost all the sites present in the Imphal city.

## 7. SITE COEFFICIENT DETERMINATION

The above analysis gives an idea about the amplification of ground motion in Imphal city. To make it simpler for estimating the site response in Imphal city for application purpose, the soil sites in Imphal are modeled in terms of seismic site coefficients defined as the ratio of surface level response to rock level response at different periods, as shown below.

$$F_s = \frac{\text{surface level response}}{\text{rock level response}} = \frac{S_r}{r_{br}} \quad (9)$$

For each site, site response analysis has been performed using Idriss and Sun (1992) procedure for all the 700 time histories and correspondingly 700  $F_s$  values were estimated for one site for all periods of engineering interest (PGA to 3.0 s). Then, making use of statistical regression, single site coefficient for all periods has been estimated for the site. Similar procedure has

been chosen for all other sites, with soil category of type D and E present in Imphal city.

In this study, the reference site is taken as B type rock site ( $760 \text{ m/s} < V_s < 1500 \text{ m/s}$ ) found as hillock in Imphal (*e.g.*, Chingmirong, Langol hill). The 700 response spectra were established for each of the two soil categories (D, E type) present in Imphal city, and the site coefficients at various selected periods were calculated. As the site coefficient ( $F_s$ ) is not a constant value (varies with rock level motion) for a particular site, regression analysis has been used to obtain an empirical relation of the form  $\ln(F_s) = a_1 r_{br} + a_2 + \delta$  between site coefficient ( $F_s$ ) and rock level motion  $r_{br}$ , where  $a_1$  and  $a_2$  are regression coefficients and  $\delta$  is the standard deviation. The distribution of  $F_s$  corresponding to zero natural periods is plotted with respect to the corresponding bedrock, as shown in Figs. 8 and 9. Similarly, regression analysis has been performed for various natural periods (*i.e.*, PGA of 0.04, 0.1, 0.2, 0.4, 1, 2, and 3 s) and the variations of  $a_1$ ,  $a_2$  and standard deviation are estimated at zero period, at PGA of 0.3 and 1.0 s, respectively. For two typical

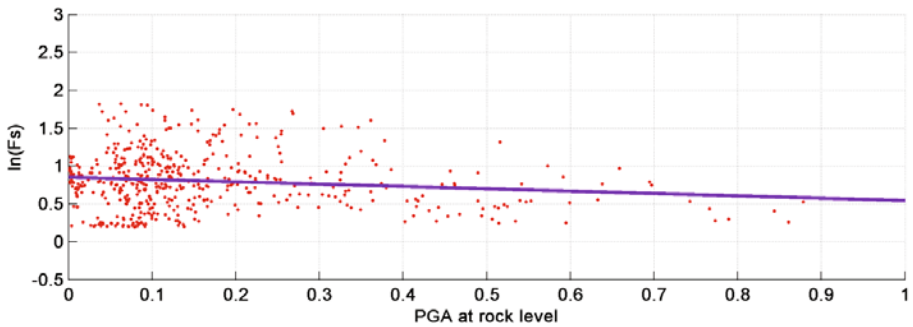


Fig. 8. Site coefficients for surface level ground motion corresponding to zero period for D type soil.

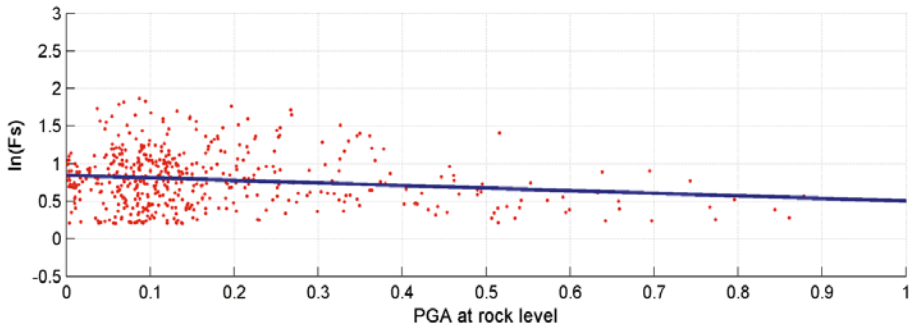


Fig. 9. Site coefficients for surface level ground motion corresponding to zero period for E type soil.

types of sites present in Imphal city, *viz.*, D and E types, the values of  $a_1$ ,  $a_2$ , and  $\delta$  are shown in Table 2. These values can be used to compute the surface level response at different periods. Further Figs. 9a-c show the spatial variation of  $a_1$ ,  $a_2$ , and standard deviation in Imphal city at PGA. Using  $a_1$ ,  $a_2$ , and  $\delta$  values, it is possible to obtain surface level spectral acceleration by using Eq. 10.

Table 2

Regression coefficients for typical D and E types

Period	$F_s$ for D type site			$F_s$ for E type site		
	$a_1$	$a_2$	$\delta$	$a_1$	$a_2$	$\delta$
0.0100	-0.1940	0.4384	0.1464	-0.5714	0.4851	0.1498
0.0300	-0.1398	0.4327	0.1484	-0.5579	0.4863	0.1501
0.0400	-0.2025	0.4393	0.1464	-0.5715	0.4852	0.1498
0.1000	-0.3108	0.4306	0.1307	-0.8697	0.4581	0.1555
0.2000	-0.3276	0.5779	0.1342	-0.5310	0.4622	0.1282
0.3000	-0.0428	0.3422	0.1239	-0.4141	0.5727	0.1154
0.4000	-0.1490	0.4407	0.1243	-0.3084	0.4232	0.1298
1.0000	0.3080	0.3801	0.1143	-0.0558	0.6763	0.1804
2.0000	0.0607	0.1618	0.1180	0.3532	0.2332	0.1546
3.0000	-0.2362	0.1652	0.1347	-0.0951	0.1950	0.1681

Table 3

Average regression coefficients for D and E types soils

Period	$F_s$ for D type			$F_s$ for E type		
	$a_1$	$a_2$	$\delta$	$a_1$	$a_2$	$\delta$
0.0100	-0.3065	0.5651	0.1913	-0.6254	0.6784	0.2204
0.0300	-0.2830	0.5648	0.1933	-0.6182	0.6800	0.2223
0.0400	-0.3075	0.5652	0.1913	-0.6254	0.6784	0.2204
0.1000	-0.5640	0.5413	0.1767	-0.7886	0.6379	0.2047
0.2000	-0.6609	0.6308	0.1677	-0.7639	0.7343	0.2143
0.3000	-0.1006	0.5635	0.1735	-0.3020	0.6205	0.2009
0.4000	-0.1627	0.6066	0.1598	-0.4191	0.7035	0.2041
1.0000	-0.3406	0.4341	0.1569	+0.0833	0.6157	0.2058
2.0000	-0.1430	0.1840	0.1478	+0.0837	0.2437	0.2082
3.0000	-0.2193	0.1848	0.1652	-0.3011	0.2249	0.1927

$$S_r = r_{br} F_s . \quad (10)$$

The average values of  $a_1$ ,  $a_2$ , and  $\delta$  of all the sites, typically composed of two types of soil, *i.e.*, D and E, are presented in Table 3. This table may serve as a quick reference for using the site coefficients of soils of categories D and E, present in Imphal city.

## 8. PROBABILISTIC SEISMIC HAZARD

The present methodology of PSHA follows those proposed by Cornell (1968) and Algermissen *et al.* (1982) and is based on the following four steps: (i) identification of sources, (ii) assessment of earthquake recurrence and magnitude distribution, (iii) selection of attenuation model for ground motion, and (iv) calculation of seismic hazard. Details of PSHA methodology adopted here have been published by the authors elsewhere (see Pallav *et al.* 2012) and are not repeated here. As Imphal city lies in the Imphal East District of Manipur state, seismic hazard curves for Imphal city at rock level have been taken to be same as that of Imphal East District (see Pallav *et al.*

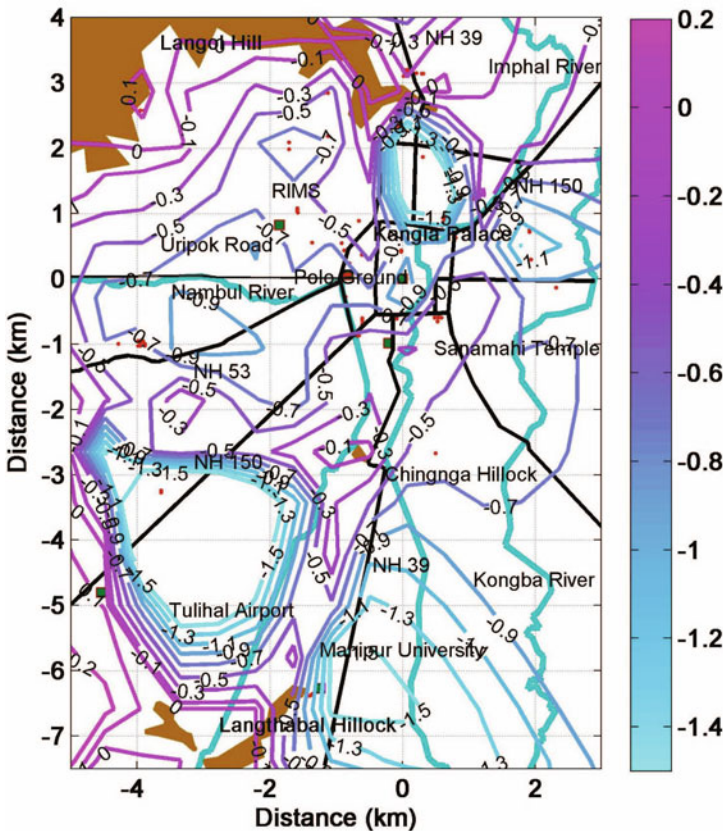


Fig. 10a. Coefficient  $a_1$  at PGA in Imphal city (5% damping).

2012, for estimation of seismic hazard curves for Imphal East District) and are shown in Figs. 10a-c. It shows the seismic hazard curves for PGA at rock level obtained by means of the above-mentioned method along with the individual contributions of the seven zones. It can be seen from Fig. 11 that the hazard at Imphal is mainly controlled by IBR and SP. The contributions from other zones (EH, BB, MT, AV) are relatively low, and this may be attributed to their location at larger distances. Further on, total hazard curves are also plotted for time periods of engineering interest (*e.g.*, 0.04, 0.1, 0.2, 0.4, 1, 2, 3 s; Fig. 12). Figure 13 shows UHRS for Imphal city at standard return periods of  $\sim 500$  and  $\sim 2500$  years, as suggested by IBC-2006. Based on the comparison with spectral acceleration ( $S_a$ ) values recommended by IS-1893 (2002) (as most of the building design are performed using this code), it can be seen that IS code overestimates the values and is on conservative side for periods from 0.2 to 0.7 s, whilst for long period ( $> 1.0$  s) the IS-1893 (2002)  $S_a$  values are on the lower side.

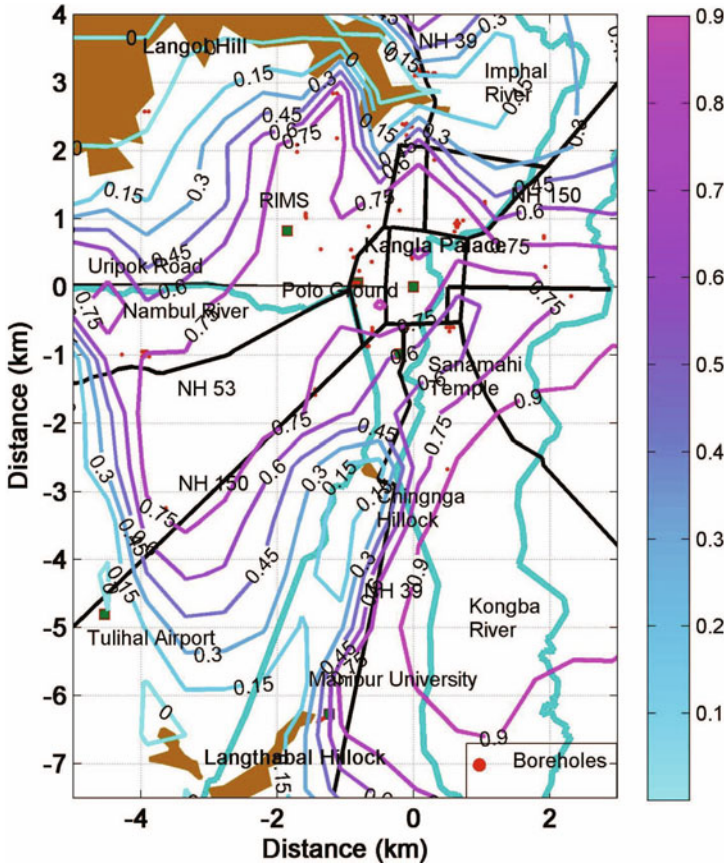


Fig. 10b. Coefficient  $a_2$  at PGA in Imphal city (5% damping).

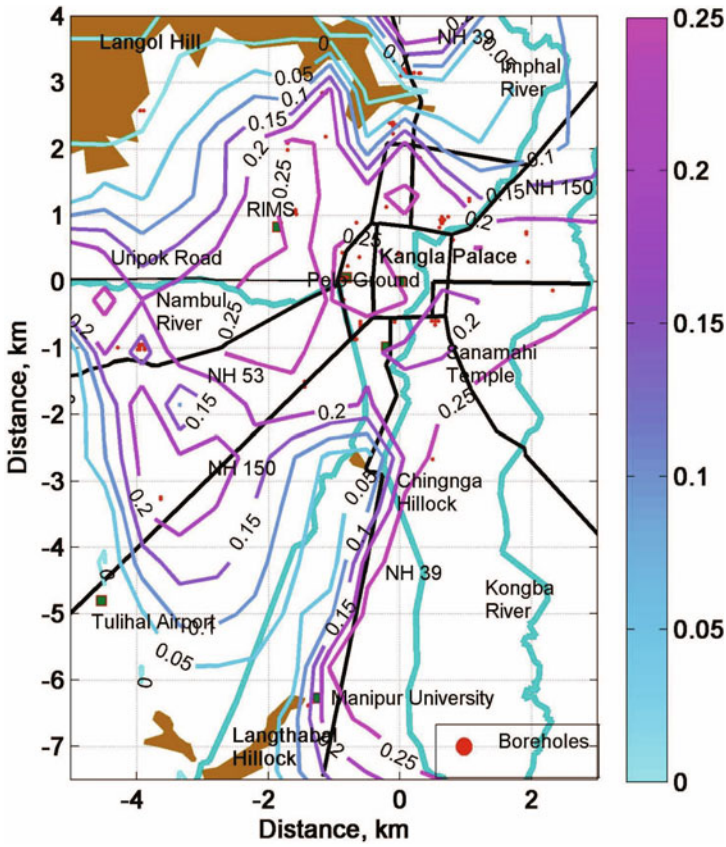


Fig. 10c. Standard deviation at PGA in Imphal city (5% damping).

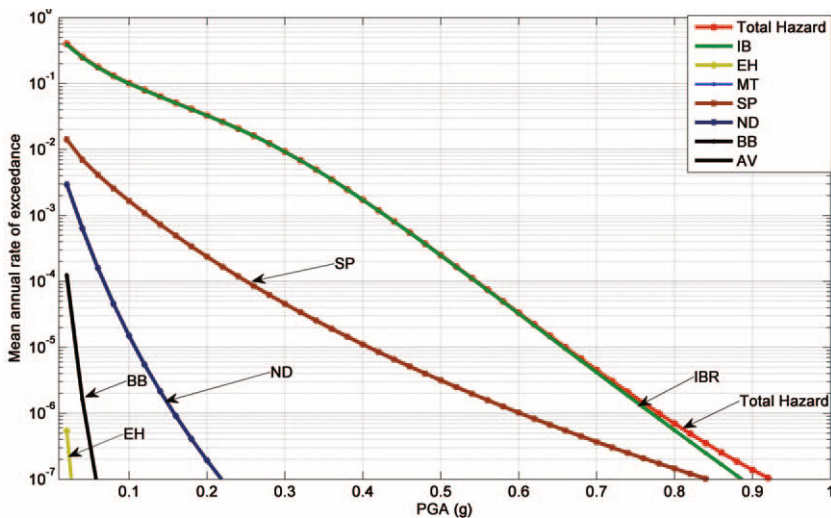


Fig. 11. Seismic hazard curves for Imphal city at rock level.

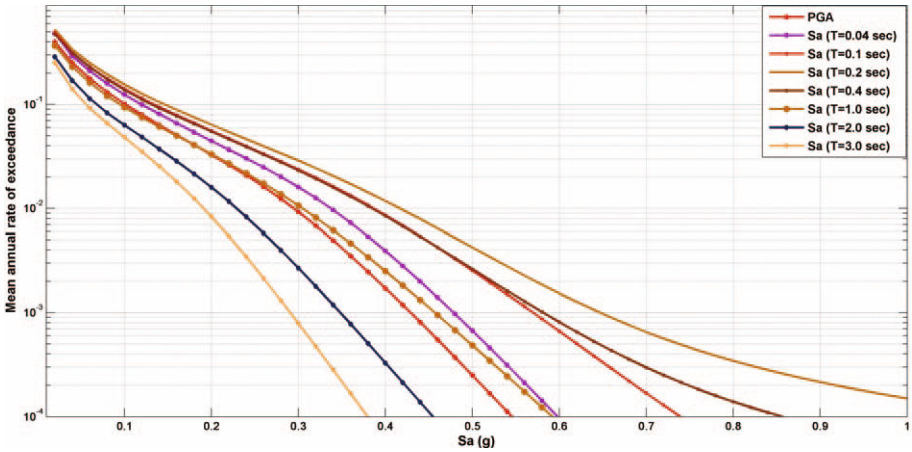


Fig. 12. Seismic hazard curves for Imphal city at rock level for all eight frequencies.

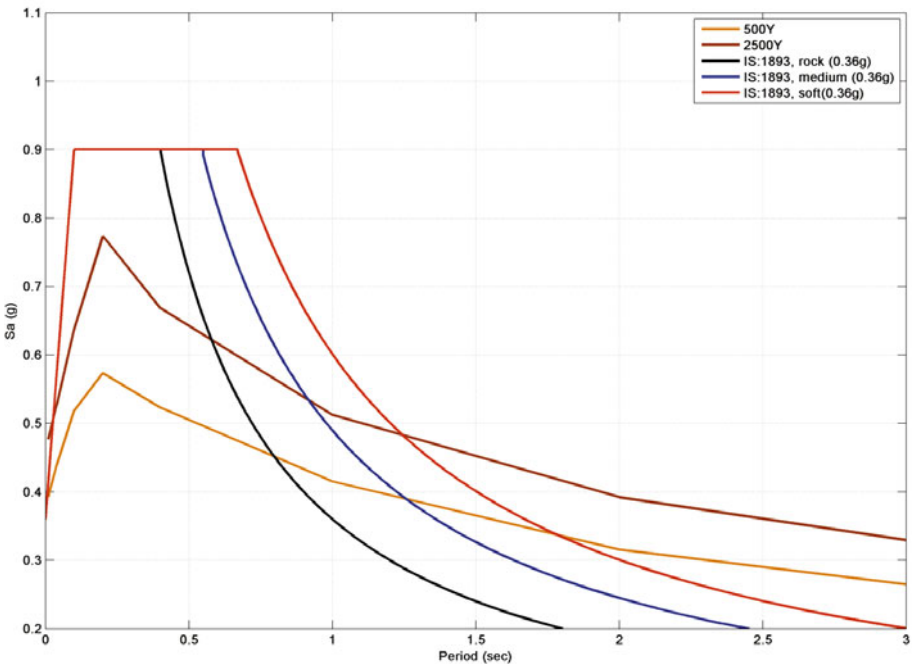


Fig. 13. Comparison of IS-1893 with Uniform Hazard Response Spectra for ~500 and ~2500 year return periods at rock level.

**9. SURFACE LEVEL HAZARD MAP FOR IMPHAL CITY**

The surface level ground motion has been estimated for ~500 and ~2500 years return period at Imphal city using  $F_s$ . Here, the UHRS computed at rock level have been multiplied by  $F_s$  estimated at different periods for all

122 sites in Imphal city. The results are shown in Figs. 14a-c in the form of contour plots at PGA of 0.3 and 1.0 s for  $\sim 500$  and  $\sim 2500$  year return periods with 5% damping, as suggested by IBC-2006.

Figure 14a shows the variation of spectral acceleration at PGA for  $\sim 500$  year return period at Imphal city. The maximum  $S_a$  value attained is 0.8 g

near the Polo Ground, whereas for short period (0.3 s) and long period (1.0 s) the  $S_a$  maximum values observed near the Polo Ground and Kangla Palace are 1.2 and 0.9 g, respectively (Figs. 14b-c). Further, it can be seen that at these locations  $S_a$  exceeds the value of 0.36 g/2 given in IS-1893 (2002), hence the structures designed using the IS-1893 recommended value are vulnerable.

Figure 14b shows short period spectral acceleration variation for 0.3 s time period with return period of  $\sim 500$  years. Almost entire Imphal city is vulnerable to seismic hazard ( $S_a > 0.36$  g/2). In Kangla Palace, Polo Ground, RIMS and Sanamah Temple areas, spectral acceleration values reach around

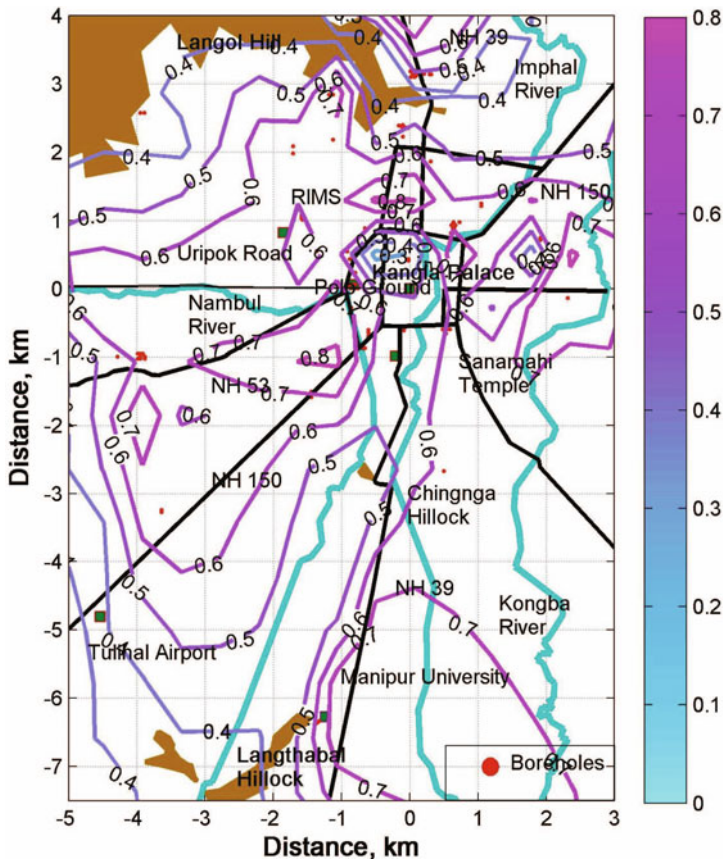


Fig. 14a. PGA contours with 10% probability of exceedence in 50 years (return period  $\sim 500$  years) over Imphal city (5% damping).

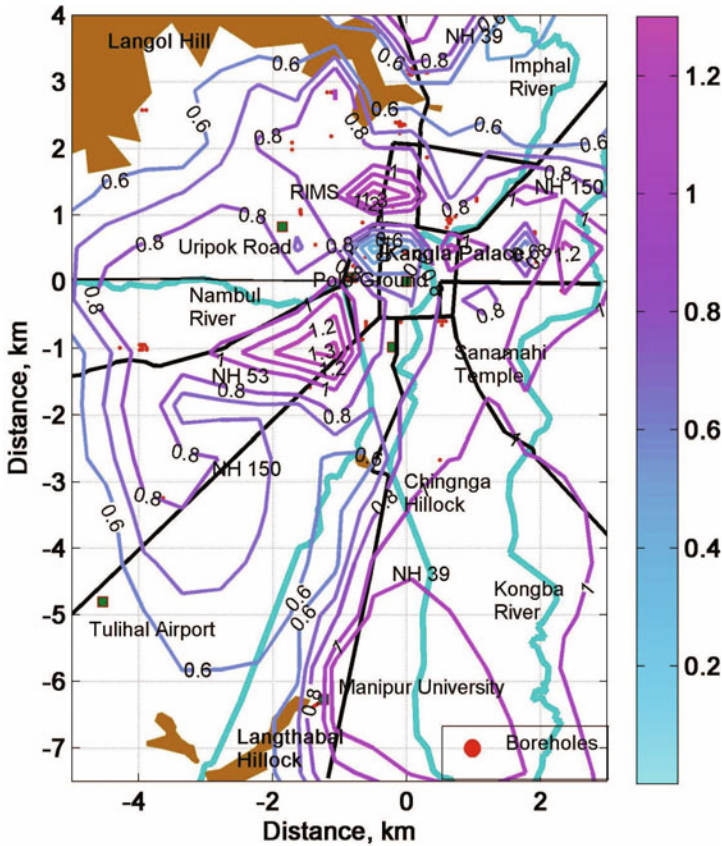


Fig. 14b. Short period spectral acceleration at 0.3 s with return period of ~500 years city over Imphal city (5% damping).

0.8 to 1.2 g. However, at the outskirts of Imphal city, *i.e.*, near east of Langol hill, Langthabal hill, and Tulihal airport, the spectral acceleration varies between 0.6 and 0.8 g. Variation of long period spectral acceleration for ~500 year return period at 1.0 s is shown in Fig. 14c. The maximum value (*i.e.*, 1.0 g) of spectral acceleration is observed near the Polo Ground and Kangla Palace area.

It may be mentioned that although in most of the codes a lesser amplification is suggested at longer periods (as compared to shorter periods), there are reports in the literature (Bazzurro and Cornell 2004, Wang *et al.* 2006) where soil gets amplified at long periods. The reason behind such amplification in the present case may be due soft soil deposits and presence of high water table level in the Kangla Palace area, *etc.*

Contours maps have also been plotted for 2500 year return periods at PGA, 0.3 and 1.0 s (Figs. 14a-c). From Fig. 15a, it can be observed that the maximum value of  $S_a$  (0.5 g) is observed near Kangla Palace area, whereas

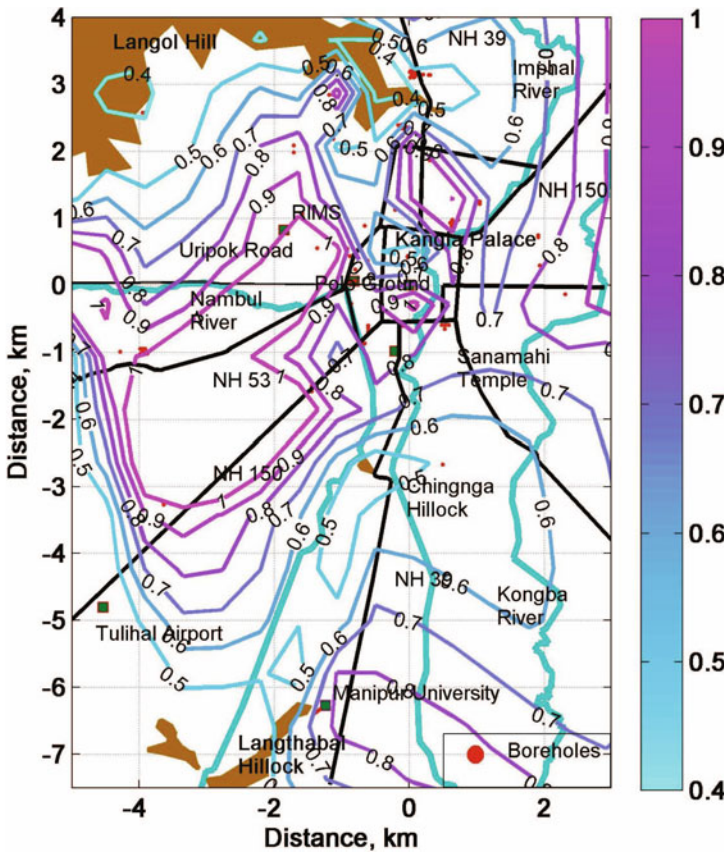


Fig. 14c. Long period spectral acceleration at 1.0 s with return period of ~500 years over Imphal city (5% damping).

at nearby locations, *i.e.*, Polo Ground area, there is a drastic increase in the  $S_a$  value to 0.9 g.

Figure 15b shows short-period spectral acceleration variation at surface level at time period of 0.3 s in Imphal city, for 2500 year return period. It can be seen that maximum value of  $S_a$  attained is 1.6 g near Polo Ground and towards north of Kangla Palace areas. Long period spectral acceleration variation for 1.0 s time period has been shown in Fig. 15c for 2500 year return period. Maximum  $S_a$  value (1.2 g) has been observed at RIMS, near Nambul river and NH-150 area (Fig. 15c).

Surface level response spectra are plotted for all 122 sites for ~500 and ~2500 year return periods in Figs. 16 and 17, respectively. It can be seen that at almost all the 122 sites the amplifications of rock level ground motion have been observed at surface levels. Comparing the present results with  $S_a$  recommended by IS-1893 (2002) it can be found that the IS-1893 underestimates the spectra acceleration value at many locations in Imphal city, which

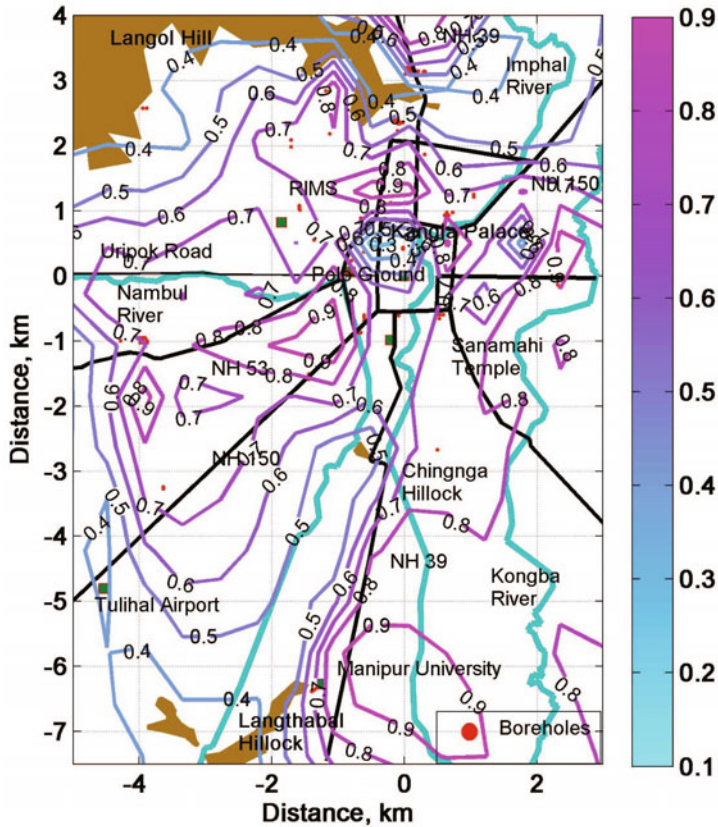


Fig. 15a. PGA contours with 2% probability of exceedance in 50 years (return period ~2500 years) over Imphal city (5% damping).

is quite a threat to this city from future hazard due to earthquake. It has been seen that the predicted mean surface level UHRS (for ~500 return period) overestimate the  $S_a$  recommended by IS-1893 at longer period ( $> 1.0$  s), whereas for periods greater than 0.2 s, the IS-1893 (2002)  $S_a$  values are underestimated for ~2500 return period.

## 10. CONCLUSIONS

Effect of near surface soil layer on seismic susceptibility of Imphal city with respect to synthetically generated 700 earthquake samples ranging in  $M_w$  from 5.0 to 8.5 has been presented in terms of  $F_s$ . Soil data collected from 122 boreholes located in Imphal city have been used as inputs in the equivalent linear site response analysis (Idriss and Sun 1992), and surface level responses were simulated for all scenario earthquakes. The shear wave velocity ( $V_s$ ) has been obtained from SPT-N values through an empirical relation proposed by Imai and Tonouchi (1982). For each site, site response

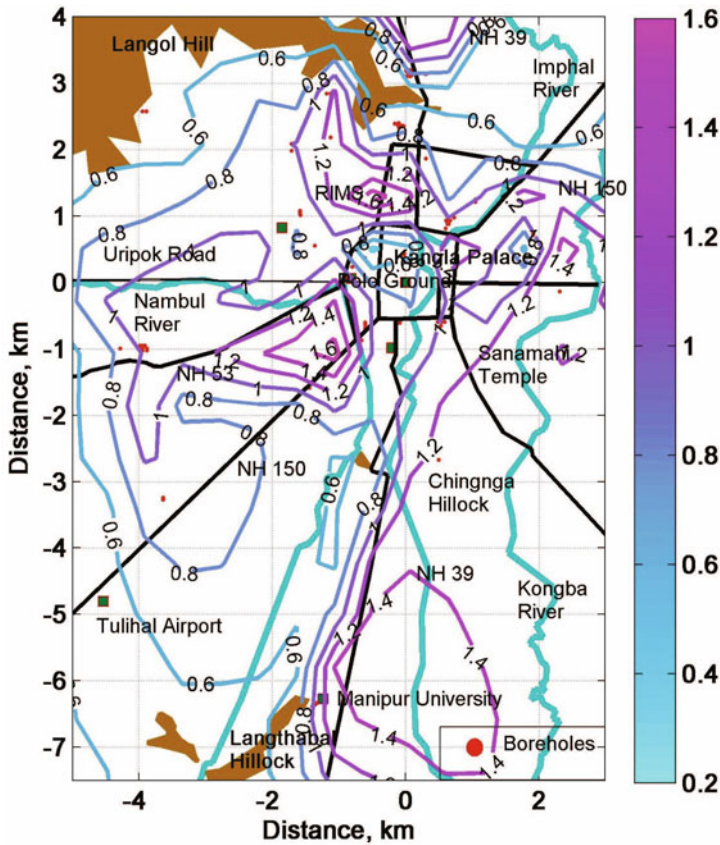


Fig. 15b. Short period spectral acceleration at 0.3 s with return period of ~2500 years over Imphal city (5% damping).

analysis (through SHAKE-91) has been performed for all 700 time-histories and correspondingly 700 site coefficients were estimated for one site for all periods of engineering interest (PGA to 3.0 s) and by statistical regression, single seismic site coefficient were developed.  $F_s$  developed in the present study have been computed at different periods of engineering purposes and these can be used for estimating surface level responses if one can know the rock level response through Eq. 3.

The present article investigates surface level ground motion using site coefficients at Imphal city using Probabilistic Seismic Hazard Analysis (PSHA). The PSHA study has been performed by incorporating site coefficients to assess the ground motion induced by potential seven seismic zones present around Imphal. Seismic hazard curves are obtained for Imphal city. Further, UHRS results are presented for 2 and 10% probability of exceedance in 50 year (~2500 and ~500 year) return period. It is observed that for ~500 and ~2500 year return periods, the Kangle Palace, Polo

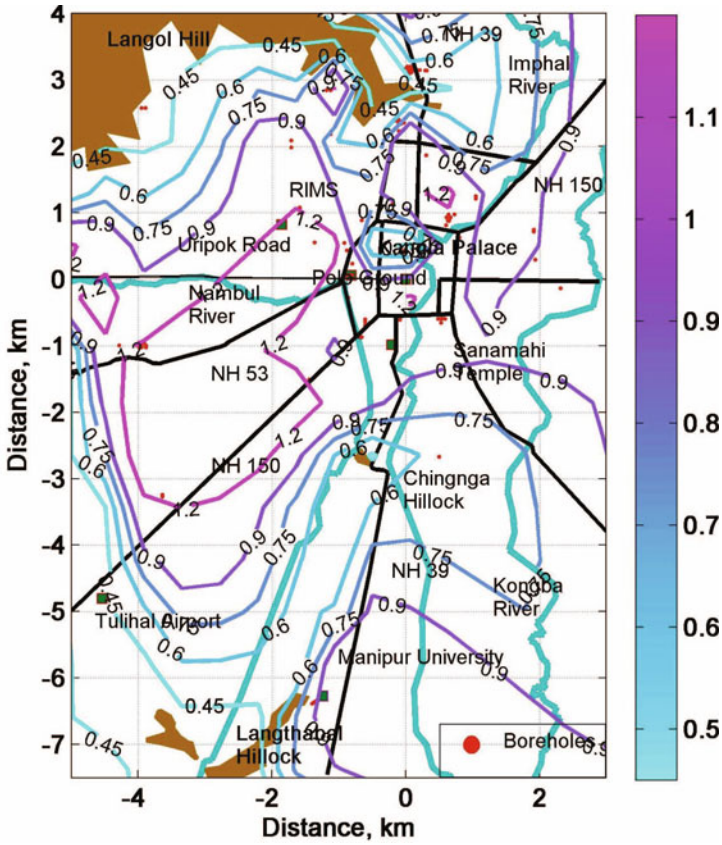


Fig. 15c. Long period spectral acceleration at 1.0 s with return period of ~2500 years over Imphal city (5% damping).

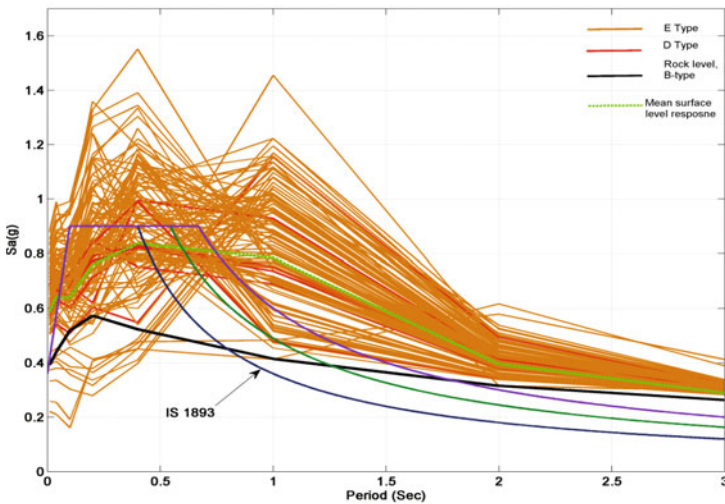


Fig. 16. Surface level response spectra for ~500 year return period for all sites in Imphal city (5% damping).

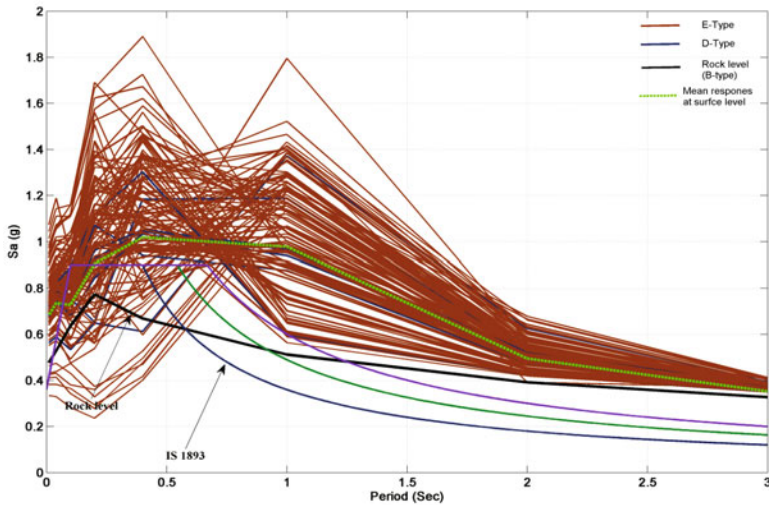


Fig. 17. Surface level response spectra for ~2500 year return period for all sites in Imphal city (5% damping).

Ground RIMS, and near Nambul river areas of Imphal city are vulnerable. Furthermore, the predicted mean surface level response spectra were found to be higher (for longer periods, *i.e.*, > 1.0 s) for ~500 year return period, and lower for periods shorter than 0.2 s (for ~2500 return period) than the spectral acceleration values recommended by IS-1893 (2002).

**Acknowledgement.** We thank the anonymous reviewers for their valuable comments which helped us to improve the quality of the manuscript.

## References

- Algermissen, S.T., D.M. Perkins, P.C. Thenhaus, S.L. Hanson, and B.L. Bender (1982), Probabilistic estimates of maximum acceleration and velocity in rock in the contiguous United States, Open-file report 82-1033, United States Department of the Interior, Geological Survey, Washington, D.C., USA, 99 pp.
- Anderson, J.G., and S.E. Hough (1984), A model for the shape of the Fourier amplitude spectrum of acceleration at high frequencies, *Bull. Seismol. Soc. Am.* **74**, 5, 1969-1993.
- Bazzurro, P., and C.A. Cornell (2004), Ground-motion amplification in nonlinear soil sites with uncertain properties, *Bull. Seismol. Soc. Am.* **94**, 6, 2090-2109, DOI: 10.1785/0120030215.

- Boore, D.M. (1983), Stochastic simulation of high-frequency ground motions based on seismological models of the radiated spectra, *Bull. Seismol. Soc. Am.* **73**, 6A, 1865-1894.
- Boore, D.M., and G.M. Atkinson (1987), Stochastic prediction of ground motion and spectral response parameters at hard-rock sites in eastern North America, *Bull. Seismol. Soc. Am.* **77**, 2, 440-467.
- Brunschweiler, R.O. (1974), Indoburman ranges. **In:** A.M. Spenceer (ed.), *Mesozoic-Cenozoic Orogenic Belts: Data for Orogenic Studies*, Special Publ., Vol. 4, Scottish Academic Press Ltd for the Geological Society, London, 279-299.
- BSSC (1995), *1994 Edition – NEHRP Recommended Provisions for Seismic Regulations for New Buildings. Part 1 – Provisions (FEMA 222A)*, Building Seismic Safety Council, Washington, DC.
- Cornell, C.A. (1968), Engineering seismic risk analysis, *Bull. Seismol. Soc. Am.* **58**, 5, 1583-1606.
- Goswami, H.C., and S.K. Sarmah (1982), Probabilistic earthquake expectancy in the northeast Indian region, *Bull. Seismol. Soc. Am.* **72**, 3, 999-1009.
- GSI (2000), *Seismotectonic Atlas of India and its Environs*, Geological Survey of India, Calcutta, 86 pp.
- Haokip, S.N. (2007), *Basine Delineation Map of Manipur. Profile on State of Environment Report of Manipur*, Ministry of Environment and Forests, Manipur, India, 4 pp.
- Hwang, H.H.M., H. Lin, and J.R. Huo (1997), Site coefficients for design of buildings in eastern United States, *Soil Dyn. Earthq. Eng.* **16**, 1, 29-40, DOI: 10.1016/S0267-7261(96)00031-0.
- IBC-2006 (2006), *International Building Code 2006 Edition*, International Code Council.
- Ibotombi, S. (2000), Structural and tectonic framework of Manipur. **In:** *Manipur Science Congress, Manipur University, Imphal, India*.
- Idriss, I.M., and J.I. Sun (1992), SHAKE-91: A computer program for conducting equivalent linear seismic response analyses of horizontally layered soil deposits, Center for Geotechnical Modeling, Department of Civil and Environmental Engineering, University of California, Davis, USA.
- Imai, T., and K. Tonouchi (1982), Correlation of N-value with S-wave velocity and shear modulus. **In:** *Proc. 2nd European Symposium on Penetration Testing, May 1982, Amsterdam, The Netherlands*, 57-72.
- IS-1893 (2002), *Criteria for earthquake resistant design of structures. Part 1 – General provisions and buildings*, 5th revision, Bureau of Indian Standards, New Delhi, India.
- Laiba, M.T. (1992), *The Geography of Manipur*, Public Book Store, Imphal.
- Martin, G.R., and R. Dobry (1994), Earthquake site response and seismic code provisions, *NCEER Bull.* **8**, 4, 121-129.

- MASTEC (2007), Final report on water harvesting and water conservation in Imphal East I Block, Imphal East District, Manipur, Manipur Science and Technology Council, Imphal, India, 90 pp., <http://mastec.nic.in/mastec/report%20water%20harvesting.pdf>.
- Motazedian, D., and G.M. Atkinson (2005), Stochastic finite-fault modeling based on a dynamic corner frequency, *Bull. Seismol. Soc. Am.* **95**, 3, 995-1010, DOI: 10.1785/0120030207.
- Nandy, D.R. (2001), *Geodynamics of Northeastern India and the Adjoining Region*, ACB Publications, Kolkata, 209 pp.
- Pallav, K., S.T.G. Raghukanth, and K.D. Singh (2010), Surface level ground motion estimation for 1869 Cachar earthquake (Mw 7.5) at Imphal city, *J. Geophys. Eng.* **7**, 3, 321-331, DOI: 10.1088/1742-2132/7/3/010.
- Pallav, K., S.T.G. Raghukanth, and K.D. Singh (2012), Probabilistic seismic hazard estimation of Manipur, India, *J. Geophys. Eng.* **9**, 5, 516-533, DOI: 10.1088/1742-2132/9/5/516.
- Park, D., and Y.M.A. Hashash (2005), Evaluation of seismic site factors in the Mississippi Embayment. II. Probabilistic seismic hazard analysis with nonlinear site effects, *Soil Dyn. Earthq. Eng.* **25**, 2, 145-156, DOI: 10.1016/j.soildyn.2004.10.003.
- PTI (2010), Rail link from Manipur to Vietnam on cards: Tharoor, Press Trust of India, April 9, <http://timesofindia.indiatimes.com/india/Rail-link-from-Manipur-to-Vietnam-on-cards-Tharoor/articleshow/5778641.cms>.
- Raghukanth, S.T.G., and S.N. Somala (2009), Modeling of strong-motion data in northeastern India: Q, stress drop, and site amplification, *Bull. Seismol. Soc. Am.* **99**, 2A, 705-725, DOI: 10.1785/0120080025.
- Raghukanth, S.T.G., K.D. Singh, and K. Pallav (2009), Deterministic seismic scenarios of Imphal City, *Pure Appl. Geophys.* **166**, 4, 641-672, DOI: 10.1007/s00024-009-0460-y.
- Schnabel, P.B., J. Lysmer, and H.B. Seed (1972), SHAKE – a computer program for earthquake response analysis of horizontally layered sites, Report No. EERC-72/12, University of California, Berkeley, USA.
- Singh, R.K.H. (2004), Tectonic significance of minor structures of the rocks of Imphal Valley, Ph.D. Thesis, Manipur University, Imphal, India.
- Vucetic, M., and R. Dobry (1991), Effect of soil plasticity on cyclic response, *J. Geotech. Eng.* **117**, 1, 89-107, DOI: 10.1061/(ASCE)0733-9410(1991)117:1(89).
- Wang, K., Q.F. Chen, S. Sun, and A. Wang (2006), Predicting the 1975 Haicheng earthquake, *Bull. Seismol. Soc. Am.* **96**, 3, 757-795, DOI: 10.1785/0120050191.

Received 17 April 2014

Received in revised form 16 October 2014

Accepted 28 October 2014



## **Numerical Simulation of Response Characteristics of Audio-magnetotelluric for Gas Hydrate in the Qilian Mountain Permafrost, China**

Kun XIAO<sup>1,2</sup>, Changchun ZOU<sup>2</sup>, Changqing YU<sup>3</sup>, and Jinyun PI<sup>3</sup>

<sup>1</sup>School of Nuclear Engineering and Geophysics, East China University of Technology, Nanchang, People's Republic of China

<sup>2</sup>School of Geophysics and Information Technology, China University of Geosciences (Beijing), Beijing, People's Republic of China;  
e-mail: xiaokun0626@163.com (corresponding author)

<sup>3</sup>Institute of Geology, Chinese Academy of Geological Sciences, Beijing, People's Republic of China

### **A b s t r a c t**

Audio-magnetotelluric (AMT) method is a kind of frequency-domain sounding technique, which can be applied to gas hydrate prospecting and assessments in the permafrost region due to its high frequency band. Based on the geological conditions of gas hydrate reservoir in the Qilian Mountain permafrost, by establishing high-resistance abnormal model for gas hydrate and carrying out numerical simulation using finite element method (FEM) and nonlinear conjugate gradient (NLCG) method, this paper analyzed the application range of AMT method and the best acquisition parameters setting scheme. When porosity of gas hydrate reservoir is less than 5%, gas hydrate saturation is greater than 70%, occurrence scale is less than 50 m, or bury depth is greater than 500 m, AMT technique cannot identify and delineate the favorable gas hydrate reservoir. Survey line should be more than twice the length of probable occurrence scale, while tripling the length will make the best result. The number of stations should be no less than 6, and 11

stations are optimal. At the high frequency section (10~1000 Hz), there should be no less than 3 frequency points, 4 being the best number.

**Key words:** Qilian Mountain permafrost, gas hydrate, AMT, response characteristic, numerical simulation.

## 1. INTRODUCTION

Gas hydrate is a solid crystal with cage structure consisting of water molecules and natural gas (mainly CH<sub>4</sub>), which mainly exists in the terrestrial permafrost regions and beneath the sea along the outer continental margins of the world's oceans (Sloan 1998). In permafrost regions, gas hydrates may exist at subsurface depths ranging from about 130 to 2000 m (Collett 2002, Collett *et al.* 2011, Lu *et al.* 2011). Gas hydrates in offshore continental margins have been mapped at depths below the sea floor ranging from about 100 to 1100 m (Collett 2002, Dickens 2001, Huo and Zhang 2009, Xiao *et al.* 2013, Yang *et al.* 2014). As a new clean alternative energy source of huge reserve, gas hydrates have attracted more and more attention, and more than 100 regions have directly or indirectly found the occurrence zones (Boswell and Collett 2011, Moridis *et al.* 2011). In November 2008, gas hydrate samples were recovered in the Qilian Mountain permafrost, Qinghai Province of China (Zhu *et al.* 2010, Lu *et al.* 2011). This is the first discovery of gas hydrate in China's permafrost and in the low-middle latitude permafrost of the world. The Qilian Mountain permafrost region may be the most promising strategic area for gas hydrate (Wang 2010, Zhao *et al.* 2013).

In recent years, in order to further optimize the promising areas of gas hydrate, and to provide support for drilling deployment to explore gas hydrate, gas hydrate AMT sounding project has been launched. Field data acquisition and indoor data processing have been underway. AMT survey has already displayed its unusual advantages in prospecting for metal ore, terrestrial heat and geological structures (Schnegg *et al.* 1983, Clerc *et al.* 1984, Bronner and Fournon 1992, Ogawa *et al.* 1994, Balyavskii and Sukhoi 2004, Santos *et al.* 2006, 2007; Strangway *et al.* 1973, Yamaguchi *et al.* 2010, Abdelzaher *et al.* 2011). However, because research on the gas hydrate in the permafrost region in our country has been at its very early stage, the AMT method is rarely used to prospect for gas hydrates and few related reports come into sight. Determining appropriate survey line length, station spacing and the number of frequency points which must be considered in the field data acquisition, will be convenient to indoor AMT data processing and interpretation. Generally, more stations can bring abundant information for indoor data interpretation, while human and financial investments increase correspondingly, which may reduce the efficiency of field data acquisition. As a result, how to realize an efficient field data acquisition with reasonable

cost is a problem to be solved urgently. Due to the different occurrences of gas hydrate in the Qilian Mountain permafrost region, resistivity, occurrence scale, and bury depth of gas hydrate vary a lot, and the corresponding AMT response modes are unclear, making data processing and interpretation difficult. Therefore, in order to provide some technical support for the gas hydrate prospecting, it is necessary to carry out numerical simulation on AMT response characteristics of different gas hydrate reservoirs.

Based on the geological conditions of gas hydrate in the Qilian Mountain permafrost, by establishing high-resistivity anomaly model for gas hydrate and carrying out forward modeling with finite element method, this paper obtained the AMT response characteristics of the corresponding models. By further analyzing the response characteristics of different gas hydrate reservoirs, application range of AMT method was attained. Nonlinear conjugate gradient method (NLCG) was used to simulate AMT response characteristics under the conditions of different acquisition parameters, including survey line length, station spacing, and number of frequency points. Through comparing and analyzing the differences of response characteristics resulted from different acquisition parameters, an acquisition parameter setting scheme in favor of prospecting gas hydrate reservoir in the study area was obtained.

## 2. GEOLOGICAL SETTING

### 2.1 Geotectonics and stratigraphic characteristics

Qilian Mountain is located in the northeastern part of the Qinghai-Tibetan Plateau in China. Its tectonic units are usually divided into the northern Qilian belt, the middle Qilian land, and the southern Qilian belt. This area had a complex history, experiencing a continental rift stage (Sinian to Middle Cambrian), an ocean expansion and trench-arc-basin formation stage (Late Cambrian to Middle Ordovician), and an orogenic stage (thrust-down orogeny, collision orogeny, and intra-land orogeny), resulting in the present geological tectonics framework (Lu *et al.* 2011).

During the early Paleozoic era, the Qilian Mountain region was a small ocean basin between the Tsaidam block and the North China block. The Caledonian movement in the late Silurian made the ancient ocean basin close, uplift and erode. In the Carboniferous, it began to sink and become a wide shallow-sea shelf or epicontinental sea. During the Triassic, South Qilian was still a sea basin, and marine sandstone-mudstone bearing limestone deposited. At the end of Late Triassic, influenced by Indosinian movement, Paleo-Tethys Ocean completely closed, with the whole Qilian Mountains uplifting to be a land, *i.e.*, a denuded zone. Early Yanshan tectonic movements resulted in local tension of the Qilian Mountain areas. A series of inter-

mountain faulted depression basins formed, and a suite of Jurassic age fluviolacustrine coal-bearing marsh facies and other clastic sediments were deposited. Cretaceous and Tertiary strata are mainly constituted by fine-grained red clastic rocks and claystones. In the Quaternary, deposits mainly composed of glaciofluvial facies and glacial facies have been widely distributed in the basin (Fu and Zhou 1998).

The Qilian Mountain region, where permafrost conditions extend over the area of about  $10^5 \text{ km}^2$  (Li *et al.* 2012), is one of the regions with widespread permafrost. “Scientific Drilling Project of Gas Hydrate” in the Qilian mountain permafrost is located in Muli coalfield, Tianqun County, Qinghai Province of China (Fig. 1), where altitude is 4000~4300 m, the mean annual

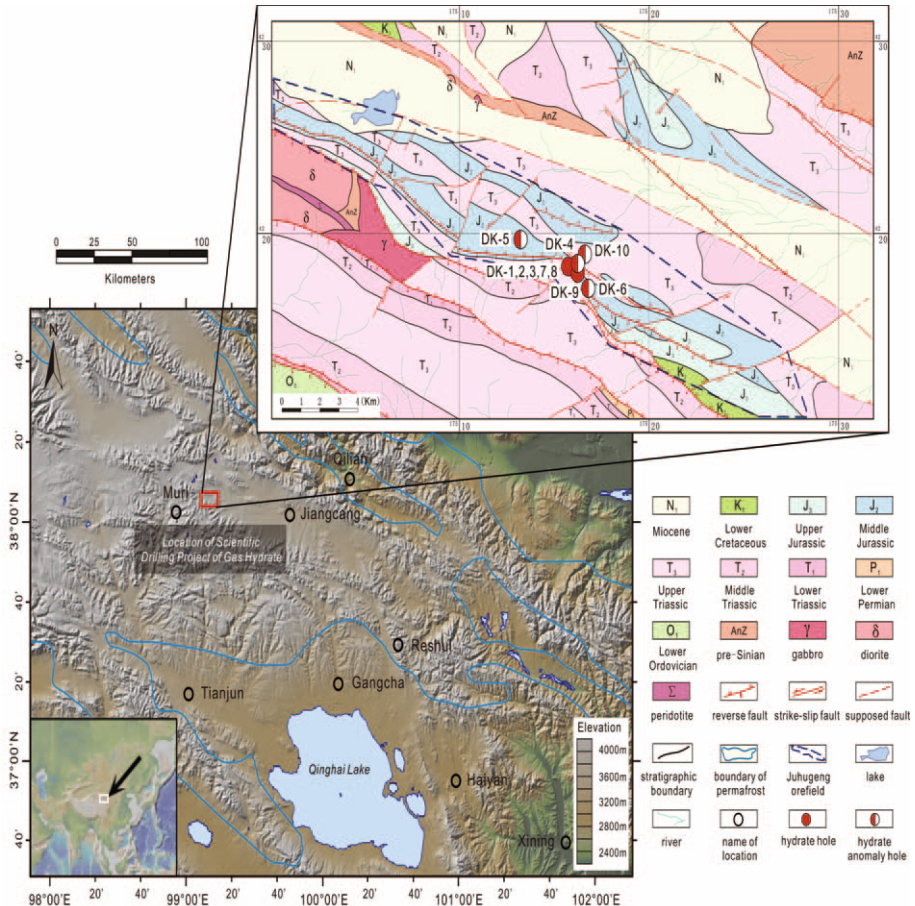


Fig. 1. The location of the Scientific Drilling Project of Gas Hydrate and the geological map for the study area in the Qilian Mountain permafrost (Ryan *et al.* 2009, Wang *et al.* 2014).

ground surface temperature is about  $-2$  to  $-2.5^{\circ}\text{C}$  (Wu *et al.* 2010). The thickness of permafrost ranges from 60 to 95 m, and in a considerable part of the region the permafrost thickness is greater than 100 m (Wu *et al.* 2010), severing as a favorable capping for gas hydrate. Except of Quaternary, Jurassic Jiangcang Formation ( $J_2j$ ) and Muli Formation ( $J_2m$ ) also expose in the study area. The two sets of strata contain multiple minable coal layers, whose coal layers occur at intervals of several to hundreds of meters below ground. The Jiangcang Formation is mainly composed of black and gray oily shale and mudstone with siltstone, fine sandstone, and middle sandstone. The Muli Formation mainly consists of gray siltstone, fine sandstone, middle sandstone, coarse sandstone, mixed with dark gray oily shale. The content of organic carbon in oily shale is 0.98~5.76% (Sun *et al.* 2014), which has achieved the standard of high-quality source rock. Oily shale has entered the post-mature phase and is a kind of favorable gas source (Lu *et al.* 2013a, b).

## 2.2 Geological characteristics of gas hydrate

In total, ten scientific drilling wells for gas hydrate, namely DK-1, DK-2, DK-3, DK-4, DK-5, DK-6, DK-7, DK-8, DK-9, and DK-10, were completed in the study area (Fig. 1). Holes where gas hydrate samples were recovered include DK-1, DK-2, DK-3, DK-7, and DK-8, while in the holes of DK-4, DK-5, DK-6, DK-9, and DK-10, only anomalies indicating the likely existence of gas hydrate were discovered. Gas hydrate in the study area can accumulate in two forms. One form of gas hydrate is of thin-bedded, flaky, lumpy shape, and occurs in the fissures of siltstone, mudstone, and oily shale. Gas hydrate of this form observed by naked eyes is milky crystals with a thickness of several millimeters. Gas hydrate of the other form distributes in the pores of siltstone and fine sandstone, and cannot be identified by naked eyes, while an obvious low temperature anomaly can be identified by infrared camera.

In the winter of 2008, the DK-1 hole was mud-fluid drilled and intermittently cored with a wire line core barrel to 182.23 m. In the summer of 2009, three holes, DK-2, DK-3, and DK-4, were drilled with low temperature mud-fluid and intermittently cored with a wire line core barrel and a splitting tube to target depths of 635.20, 765.01, and 466.65 m, respectively (Fig. 2). The four wells in the lateral areas are distributed relatively close. The distance of hole DK-2 and hole DK-3 is the nearest, and the distance is only 10 m. In the four wells, gas hydrate and its associated anomalies occur between about 115 and 396 m, beneath the permafrost (Table 1). In addition, the thickness of permafrost is about 95~115 m.

The combined information from drilling and core experiment studies shows that gas hydrates mainly occur in the Jiangcang Formation of Middle

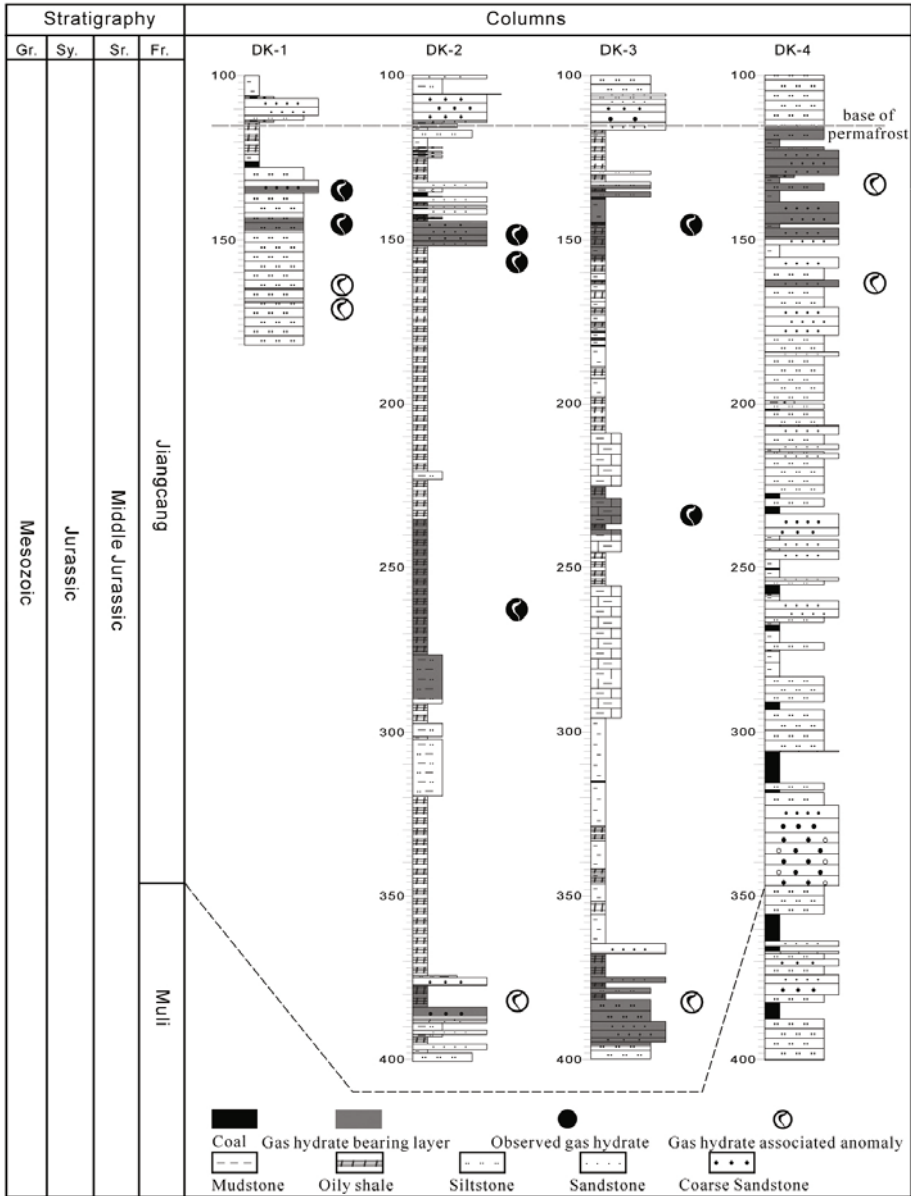


Fig. 2. Lithological columns of the DK-1 to DK-4 holes in Qilian Mountain permafrost (Lu *et al.* 2011).

Jurassic in the Muli permafrost. The porosity of the samples recovered from core data in the four wells ranges from 5 to 20%, and the gas hydrate saturation ranges from 30 to 80% (Guo and Zhu 2011, Lin *et al.* 2013). The geo-

Table 1

Gas hydrate drilling locations and its general characteristics (Lu *et al.* 2011)

Holes	Coordinates			Borehole depth [m]	Base of perma [m]	Top of GH [m]	Base of GH [m]
	Longitude [°E]	Latitude [°N]	Elevation [m]				
DK-1	4217899.114	33514986.723	4053.336	182.23	115	133.50	170.50
DK-2	4217882.361	33514977.515	4053.460	635.20	115	144.40	387.50
DK-3	4217894.413	33515000.925	4054.761	765.01	115~120	133.00	396.00
DK-4	4218130.803	33515164.170	4038.451	466.65	110~115	115.00	163.00

**Note:** GH indicates gas hydrate.

logical and occurrence characteristics indicate that gas hydrates occur in separate reservoirs below the base of permafrost. The reservoir type is considered by Boswell *et al.* (2011) and Koh *et al.* (2012) to be Type R-unique hydrate deposits within rocks. In addition, gas hydrates are distributed non-continuously in the vertical direction in each borehole, and the law of gas hydrate distribution in the lateral areas between drill holes is not apparent due to the rock fracture system that plays an important role in gas hydrate distribution (Wang *et al.* 2014).

Specific geological characteristics of gas hydrate reservoir are summarized in Table 2. Compared to gas hydrate samples of the Mackenzie Delta of Canada, gas hydrate in the Qilian Mountain permafrost can be regarded as a new-type gas hydrate characterized by a relatively shallow bury depth, thin thickness of permafrost, complex gas components, and coal-bed methane gas source, which is of scientific, economic, and environmental significance (Zhu *et al.* 2010).

Table 2

Comparison of formation properties in the Qilian Mountain and Mackenzie Delta

District Property	Mackenzie Delta (Bybee 2004, Collett 2005)	Qilian Mountain (Zhu <i>et al.</i> 2010, Lu <i>et al.</i> 2011)
Gas component	CH <sub>4</sub>	CH <sub>4</sub> , C <sub>2</sub> H <sub>6</sub> , C <sub>3</sub> H <sub>8</sub> , C <sub>4</sub> H <sub>10</sub> , CO <sub>2</sub>
Structure type	sI	sII
Stratum	Oligocene (Kugmallit, Mackenzie Bay)	Middle Jurassic (Jiangcang)
Reservoir lithology	Sandstone	Oily shale, siltstone, fine sandstone
Permafrost	Arctic	Mountain
Permafrost thickness	640 m	95 m
Buried depth	> 1000 m	133~396 m

### 3. NUMERICAL SIMULATION METHODS

The AMT numerical simulation contains two aspects, forward modeling and inversion. Methods for AMT forward modeling include finite difference method (FDM) (Mackie *et al.* 1994, Newman and Alumbaugh 1997), finite element method (FEM) (Wannamaker *et al.* 1987, De Lugão and Wannamaker 1996), and integral equation method (IEM) (Wannamaker 1991, Xiong and Trippz 1997). Two dimensional AMT forward modeling using FEM will bring some convenience in dealing with the inner boundary conditions which FDM and IEM fail to offer. What else, the coefficient matrix of FEM is positive definite, assuring the uniqueness of solution, so that FEM is an effective and universal method for forward problems. Inversion methods, which can be divided into direct inversion and indirect inversion, mainly include BOSTICK inversion, OCCAM inversion, RRI inversion, CG inversion, NLCG inversion, *etc.* (Goldberg and Rotstein 1982, Smith and Booker 1991, Constable *et al.* 1987, Hestenes 1973, Hestenes and Stiefel 1952, Rodi and Mackie 2001, Israil 2006, Spichak 2012). Among them, NLCG algorithm can avoid calculating the complete Jacobian matrix in each iteration and solving nonlinear equations of the whole model. This algorithm breaks out the framework of linear inversion, enhances the calculation efficiency, and is relatively stable in calculation. As a result, NLCG is an effective inversion method and widely applied to geophysical inversion (Newman and Alumbaugh 2000, Rodi and Mackie 2001, Hu *et al.* 2006). Based on the above analysis, in this paper we have chosen the FEM and NLCG algorithm to carry out the simulation. The followings are the basic AMT numerical simulation theories of the two algorithms.

#### 3.1 AMT forward modeling based on FEM

According to Maxwell equations, steady-state electromagnetic field equations with angular frequency  $\omega$  (time factor  $e^{-i\omega t}$ ) write (Xu 1994):

$$\nabla \times \mathbf{E} = i\omega\mu\mathbf{H} \ , \quad (1)$$

$$\nabla \times \mathbf{H} = (\sigma - i\omega\varepsilon)\mathbf{E} \ , \quad (2)$$

where  $\mathbf{E}$  is electric field intensity [V/m],  $\mathbf{H}$  is magnetic field intensity [A/m],  $\omega$ ,  $\mu$ ,  $\sigma$ , and  $\varepsilon$  are angular frequency, magnetic permeability, electrical conductivity, and dielectric constant, respectively.

Let us assume the underground to be a two-dimensional electrical structure,  $x$  axis and  $y$  axis horizontal,  $z$  axis vertical down, and  $x$  axis parallel to the structural strike direction. When plane electromagnetic wave transmits to ground at any angle, the underground electromagnetic wave always travels downwards in the form of plane wave. At this time, Maxwell equations can

be decomposed into two independent fields, TE polarization mode ( $\mathbf{E}_x$ ,  $\mathbf{H}_y$ ,  $\mathbf{H}_z$ ), and TM polarization mode ( $\mathbf{H}_x$ ,  $\mathbf{E}_y$ ,  $\mathbf{E}_z$ ). Expanding Eqs. 1 and 2 with consideration of  $\partial/\partial x = 0$ , we can get two independent equation systems, which indicate TE mode and TM mode, respectively, with respect to  $x$ -component (Wannamaker *et al.* 1987).

TE polarization mode writes:

$$\begin{cases} \frac{\partial \mathbf{H}_z}{\partial y} - \frac{\partial \mathbf{H}_y}{\partial z} = (\sigma - i\omega\varepsilon)\mathbf{E}_x \\ \mathbf{H}_y = \frac{1}{i\omega\mu} \frac{\partial \mathbf{E}_x}{\partial z} \\ \mathbf{H}_z = -\frac{1}{i\omega\mu} \frac{\partial \mathbf{E}_x}{\partial y} \end{cases} \quad (3)$$

TM polarization mode writes:

$$\begin{cases} \frac{\partial \mathbf{E}_z}{\partial y} - \frac{\partial \mathbf{E}_y}{\partial z} = i\omega\mu\mathbf{H}_x \\ \mathbf{E}_y = \frac{1}{\sigma - i\omega\varepsilon} \frac{\partial \mathbf{H}_x}{\partial z} \\ \mathbf{E}_z = -\frac{1}{\sigma - i\omega\varepsilon} \frac{\partial \mathbf{H}_x}{\partial y} \end{cases} \quad (4)$$

From Eqs. 3 and 4,  $\mathbf{H}_y$ ,  $\mathbf{H}_z$ ,  $\mathbf{E}_y$ , and  $\mathbf{E}_z$  can be worked out. By substituting them into Eqs. 1 and 2, we get the partial difference equations for  $\mathbf{E}_x$  and  $\mathbf{H}_x$ :

$$\frac{\partial}{\partial y} \left( \frac{1}{i\omega\mu} \frac{\partial \mathbf{E}_x}{\partial y} \right) + \frac{\partial}{\partial z} \left( \frac{1}{i\omega\mu} \frac{\partial \mathbf{E}_x}{\partial z} \right) + (\sigma - i\omega\varepsilon)\mathbf{E}_x = 0, \quad (5)$$

$$\frac{\partial}{\partial y} \left( \frac{1}{\sigma - i\omega\varepsilon} \frac{\partial \mathbf{H}_x}{\partial y} \right) + \frac{\partial}{\partial z} \left( \frac{1}{\sigma - i\omega\varepsilon} \frac{\partial \mathbf{H}_x}{\partial z} \right) + i\omega\mu\mathbf{H}_x = 0. \quad (6)$$

Equations 5 and 6 can be uniformly expressed as:

$$\nabla(\tau\nabla u) + \lambda u = 0. \quad (7)$$

For the TE mode, we have

$$u = \mathbf{E}_x, \quad \tau = \frac{1}{i\omega\mu}, \quad \lambda = \sigma - i\omega\varepsilon. \quad (8)$$

For the TM mode, we have

$$u = H_x, \quad \tau = \frac{1}{\sigma - i\omega\epsilon}, \quad \lambda = i\omega\mu. \tag{9}$$

Considering boundary conditions, the variational problem equivalent to Eq. 7 writes:

$$\begin{cases} F(u) = \int_{\Omega} \left[ \frac{1}{2} \tau (\nabla u)^2 - \frac{1}{2} \lambda u^2 \right] d\Omega + \int_{CD} \frac{1}{2} \tau k u^2 d\Gamma \\ u|_{AB} = 1 \\ \delta F(u) = 0 \end{cases} \tag{10}$$

AB and CD are the upper boundary and lower boundary, respectively, in the 2D domain.

Solving AMT two-dimensional forwarding modeling problem with FEM in Eq. 10 (Coggon 1971, De Lugão and Wannamaker 1996), a complex coefficients equation can be obtained, writing

$$Ku = 0. \tag{11}$$

By solving the above system of linear algebraic equations, the field value  $u$  can be obtained, and  $E_x$  in TE mode and  $H_x$  in TM mode can be attained.

According to the definition of apparent resistivity, the TE and TM mode calculation equations are derived and expressed as:

$$\rho_{TE} = \frac{i}{\omega\mu} \left( \frac{E_x}{H_y} \right)^2 \Bigg|_{y=0}, \tag{12}$$

$$\rho_{TM} = \frac{i}{\omega\mu} \left( \frac{E_y}{H_x} \right)^2 \Bigg|_{y=0}. \tag{13}$$

By substituting the second formula in Eq. 2 into Eq. 12, and letting  $u = E_x$ , we have

$$\rho_{TE} = -i\omega\mu \left( u / \frac{\partial u}{\partial y} \right)^2 \Bigg|_{y=0}. \tag{14}$$

By substituting the second formula in Eq. 4 into Eq. 13, and letting  $u = H_x$ , we have

$$\rho_{TM} = \frac{i}{\omega\mu\sigma^2} \left( \frac{\partial u}{\partial y} / u \right)^2 \Big|_{y=0} . \quad (15)$$

Through Eqs. 14 and 15, the apparent resistivity of the two polarization modes can be deduced, and electric stratification of the underground media can be judged intuitively.

### 3.2 AMT inversion based on NLCG

Generally, the AMT inversion problem can be expressed as:

$$\mathbf{d} = F(\mathbf{m}) + \mathbf{e} , \quad (16)$$

where  $\mathbf{d} = [d^1, d^2, \dots, d^N]^T$  is the data vector,  $d^i$  is the apparent resistivity or phase of impedance in TE mode or TM mode at a specific frequency point,  $\mathbf{m} = [m^1, m^2, \dots, m^M]^T$  is the model vector,  $\mathbf{e}$  is the discrepancy vector, and  $F$  is the response function of forward modeling.  $m$  is set as model grid with  $M$  elements, and each  $M_R$  stands for the logarithmic resistivity of a specific grid.  $\psi$  is defined as (Tikhonov and Arsenin 1978, Rodi and Mackie 2001):

$$\psi(\mathbf{m}) = (\mathbf{d} - F(\mathbf{m}))^T \mathbf{V}^{-1} (\mathbf{d} - F(\mathbf{m})) + \lambda \mathbf{m}^T \mathbf{L}^T \mathbf{L} \mathbf{m} . \quad (17)$$

If  $\lambda$ ,  $\mathbf{V}$ , and  $\mathbf{L}$  are given specific values, regularization factor  $\lambda$  is a positive number. The positive definite matrix  $\mathbf{V}$  and the discrepancy vector  $\mathbf{e}$  are related in the form of covariation.  $\mathbf{L}$  is a second order difference operator. When the model grid is unique,  $\mathbf{Lm}$  can be approximated to be the Laplace operator of  $\log \rho$ . The  $\lambda \mathbf{m}^T \mathbf{L}^T \mathbf{L} \mathbf{m}$  denotes a stable factor in the model space.

The gradient and Hesse matrix of objective function are defined as  $\mathbf{g}(1 \times M)$  and  $\mathbf{H}(H \times M)$ , respectively. Define  $\mathbf{A}$  as the Jacobian matrix of response function  $F$ , and we have

$$A^{ij}(\mathbf{m}) = \partial_j F^i(\mathbf{m}) , \quad i = 1, \dots, N , \quad j = 1, \dots, M . \quad (18)$$

Substitute Eq. 18 into 17, and we get

$$\mathbf{g}(\mathbf{m}) = -2\mathbf{A}(\mathbf{m})^T \mathbf{V}^{-1} (\mathbf{d} - F(\mathbf{m})) + 2\lambda \mathbf{L}^T \mathbf{L} \mathbf{m} , \quad (19)$$

$$\mathbf{H}(\mathbf{m}) = 2\mathbf{A}(\mathbf{m})^T \mathbf{V}^{-1} \mathbf{A}(\mathbf{m}) + 2\lambda \mathbf{L}^T \mathbf{L} - 2 \sum_{i=1}^N \mathbf{q}^i \mathbf{B}_i(\mathbf{m}) , \quad (20)$$

where  $\mathbf{B}_i$  is the Hesse matrix of  $F^i$ ,  $\mathbf{q} = \mathbf{V}^{-1}(\mathbf{d} - F(\mathbf{m}))$ ,  $\mathbf{A}(\mathbf{m})^T \mathbf{V}^{-1}(\mathbf{d} - F(\mathbf{m}))$ , and  $\mathbf{A}(\mathbf{m})^T \mathbf{V}^{-1} \mathbf{A}(\mathbf{m})$  can be derived without calculating Jacobian matrix  $\mathbf{A}$ .

Using NLCG algorithm, we can directly solve the minimization problem. NLCG by Polak–Ribiere is introduced to calculate the minimum value of Eq. 17, with detail process as follows:

$$\mathbf{m}_0 = \mathbf{m}_{\text{given}} ,$$

$$\psi(\mathbf{m}_k + \alpha_k \mathbf{p}_k) = \min \psi(\mathbf{m}_k + \alpha \mathbf{p}_k) , \quad \mathbf{m}_{k+1} = \mathbf{m}_k + \alpha_k \mathbf{p}_k , \quad k = 0, 1, 2 , \quad (21)$$

$$\alpha_{k,j+1} = \alpha_{k,j} - \frac{\mathbf{g}_{k,j}^T \mathbf{p}_k}{\mathbf{p}_k^T \tilde{\mathbf{H}}_{k,j} \mathbf{p}_k} ,$$

where  $\mathbf{m}_{\text{given}}$  is the vector sequence of a known initial model. By calculating the searching step  $\alpha_k$  along the searching direction  $\mathbf{p}_k$ , the objective function of minimization can be iterated. The iterations along the searching direction are as follows:

$$\mathbf{p}_0 = -\mathbf{C}_0 \mathbf{g}_0 ,$$

$$\mathbf{p}_k = -\mathbf{C}_k \mathbf{g}_k + \beta_k \mathbf{p}_{k-1} , \quad k = 1, 2 , \quad (22)$$

where,  $\mathbf{g}_k$  denotes the gradient of  $\psi$  when  $m = m_k$ ,  $C_k$  is the precondition factor,  $\beta_k$  is the weighting factor of conjugate direction vector. There are many expression approaches of  $\beta_k$ , and a different expression approach stands for different conjugate gradient method. This paper adopts the PRP (Polak–Ribiere–Polyak) nonlinear conjugate gradient algorithm to calculate  $\beta_k$ :

$$\beta_k = \frac{\mathbf{g}_k^T \mathbf{C}_k (\mathbf{g}_k - \mathbf{g}_{k-1})}{\mathbf{g}_{k-1}^T \mathbf{C}_{k-1} \mathbf{g}_{k-1}} . \quad (23)$$

It is not necessary to conjugate the searching direction with any certain fixed matrices, but the following condition should be fulfilled:

$$\mathbf{p}_k^T (\mathbf{g}_k - \mathbf{g}_{k-1}) = 0 , \quad k > 0 . \quad (24)$$

The Gauss–Newton iteration is adopted to solve the problem, and cubic difference is adopted to calculate  $\alpha_{k,j+1}$ . Following the secondary iteration, the optimized  $\alpha$  will be obtained firstly, and then it is substituted to the minimum functional iteration to calculate the model variation. The iteration will not stop until the termination condition is fulfilled or the iteration achieves the termination number, when the best fit model is obtained.

#### 4. GEOELECTRICAL MODEL FOR THE STUDY AREA

To carry out AMT numerical simulation for gas hydrate in the Qilian Mountain permafrost, it is necessary to set appropriate resistivity value for gas hydrate reservoirs based on the occurrence of gas hydrate in the study area, and establishing an actual geoelectrical model to simulate the variation characteristics is a must. The physical parameters that affect the electrical property consist of porosity and saturation of the gas hydrate, so that Archie equation, usually used in the reservoir evaluation, can be applied to the gas hydrate assessment, writing (Archie 1942):

$$R_t = \frac{aR_w}{\phi^m S_w^n}, \quad (25)$$

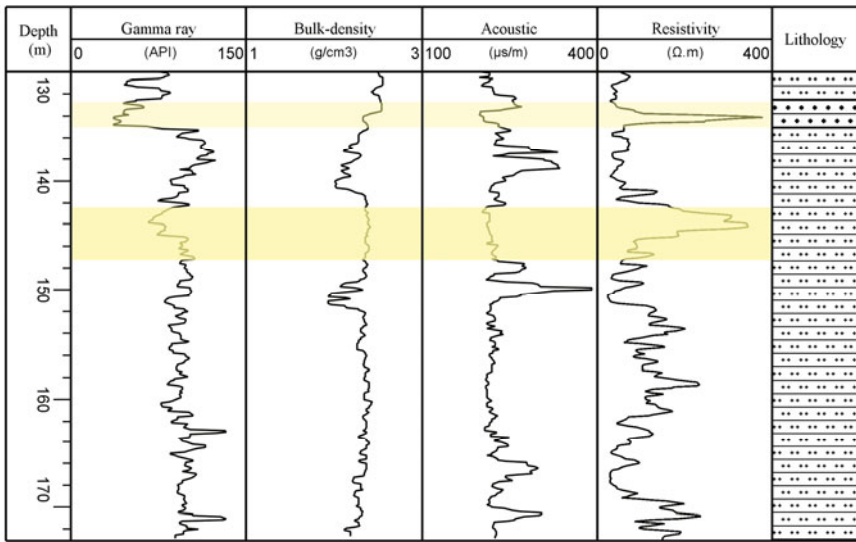
where  $R_t$  is the resistivity value in the formation,  $R_w$  is the resistivity value of formation water,  $\phi$  indicates the porosity, and  $S_w$  denotes the water saturation of the pores in the formation. Parameters  $a$ ,  $m$ , and  $n$  are empirical indices, which can be determined by the actual stratum, and  $1.5 < m < 3$ ,  $0.5 < a < 2.5$ .

According to the previous research for gas hydrate reservoirs (Lee and Collett 2011, Guo and Zhu 2011), it can be determined that  $R_w = 2 \Omega \cdot \text{m}$ ,  $n = 1.9386$ ,  $a = 0.5$ , and  $m = 1.32$ , so that Eq. 25 can be transformed to be

$$R_t = \frac{1.02}{\phi^{1.32} (1 - S_h)^{1.9386}}. \quad (26)$$

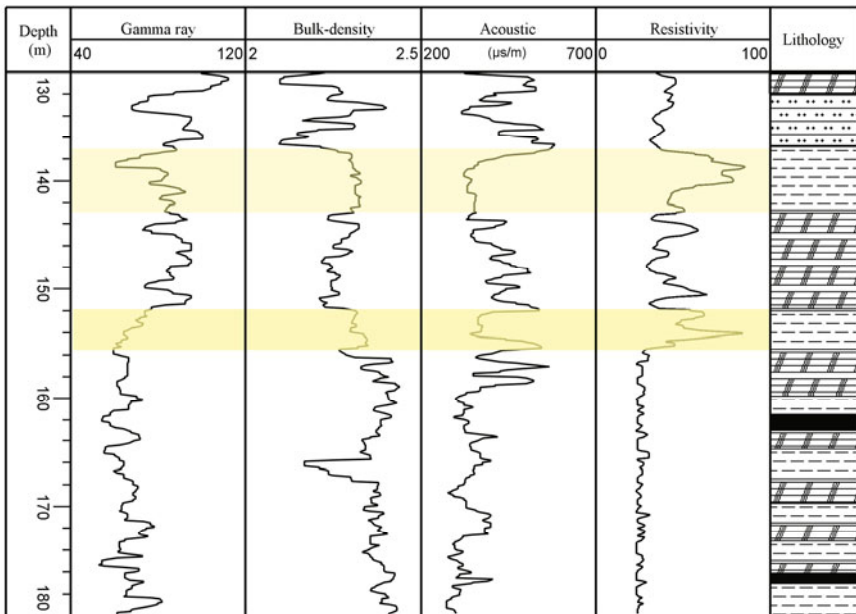
It can be seen from Eq. 26 that the resistivity of gas hydrate reservoir is a function of porosity and saturation of gas hydrate. Here Eq. 26 is defined to be the resistivity calculation model for the gas hydrate reservoir. Therefore, according to the porosity and saturation of the gas hydrate reservoir in the study area, the reservoir resistivity can be deduced.

The application of AMT method is conditioned on the resistivity difference of the target reservoir and surrounding rock. AMT sounding can reflect the electrical property of formation owing to its wide frequency range, and then, using related inversion technique, the geological information of the target reservoirs can be acquired. Therefore, to simulate the gas hydrate in the Qilian Mountain permafrost with AMT method, the resistivity value of gas hydrate and surrounding rock should be determined first. Gas hydrates at normal temperatures and pressures are very unstable and easy to decompose, making it impossible to measure resistivity value with conventional samples. However, it is a direct and effective method to analyze the resistivity of the gas hydrate reservoir and surrounding rock using the *in situ* log results. So the well log data of DK-1 and DK-3 holes where gas hydrate was recovered in the Qilian Mountain permafrost is used to analyze formation electrical characteristics of the study area (Fig. 3).



Siltstone    
 Sandstone

(a) DK-1



Oily shale    
 Mudstone    
 Siltstone    
 Coal

(b) DK-3

Fig. 3. Downhole logs from gas hydrate scientific drilling holes in the Qilian Mountain permafrost (Lu *et al.* 2011, Guo and Zhu 2011). Data shown include the natural gamma ray log, bulk-density, acoustic, and electrical resistivity data. Yellow bands indicate the gas hydrate bearing layers.

Gas hydrate occurrences are supported by macroscopically high-resistivity and acoustic velocity in the well log profiles (Carcione and Gei 2004, Lee and Collett 2011). It is very clear that the resistivity and velocity of the gas hydrate bearing layer are relatively higher than the surrounding rock in the holes of DK-1 and DK-3 (Fig. 3). Although the coal layer has a relatively high signal of resistivity, its velocity signals are relatively low. Hence, four intervals (133.5~135.5, 142.9~147.7, 137.4~143.3, and 152~155.5 m) are interpreted as gas hydrate bearing layers from the comprehensive well log data, where resistivity and velocity are relatively high and natural gamma ray and density are relatively low. These well log data interpretations are supported by field observations of gas hydrate occurrences and associated anomalies.

The high-resistivity anomaly tends to be more distinct along with the increase of the thickness of gas hydrate bearing layer. By statistically classifying the resistivity value of gas hydrate bearing layers in terms of lithological characteristics (Table 3), we can see that the gas hydrate revealed by the hole of DK-1 exists in sandstone and siltstone (Fig. 3a), and the average resistivity value of gas hydrate bearing layers is 2.97 times higher than that of the surrounding rock. The gas hydrate revealed by DK-3 hole exists in mudstone (Fig. 3b), and the average resistivity value of gas hydrate bearing layers is 2.96 times higher than that of the surrounding rock.

Table 3  
Statistics of the values of resistivity logging in gas hydrate reservoirs

Borehole	Gas hydrate bearing layers [m]	Reservoir lithology	Resistivity value of reservoir [ $\Omega$ .m]	Resistivity value of surrounding rock [ $\Omega$ .m]
DK-1	133.5~135.5	Sandstone	113.97~378.41	50.99~98.10
	142.9~147.7	Siltstone	287.85~349.92	37.7~168.32
DK-3	137.4~143.3 152.0~155.5	Mudstone	52.95~83.36	25.12~28.13

Based on the electrical characteristics of reservoirs with different lithology, the resistivity value of the gas hydrate reservoir in the geoelectrical model is set to be 3 times higher than that of the surrounding rock. According to the resistivity variation characteristics of the permafrost in the study area, the resistivity value of the permafrost layer is set to be 2 times higher than the resistivity value of the gas hydrate reservoir (Zhu *et al.* 2010, Lin *et al.* 2013). In accordance with resistivity calculation model, by setting differ-

ent porosities and saturation of the gas hydrate reservoir, different geoelectrical models can be established with the above electrical relationships to lay a foundation for AMT numerical simulation.

## 5. RESULTS AND DISCUSSION

### 5.1 Response characteristics of high-resistance abnormal body of gas hydrate

As gas hydrate in the Qilian Mountain permafrost occurs abnormally in the local scope, the gas hydrate reservoir can be modeled as high-resistance abnormal body. To determine gas hydrate reservoirs favorable to AMT prospecting in the study area, the response characteristics of AMT forward modeling for high-resistance abnormal body of gas hydrate are analyzed with variation of resistivity, occurrence scale, and bury depth. Based on the occurrences variation of gas hydrate, different geoelectrical models are designed, of which: the first layer is the permafrost layer with resistivity  $2\rho$ , thickness 100 m (Zhu *et al.* 2010, Lu *et al.* 2011, Pang *et al.* 2013); the second layer is the gas hydrate reservoir, while surrounding rock resistivity is  $1/3\rho$ , and a distance of  $h$  below the permafrost layer there is a high-resistance abnormal body of gas hydrate with resistivity  $\rho$ , and  $d \times 200$  m of size (Fig. 4).

Because gas hydrate samples recovered from the study area have been shallow buried and had a high resistivity (Lu *et al.* 2011, Zhu *et al.* 2010), and the earth's surface is covered by high-resistivity permafrost, parameters for forward modeling are set as follows: frequencies range from 0.1 to 10 000 Hz with detail frequencies shown in Table 4. Note that the length of profile line is 5 km and the station spacing is 25 m.

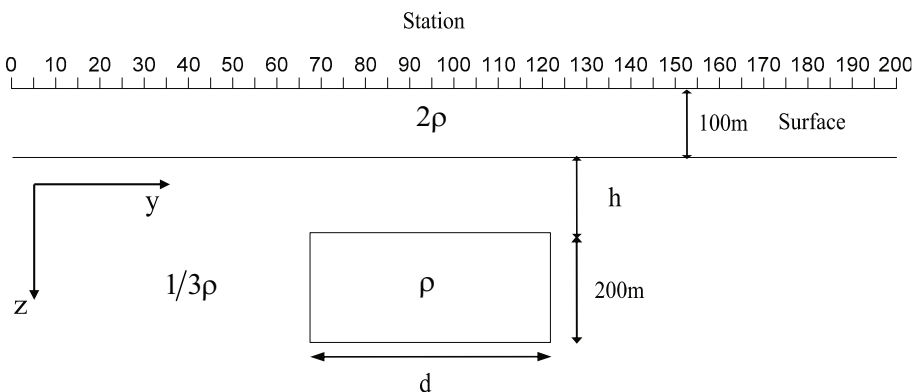


Fig. 4. The geoelectrical model of high-resistance abnormal body of gas hydrate.

Table 4

Frequency points for AMT forward modeling

Count	Frequency point [Hz]
91	8577, 7365, 6310, 5412, 4642, 3981, 3415, 2929, 2512, 2154, 1848, 1585, 1359, 1166, 1000, 858, 736, 631, 541, 464, 398, 341, 293, 251, 215, 185, 158, 136, 117, 100, 85.8, 73.6, 63.1, 54.1, 46.4, 39.8, 34.1, 29.3, 25.1, 21.5, 18.5, 15.8, 13.6, 11.7, 10.0, 8.58, 7.36, 6.31, 5.41, 4.64, 3.98, 3.42, 2.93, 2.51, 2.15, 1.85, 1.59, 1.36, 1.17, 1.00, 0.858, 0.736, 0.631, 0.541, 0.464, 0.398

### 5.1.1 Forward modeling of different resistivities

To study the influence of resistivity on AMT response characteristics of gas hydrate in the Qilian Mountain permafrost, different resistivities are assumed based on the porosity and saturation of gas hydrate. Based on the actual data, the porosity of the high-resistance abnormal body of gas hydrate is set to be 10%, and the saturations are assumed to be 30, 40, 50, 60, 70, and 80%, corresponding to 43, 57, 82, 126, 220, and 483  $\Omega\cdot\text{m}$  of resistivity with an average value of 168.5  $\Omega\cdot\text{m}$ . These values can be derived according to the resistivity model. By fixing depth  $h = 100$  m and width  $d = 500$  m, and changing  $\rho$ , whose values are 43, 168, and 483  $\Omega\cdot\text{m}$ , the apparent resistivity section diagrams of TE and TM modes by AMT forward modeling with FEM can be obtained, as shown in Fig. 5.

From Figure 5, we can see that there are different levels of concaves in the apparent resistivity contour, meaning the high-resistivity anomaly appears, and indicating the existence of gas hydrate. So simulation of the high resistance abnormal body of gas hydrate in the surrounding rock with lower resistivity is effective. In the section diagrams of apparent resistivity in TE mode, the high-resistance abnormal body of gas hydrate can be well distinguished longitudinally, and electrical influence scope of the high-resistivity anomaly can be delineated in the longitudinal direction. The TM mode apparent resistivity can well distinguish anomalies in the horizontal direction, and delineate the horizontal electrical influence scope of the high resistance abnormal body of gas hydrate.

When the resistivity of gas hydrate reservoir reaches 43  $\Omega\cdot\text{m}$  (Fig. 5a), there will be a high-resistivity anomaly at the top around 100 Hz in TE mode, with a wide influence scope ranging from 0.4 to 100 Hz. The high-resistivity anomaly in TM mode ranges from 2250 to 2750 m, with a width of 500 m, which shows good compatibility with the actual scope of high-resistance abnormal body. When the resistivity reaches 168  $\Omega\cdot\text{m}$  (Fig. 5b), a high-resistivity anomaly appears at the top of 300 Hz in TE mode, and the

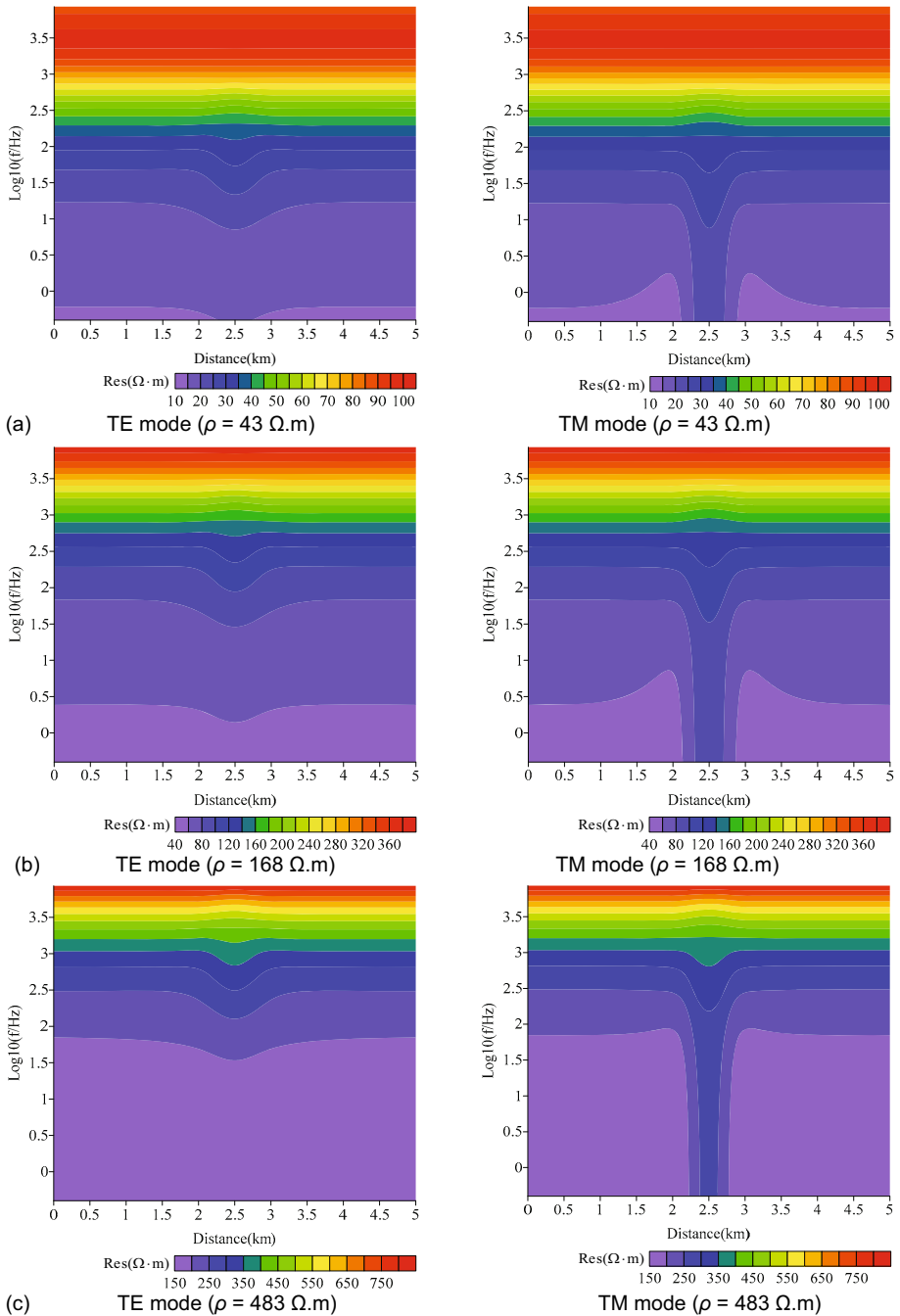


Fig. 5. The apparent resistivity section diagrams of the high-resistance abnormal body of gas hydrate with different resistivities.

influential frequency range reduces to 3~300 Hz. The horizontal influence scopes of the high-resistivity anomaly in TM mode are similar when the resistivity is 43 and 168  $\Omega\cdot\text{m}$ , meaning the results in TM mode can reflect the actual condition. When the resistivity for gas hydrate reservoir is 483  $\Omega\cdot\text{m}$  (Fig. 5c), the high-resistivity anomaly appears around 1000 Hz in TE mode, and the frequency range reduces further, mainly from 100 to 1000 Hz; the horizontal influence scope of the high-resistivity anomaly in TM mode ranges from 2350 to 260 m, with a width of 300 m, which differs largely from the actual condition.

It can be seen from the above analysis that when the bury depth and occurrence scale of gas hydrate reservoir are fixed, with the increase of resistivity, the influence scopes of the high-resistivity anomaly in TE and TM modes decrease, and response characteristics of AMT forward modeling weaken, indicating that the formation with high resistivity in the study area will not benefit to the identification and delineation of gas hydrate reservoir with AMT sounding.

When the resistivity of the high-resistance abnormal body of gas hydrate is 483  $\Omega\cdot\text{m}$ , the response characteristics of forward modeling will deviate from the actual condition largely, indicating that AMT method cannot prospect the gas hydrate reservoirs when the resistivity of the reservoir is higher than 483  $\Omega\cdot\text{m}$ . According to the porosity and saturation of the gas hydrate in the Qilian Mountain permafrost, resistivities of the reservoirs can be estimated with Eq. 26 (Table 5). From Table 3 we can see that when the resistivity

Table 5

The resistivity values of gas hydrate model under different reservoir conditions

Gas hydrate model	Reservoir condition		Resistivity [ $\Omega\cdot\text{m}$ ]	Gas hydrate model	Reservoir condition		Resistivity [ $\Omega\cdot\text{m}$ ]
	$\phi$ [%]	$Sh$ [%]			$\phi$ [%]	$Sh$ [%]	
1	5	30	106	13	15	30	25
2	5	40	143	14	15	40	34
3	5	50	204	15	15	50	48
4	5	60	314	16	15	60	74
5	5	70	549	17	15	70	129
6	5	80	1205	18	15	80	283
7	10	30	43	19	20	30	17
8	10	40	57	20	20	40	23
9	10	50	82	21	20	50	33
10	10	60	126	22	20	60	50
11	10	70	220	23	20	70	88
12	10	80	483	24	20	80	193

of gas hydrate reservoir is higher than  $483 \Omega \cdot \text{m}$ , the corresponding porosity will be less than 5%, and saturation will be higher than 70%, indicating that the reservoirs are of low porosity and high saturation.

From the above analysis it follows that for gas hydrate reservoirs in the Qilian Mountain permafrost, when the porosity is less than 5%, saturation is higher than 70%, the AMT method cannot identify and delineate gas hydrate reservoirs.

### **5.1.2 Forward modeling of occurrence scales**

To reflect the general electrical properties of gas hydrate reservoirs in the Qilian Mountain permafrost, the average resistivity derived from the conditions that porosity is assumed to be 10% and saturation is assumed to be 30~80% is set as  $\rho$  for the high resistance abnormal body of gas hydrate.  $\rho$  is set to be  $168 \Omega \cdot \text{m}$ . The upper boundary is 100 m far from the permafrost layer. The width of the high-resistance abnormal body is set to be 50, 350, and 400 m. Other parameters for the forward simulation are the same as the above-mentioned values. So, after AMT forward simulation with FEM, the apparent resistivity section diagrams can be obtained, as illustrated in Fig. 6.

From Figure 6, it can be seen that with the increase of the width of the high-resistance abnormal body from 50 to 400 m, influence scopes of the high-resistivity anomaly in TE and TM modes are increasing, and the response characteristics of AMT forward modeling are strengthening. When the width of the high-resistance abnormal body is 50 m (Fig. 6a), the contour of apparent resistivity in TE mode expands horizontally, *i.e.*, no response characteristic occurs. There is also no response characteristic of the high-resistivity anomaly in the horizontal direction in TM mode, indicating that the contour cannot reflect the distribution of anomalies. When the width of the high-resistance abnormal body is 350 m (Fig. 6b), the contour of apparent resistivity concaves downward distinctly, and the anomaly appears at the top around 300 Hz, with frequencies ranging from 3 to 300 Hz. In the TM mode, the high-resistivity anomaly distributes from 2350 to 2650 m, with a width of 300 m, which is not totally consistent with the high-resistance abnormal body. When the width of the high-resistance abnormal body is 400 m (Fig. 6c), a more distinct downward concave appears in the contour of TE mode, and AMT response characteristics are also strengthen. In the TM mode, the high-resistivity anomaly distributes from 2300 to 2700 m, with a width of 400 m, which coincides well with the actual high-resistance abnormal body of gas hydrate.

From the above analysis it follows that for the high-resistance abnormal body of gas hydrate in the Qilian Mountain permafrost, when the resistivity and bury depth are fixed at certain values, with the increase of occurrence scale of the abnormal body, influence scopes of high-resistivity anomalies

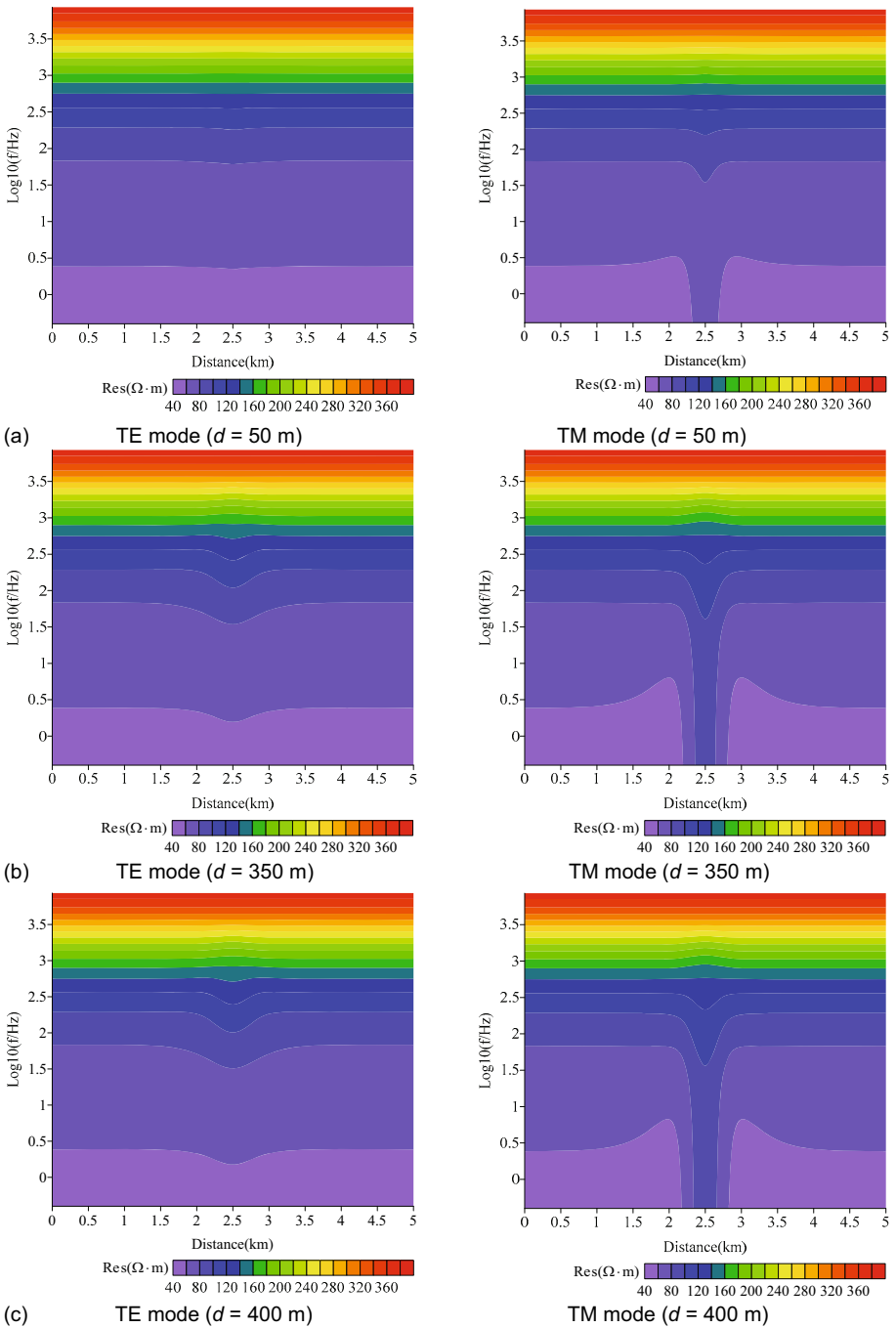


Fig. 6. The apparent resistivity section diagrams of the high-resistance abnormal body of gas hydrate with different occurrence scales.

illustrated in the apparent resistivity section diagrams increase, and the response characteristics of AMT forward modeling strengthen. When the occurrence scale of the gas hydrate reservoir is less than 50 m, the AMT method cannot identify it, while when the occurrence scale is larger than 400 m, the AMT method can identify and delineate the reservoir.

### 5.1.3 Forward modeling of different depths

To study the influence of gas hydrate reservoir bury depth on AMT response characteristics,  $\rho$  is fixed to be 168  $\Omega\cdot\text{m}$ , and width is fixed to be 400 m ( $d = 400$  m). The distances between upper boundary of the abnormal body and the permafrost layer,  $h$ , are set to be 100, 350, and 400 m, respectively. The other parameters are the same as the above-mentioned values. After AMT forward simulation with FEM, the apparent resistivity section diagrams can be obtained, as illustrated in Fig. 7.

From Figure 7 it follows that, when the bury depth increases from 200 to 500 m, the influence scope of apparent resistivity in TE and TM modes decreases, and the AMT forward modeling response characteristics weaken. When the bury depth of the high-resistance abnormal body is 200 m (Fig. 7a), the contour of apparent resistivity in TE mode concaves downwards distinctly, and the high-resistivity anomaly appears at the top around 300 Hz with frequencies ranging from 3 to 300 Hz. In the TM mode, the high-resistivity anomaly ranges from 2300 to 2700 m, with a width of 400 m which shows good compatibility with the actual conditions. When the bury depth of the high-resistance abnormal body is 450 m (Fig. 7b), the bending degree of the apparent resistivity contour in TE mode gets weak distinctly, and the AMT response characteristics also weaken. There is no horizontal response in the contour of apparent resistivity in TM mode, meaning the contour cannot reflect the distribution of anomalies. When the bury depth of the high-resistance abnormal body is 500 m (Fig. 7c), the contour of apparent resistivity in TE mode expands horizontally, *i.e.*, no response characteristic occurs. No response characteristic occurs in TM mode, indicating that the contour cannot reflect the distribution of anomalies.

From the above analysis it follows that, for the high-resistance abnormal body of gas hydrate in the Qilian Mountain permafrost, when the resistivity and occurrence scale are fixed to certain values, with the increase of bury depth of the abnormal body, apparent resistivity influence scopes in both TE and TM modes decrease, and the response characteristics of AMT forward modeling weaken. When the bury depth of the gas hydrate reservoir is higher than 500 m, AMT method cannot identify and delineate the reservoir.

Based on the measured gas components of gas hydrate, combined with the data of the mean annual ground temperature, temperature gradient, and

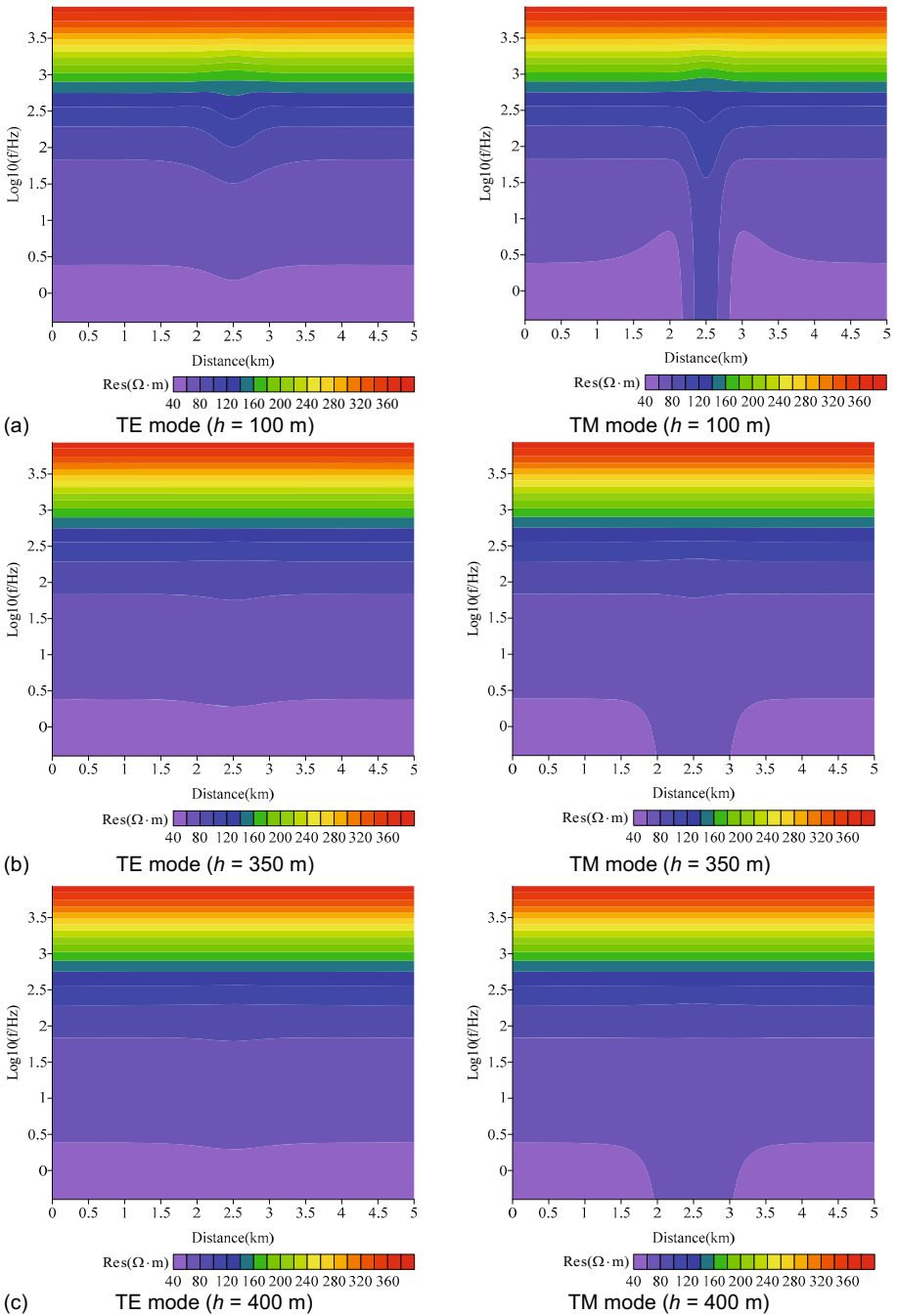


Fig. 7. The apparent resistivity section diagrams of the high-resistance abnormal body of gas hydrate with different bury depths.

thickness of permafrost in Muli coalfield, the gas hydrate stability zone (GHSZ) of the study area has been studied. The results showed that the top depth of the GHSZ is 171 m, and the bottom depth of the GHSZ is 574 m, respectively (Zhu *et al.* 2010). Besides, gas hydrate samples recovered from the study area are shallow-buried, ranging from 133 to 396 m in depth (Fig. 2). Therefore, for the above bury depth condition, the AMT method can be effectively used to identify and delineate the gas hydrate reservoir in the Qilian mountain permafrost.

## 5.2 Influence of acquisition parameters on AMT inversion results

Because the difference of electrical properties between the permafrost layer and gas hydrate reservoir is not that obvious, and gas hydrate occurs closely below the permafrost layer, the inversion results will be affected largely. So the geoelectric model built here will not consider the overlying permafrost layer. To reflect the general electrical properties of gas hydrate reservoir, the average resistivity, approximated to be  $170 \Omega \cdot \text{m}$ , derived from Eq. 26 with porosity 10% and saturation 30~80% is used as the resistivity for inversion model. According to the resistivity logging data of the DK-1 hole (Fig. 3a, Table 3), the maximum ratio of resistivity value of gas hydrate reservoir to resistivity value of surrounding rock can be 10 (Lu *et al.* 2011, Yao *et al.* 2013). Therefore, to improve the inversion results and to better analyze the effect of acquisition data to inversion, the resistivity value of surrounding rock is set to be  $17 \Omega \cdot \text{m}$ . According to the electrical characteristics of gas hydrate, a typical geoelectrical model is built for gas hydrate reservoir in the study area (Fig. 8).

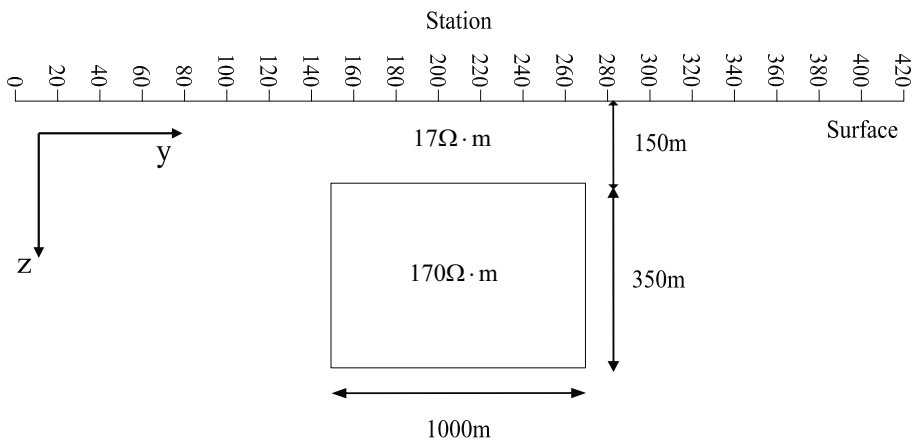


Fig. 8. Typical geoelectrical model of the high-resistance abnormal body of gas hydrate.

Table 6

## Frequency points for AMT forward modeling

Count	Frequency point [Hz]
91	398, 369, 341, 316, 293, 271, 251, 233, 215, 200, 185, 171, 158, 147, 136, 126, 117, 108, 100, 92.6, 85.8, 79.4, 73.6, 68.1, 63.1, 58.4, 54.1, 50.1, 46.4, 43.0, 39.8, 36.9, 34.1, 31.6, 29.3, 27.1, 25.1, 23.3, 21.5, 20.0, 18.5, 17.1, 15.8, 14.7, 13.6, 12.6, 11.7, 10.8, 10.0, 9.26, 8.58, 7.94, 7.36, 6.81, 6.31, 5.84, 5.41, 5.01, 4.64, 4.30, 3.98, 3.69, 3.42, 3.16, 2.93, 2.71, 2.51, 2.33, 2.15, 2.00, 1.85, 1.71, 1.59, 1.47, 1.36, 1.26, 1.17, 1.08, 1.00, 0.926, 0.858, 0.794, 0.736, 0.681, 0.631, 0.584, 0.541, 0.501, 0.464, 0.430, 0.398
46	398, 341, 293, 251, 215, 185, 158, 136, 117, 100, 85.8, 73.6, 63.1, 54.1, 46.4, 39.8, 34.1, 29.3, 25.1, 21.5, 18.5, 15.8, 13.6, 11.7, 10.0, 8.58, 7.36, 6.31, 5.41, 4.64, 3.98, 3.42, 2.93, 2.51, 2.15, 1.85, 1.59, 1.36, 1.17, 1.00, 0.858, 0.736, 0.631, 0.541, 0.464, 0.398
31	398, 316, 251, 200, 158, 126, 100, 79.4, 63.1, 50.1, 39.8, 31.6, 25.1, 20.0, 15.8, 12.6, 10.0, 7.94, 6.31, 5.01, 3.98, 3.16, 2.51, 2.00, 1.58, 1.26, 1.00, 0.794, 0.631, 0.501, 0.398
16	398, 251, 158, 100, 63.1, 39.8, 25.1, 15.8, 10.0, 6.31, 3.98, 2.51, 1.58, 1.00, 0.631, 0.398
7	398, 126, 39.8, 12.6, 3.98, 1.26, 0.398

The parameters are as follows: frequencies for forward modeling range from 0.1 to 1000 Hz, and 91 frequency points are deployed (Table 6), the length of survey line is 10.5 km, station spacing is 25 m, the scale of the high-resistance abnormal body of gas hydrate is  $350 \times 1000$  m, and the bury depth is 150 m. The response characteristics of forward modeling in TE and TM modes can be obtained by AMT simulation with FEM.

Response characteristics of the high-resistivity anomaly of gas hydrate in TE and TM modes can be seen clearly from the section diagrams of apparent resistivity and phases of impedance (Fig. 9), conducive to the analysis of influence of acquisition data on AMT inversion results. At the top around 100 Hz the high-resistivity anomalies appear in TE and TM modes (Fig. 9a, c). The high-resistivity anomaly area closes up around 1 Hz in TE mode, while the high-resistivity anomaly area does not close up in the low frequency part in TM mode. In the section diagrams of TE and TM modes (Fig. 9b, d), the high-resistivity anomalies appear around 100 Hz, and close up at high frequencies, indicating that the simulation can reflect the configuration of the high-resistance abnormal body of gas hydrate.

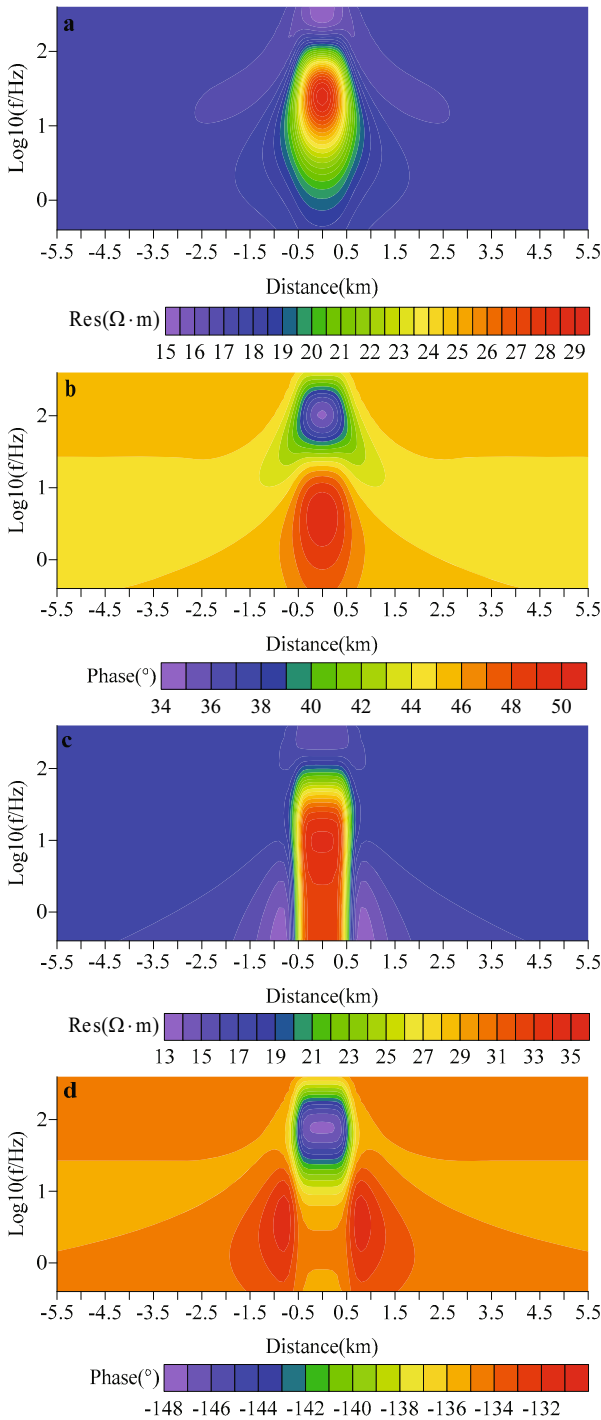


Fig. 9. AMT forward modeling responses for typical high-resistance abnormal body of gas hydrate: (a) apparent resistivity of TE mode, (b) phase of TE mode, (c) apparent resistivity of TM mode, and (d) phase of TM mode.

### 5.2.1 Survey line length

To investigate the influence of survey line length on the response characteristics of AMT inversion, the lengths of survey line are set to be 4, 3, 2, and 1 km. To better simulate the field data, 2% Gaussian noise is added to the original data, station spacing is 50 m, frequency points range from 0.398 to 398 Hz, and 46 frequency points are extracted at an interval of 0.06 in the log-domain (Table 6). The standardized parameter is set to be 10, initial resistivity is set to be 17  $\Omega\cdot\text{m}$ , and grid is set to be  $92 \times 50$ , with extended grid not included. Inversion mode is TE + TM.

Figure 10 shows the comparison diagrams of NLCG inversion results with different survey line lengths, where black frame indicates the size and position of actual model for the high-resistance abnormal body of gas hydrate. With the gradual increase of survey line length from 1 to 4 km, the anomalies reflected by inversion are consistent with the actual model in size and position. When survey line length equals the width of the high-resistance abnormal body (Fig. 10d), the width of the high-resistivity anomaly by inversion is only about 800 m, and the bottom boundary is about 550 m. Inversion results do not coincide with the actual model. When survey line is twice the length of the width of the high-resistance abnormal body (Fig. 10c), the width of the high-resistivity anomaly by inversion is 970 m. The top and bottom boundaries are consistent with the actual model, but the size of the anomaly is smaller than the actual model. When survey line length is more than triple the width of the high-resistance abnormal body (Fig. 10a-b), the size and position by inversion show good compatibility with the actual model.

From the above analysis it follows that, for AMT prospecting of gas hydrate in the Qilian Mountain permafrost, relatively longer survey line is more favorable to the identification of the high-resistance abnormal body. But with the increase of survey line length, expenses for field data acquisition and time for indoor data processing will increase correspondingly. Therefore, survey line length should be determined based on the actual occurrence of gas hydrate reservoir in the Qilian Mountain permafrost. Generally, double size of the possible occurrence region will be suitable, while triple size makes the best results.

### 5.2.2 Station space

To discuss the influence of station spacing on AMT inversion results, station spacings are defined to be 25, 50, 100, and 200 m. Survey line length is fixed to be 4 km, and the other parameters are the same for the above-mentioned data.

Figure 11 shows the comparison diagrams of NLCG inversion results with different station spacing. With the increase of station spacing from 25

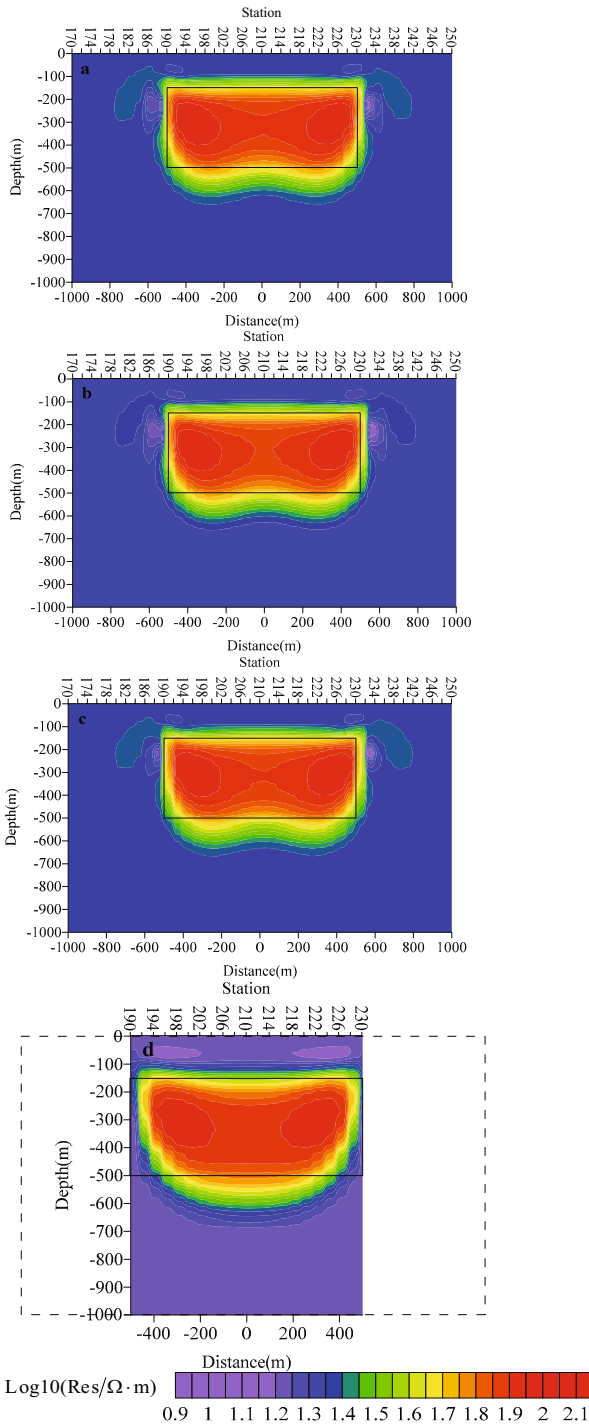


Fig. 10. 2D NLCG inversion results of the high-resistance abnormal body of gas hydrate with different survey line lengths: (a) 4 km, (b) 3 km, (c) 2 km, and (d) 1 km.

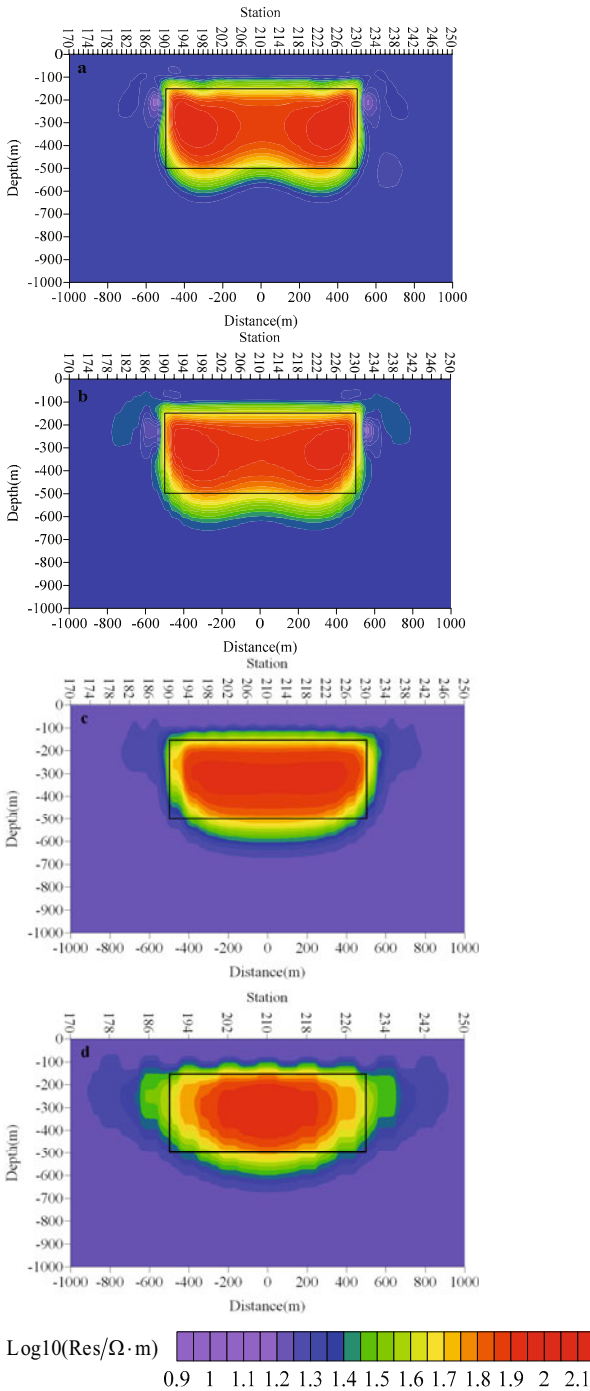


Fig. 11. 2D NLCG inversion results of the high-resistance abnormal body of gas hydrate with different station spacing: (a) 25 m, (b) 50 m, (c) 100 m, and (d) 200 m.

to 200 m, corresponding to the number of stations 41, 21, 11, and 5, AMT inversion results get worse, that is, the widths of anomalies decrease and the deviations get larger. When station spacings are 25 and 50 m (Fig. 11a-b), the size and position of high-resistivity anomaly by inversion are similar and coincide well with the actual model. When the spacing is 100 m (Fig. 11c), the width of high-resistivity anomaly by inversion is 900 m, and the depths of top boundary and bottom boundary are consistent with the actual model, but the size of high-resistivity anomaly is smaller than the actual model. When spacing is 20 m (Fig. 11d), the size and position by inversion differ largely from the actual model. It cannot reflect the size and position of the high-resistance abnormal body of gas hydrate.

From above analysis it follows that relatively short station spacing is more favorable to the identification of the high-resistance abnormal body of gas hydrate. But with the decrease of station spacing, expenses for field data acquisition and time for indoor data processing will increase correspondingly. The law of gas hydrate distribution in the lateral areas between drill holes is not apparent, and the continuity is relatively poor (Fig. 2). So when the AMT method is carried out, the number of stations should be no less than 6, and 11 stations make the best results.

### **5.2.3 Number of frequency points**

To discuss the influence of the number of frequency points on AMT inversion results for gas hydrate reservoir, the numbers of frequency points are assumed to be 46, 31, 16, and 7, and Table 6 gives the specific frequencies. The survey line length is fixed to be 4 km, and the station spacing is set to be 50 m. The other parameters are the same as for the above mentioned data.

Figure 12 shows the comparison diagrams of NLCG inversion results with different number of frequency points. With the decrease of the number of frequency points from 46 to 7, corresponding to 10, 7, 4, and 2 of the number of frequency points in the influence range of the high-resistivity anomaly (100~1000 Hz), AMT inversion results get worse, that is, the reflected size and position of anomalies deviate from the actual model gradually. When the numbers of frequency points are 46 and 31 (Fig. 12a-b), the size and position of the high-resistivity anomaly coincide well with the actual model. When the number of frequency points is 16 (Fig. 12c), the width of the high-resistivity anomaly by inversion is 970 m. The top boundary and bottom boundary are consistent with the actual model, but the high-resistivity anomaly is smaller than the actual model in size. When the number of frequency points is 7 (Fig. 12d), the width of the high-resistivity anomaly by inversion is 950 m, and the bottom boundary is about 580 m. The size and position of the high-resistivity anomaly by inversion do not coincide with the actual model.

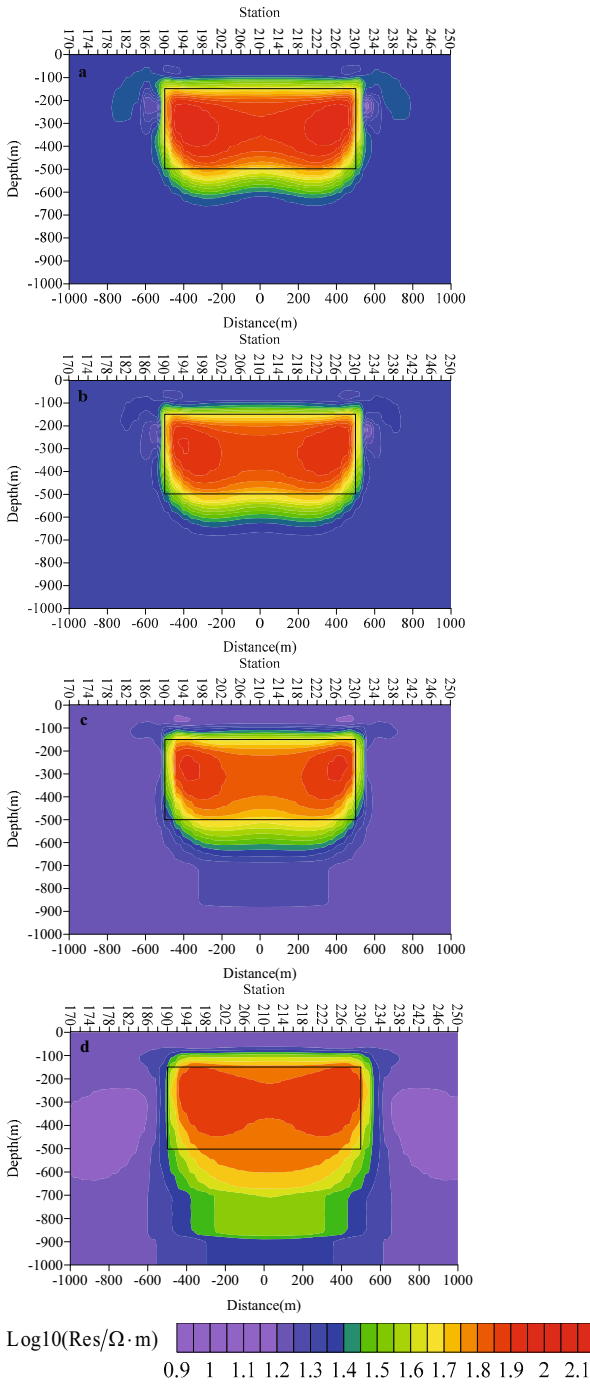


Fig. 12. 2D NLCG inversion results of the high-resistance abnormal body of gas hydrate with different numbers of frequency points: (a) 46, (b) 37, (c) 16, and (d) 7.

From above analysis it follows that more frequency points are favorable to the identification of the high-resistance abnormal body of gas hydrate. But with the increase of frequency points, expenses for field data acquisition and time for indoor data processing will increase correspondingly. Gas hydrate samples recovered from the study area are shallow-buried, ranging from 133 to 396 m in depth (Fig. 2), which belongs to the high-frequency section of AMT method. Therefore, if the AMT method in this area is carried out, the number of frequency points set in high-frequency section (100~1000 Hz) should be no less than 3, 4 points as best.

## 6. CONCLUSIONS

(1) Using the resistivity calculation model based on the Archie's equations for the gas hydrate reservoir, combined with resistivity logging data of gas hydrate scientific drilling holes in the Qilian Mountain permafrost, electrical characteristics of gas hydrate reservoirs of different lithology are analyzed to lay a foundation for the establishment of the geoelectrical model.

(2) The AMT response characteristics of the gas hydrate reservoir in the Qilian Mountain permafrost with variations of resistivity, occurrence scale and bury depth are simulated by finite element method, and the application range of AMT prospecting for the gas hydrate reservoir is obtained. If porosity is less than 5%, saturation of gas hydrate is higher than 70%, occurrence scale is less than 50 m, or bury depth is greater than 500 m, the AMT sounding cannot identify and delineate the favorable gas hydrate reservoir.

(3) With NLCG algorithm influences of acquisition parameters on AMT inversion results are studied, and an optimized acquisition parameters scheme favorable to prospecting the gas hydrate reservoir is obtained. Survey line should be twice the length of occurrence scale, while triple the length makes the best result. The number of stations in the possible occurrence region should be no less than 6, while 11 stations will be optimal. Frequency points setting at high frequency section (100~1000 Hz) should be no less than 3, 4 points as best.

**Acknowledgments.** This work was supported by National Special Research Fund (Gas Hydrate Resource Exploration and Production Testing Project) (No. GZHL20110313) and National Natural Science Foundation of China (No. 41274185). We wish to thank the anonymous reviewers for their valuable and constructive comments and suggestions which helped us to improve our manuscript.

## References

- Abdelzaher, M., J. Nishijima, G. El-Qady, E. Aboud, O. Masoud, M. Soliman, and S. Ehara (2011), Gravity and magnetotelluric investigations to elicit the origin of Hammam Faraun hot spring, Sinai Peninsula, Egypt, *Acta Geophys.* **59**, 3, 633-656, DOI: 10.2478/s11600-011-0006-4.
- Archie, G.E. (1942), The electrical resistivity log as an aid in determining some reservoir characteristics, *Trans. AIME* **146**, 1, 54-62, DOI: 10.2118/942054-G.
- Balyavskii, V.V., and V.V. Sukhoi (2004), The method of audio-frequency magnetotelluric sounding in mineral exploration, *Izv. – Phys. Solid Earth.* **40**, 6, 515-533.
- Boswell, R., and T.S. Collett (2011), Current perspectives on gas hydrate resources, *Energy Environ. Sci.* **4**, 1206-1215, DOI: 10.1039/c0ee00203h.
- Boswell, R., G. Moridis, M. Reagan, and T.S. Collett (2011), Gas hydrate accumulation types and their application to numerical simulation. **In:** *Proc. 7th Int. Conf. on Gas Hydrates (ICGH 2011), 17-22 July 2011, Edinburgh, Scotland*, Manuscript No. 130.
- Bronner, G., and J.P. Fournou (1992), Audio-magnetotelluric investigation of allochthonous iron formations in the Archaean Reguibat shield (Mauritania): structural and mining implications, *J. Afr. Earth Sci.* **15**, 3-4, 341-351, DOI: 10.1016/0899-5362(92)90019-9.
- Bybee, K. (2004), Natural gas technology/monetization: Overview of the Mallik gas-hydrate production research well, *J. Petrol. Technol.* **56**, 4, 53-54, DOI: 10.2118/0404-0053-JPT.
- Carcione, J.M., and D. Gei (2004), Gas-hydrate concentration estimated from P- and S-wave velocities at the Mallik 2L-38 research well, Mackenzie Delta, Canada, *J. Appl. Geophys.* **56**, 1, 73-78, DOI: 10.1016/j.jappgeo.2004.04.001.
- Clerc, G., J.P. Décriaud, G. Doyen, M. Halbwegs, M. Henrotte, J. Rémy, and X.C. Zhang (1984), An automatic audio-magnetotelluric equipment, controlled by microprocessor, for the telesurveillance of the volcano Momotombo (Nicaragua), *Surv. Geophys.* **6**, 3-4, 291-304, DOI: 10.1007/BF01465544.
- Coggon, J.H. (1971), Electromagnetic and electrical modeling by the finite element method, *Geophysics* **36**, 1, 132-155, DOI: 10.1190/1.1440151.
- Collett, T.S. (2002), Energy resource potential of natural gas hydrates, *AAPG Bull.* **86**, 11, 1971-1992.
- Collett, T.S. (2005), Results at Mallik highlight progress in gas hydrate energy resource research and development, *Petrophysics* **46**, 3, 237-243.
- Collett, T.S., M.W. Lee, W.F. Agena, J.J. Miller, K.A. Lewis, M.V. Zyrianova, R. Boswell, and T.L. Inks (2011), Permafrost-associated natural gas hydrate occurrences on the Alaska North Slope, *Mar. Petrol. Geol.* **28**, 2, 279-294, DOI: 10.1016/j.marpetgeo.2009.12.001.

- Constable, S.C., R.L. Parker, and C.G. Constable (1987), Occam's inversion: A practical algorithm for generating smooth models from electromagnetic sounding data, *Geophysics* **52**, 3, 289-300, DOI: 10.1190/1.1442303.
- De Luga, P.P., and P.E. Wannamaker (1996), Calculating the two-dimensional magnetotelluric Jacobian in finite elements using reciprocity, *Geophys. J. Int.* **127**, 3, 806-810, DOI: 10.1111/j.1365-246X.1996.tb04060.x.
- Dickens, G.R. (2001), The potential volume of oceanic methane hydrates with variable external conditions, *Org. Geochem.* **32**, 10, 1179-1193, DOI: 10.1016/S0146-6380(01)00086-9.
- Fu, J.H., and L.F. Zhou (1998), Carboniferous-Jurassic stratigraphic provinces of the southern Qilian basin and their petrogeological features, *Northwest Geosci.* **19**, 2, 47-54 (in Chinese).
- Goldberg, S., and Y. Rotstein (1982), A simple form of presentation of magnetotelluric data using the Bostick transform, *Geophys. Prosp.* **30**, 2, 211-216, DOI: 10.1111/j.1365-2478.1982.tb01299.x.
- Guo, X.W., and Y.H. Zhu (2011), Well logging characteristics and evaluation of hydrates in Qilian Mountain permafrost, *Geol. Bull. China* **30**, 12, 1869-1873 (in Chinese).
- Hestenes, M.R. (1973), Iterative methods for solving linear equations, *J. Optimiz. Theory App.* **11**, 4, 323-334, DOI: 10.1007/BF00932484.
- Hestenes, M.R., and E. Stiefel (1952), Methods of conjugate gradients for solving linear systems, *J. Res. Nat. Bur. Stand.* **49**, 6, 409-436, DOI: 10.6028/jres.049.044.
- Hu, Z.Z., X.Y. Hu, and Z.X. He (2006), Pseudo-three-dimensional magnetotelluric inversion using nonlinear conjugate gradients, *Chinese J. Geophys.* **49**, 4, 1111-1120, DOI: 10.1002/cjg2.934.
- Huo, Y.Y., and M. Zhang (2009), Full waveform inversion of gas hydrate reflectors in Northern South China Sea, *Acta Geophys.* **57**, 3, 716-727, DOI: 10.2478/s11600-009-0011-z.
- Israil, M. (2006), Delineation of layer boundaries from smooth models obtained from the geoelectrical sounding data inversion, *Acta Geophys.* **54**, 2, 126-141, DOI: 10.2478/s11600-006-0012-0.
- Koh, C.A., A.K. Sum, and E.D. Sloan (2012), State of the art: Natural gas hydrates as a natural resource, *J. Nat. Gas Sci. Eng.* **8**, 132-138, DOI: 10.1016/j.jngse.2012.01.005.
- Lee, M.W., and T.S. Collett (2011), In-situ gas hydrate saturation estimated from various well logs at the Mount Elbert Gas Hydrate Stratigraphic Test Well, Alaska North Slope, *Mar. Petrol. Geol.* **28**, 2, 439-449, DOI: 10.1016/j.marpetgeo.2009.06.007.
- Li, X.S., B. Yang, G. Li, and B. Li (2012), Numerical simulation of gas production from natural gas hydrate using a single horizontal well by depressurization

- in Qilian Mountain permafrost, *Ind. Eng. Chem. Res.* **51**, 11, 4424-4432, DOI: 10.1021/ie201940t.
- Lin, Z.Z., Y. Li, W.L. Gao, G.S. Kong, and S.Z. Sun (2013), Physical character analysis of logging data for natural gas hydrate in Qilian Mountain permafrost area, *Geophys. Geochem. Explor.* **37**, 5, 834-838.
- Lu, Z.Q., Y.H. Zhu, Y.Q. Zhang, H.J. Wen, Y.H. Li, and C.L. Liu (2011), Gas hydrate occurrences in the Qilian Mountain permafrost, Qinghai Province, China, *Cold Reg. Sci. Technol.* **66**, 2-3, 93-104, DOI: 10.1016/j.coldregions.2011.01.008.
- Lu, Z.Q., Y.H. Zhu, H. Liu, Y.Q. Zhang, C.S. Jin, X. Huang, and P.K. Wang (2013a), Gas source for gas hydrate and its significance in the Qilian Mountain permafrost, Qinghai, *Mar. Petrol. Geol.* **43**, 341-348, DOI: 10.1016/j.marpetgeo.2013.01.003.
- Lu, Z.Q., X.H. Xue, Z.W. Liao, and H. Liu (2013b), Source rocks for gases from gas hydrate and their burial depth in the Qilian Mountain permafrost, Qinghai: Results from thermal stimulation, *Energy Fuels* **27**, 12, 7233-7244, DOI: 10.1021/ef4010797.
- Mackie, R.L., J.T. Smith, and T.R. Madden (1994), Three-dimensional electromagnetic modeling using finite difference equations: The magnetotelluric example, *Radio Sci.* **29**, 4, 923-935, DOI: 10.1029/94RS00326.
- Moridis, G.J., T.S. Collett, M. Pooladi-Darvish, S. Hancock, C. Santamarina, R. Boswell, T. Kneafsey, J. Rutqvist, M.B. Kowalsky, M.T. Reagan, E.D. Sloan, A.K. Sum, and C.A. Koh (2011), Challenges, uncertainties, and issues facing gas production from gas hydrate deposits, *SPE Reserv. Eval. Eng.* **14**, 1, 76-112, SPE-131792, DOI: 10.2118/131792-PA.
- Newman, G.A., and D.L. Alumbaugh (1997), 3D electromagnetic modeling using staggered finite differences. **In:** 1997 *IEEE Int. Geosci. Remote Sens. Symp. "Remote Sensing – A Scientific Vision for Sustainable Development"*, 3-8 August 1997, Singapore, Vol. 2, 929-932, DOI: 10.1109/IGARSS.1997.615301.
- Newman, G.A., and D.L. Alumbaugh (2000), Three-dimensional magnetotelluric inversion using non-linear conjugate gradients, *Geophys. J. Int.* **140**, 2, 410-424, DOI: 10.1046/j.1365-246x.2000.00007.x.
- Ogawa, Y., M. Uyeshima, Y. Honkura, H. Utada, and S. Koyama (1994), Audio-frequency magnetotelluric imaging of an active strike-slip fault, *J. Geomagn. Geoelectr.* **46**, 5, 403-408, DOI: 10.5636/jgg.46.403.
- Pang, S.J., X. Su, H. He, Q. Zhao, Y.H. Zhu, P.K. Wang, Y.H. Li, and Q.H. Li (2013), Geological controlling factors of gas hydrate occurrence in Qilian Mountain permafrost, China, *Earth Sci. Front.* **20**, 1, 223-239 (in Chinese).
- Rodi, W., and R.L. Mackie (2001), Nonlinear conjugate gradients algorithm for 2-D magnetotelluric inversion, *Geophysics* **66**, 1, 174-187, DOI: 10.1190/1.1444893.

- Ryan, W.B.F., S.M. Carbotte, J.O. Coplan, S. O'Hara, A. Melkonian, R. Arko, R.A. Weissel, V. Ferrini, A. Goodwillie, F. Nitsche, J. Bonczkowski, and R. Zemsky (2009), Global multi-resolution topography synthesis, *Geochem. Geophys. Geosyst.* **10**, 3, DOI: 10.1029/2008GC002332.
- Santos, F.A.M., A. Trota, A. Soares, R. Luzio, N. Lourenço, L. Matos, E. Almeida, J.L. Gaspar, and J.M. Miranda (2006), An audio- magnetotelluric investigation in Terceira Island (Azores), *J. Appl. Geophys.* **59**, 4, 314-323, DOI: 10.1016/j.jappgeo.2005.12.001.
- Santos, F.A.M., A.R.A. Afonso, and A. Dupis (2007), 2D joint inversion of dc and scalar audio-magnetotelluric data in the evaluation of low enthalpy geothermal fields, *J. Geophys. Eng.* **4**, 1, 53-62, DOI: 10.1088/1742-2132/4/1/007.
- Schnegg, P.A., B.V. Lequang, G. Fischer, and J.T. Weaver (1983), Audio-magnetotelluric study of a structure with a reverse fault, *J. Geomagn. Geoelectr.* **35**, 11-12, 653-671, DOI: 10.5636/jgg.35.653.
- Sloan, E.D., Jr. (1998), *Clathrate Hydrates of Natural Gases*, 2nd ed., Marcel Dekker Inc., New York.
- Smith, J.T., and J.R. Booker (1991), Rapid inversion of two- and three-dimensional magnetotelluric data, *J. Geophys. Res.* **96**, B3, 3905-3922, DOI: 10.1029/90JB02416.
- Spichak, V.V. (2012), Evaluation of the feasibility of recovering the magma chamber's parameters by 3D Bayesian statistical inversion of synthetic MT data, *Acta Geophys.* **60**, 3, 942-958, DOI: 10.2478/s11600-012-0008-x.
- Strangway, D.W., C.M. Swift, Jr., and R.C. Holmer (1973), The application of audio-frequency magnetotellurics (AMT) to mineral exploration, *Geophysics* **38**, 6, 1159-1175, DOI: 10.1190/1.1440402.
- Sun, Z.J., Z.B. Yang, H. Mei, A.H. Qin, F.G. Zhang, Y.L. Zhou, S.Y. Zhang, and B.W. Mei (2014), Geochemical characteristics of the shallow soil above the Muli gas hydrate reservoir in the permafrost region of the Qilian Mountains, China, *J. Geochem. Explor.* **139**, 160-169, DOI: 10.1016/j.gexplo.2013.10.006.
- Tikhonov, A.N., and V.Y. Arsenin (1978), Solutions of ill-posed problems, *Math. Comput.* **32**, 144, 1320-1322, DOI: 10.2307/2006360.
- Wang, P.K., Y.H. Zhu, Z.Q. Lu, X. Huang, S.J. Pang, and S. Zhang (2014), Gas hydrate stability zone migration occurred in the Qilian Mountain permafrost, Qinghai, Northwest China: Evidences from pyrite morphology and pyrite sulfur isotope, *Cold Reg. Sci. Technol.* **98**, 8-17, DOI: 10.1016/j.coldregions.2013.10.006.
- Wang, T. (2010), Gas hydrate resource potential and its exploration and development prospect of the Muli coalfield in the northeast Tibetan plateau, *Energ. Explor. Exploit.* **28**, 3, 147-158, DOI: 10.1260/0144-5987.28.3.147.

- Wannamaker, P.E. (1991), Advances in three-dimensional magnetotelluric modeling using integral equations, *Geophysics* **56**, 11, 1716-1728, DOI: 10.1190/1.1442984.
- Wannamaker, P.E., J.A. Stodt, and L. Rijo (1987), A stable finite element solution for two-dimensional magnetotelluric modelling, *Geophys. J. Int.* **88**, 1, 277-296, DOI: 10.1111/j.1365-246X.1987.tb01380.x.
- Wu, Q.B., G.L. Jiang, and P. Zhang (2010), Assessing the permafrost temperature and thickness conditions favorable for the occurrence of gas hydrate in the Qinghai-Tibet Plateau, *Energ. Conv. Manage.* **51**, 4, 783-787, DOI: 10.1016/j.enconman.2009.10.035.
- Xiao, K., C.C. Zou, B. Xiang, and J.Q. Liu (2013), Acoustic velocity log numerical simulation and saturation estimation of gas hydrate reservoir in Shenhu area, South China Sea, *Sci. World J.* **2013**, 101459, DOI: 10.1155/2013/101459.
- Xiong, Z.H., and A.C. Tripp (1997), 3-D electromagnetic modeling for near-surface targets using integral equations, *Geophysics* **62**, 4, 1097-1106, DOI: 10.1190/1.1444210.
- Xu, S.Z. (1994), *The Finite Element Method in Geophysics*, Science Press, Beijing (in Chinese).
- Yamaguchi, S., Y. Ogawa, K. Fuji-ta, N. Ujihara, H. Inokuchi, and N. Oshiman (2010), Audio-frequency magnetotelluric imaging of the Hijima fault, Yamasaki fault system, southwest Japan, *Earth Planets Space* **62**, 4, 401-411, DOI: 10.5047/eps.2009.12.007.
- Yang, R., P. Yan, N.Y. Wu, Z.B. Sha, and J.Q. Liang (2014), Application of AVO analysis to gas hydrates identification in the northern slope of the South China Sea, *Acta Geophys.* **62**, 4, 802-817, DOI: 10.2478/s11600-013-0193-2.
- Yao, D.W., S.M. Wang, D. Lei, W. Zhu, and G. Wang (2013), Application of CSAMT to Qilian Mountain permafrost region gas hydrate investigation, *Chin. J. Eng. Geophys.* **10**, 2, 132-137 (in Chinese).
- Zhao, J.F., T. Yu, Y.C. Song, D. Liu, W.G. Liu, Y. Liu, M.J. Yang, X.K. Ruan, and Y.H. Li (2013), Numerical simulation of gas production from hydrate deposits using a single vertical well by depressurization in the Qilian Mountain permafrost, Qinghai-Tibet Plateau, China, *Energy* **52**, 308-319, DOI: 10.1016/j.energy.2013.01.066.
- Zhu, Y.H., Y.Q. Zhang, H.J. Wen, Z.Q. Lu, Z.Y. Jia, Y.H. Li, Q.H. Li, C.L. Liu, P.K. Wang, and X.W. Guo (2010), Gas hydrates in the Qilian Mountain permafrost, Qinghai, Northwest China, *Acta Geol. Sin. (Engl. Ed.)* **84**, 1, 1-10, DOI: 10.1111/j.1755-6724.2010.00164.x.

Received 11 June 2014

Received in revised form 10 August 2014

Accepted 25 August 2014



# Experimental Investigation of Kinetic Energy and Momentum Coefficients in Regular Channels with Stiff and Flexible Elements Simulating Submerged Vegetation

Elżbieta KUBRAK, Janusz KUBRAK, and Adam KICZKO

Faculty of Civil and Environmental Engineering,  
Warsaw University of Life Sciences, Warszawa, Poland;  
e-mails: Elzbieta\_Kubrak@sggw.pl, Janusz\_Kubrak@sggw.pl,  
Adam\_Kiczko@sggw.pl (corresponding author)

## Abstract

The paper addresses the problem of determination of the energy and momentum coefficients for flows through a partly vegetated channel. These coefficients are applied to express the fluid kinetic energy and momentum equations as functions of a mean velocity. The study is based on laboratory measurements of water velocity distributions in a straight rectangular flume with stiff and flexible stems and plastic imitations of the Canadian waterweed. The coefficients were established for the vegetation layer, surface layer and the whole flow area. The results indicate that the energy and momentum coefficients increase significantly with water depth and the number of stems per unit channel area. New regression relationships for both coefficients are given.

**Key words:** submerged flexible and rigid vegetation, velocity profile, energy and momentum coefficients.

## 1. INTRODUCTION

Understanding the impact of vegetation on water flow conditions has become important in river restoration projects. In the last decades a turbulent flow structure in rivers and channels with vegetation have been extensively studied by Nepf and Vivoni (2000), Nepf and Ghisalberti (2008), Nepf (2012), Cameron *et al.* (2013), Poggi *et al.* (2004), Righetti (2008), and others. In the same time, studies to find an appropriate way of description of the vegetation roughness (see, *e.g.*, Kubrak *et al.* 2008, 2012, 2013) were evaluated. River flows can be described in detail by the Navier–Stokes equation. However, in many practical applications it is possible to simplify the model, reducing computational and data costs. In engineering applications an assumption of a one-dimensional character of a flow is often used, where all state variables refer to averaged quantities. For a channel flow, variables in a wide cross-section are averaged over the water depth and width. The common practical problem is the determination of water profiles in rivers and channels. The solution is based on a one-dimensional form of the energy equation, or the momentum equation, if the water surface profile varies rapidly and is established under a mixed flow regime. Both these equations use different velocity-distributions coefficients, whose values are nearly equal, but involve different meanings of the frictional losses (Chow 1959, Yen 2002).

The expression for the fluid kinetic energy equation as a function of mean velocity requires the energy coefficient  $\alpha$  (also termed as the Coriolis coefficient or the Saint Venant coefficient) to be introduced. In the case of the momentum equation it is the momentum coefficient  $\beta$  (also termed as the Boussinesq coefficient). These coefficients might be elaborated on account of velocity measurements or an assumed velocity profile with depth. Fenton (2005) stated that neglecting these coefficients in hydraulic calculations of an open channel flow might introduce an error of 5-10%. The presence of vegetation within a channel causes a distortion of a flow field, which is shaped by plant heights, spacing geometrical and mechanical properties. If a plant height is lower than the water depth, vegetation is considered as short and within the flow field at least two layers can be distinguished, namely: vegetated and surface ones. This simplified classification is an introduction into assessing the vegetation impact on analyzed coefficient values.

To express the kinetic energy in the channel cross-section using the mean velocity, it is necessary to adopt the correction coefficient, defined as:

$$\alpha = \frac{\int v^3 dA}{v_m^3 A} . \quad (1)$$

Similarly, the stream momentum in the channel cross-section, expressed as a function of the mean velocity, requires the momentum coefficient  $\beta$ :

$$\beta = \frac{\int v^2 dA}{v_m^2 A}, \quad (2)$$

where  $v_m$  is the mean water velocity in the cross-section calculated as  $v_m = Q/A$ ,  $Q$  is the discharge, and  $A$  is the cross-sectional area.

For a uniform velocity field, the energy and momentum coefficients are equal to one. On the contrary, the coefficients take values higher than one. Analyzing Eqs. 1 and 2 it can be seen that the momentum coefficient  $\beta$  should be smaller than the energy coefficient  $\alpha$ . Chow (1959) presented values of the energy and momentum coefficients for natural and artificial channels of uniform cross-sections. In this study, the reported energy coefficient  $\alpha$  is within the range of  $\alpha \in (1.10 \div 2.00)$ , and the momentum coefficient satisfies the following:  $\beta \in (1.03 \div 1.33)$ . Strauss (1967) stated that the energy and momentum coefficients are functions of a velocity profile over the depth and a cross-sectional shape, parameterized with lengths of the bottom and slope. For wide, rectangular channels, the coefficient values are mostly determined only by the velocity profile over the depth (Rehbock 1922). In the literature there is a lack of information concerning values of these coefficients for uniform channels with vegetation.

This article accounts for the determination of the energy and momentum coefficients in a rectangular, wide channel with a short vegetation simulated with stiff and flexible stems, as well as with plastic imitations of the Canadian waterweed (*Elodea Canadensis sp.*). The outcome and the main novelty of the research are methodological grounds to improve accuracy of one-dimensional flow routing models of partly vegetated channels, used to solve practical problems like calculations of water depths in drainage-irrigation systems.

The application of the rectangular channel allowed to exclude the effect of the channel cross-section shape on the velocity profile and as a result on the computed coefficients. The values of energy and momentum coefficient were determined in three sets: for vegetation and surface layers, and for the total cross-section. As a result it was possible to assess the energy and momentum coefficients for a velocity field affected by the presence of vegetation, also in a free region when values were computed for a surface layer. The common approach in practical studies, involving a one-dimensional modeling of water profiles, is an assumption of a zero flow in a vegetation layer. The article is based on laboratory experiments whose results were already presented by Kubrak *et al.* (2008, 2012, 2013), wherein they were used to verify the model of the velocity profile for a channel with different

elements imitating vegetation. The methodology and outcomes of laboratory experiments are given here briefly.

## 2. EXPERIMENTAL INVESTIGATIONS

The hydraulic experiments were settled in the Hydraulics Laboratory of the Warsaw University of Life Sciences – SGGW. The laboratory channel is characterized by a straight run with an adaptable slope, a rectangular cross-section, and the following dimensions: the length of 16 m, width of 0.58 m, and height of 0.60 m (Fig. 1). The measurements were conducted for steady flow conditions, in the channel with elements simulating the stiffness and flexibility, as a result of the pressure force of a stream on vegetation.

The vegetation was simulated by:

- Stiff wooden stems of a cylindrical shape (Fig. 2a), diameter  $d = 0.0022$  m and a height of 0.11 m (Kubrak 2007).
- Flexible stems, made from the PVC, of the elliptical shape, diameters  $d_1 = 0.00095$  m,  $d_2 = 0.0007$  m, and a height of 0.165 m (Fig. 2b); with a mean value of elasticity modulus  $E = 3630$  MPa, determined on the basis of measurements performed with the strength testing machine – INSTRON 5582 (Kubrak 2007).
- Artificial plants imitating the Canadian waterweed (*Elodea Canadensis* sp.), made of a PVC with a height of 0.11 m, presented in Fig. 2c (Wójtowicz *et al.* 2010, Kubrak *et al.* 2013).

The vegetation models were installed on a plate of the  $k_s = 0.0001$  m roughness height. The mounting nodes were organized in squares of the side length  $s$  (Fig. 3). Two horizontal components of mean velocities (longitudinal and transversal) were measured with the use of a programmable electromagnetic liquid velocity meter (PEMS) manufactured by Delft Hydraulics. The velocity measurements were made for two channel slopes:  $i = 0.0087$  and  $i = 0.0174$ . The experimental variants are set up in Table 1.

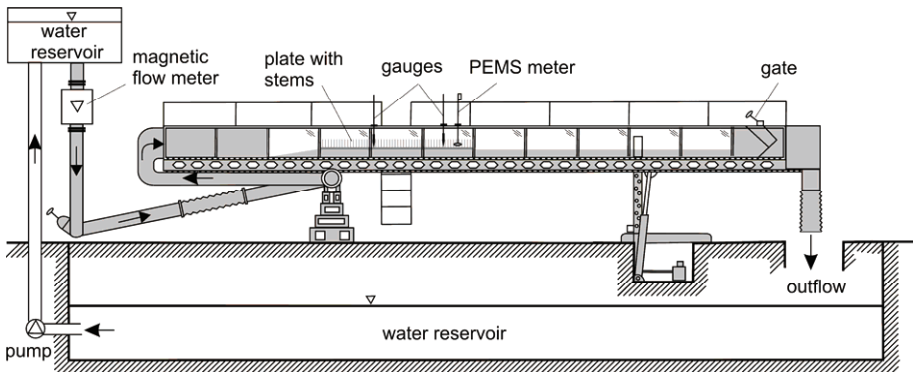


Fig. 1. The layout of the experimental flume.

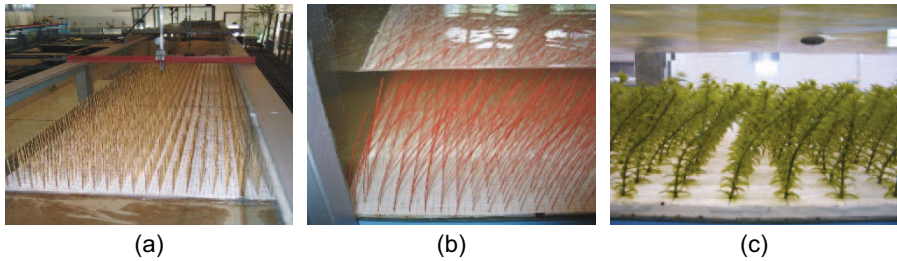


Fig. 2. Setup of plant models in the laboratory channel: (a) stiff elements, (b) flexible elements, and (c) submerged elastic elements of artificial plants simulating Canadian waterweed (*Elodea Canadensis* sp.). Photos acquired from Kubrak (2007) and Wójtowicz *et al.* (2010).

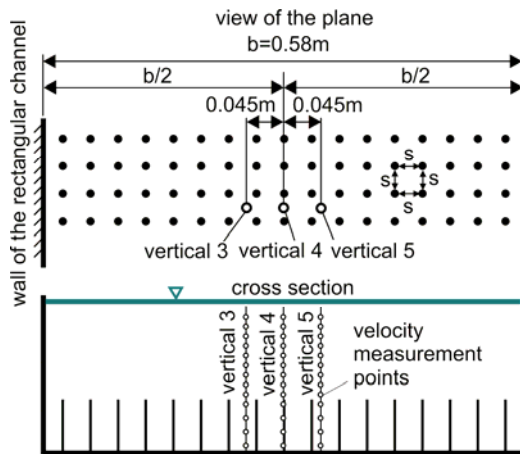


Fig. 3. The artificial vegetation pattern and the placement of measure cross-sections and velocity measure points.

The water discharge was measured with the electromagnetic flow meter, situated at the inflow pipe. The water depth was captured with 0.1 mm accuracy. The water level was controlled with a gate, placed at the channel end (Fig. 1).

Examples of measured and calculated velocity profiles, taken above the stiff and flexible stems, are presented in Fig. 4. Profiles were modeled, basing on the mixing length concept (Kubrak 2007, Kubrak *et al.* 2008, 2013). Because of the high agreement between calculated and measured velocity profiles, resulting in high values of the Linear Correlation Coefficient  $R$  and small differences between calculated and measured values (MRE), the energy and momentum coefficients were determined taking the calculated profiles.

Table 1

## Basic set-up of the experiments of velocity measurements

Element types	Spacing stems $s$ [m]	Number of stems per unit channel area $m$ [stems/m <sup>2</sup> ]	Slope $i$ [-]	Case
Stiff stems	0.015	4032	0.0087 0.0174	S.1.1 S.1.2
	0.030	1008	0.0087 0.0174	S.2.1 S.2.2
Flexible stems	0.010	10000	0.0087 0.0174	E.1.1 E.1.2
	0.020	2500	0.0087 0.0174	E.2.1 E.2.2
Elements simulating Canadian waterweed	0.045	507	0.0087	C.1.1
			0.0174	C.1.2

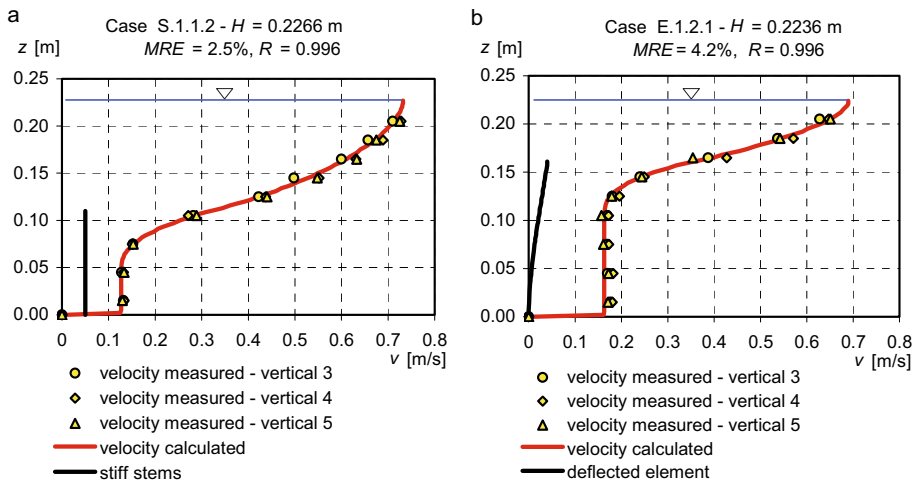


Fig. 4. The calculated and measured velocity profiles: (a) in the channel with stiff stems, and (b) in the channel with flexible stems.

Integration of velocity over the cross-sectional surface  $A$  was done using a grid method (Hulsing *et al.* 1966), where the flow field is discretized with the Cartesian grid. For greater accuracy, the size of the grid should be chosen as small as possible and here it always was below 0.0025 m. Assuming that the effective velocity through each grid is equal to that at the center of gravity of the grid, the quantities  $\Sigma v dA$ ,  $\Sigma v^2 dA$ , and  $\Sigma v^3 dA$  are computed. The val-

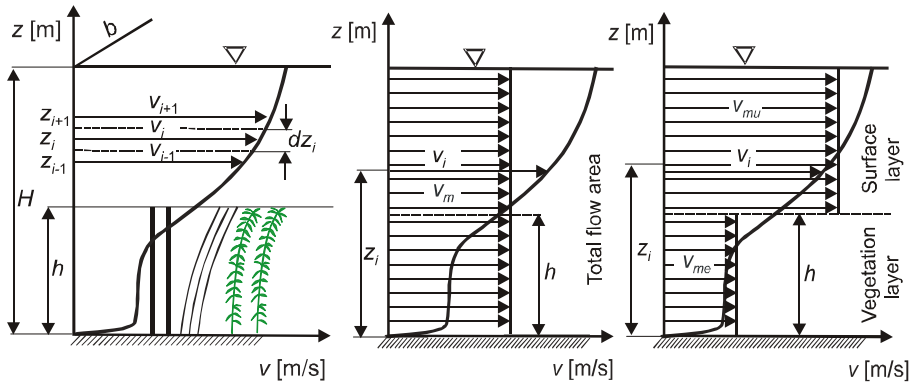


Fig. 5. Vertical profiles of the velocity in the channel used in energy  $\alpha$  and momentum  $\beta$  coefficients calculations;  $v_i$  is the velocity at the center of gravity of the grid,  $h$  – height of the submerged stiff or deflected elements,  $v_{me}$  – mean velocity in layer with elements,  $v_{mu}$  – mean velocity in layer over elements, and  $v_m$  – mean velocity in profile.

ues of  $\alpha$  and  $\beta$  are computed according to Eqs. 1 and 2. As the flow field significantly differs in the layer of vegetation and above, the calculations were performed separately for each layer and also for the whole profile (Fig. 5). The coefficients determined for the surface layer reflect the values used in practical applications of the one-dimensional water depth modeling where a flow through vegetation layer is neglected.

### 3. RESULTS OF CALCULATION AND DISCUSSION

Examples of velocity profiles shaped by stiff stems for which, *i.e.*, coefficients were determined are presented in Fig. 6. Computed energy and momentum coefficients for vegetation layer, upper layer over elements and a total flow area as a function of the ratio of mean velocities of surface and vegetation layers,  $v_{mu}/v_{me}$ , are presented in Figs. 7 and 8. The numerical values used in the plots (Figs. 7 and 8) are set together in Table 2.

Figures 6-8 show that the energy  $\alpha$  and the momentum  $\beta$  coefficients increase with a variation of the velocity profile. The velocity distribution in the vegetated layer for elements simulating the Canadian waterweed have a similar shape as those for stiff stems: just above a bottom the velocity significantly increases to become uniform for the major part of the vegetated layer and again increases while getting closer to a top of elements. The height of the constant velocity zone decreases with reduction of elements' density and the ratio of water depth and the element height  $H/h$ . For smaller elements' densities, the velocity in a constant zone is higher, which results in a more even profile (Fig. 6). That explains why energy  $\alpha$  and momentum  $\beta$  coeffi-

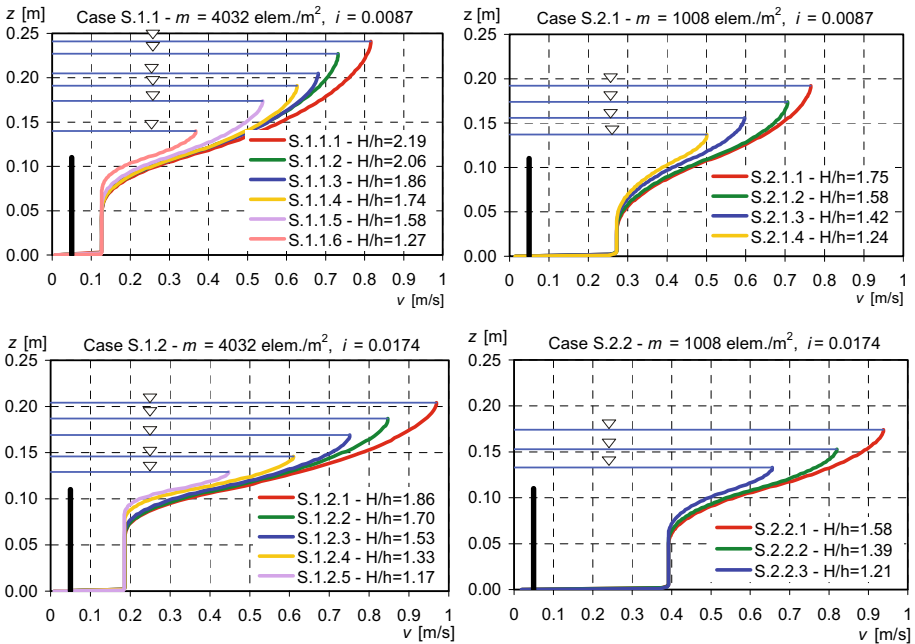


Fig. 6. Computed velocity profiles for flume with stiff elements (cases S.1.1, S.1.2, S.2.1, S.2.2) used for calculation of energy  $\alpha$  and momentum  $\beta$  coefficients.

coefficients for dense elements spacing reach higher values and are characterized by stronger variation than for the surface layer.

The highest variation of the velocity occurs when the total flow area is considered and increases with the flow depth. This is seen in the energy and momentum coefficients values, which follow this schema: they are highest for the total flow area and increase with a flow depth.

The variation of the flow profile decreases with an increase of plant spacing. For spacing of  $m = 4032$  stems/ $m^2$  with a flow depth and the stiff stems height ratio of  $H/h \in (1.17 \div 2.19)$ , the relationship of a mean velocity in the surface and vegetation layer is in the range of  $v_{mu}/v_{me} \in (2.00 \div 4.01)$ . The corresponding values of the energy coefficient are in the range  $\alpha \in (1.44 \div 2.29)$ . In the surface layer, where the velocity variation is the lowest, the energy coefficient is within the range of  $\alpha \in (1.04 \div 1.13)$ . In the vegetation layer, where usually an even velocity distribution is presupposed, values of  $\alpha$  coefficients appeared to be higher than in the surface layer and fall within  $\alpha \in (1.05 \div 1.42)$ . An increase in the spacing of stiff stems from  $m = 4032$  stems/ $m^2$  to  $m = 1008$  stems/ $m^2$  causes a reduction of the velocity profile variation, characterized by the velocity ratio  $v_{mu}/v_{me} \in (1.42 \div 2.04)$ .

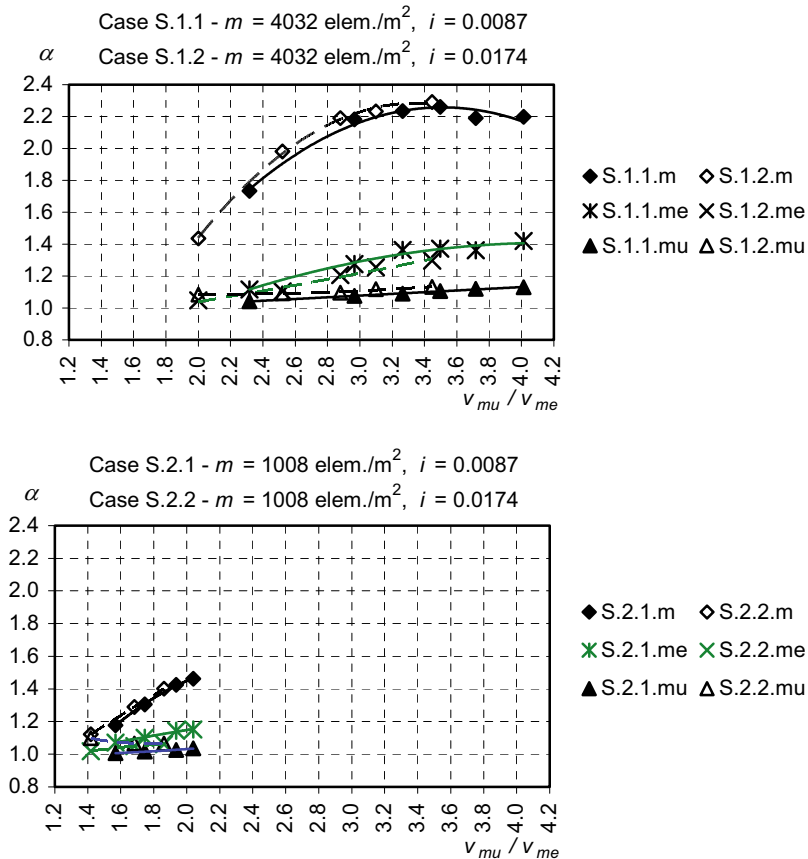


Fig. 7. Computed energy  $\alpha$  coefficients in relation to the quotient of mean velocities in layer with stiff elements, over elements and the mean velocity in profile (cases S.1.1, S.1.2, S.2.1, S.2.2), where  $me$  is the mean velocity in layer with elements,  $mu$  – mean velocity in layer over elements, and  $m$  – mean velocity in profile.

Consequently, the values of the energy coefficient are reduced to  $\alpha \in (1.12 \div 1.46)$  for the total flow area and  $\alpha \in (1.01 \div 1.10)$  for the surface layer. In a vegetation layer, the energy coefficient is in the scope of  $\alpha \in (1.02 \div 1.15)$  and slightly surpasses values reported in the surface layer.

The highest values of the momentum coefficient,  $\beta \in (1.12 \div 1.40)$ , are recorded for the total flow area in a channel with stiff stems of  $m = 4032 \text{ stems/m}^2$  spacing. The increase of the spacing to  $m = 1008 \text{ stems/m}^2$  reduces the momentum coefficient to the range of  $\beta \in (1.04 \div 1.15)$ . In the vegetation and surface layers the values of the momentum coefficient are close to unity:  $\beta \in (1.00 \div 1.05)$ .

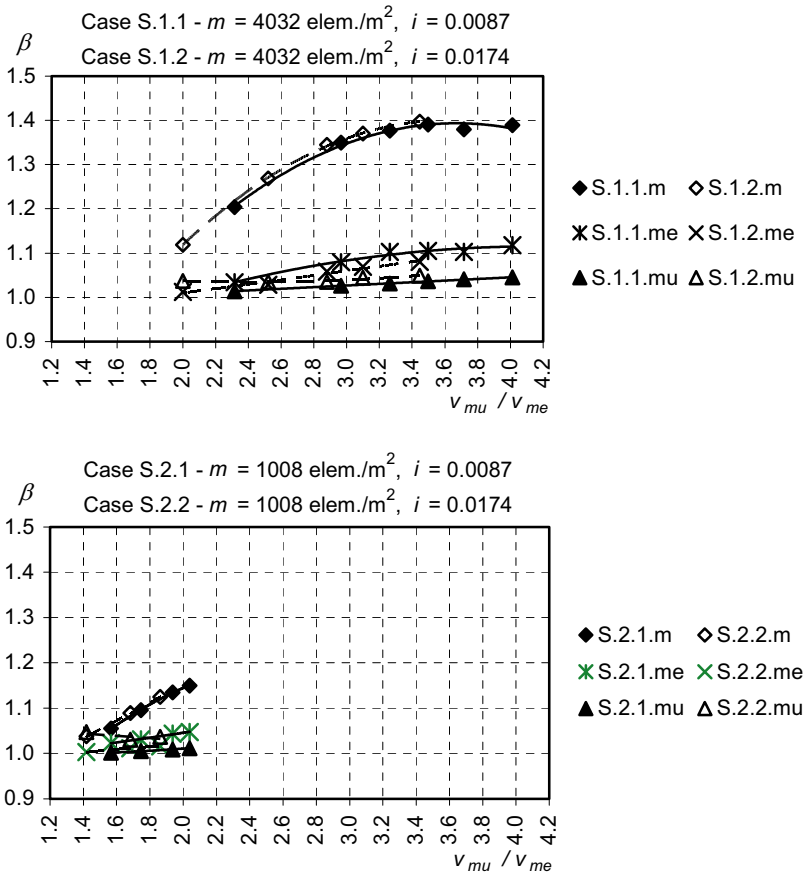


Fig. 8. Computed momentum  $\beta$  coefficients in relation to quotient of mean velocities in layer with stiff elements, over elements and mean velocity in profile (cases S.1.1, S.1.2, S.2.1, S.2.2), where  $me$  is the mean velocity in layer with elements,  $mu$  – mean velocity in layer over elements, and  $m$  – mean velocity in profile.

The results presented in Figs. 7 and 8 suggest that the energy and momentum coefficients depend on the water height above the vegetation and they are not influenced by the channel bottom slope.

A similar dependence was constructed for flexible stems ( $m = 10000 \text{ stems/m}^2$ ,  $m = 2500 \text{ stems/m}^2$ ) and for plastic imitations of the Canadian waterweed ( $m = 507 \text{ stems/m}^2$ ). The calculated ranges of the energy and momentum coefficients as a function of water depth  $H$  and the plant height ratio  $h$  are presented in Table 2. The results for all investigated plant models are shown in Figs. 9 and 10.

Table 2

The energy and momentum coefficients computed for the vegetation, surface layers, and the total flow area

Case	$H$ [m]	$h$ [m]	Total flow area			Vegetation layer			Surface layer					
			$Q$ [m <sup>3</sup> /s]	$v_m$ [m/s]	$\alpha$ [-]	$\beta$ [-]	$Q_{ve}$ [m <sup>3</sup> /s]	$v_{ve}$ [m/s]	$\alpha$ [-]	$\beta$ [-]	$Q_{su}$ [m <sup>3</sup> /s]	$v_{su}$ [m/s]	$\alpha$ [-]	$\beta$ [-]
S.1.1	S.1.1.1	0.2414	0.0602	0.430	2.20	1.39	0.0104	0.163	1.42	1.12	0.0498	0.654	1.13	1.05
	S.1.1.2	0.2266	0.0501	0.381	2.19	1.38	0.0102	0.159	1.36	1.10	0.0400	0.591	1.12	1.04
	S.1.1.3	0.2047	0.0406	0.342	2.26	1.39	0.0101	0.159	1.37	1.11	0.0305	0.556	1.11	1.04
	S.1.1.4	0.1911	0.0346	0.312	2.23	1.38	0.0102	0.159	1.36	1.10	0.0244	0.519	1.09	1.03
	S.1.1.5	0.1736	0.0263	0.261	2.18	1.35	0.0097	0.152	1.28	1.08	0.0166	0.451	1.08	1.03
	S.1.1.6	0.1399	0.0144	0.178	1.73	1.20	0.0089	0.139	1.12	1.03	0.0056	0.322	1.04	1.01
S.1.2	S.1.2.1	0.2043	0.0570	0.481	2.29	1.40	0.0144	0.226	1.30	1.08	0.0426	0.779	1.13	1.05
	S.1.2.2	0.1869	0.0450	0.415	2.23	1.37	0.0142	0.223	1.25	1.07	0.0308	0.691	1.12	1.04
	S.1.2.3	0.1686	0.0349	0.357	2.19	1.35	0.0138	0.216	1.21	1.06	0.0212	0.622	1.10	1.04
	S.1.2.4	0.1464	0.0237	0.279	1.98	1.27	0.0129	0.203	1.10	1.03	0.0108	0.512	1.09	1.04
	S.1.2.5	0.1292	0.0168	0.224	1.44	1.12	0.0125	0.195	1.05	1.01	0.0043	0.390	1.08	1.04
S.2.1	S.2.1.1	0.1920	0.0534	0.480	1.46	1.15	0.0212	0.332	1.15	1.05	0.0322	0.677	1.04	1.01
	S.2.1.2	0.1735	0.0443	0.440	1.43	1.14	0.0209	0.328	1.14	1.04	0.0234	0.635	1.03	1.01
	S.2.1.3	0.1559	0.0346	0.383	1.31	1.10	0.0200	0.314	1.10	1.03	0.0146	0.548	1.02	1.01
	S.2.1.4	0.1365	0.0268	0.338	1.18	1.06	0.0195	0.305	1.07	1.02	0.0073	0.476	1.01	1.00
S.2.2	S.2.2.1	0.1742	0.0587	0.581	1.40	1.13	0.0281	0.441	1.06	1.02	0.0306	0.821	1.07	1.04
	S.2.2.2	0.1531	0.0460	0.518	1.29	1.09	0.0277	0.435	1.05	1.01	0.0183	0.732	1.07	1.03
	S.2.2.3	0.1331	0.0349	0.542	1.12	1.04	0.0269	0.421	1.02	1.00	0.0080	0.597	1.10	1.05
E.1.1	E.1.1.1	0.2661	0.0405	0.262	2.85	1.52	0.0122	0.127	1.21	1.05	0.0283	0.482	1.17	1.06
	E.1.1.2	0.2576	0.0354	0.237	2.74	1.48	0.0118	0.124	1.15	1.04	0.0235	0.438	1.16	1.06

to be continued

Table 2 (continuation)

Case	$H$ [m]	$h$ [m]	Total flow area				Vegetation layer				Surface layer			
			$Q$ [m <sup>3</sup> /s]	$v_m$ [m/s]	$\alpha$ [-]	$\beta$ [-]	$Q_{me}$ [m <sup>3</sup> /s]	$v_{me}$ [m/s]	$\alpha$ [-]	$\beta$ [-]	$Q_{ms}$ [m <sup>3</sup> /s]	$v_{ms}$ [m/s]	$\alpha$ [-]	$\beta$ [-]
E.1.1	E.1.1.3	0.2475	0.0308	0.215	2.65	1.45	0.0117	0.123	1.10	1.02	0.0191	0.398	1.18	1.07
	E.1.1.4	0.2275	0.0245	0.186	2.42	1.38	0.0115	0.120	1.08	1.02	0.130	0.354	1.14	1.05
E.1.2	E.1.2.1	0.2236	0.0376	0.290	2.51	1.41	0.0172	0.184	1.19	1.05	0.0204	0.568	1.12	1.05
	E.1.2.2	0.2184	0.0348	0.275	2.46	1.39	0.0171	0.182	1.18	1.05	0.0177	0.541	1.12	1.05
	E.1.2.3	0.2068	0.0292	0.243	2.15	1.30	0.0166	0.178	1.12	1.03	0.0126	0.473	1.11	1.05
	E.1.2.4	0.1951	0.0242	0.214	1.79	1.21	0.0163	0.174	1.07	1.02	0.0078	0.407	1.12	1.05
E.2.1	E.2.1.1	0.2386	0.0509	0.368	1.49	1.15	0.0241	0.271	1.09	1.03	0.0286	0.540	1.06	1.02
	E.2.1.2	0.2136	0.0400	0.323	1.35	1.11	0.0237	0.265	1.07	1.02	0.0164	0.473	1.06	1.02
	E.2.1.3	0.1935	0.0322	0.287	1.20	1.06	0.0231	0.257	1.03	1.01	0.0091	0.407	1.07	1.03
E.2.2	E.2.2.1	0.2131	0.0742	0.600	1.44	1.14	0.0340	0.444	1.17	1.05	0.0402	0.854	1.05	1.02
	E.2.2.1	0.1925	0.0642	0.575	1.45	1.14	0.0340	0.448	1.18	1.05	0.0301	0.845	1.05	1.02
	E.2.2.1	0.1799	0.0536	0.513	1.35	1.11	0.0322	0.431	1.14	1.05	0.0203	0.747	1.06	1.03
C.1.1	C.1.1.1	0.1514	0.0366	0.417	1.68	1.23	0.0055	0.184	1.04	1.02	0.0311	0.539	1.16	1.06
	C.1.1.2	0.1557	0.0377	0.417	1.74	1.24	0.0057	0.179	1.04	1.02	0.0318	0.544	1.19	1.07
	C.1.1.3	0.1604	0.0382	0.410	1.72	1.24	0.0052	0.169	1.04	1.02	0.0330	0.530	1.18	1.06
C.1.1	C.1.1.4	0.1618	0.0407	0.434	1.66	1.22	0.0050	0.175	1.04	1.02	0.0358	0.547	1.18	1.06
	C.1.1.5	0.1481	0.0337	0.393	1.65	1.21	0.0061	0.190	1.04	1.02	0.0277	0.512	1.15	1.05
	C.1.1.6	0.1432	0.0318	0.383	1.62	1.20	0.0064	0.197	1.04	1.02	0.0254	0.502	1.14	1.05
	C.1.1.7	0.1400	0.0305	0.375	1.62	1.20	0.0065	0.199	1.02	1.01	0.0240	0.493	1.15	1.05

to be continued

Table 2 (continuation)

Case	H [m]	h [m]	Total flow area			Vegetation layer			Surface layer							
			Q [m <sup>3</sup> /s]	v <sub>m</sub> [m/s]	α [-]	β [-]	Q <sub>veg</sub> [m <sup>3</sup> /s]	v <sub>veg</sub> [m/s]	α [-]	β [-]	Q <sub>sur</sub> [m <sup>3</sup> /s]	v <sub>sur</sub> [m/s]	α [-]	β [-]		
C.1.1	C.1.1.8	0.1371	0.056	0.0279	0.350	1.62	1.20	0.0064	0.190	1.04	1.02	0.0215	0.468	1.13	1.04	
	C.1.1.9	0.1291	0.058	0.0251	0.335	1.55	1.18	0.0068	0.199	1.02	1.01	0.0182	0.448	1.11	1.04	
	C.1.1.10	0.1330	0.055	0.0273	0.354	1.61	1.19	0.0064	0.196	1.02	1.01	0.0210	0.470	1.14	1.05	
	C.1.1.11	0.1207	0.062	0.0210	0.300	1.64	1.20	0.0068	0.186	1.02	1.01	0.0142	0.424	1.12	1.04	
	C.1.1.12	0.1198	0.062	0.0201	0.290	1.65	1.20	0.0067	0.180	1.03	1.02	0.0134	0.416	1.10	1.03	
	C.1.1.13	0.1146	0.062	0.0184	0.277	1.59	1.18	0.0066	0.181	1.02	1.01	0.0118	0.394	1.11	1.04	
	C.1.1.14	0.1080	0.061	0.0166	0.265	1.47	1.14	0.0067	0.186	1.02	1.01	0.0099	0.371	1.08	1.03	
	C.1.1.15	0.1053	0.065	0.0150	0.245	1.40	1.12	0.0070	0.184	1.02	1.01	0.0079	0.348	1.06	1.02	
	C.1.2	C.2.1.1	0.1432	0.050	0.0411	0.495	1.54	1.18	0.0076	0.254	1.04	1.02	0.0335	0.633	1.12	1.04
		C.2.1.2	0.1400	0.050	0.0437	0.538	1.54	1.18	0.0083	0.281	1.00	1.00	0.0354	0.685	1.13	1.05
		C.2.1.3	0.1355	0.049	0.0381	0.485	1.07	1.19	0.0071	0.246	1.02	1.01	0.0309	0.624	1.13	1.04
		C.2.1.4	0.1331	0.049	0.0369	0.478	1.64	1.21	0.0070	0.235	1.04	1.02	0.0300	0.629	1.13	1.04
		C.2.1.5	0.1301	0.051	0.0362	0.479	1.59	1.19	0.0075	0.253	1.02	1.01	0.0287	0.625	1.13	1.04
		C.2.1.6	0.1224	0.053	0.0321	0.452	1.44	1.14	0.0088	0.282	1.02	1.01	0.0232	0.585	1.09	1.03
	C.2.1.7	C.2.1.7	0.1198	0.056	0.0280	0.403	1.56	1.18	0.0081	0.246	1.00	1.00	0.0199	0.546	1.12	1.04
C.2.1.8		0.1166	0.058	0.0285	0.421	1.44	1.14	0.0098	0.281	1.04	1.02	0.0187	0.570	1.06	1.02	
C.2.1.9		0.1131	0.062	0.0270	0.411	1.45	1.14	0.0104	0.284	1.02	1.01	0.0166	0.571	1.07	1.02	
C.2.1.10		0.1093	0.061	0.0224	0.353	1.53	1.16	0.0086	0.238	1.02	1.01	0.0138	0.503	1.08	1.02	

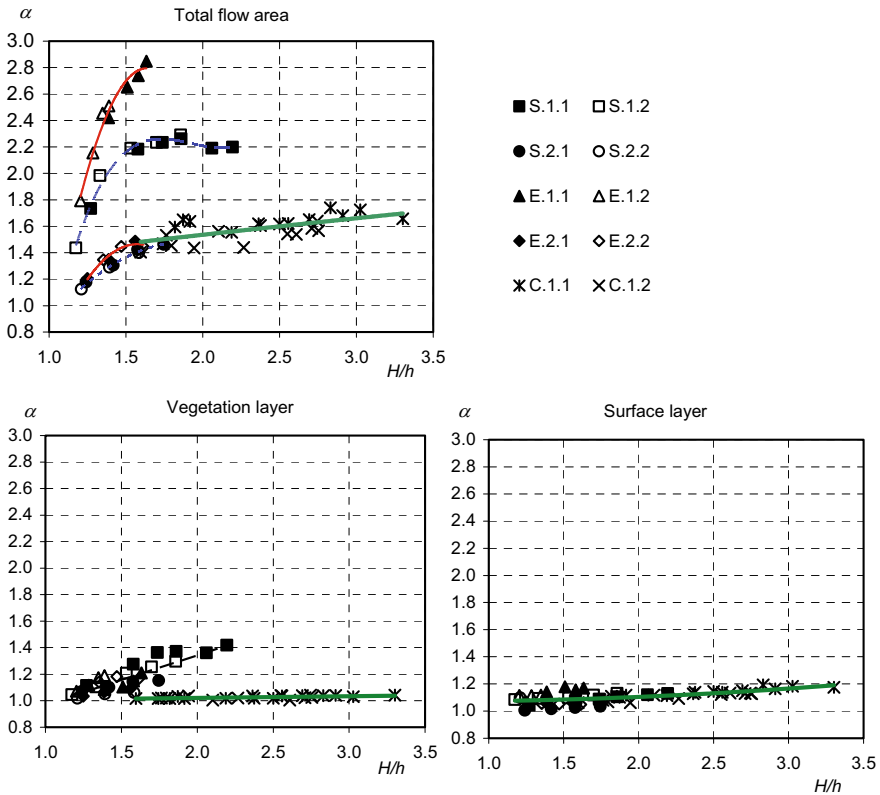


Fig. 9. Calculated energy  $\alpha$  coefficients for the velocity profile in the channel and relation between coefficients for different types of artificial vegetation: stiff, flexible stems, and plastic imitations of the Canadian waterweed (*Elodea Canadensis* sp.).

**Total flow area.** The highest values of the energy coefficient, falling in the range of  $\alpha \in (1.79 \div 2.85)$ , were obtained for a total flow area with flexible stems of  $m = 10000$  stems/m<sup>2</sup> spacing (E.1.1 and E.1.2). Meanwhile, the lowest values of the energy coefficient for the total flow area, in the range of  $\alpha \in (1.12 \div 1.49)$ , are reported for high spacing of both stiff and flexible stems, respectively,  $m = 1008$  stems/m<sup>2</sup> and  $m = 2500$  stems/m<sup>2</sup> (S.2.1, S.2.2 and E.2.1, E.2.2). The energy coefficient for the artificial Canadian waterweed was within the range of  $\alpha \in (1.40 \div 1.74)$ .

As the energy coefficient, the momentum coefficient  $\beta$  reached the highest values of  $\beta \in (1.21 \div 1.52)$  for flexible stems of  $m = 10000$  stems/m<sup>2</sup> spacing. The lowest values of the momentum coefficient, in the range of  $\beta \in (1.04 \div 1.15)$ , correspond to the total flow area for high spacing of both stiff and flexible stems. The momentum coefficient for the artificial Canadian waterweed did not exceed the value of  $\beta = 1.25$ .

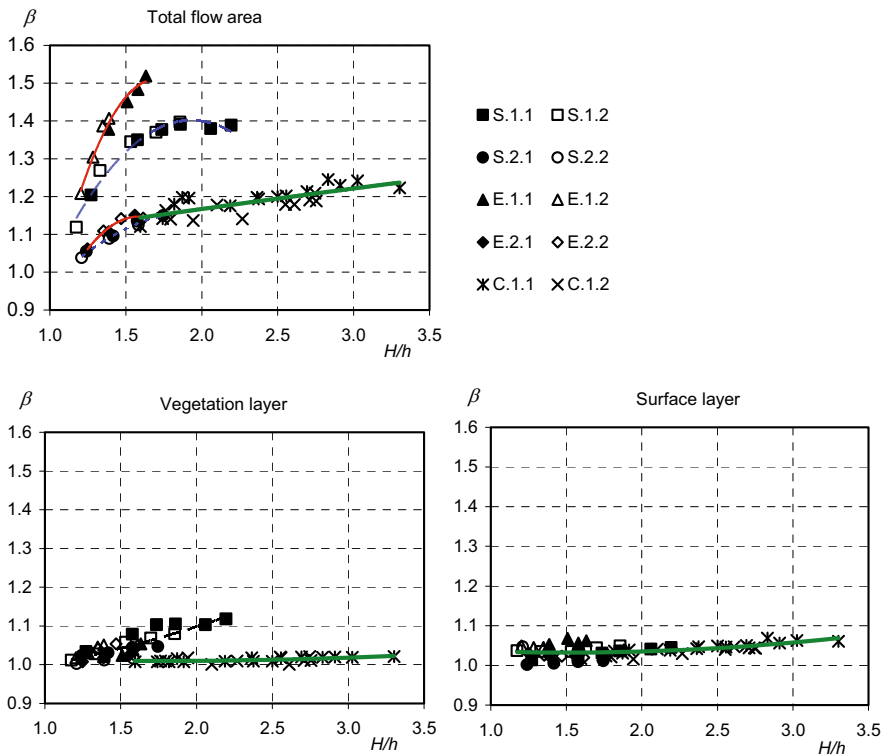


Fig. 10. Calculated momentum  $\beta$  coefficients for the velocity profile in the channel and relation between coefficients for different types of artificial vegetation: stiff, flexible stems, and plastic imitations of the Canadian waterweed (*Elodea Canadensis* sp.).

**Vegetation layer.** Values of the energy coefficient calculated only for the mean velocity in a vegetation layer, were significantly lower from those for the total velocity profile. There were no strong differences between the energy coefficient determined for stiff or flexible stems and it did not exceed the value of 1.42. Values of the energy coefficient  $\alpha$  calculated for the Canadian waterweed were close to unity. A similar behavior is shown by the momentum coefficient  $\beta$  for the vegetation layer, for all types of plant models.

**Surface layer.** Values of the energy coefficient for the surface layer were close together in all experimental variants and did not exceed the value of 1.19. The corresponding value of the momentum coefficient did not exceed 1.05.

As it is shown in Figs. 7-9, the highest values of the energy and momentum coefficients for the total flow are found for densely spaced flexible

stems. These values are higher than those given by Chow (1959) for regular channels without vegetation. Only coefficient values for the total flow with stiff stems were found slightly smaller. Decrease of elements spacing density reduces the coefficients values to the point where they are equal for all analyzed element types.

The calculated values of the energy and momentum coefficients for the total flow area were related to each other (Fig. 11), which allowed to establish a linear relationship between the coefficients:

$$\beta = 0.27\alpha + 0.75, \quad (R^2 = 0.98), \quad (3)$$

or

$$\alpha = 3.70\beta - 2.78. \quad (4)$$

By analogy, the similar relationship was identified for the vegetation layer (Fig. 11).

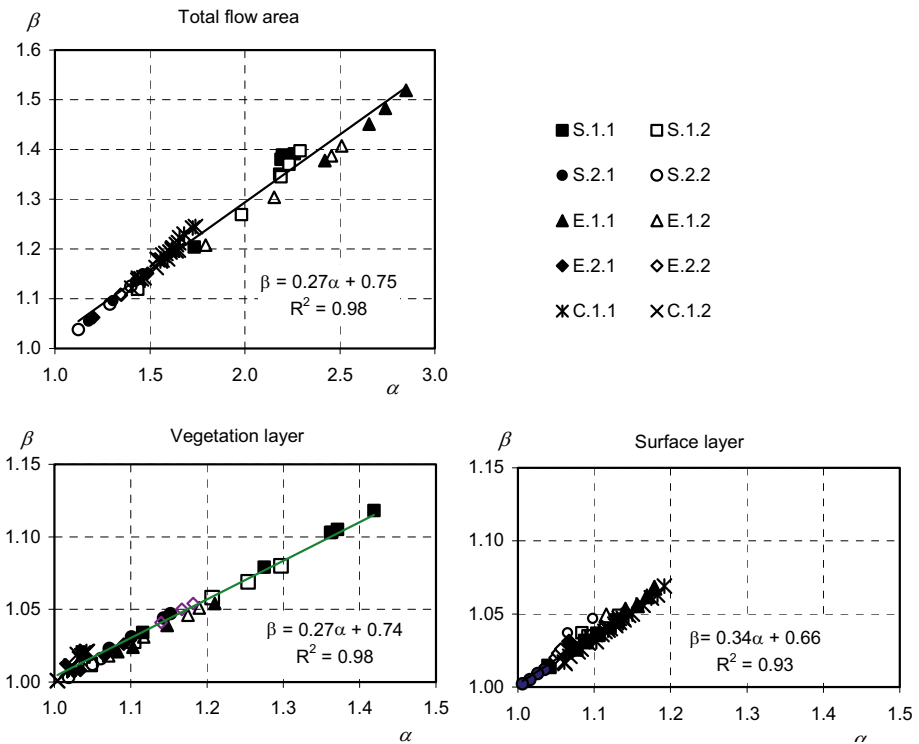


Fig. 11. The relationship between the energy  $\alpha$  and momentum  $\beta$  coefficients calculated for the vegetation layer for stiff, flexible stems, and plastic imitations of the Canadian waterweed.

#### 4. CONCLUDING REMARKS

The analysis of calculated values of the energy  $\alpha$  and momentum  $\beta$  coefficients for the rectangular channel with stiff, flexible stems, and plastic imitations of the Canadian waterweed, allows to state that:

- The energy and momentum coefficients depend on the velocity variations. The highest velocity variability is obtained in the total profile, smaller in vegetated layer, and the smallest in the surface layer. Therefore, the highest values of the energy  $\alpha$  and momentum  $\beta$  coefficients characterize the total flow area, whilst the smallest a surface layer above stiff and flexible elements.
- For the plastic imitations of the Canadian waterweed, the highest velocity variability is found in the surface layer.
- With an increase of plant spacing, the shape of the velocity profile in the vegetation layer gets closer to that in the surface layer; as a result of a velocity variation reduction, also values of the energy and momentum coefficients are reduced.
- The energy and momentum coefficients do not depend on the channel slope.
- The energy and momentum coefficients were related to linear regression relationships 3 or 4. Analogical relationships were elaborated for the vegetation and surface layer.
- In models of one-dimensional channel flow for partly vegetated flow area a higher energy and momentum coefficient values than those given by the present literature should be used. For fully vegetated flow areas, these coefficients should be close to a unity.

#### References

- Cameron, S.M., V.I. Nikora, I. Albayrak, O. Miler, M. Stewart, and F. Siniscalchi (2013), Interactions between aquatic plants and turbulent flow: a field study using stereoscopic PIV, *J. Fluid Mech.* **732**, 345-372, DOI: 10.1017/jfm.2013.406.
- Chow, V.T. (1959), *Open-Channel Hydraulics*, McGraw-Hill Book Co., New York, 680 pp.
- Fenton, J.D. (2005), On the energy and momentum principles in hydraulics. **In:** *Proc. 31st Congress of International Association for Hydro-Environment Engineering and Research, 11-16 September 2005, Seoul, Korea*, 625-636.
- Hulsing, H., W. Smith, and E.D. Cobb (1966), Velocity-head coefficients in open channels, Water-Supply Paper, Rep. No. 1869-C, U.S. Geological Survey, Washington.
- Kubrak, E. (2007), Distributions of water velocities in open-channels with stems simulating vegetation, Ph.D. Thesis, Faculty of Civil and Environmental

- Engineering, Warsaw University of Life Sciences, Warszawa, Poland (in Polish).
- Kubrak, E., J. Kubrak, and P.M. Rowiński (2008), Vertical velocity distributions through and above submerged, flexible vegetation, *Hydrolog. Sci. J.* **53**, 4, 905-920, DOI: 10.1623/hysj.53.4.905.
- Kubrak, E., J. Kubrak, and P.M. Rowiński (2012), Influence of a method of evaluation of the curvature of flexible vegetation elements on vertical distributions of flow velocities, *Acta Geophys.* **60**, 4, 1098-1119, DOI: 10.2478/s11600-011-0077-2.
- Kubrak, E., J. Kubrak, and P.M. Rowiński (2013), Application of one-dimensional model to calculate water velocity distributions over elastic elements simulating Canadian waterweed plants (*Elodea Canadensis*), *Acta Geophys.* **61**, 1, 194-210, DOI: 10.2478/s11600-012-0051-7.
- Nepf, H.M. (2012), Flow and transport in regions with aquatic vegetation, *Ann. Rev. Fluid Mech.* **44**, 123-142, DOI: 10.1146/annurev-fluid-120710-101048.
- Nepf, H.M., and M. Ghisalberti (2008), Flow and transport in channels with submerged vegetation, *Acta Geophys.* **56**, 3, 753-777, DOI: 10.2478/s11600-008-0017-y.
- Nepf, H.M., and E.R. Vivoni (2000), Flow structure in depth-limited, vegetated flow, *J. Geophys. Res.* **105**, C12, 28547-28557, DOI: 10.1029/2000JC900145.
- Poggi, D., G.G. Katul, and J.D. Albertson (2004), Momentum transfer and turbulent kinetic energy budgets within a dense model canopy, *Bound.-Lay. Meteorol.* **111**, 3, 589-614, DOI: 10.1023/B:BOUN.0000016502.52590.af.
- Rehbock, T. (1922), Die Bestimmung der Lage der Energielinie bei fließenden Gewässern mit Hilfe des Geschwindigkeitshöhen-Ausgleichwertes, *Der Bauingenieur Berlin* **3**, 15, 453-455 (in German).
- Righetti, M. (2008), Flow analysis in a channel with flexible vegetation using double-averaging method, *Acta Geophys.* **56**, 3, 801-823, DOI: 10.2478/s11600-008-0032-z.
- Strauss, V. (1967), The kinetic energy correction factor and the momentum correction factor in open channels. **In:** *Proc. 12th Congress of International Association for Hydro-Environment Engineering and Research, 11-14 September 1967, Fort Collins, USA*, 314-323.
- Wójtowicz, A., E. Kubrak, and M. Krukowski (2010), Distributions of water velocities in open-channels with aquatic vegetation, *Sci. Rev. – Eng. Environ. Sci.* **18**, 2, 11-20 (in Polish).
- Yen, B. (2002), Open channel flow resistance, *J. Hydraul. Eng.* **128**, 1, 20-39, DOI: 10.1061/(ASCE)0733-9429(2002)128:1(20).

Received 15 July 2014

Received in revised form 14 November 2014

Accepted 5 January 2015



## Usefulness of the Modified NRCS-CN Method for the Assessment of Direct Runoff in a Mountain Catchment

Andrzej WAŁĘGA<sup>1</sup> and Agnieszka RUTKOWSKA<sup>2</sup>

<sup>1</sup>Department of Sanitary Engineering and Water Management,  
University of Agriculture in Krakow, Kraków, Poland;  
e-mail: a.walega@ur.krakow.pl

<sup>2</sup>Department of Applied Mathematics, University of Agriculture in Krakow,  
Kraków, Poland

### Abstract

The aim of this study was to evaluate the usefulness of modified methods, developed on the basis of NRCS-CN method, in determining the size of an effective rainfall (direct runoff). The analyses were performed for the mountain catchment of the Kamienica river, right-hand tributary of the Dunajec. The amount of direct runoff was calculated using the following methods: (1) Original NRCS-CN model, (2) Mishra–Singh model (MS model), (3) Sahu–Mishra–Eldho model (SME model), (4) Sahu 1-p model, (5) Sahu 3-p model, and (6) Q\_base model. The study results indicated that the amount of direct runoff, determined on the basis of the original NRCS-CN method, may differ significantly from the actually observed values. The best results were achieved when the direct runoff was determined using the SME and Sahu 3-p model.

**Key words:** direct runoff, NRCS method, antecedent moisture condition (AMC), hydrological models, base flow.

## 1. INTRODUCTION

The rainfall-runoff process is a complex, dynamic and nonlinear process, affected by many, often interrelated physical factors. Reliable predictions of quantity and rate of runoff from land surface into streams and rivers are difficult and time-consuming to obtain for ungauged watersheds. As a result, many researchers have developed various methods to estimate both, the human influence on changes in surface runoff, especially storm runoff, and consequent effects on downstream activities (Fan *et al.* 2013).

In the recent years, the rainfall-runoff models have been commonly used to simulate the hydrological phenomena in uncontrolled catchments. By using these methods, it is not only possible to calculate the design flows necessary for the design of hydraulic facilities, but also to determine the flood parameters (duration, time to peak, wave volume, *etc.*), and to analyze the catchment response to the changes triggered, *e.g.*, by human activities. However, hydrological modeling requires an input consisting of a large number of parameters that are sometimes difficult to determine. One of the characteristics to be provided as the input data to a model is the effective rainfall intensity. The Soil Conservation Service Curve Number (SCS-CN) method (SCS 1956) (now National Resources Conservation Service NRCS) is one of the most popular methods for computing the surface runoff depth for a given rainfall event from small watersheds. Although the SCS-CN method was originally developed in the United States and mainly for the evaluation of storm runoff in small agricultural watersheds, it soon evolved well beyond its original objective. Its scope also expanded beyond the evaluation of storm runoff and it became an integral part of more complex, long term simulation models (Chauhan *et al.* 2013).

This method is simple and easy to apply. The primary reason for its wide applicability and acceptability is the fact that it accounts for major runoff generating catchment characteristics, namely soil type, land use/treatment, surface conditions, and antecedent moisture conditions (Deshmukh *et al.* 2013, Mishra and Singh 2002, 2003a,b; Ponce 1989, Váňová and Langhammer 2011, Merz and Blöschl 2009). Many researchers developed CN calculation methods by incorporating land cover information and the original CN in TR-55 (Fan *et al.* 2013). Hong and Adler (2008) developed a global SCS-CN runoff map using land cover, soils, and antecedent moisture conditions.

The SCS-CN method is widely used by engineers, hydrologists, and watershed managers as a simple watershed model, and as a runoff estimating component in more complex watershed models (Deshmukh *et al.* 2013). Ponce and Hawkins (1996) claimed that the SCS-CN method was a conceptual model of hydrologic abstraction of storm rainfall, supported by empiri-

cal data. Kabiri *et al.* (2013) claimed that the runoff values determined by means of SCS-CN method did not differ from those calculated with Green–Ampt method. Petroselli *et al.* (2013) and Grimaldi *et al.* (2013) proposed a method combining the Green–Ampt infiltration equation and calibration of both the ponding time and the soil hydraulic conductivity, using the initial abstraction and the total volume given by the SCS-CN method. The soil conservation service curve number (NRCS-CN) method converts rainfall to surface runoff (or rainfall-excess) using the CN derived from catchment characteristics and a 5-day antecedent rainfall. This model is chosen for predicting the runoff, because it is a well-known procedure that has been used for many years around the world. It is computationally efficient, the required inputs are generally available, and it relates the runoff to the soil type, land use, and management practices. To derive CN values (valid for storm duration shorter than 1 day) for an ungauged catchment, NRCS provided tables based on the soil type, land cover and land use, hydrological conditions, and antecedent moisture condition (AMC) (Cunha *et al.* 2011, Maidment 1993, Mishra *et al.* 2013).

As shown by the works of Wałęga *et al.* (2011, 2012), correct determination of CN parameter is crucial when preparing the data for the calculations, since the hydrological models are sensitive to changes in this parameter (McCuen 2003). Research conducted on the applicability of the NRCS-CN method suggested a need for its improvement (Efstratiadis *et al.* 2014, Miler 2012, Ponce and Hawkins 1996, Caviedes-Voullième *et al.* 2012. Garen and Moore (2005) and Woodward *et al.* (2010) indicated that NRCS-CN method was not applicable at sub-daily time resolution and should not be employed for estimating water infiltration into soil, mainly because it is a lumped approach (considering space and time), developed in order to define the total direct runoff derived from a rainfall event. Although several modifications to this method have been suggested and reported in the literature (Chauhan *et al.* 2013, Mishra *et al.* 2005), further improvements are still needed. The greatest limitations of the original NRCS-CN method are as follows: the three AMC levels used with this method permit unreasonable sudden jumps in CN and hence corresponding sudden jumps in the computed runoff are possible; there is a lack of clear guidance on how to vary antecedent moisture conditions; and there is no explicit dependency between the initial abstraction and the antecedent moisture (Sahu *et al.* 2012). Smith and Williams (1980) modified the SCS-CN method and suggested the expression for a retention parameter  $S$  by introducing a weighing factor to account for the soil moisture in the soil profile, in order to avoid sudden quantum jumps in the CN values when shifting from one AMC level to the other. Michel *et al.* (2005) critically reviewed the soil moisture accounting procedure behind SCS-CN method and unveiled major inconsistencies in the treatment of an-

tecedent condition in SCS-CN procedure. Geetha *et al.* (2007) made an attempt to obviate sudden jumps in CN values when chaining from one AMC level to other by modifying the existing SCS-CN method in two ways: varying the CN using antecedent moisture condition and using antecedent moisture amount. However, as shown by numerous studies on the application of the original NRCS-CN method for calculating the effective rainfall (Banasik and Woodward 2010, Ebrahimian *et al.* 2012, Krzanowski *et al.* 2013), CN parameter values, specified theoretically and according to NRCS guidelines, are significantly different from those calculated empirically, based on the recorded rainfall-runoff events. Unfortunately, many designers unknowingly use the original method in their hydrological calculations, which can result in a significant underestimation of the actual flood parameters. Therefore, it seems necessary to verify the application of the NRCS-CN method in the local conditions, to reduce the uncertainty of modeling results and promote more common use of this method in practice.

The aim of this study was to evaluate the usefulness of modified methods, developed on the basis of the NRCS-CN method, in determining the size of the effective rainfall (direct runoff) in a mountain catchment.

## 2. CATCHMENT DESCRIPTION

The study was conducted in the catchment area of the Kamienica river, which is a right-hand tributary of the Dunajec and enters it in the city of Nowy Sącz. This catchment is located in the southern Poland. It is a part of three mesoregions: Beskid Sądecki – upper part of the catchment, Beskid Niski and Kotlina Sądecka – middle and lower part of the catchment. The riverhead is located in the Beskid Sądecki at a height of 859.5 m a.m.s.l. The total length of the river is 33.1 km and the catchment area up to the entry into the Dunajec is 237.8 km<sup>2</sup>. The catchment area includes alluvial soils, river sands and gravels, as well as shales, marls, and sandstones. They were formed from noncarbonate decomposed sedimentary rocks. The catchment of the Kamienica river is dominated by forests that cover about 60% of its area, mainly in the upper part; arable lands account for approximately 7%, grasslands cover more than 7%, built-up areas occupy about 8% of the catchment, with the highest concentration around the Kamienica entry into the Dunajec (Fig. 1). The annual precipitation in the investigated catchment is 850 mm.

## 3. MATERIALS AND METHODS

Input material for the analysis consisted of selected rainfall-runoff events recorded for the upper part of the Kamienica catchment, closed with Łabowa water-level indicator (catchment area 64.9 km<sup>2</sup>). Rainfall data with a time

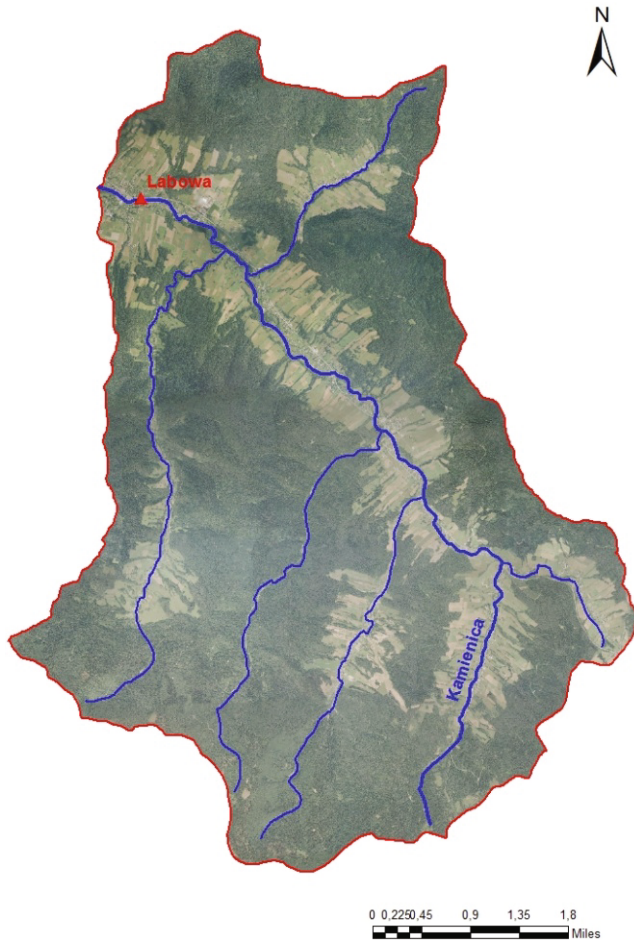


Fig. 1. The Kamienica catchment.

step of 24 hours were collected at a rainfall station in Krynica. The analysis included the greatest floods that occurred in the years 1997-2010, with a time step of 24 hours. The data were obtained from the Institute of Meteorology and Water Management – National Research Institute in Warsaw. Flood selection was based on a criterion of the lowest among the maximum annual flows (the period in which the instantaneous flows were higher than the threshold flow was selected for analysis). In total, 67 floods were recorded in the investigated multi-year period. As a result of data analyses and verification, the file analysis included 36 rainfall-runoff episodes. The dataset was divided into two subsets: the first, containing 30 episodes, was used for parameter calibration, and the second, containing 6 episodes, was used

for validation. Before the actual analysis, the data on the base runoff and direct runoff were separated. This was made by drawing a straight line on a hydrograph from the point where the flow increase begins to the point on the descending part, where the direct runoff ends. This procedure allowed us to determine the actual amount of the direct runoff layer for individual episodes. In the next step, a theoretical amount of the direct runoff was calculated, using the following methods: (1) Original NRCS-CN model, (2) Mishra-Sighn model (MS model), (3) Sahu-Mishra-Eldho model (SME model), (4) Sahu 1-p model, (5) Sahu 3-p model, and (6) Q\_base model.

### 3.1 Original NRCS-CN model

The SCS-CN method is based on the water balance equation and two fundamental hypotheses. The first hypothesis (1) equates the ratio of actual amount of direct surface runoff  $Q$  to the total precipitation  $P$  (or maximum potential surface runoff) to the ratio of actual infiltration  $F$  to the amount of the potential maximum retention  $S$ . The second hypothesis relates the initial abstraction  $I_a$  to the potential maximum retention  $S$  (Deshmukh *et al.* 2013):

$$\frac{Q}{P - I_a} = \frac{F}{S} . \quad (1)$$

A general form of the NRCS-CN model is expressed by the following equations:

$$Q = \frac{(P - I_a)^2}{P - I_a + S} \quad \text{if } P > I_a , \quad (2)$$

$$Q = 0 \quad \text{otherwise}$$

$$I_a = \lambda S , \quad (3)$$

where  $Q$  is the direct runoff [mm],  $P$  the total precipitation [mm],  $I_a$  the initial abstraction [mm],  $S$  the potential maximum retention [mm], and  $\lambda$  the initial abstraction coefficient (dimensionless).

The parameter  $S$  of the NRCS-CN method depends on soil type, land use, hydrological conditions, and antecedent moisture condition (AMC). The parameter  $S$  is expressed as:

$$S = \frac{25400}{\text{CN}} - 254 , \quad (4)$$

where  $S$  is in mm and CN is the curve number, which depends on the soil type, land cover and land use, hydrological conditions, and antecedent moisture condition (AMC).

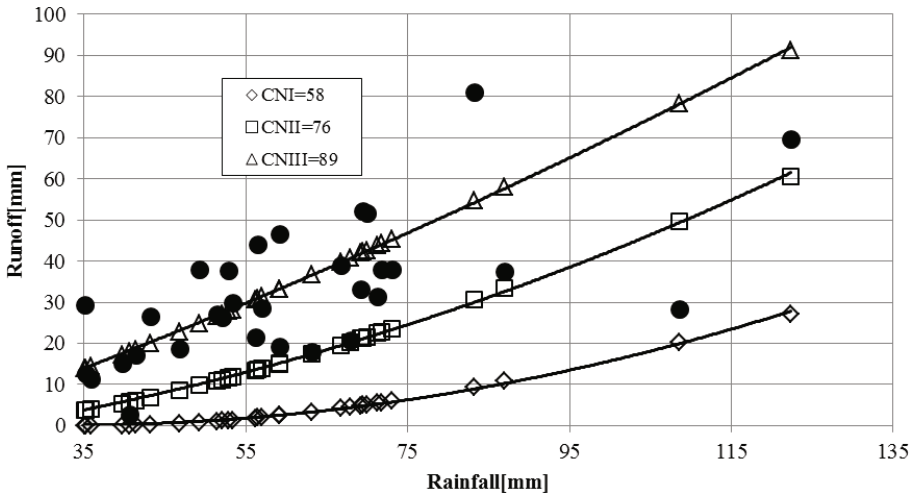


Fig. 2. Development of rainfall-runoff relation *versus* CN value according to the original NRCS-CN method.

CN = 100 represents a condition of zero potential maximum retention ( $S = 0$ ), that is, an impermeable watershed. Conversely, CN = 0 represents a theoretical upper bound to potential maximum retention ( $S = 1$ ), that is an infinitely abstracting watershed.

A theoretical value of CN parameter was determined based on an ortho-photo, with reference to current land use and 1:25 000 scale soil maps. It was found to correspond to normal catchment moisture conditions AMCII. The CN parameter for the two other antecedent moisture conditions, *i.e.*, AMCI and AMCIII (Hawkins *et al.* 1985), was determined using appropriate tables. The catchment AMC was determined for each event according to the distribution of the points with rainfall-runoff coordinates relative to the theoretical runoff values (see Fig. 2). This way, the direct runoff was calculated according to NRCS-CN\_PNWemp method.

Calculated values of CN were determined based on the observed rainfall-runoff events. For this purpose, the total runoff hydrograph was divided into the groundwater (base) runoff and the surface runoff. Empirical value of retention  $S_i$  [mm] is a solution of Eqs. 2 and 3 at  $\lambda = 0.201$ . The analysis assumed the value of  $\lambda$  established as a result of the calibration based on rainfall-runoff episodes.

$$S_i = 5 \cdot \left( P_i + 2 \cdot H_i - \sqrt{4 \cdot H_i^2 + 5 \cdot P_i \cdot H_i} \right), \tag{5}$$

where  $P_i$  is the total precipitation amount causing  $i$  floods [mm], and  $H_i$  is the direct runoff [mm]. The value of CN parameter was calculated according to the formula:

$$\text{CN} = \frac{25400}{254 + S} . \quad (6)$$

Runoff volume as NRCS-CN<sub>calc</sub> was calculated using formula 2.

### 3.2 Mishra-Singh model (MS model)

Mishra and Singh (2002) modified the equation for direct runoff with antecedent moisture  $M$  to:

$$Q = \frac{(P - I_a)(P - I_a + M)}{P - I_a + M + S} , \quad (7)$$

where  $M$  is the antecedent moisture [mm]:

$$M = 0.5 \cdot \left[ -(1 + \lambda S) + \sqrt{(1 - \lambda^2)S^2 + 4P_5S} \right] . \quad (8)$$

Here,  $I_a$  is the same as in Eq. 3 and  $P_5$  denotes the amount of antecedent 5-day rainfall. Equation 8 represents the amount of moisture  $M$  added to the dry soil profile by rain  $P_5$ . According to Sahu *et al.* (2010) the drawbacks of MS model can be summarized as follows:

□ There is no explicit dependency of  $I_a$  on  $M$ . It is known, however, that  $I_a$  relies on interception, surface storage and infiltration, and all these factors greatly depend on  $M$ . The larger the  $M$ , the smaller the  $I_a$ , and the other way round;

□ In Eq. 7,  $S$  is optimized as a parameter, which, however, is a varying quantity for a given watershed. Hence, it is not clear which moisture level/condition the optimized  $S$  would correspond to;

□ Evapotranspiration and other interim water losses are not accounted for.

In Eq. 8, the value of the maximum potential retention  $S$  was adopted, according to the AMC and CN, from the original NRCS-CN method. The parameter  $\lambda$  in Eq. 8 was calibrated based on recorded rainfall-runoff episodes.

### 3.3 Sahu–Mishra–Eldho model (SME model)

Though the MS model obviates sudden jumps in CN with AMC and hence seems to be a continuous model, it needs refinements. Sahu *et al.* (2010) presented the following equations for the direct runoff:

$$Q = \frac{(P - I_a)(P - I_a + M)}{P - I_a + S_0} \quad \text{if } P > I_a, \tag{9}$$

$$Q = 0 \quad \text{otherwise}$$

$$I_a = \lambda(S_0 - M), \tag{10}$$

where  $S_0$  is the absolute maximum retention capacity. Equation 10 gives an explicit relationship between  $I_a$  and  $M$ , and thus it is a continuous function (the higher the antecedent moisture  $M$ , the lower the initial abstraction  $I_a$ , and *vice versa*). When  $\beta$  and  $S_0$  are assumed as parameters, then  $M$  is given as follows:

$$M = \beta \left[ \frac{(P_5 - \lambda S_0) S_0}{(P_5 - \lambda S_0) + S_0} \right] \quad \text{for } P_5 > \lambda S_0, \tag{11}$$

$$M = 0 \quad \text{for } P_5 < \lambda S_0.$$

The SME model proposed by Sahu *et al.* (2010) has the following advantages over the MS model:

- The proposed SME model uses more rational continuous expression for estimating the antecedent moisture  $M$ . It restricts the validity of  $M$  being equal to zero for  $P_5 < \lambda S_0$ , and therefore  $M$  is never negative;

- The SME model explicitly relates  $I_a$  with  $M$ , while MS and SCS-CN models do not;

- The proposed SME model allows optimization of  $S_0$ , an intrinsic parameter, and thus a constant quantity for a specific watershed.  $S_0$  can be more rationally linked with watershed characteristics, while the MS model allows optimizing  $S$ , a varying parameter for a specific watershed.

In this method,  $\lambda$ ,  $S_0$ , and  $\beta$  were optimized. Root mean square error (RMSE), expressed by formula 23, was assumed as a goal function, and the optimization involved minimization of this function value. Due to difficulties in calibrating the parameters of SME model in uncontrolled catchments, the method was modified by making an assumption that  $S_0 = S$ . The maximum potential catchment retention  $S$  was adopted exactly in the same way as in MS model. Thus, the calibrated value of  $\lambda$  in formula 10 represents the ratio of the absolute maximum retention capacity.

### 3.4 Sahu 1-p model

Since the three AMC levels used with the original SCS-CN method permit unreasonable sudden jumps in CN, a continuous equation is needed to estimate the antecedent moisture. Sahu *et al.* (2007) developed two versions of a

model determining the volume of direct runoff in the form of an equation comprising one or three parameters.

Given the simulations carried out in 82 catchments in India,  $\alpha$  and  $\beta$  parameters in the three-parameter model were 0.1 and 0.4, mean and median values for each of these two parameters were almost the same, and these simplifications yielded a one-parameter model – Sahu 1-p, which is described by the following set of equations:

$$V_0 = 0.4P_5 \quad \text{if } P_5 \leq 0.1S, \quad (12)$$

$$V_0 = S \left( \frac{0.44P_5 - 0.004S}{P_5 + 0.9S} \right) \quad \text{if } P_5 > 0.1S, \quad (13)$$

where  $V_0$  is the soil moisture store level at the beginning of the rainfall event [mm]. Other symbols are as in the previous formulas. When  $V_0$  is known,  $Q$  can be computed as follows:

$$\text{if } V_0 + P \leq 0.1S \quad \text{then } Q = 0, \quad (14)$$

$$\text{if } 0.1S < V_0 + P \leq 0.1S + P \quad \text{then } Q = \frac{(P + V_0 - 0.1S)^2}{(P + V_0 + 0.9S)}, \quad (15)$$

$$\text{if } 0.1S \leq V_0 \leq 1.1S \quad \text{then } Q = P \left( 1 - \frac{(1.1S - V_0)^2}{S^2 + (1.1S - V_0)P} \right). \quad (16)$$

The value of  $S$  parameter was assumed in a similar way as in the above-mentioned methods.

### 3.5 Sahu 3-p model

The antecedent or initial soil moisture  $V_0$  depends not only on  $P_5$  but also on  $S$ . The dependency on  $S$  is based on the fact that the watershed with larger retention capacity  $S$  must retain higher moisture compared to the watershed with lesser  $S$  for a given  $P_5$ . In the derivation of an expression for  $V_0$ , the following assumptions are made:

□ The pre-antecedent moisture level ( $V_{00}$ ) 5 days before the onset of rainfall is zero or a fraction of  $S$ ;

□ The initial soil moisture store level ( $V_0$ ) at the time of the beginning of rainfall storm is equal to the sum of pre-antecedent moisture level ( $V_{00}$ ) and a fraction  $\beta$  of the part of rainfall that is not transformed into runoff ( $P_5 - Q$ ) owing to rainfall of  $P_5$  at the time, where  $Q$  is the corresponding runoff. This assumption is based on the fact that only a fraction, in general, of mois-

ture/water added to the soil will contribute to  $V_0$  due to evapotranspiration losses in the previous 5 days.

Using suitable assumptions, Sahu *et al.* (2007) derived the following equations for different conditions:

$$V_0 = V_{00} + \beta P_5 \quad \text{for } V_{00} \leq S_a - P_5, \tag{17}$$

$$V_0 = V_{00} + \beta \left[ P_5 - \frac{(P_5 + V_{00} - S_a)^2}{P_5 + V_{00} - S_a + S} \right] \quad \text{for } S_a - P_5 < V_{00} \leq S_a, \tag{18}$$

$$V_0 = V_{00} + \beta P_5 \left[ \frac{(S + S_a - V_{00})^2}{S^2 + (S + S_a - V_{00})P_5} \right] \quad \text{for } S_a \leq V_{00} \leq S_a + S, \tag{19}$$

where  $V_{00}$  is the old moisture level available for 5 days before the rainfall,  $S_a$  is an intrinsic parameter of soil moisture ( $S_a = \alpha S$ ), and  $\beta$  is an additional model parameter ranging from 0 to 1. Analyses performed by these authors indicated that  $V_{00} = 0$ . This simplification in the Sahu model resulted into a three parameter model that is referred to as the Sahu 3-p model. The direct runoff was calculated using the following equations:

$$Q = 0 \quad \text{for } V_0 \leq S_a - P_5, \tag{20}$$

$$Q = \frac{(P + V_0 - 0.1S_a)^2}{P + V_0 - S_a + S} \quad \text{for } S_a - P_5 < V_0 \leq S_a, \tag{21}$$

$$Q = P \left[ 1 - \frac{(S + S_a - V_0)^2}{S^2 + (S - S_a - V_0)P} \right] \quad \text{for } S_a \leq V_0 \leq S_a + S. \tag{22}$$

This method involved optimization of  $\alpha$  and  $\beta$  parameters. Root mean square error (RMSE), expressed by formula 23 was assumed as a goal function, and the optimization involved minimization of this function.

### 3.6 Q\_base model

Krzanowski *et al.* (2013) assumed that in a precipitation-free period or in the case of average rainfall, the watercourses were supplied by underground waters from the first aquifer level. Therefore, the knowledge on the base flow from before the flood period can provide sufficient information on the catchment moisture content. Higher values of the base flow may indicate high level of groundwater, and hence reduced retention capacity of the catchment. For this purpose, the authors made attempts at correlating the

base flow  $Q_b$  with CN parameter values according to the original NRCS-CN method.

CN parameter values were determined from Eqs. 5 and 6. The parameters of the established relationship were determined using the least squares method. Direct outflow volume was calculated from Eqs. 2 and 4.

Assessment of a model's prediction accuracy is an important issue in hydrological modelling. In the present study, we used the root mean square error (RMSE) and Nash–Sutcliffe model efficiency (EF) (Nash and Sutcliffe 1970) as model goodness of fit to assess the model performance. These criteria are expressed as below:

$$\text{RMSE} = \sqrt{\frac{1}{N} \sum_{i=1}^N (Q_{\text{obs},i} - Q_{\text{calc},i})^2}, \quad (23)$$

$$\text{EF} = 1 - \frac{\sum_{i=1}^N (Q_{\text{obs},i} - Q_{\text{calc},i})^2}{\sum_{i=1}^N (Q_{\text{obs},i} - \overline{Q_{\text{obs}}})^2}, \quad (24)$$

where RMSE is in mm, EF is dimensionless.  $Q_{\text{obs}}$  is the observed storm runoff [mm],  $Q_{\text{calc}}$  is the calculated runoff [mm],  $\overline{Q_{\text{obs}}}$  is a mean of the observed runoff values in the catchment,  $N$  is the total number of rainfall-runoff events, and  $i$  is an integer varying from 1 to  $N$ .

Additionally, significance of differences between the runoffs calculated using the analyzed methods was established. The calculations were performed using ANOVA with F test at a significance level  $\alpha = 0.05$ . The differences between average value of  $\text{CN}_{\text{calc}}$  parameter and empirical values of  $\text{CN}_{\text{emp}}$ , determined based on NRCS tables for the three AMC levels, were evaluated. For this purpose, Student's t test was used, testing the null hypothesis  $H_0$  that the average  $\text{CN}_{\text{calc}}$  was equal to  $\text{CN}_{\text{emp}}$  for three AMC:  $\text{CN}_{\text{cal}} = \text{CN}_{\text{emp\_AMCI}}$ ,  $\text{CN}_{\text{cal}} = \text{CN}_{\text{emp\_AMCII}}$ , and  $\text{CN}_{\text{cal}} = \text{CN}_{\text{emp\_AMCIII}}$ , against the hypothesis  $H_A$  that the average values were different:  $\text{CN}_{\text{cal}} \neq \text{CN}_{\text{emp\_AMCI}}$ ,  $\text{CN}_{\text{cal}} \neq \text{CN}_{\text{emp\_AMCII}}$ , and  $\text{CN}_{\text{cal}} \neq \text{CN}_{\text{emp\_AMCIII}}$ . The null hypothesis was tested at a significance level  $\alpha = 0.05$ . The statistical analyses were performed in Statistica for Windows 10.0.

#### 4. RESULTS

Table 1 summarizes main parameters of the analyzed floods. The greatest direct runoff was recorded for episode No. 25 that occurred in the third decade of July 2004. This flood was caused by a precipitation episode lasting 4 days, with total depth exceeding 83.2 mm. The rainfall for the analyzed floods in the catchment ranged from 28.4 to 108.6 mm, the runoff was from 2.8 to 81.1 mm, and the sum of five-day rainfall  $P_5$  ranged from 0.0 to

Table 1

Basic characteristics of the analyzed floods

No.	Total precipitation [mm]	Direct runoff [mm]	Precipitation within 5 days preceding the flood [mm]
1	66.7	39.1	7.5
2	56.2	21.5	7.9
3	108.6	28.3	0.2
4	87.0	37.5	12.8
5	57.0	28.5	26.2
6	69.9	51.6	5.8
7	73.0	38.0	1.5
8	41.4	17.1	0.5
9	20.8	17.7	2.5
10	59.2	19.2	41.1
11	51.4	27.0	42.6
12	39.7	15.2	37.0
13	29.1	23.0	7.8
14	53.3	30.0	9.2
15	31.5	22.8	0.5
16	40.6	2.8	13.4
17	69.2	33.3	53.6
18	28.4	13.8	21.6
19	35.2	12.7	25.0
20	56.5	44.2	0.0
21	67.9	20.7	25.1
22	71.2	31.3	13.5
23	43.2	26.5	8.8
24	35.1	29.3	0.3
25	83.2	81.1	23.7
26	52.1	26.3	36.0
27	71.7	37.9	61.7
28	28.6	21.9	8.7
29	59.1	46.7	0.1
30	52.9	37.8	5.3

61.7 mm. In the investigated mountain catchment, 49 out of 67 floods occurred in the summer half of the year, which accounted for 73% of all episodes. Most of the floods were recorded in July and August. This flood distribution throughout the year is typical of mountain catchments located in southern Poland.

Figure 2 shows observation-based rainfall-runoff correlations for the analyzed episodes, with relation to limit curves calculated for CN parameter, determined theoretically for three moisture levels. The theoretical value of CN parameter for normal moisture conditions was 76. The analyses showed that both empirically determined values of CN parameter and the calculated volumes of direct runoff for 28 analyzed episodes fell within the area of CN theoretical curve for the third moisture level, often exceeding the upper limit. According to NRCS, in 30 out of 36 analyzed flood events, soil moisture corresponded to level I.

The computed parameter values for all the analyzed models for the Kamiénica catchment are presented in Table 2. In order to optimize the model parameters, we used the “Solver” tool available in Microsoft Office Excel. Based on detailed calculations, a logarithmic function was adopted to describe the relationships between base flow and CN:

$$CN(Q_b) = 4.909 \ln Q_b + 90.59 . \quad (25)$$

In the case of  $Q_{base}$  model, the calculated correlation coefficient for Eq. 25) was 0.821 and the coefficient of determination was 0.679. Figure 3 presents the relationship between  $Q_b$  and CN. It was found that the increased

Table 2  
Parameter values in various models for the Kamiénica catchment

Model	Parameter	Value
Original NRCS-CN <sub>calc</sub>	CN <sub>med</sub> * $\lambda$	88.500 0.201
MS Model	$\lambda$	0.010
SME Model	$\lambda$ $\beta$	0.089 0.010
Sahu 1-p model	–	–
Sahu 3-p model	$A$ $\beta$	0.217 0.010
$Q_{base}$ model	$A$ $b$	4.909 90.590

\*)median value of empirical CN

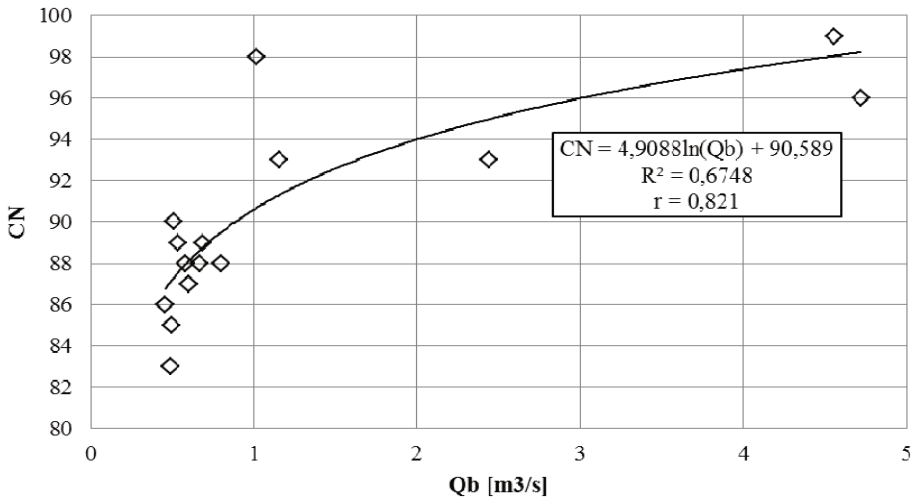


Fig. 3. Relation between empirical CN values and base flow before the floods.

base flow (and thus reduced retention capacity of the catchment) was accompanied by higher CN values.

Table 3 shows the quality assessment results for the presented models. The higher the RMSE, the poorer the performance of the model, and *vice versa*, RMSE = 0 means a perfect fit. The EF value of unity indicates perfect agreement between the observed and computed values, and decreasing values indicate poorer agreement. This measure implies that the model predicts no better than the average of the observed data. The value of model efficiency can be negative, which indicates that the average observed value is a

Table 3

Performance of the quality models for the Kamienica catchment

Model	Calibration		Verification	
	RMSE [mm]	EF	RMSE [mm]	EF
Original NRCS-CN <sub>cal</sub> (CN calibrated)	0.61	0.998	13.16	0.61
Original NRCS-CN_PNW <sub>emp</sub>	9.40	0.57	8.02	0.85
MS Model	11.54	0.37	11.39	0.70
SME Model	8.54	0.65	6.61	0.90
Sahu 1-p model	10.03	0.52	5.95	0.92
Sahu 3-p model	8.49	0.65	6.59	0.90
Q_base model	4.38	0.85	27.00	-0.39

better estimate than the model predicted, that is, the model prediction is worse than the average observation (Sahu *et al.* 2012).

Our calculations showed that model 1, based on the original NRCS-CN equation, with CN parameter calibration, the most accurately characterized the amount of the direct runoff. The calibration process yielded RMSE error of only 0.61 mm, and the coefficient of effectiveness EF was 0.998. In turn, when the model assumed average  $CN_{cal}$ , determined during the calibration, the calculations for the floods selected for verification showed much worse model performance, *i.e.*, 13.16 mm for RMSE and 0.61 for EF. Assuming the AMC level determined for the observed episodes (Fig. 2), the maximum potential retention  $S$  was calculated for empirical CN values specified with reference to the catchment use and soil conditions. Then, the size of the runoff was calculated from formula 2. Qualitative assessment of this model for the episodes used for calibration was much worse than for the model with calibrated CN (RMSE = 9.40 mm, EF = 0.57). The situation was opposite for the verification, where the model performance was much better. Analysis of the modification of the original NRCS-CN method revealed that the calibration process provided the best quality for  $Q\_base$  model, with RMSE = 4.38 mm and EF = 0.85. The other good models were SME and Sahu 3-p ones. The weakest score was achieved by MS model. All modifications of NRCS model based on verification, except for  $Q\_base$  model, were rated better than in the case of calibration. The highest scores were obtained by Sahu 1-p, Sahu 3-p, and SME models, and the lowest by  $Q\_base$  model, for which the EF = -0.39 indicated that the average observed flow provided better results than the calculated flow.

Figure 4 presents typical fitting of all considered models for the Kamienna catchment for calibration, and Fig. 5 for verification. It is apparent from this figure that the runoff values calculated using NRCS- $CN_{cal}$ , SME, and  $Q\_base$  model were the closest to the corresponding observed values, and closer than those calculated using other models for most of the events. Hence, these three models performed equally well and better than the other models. The greatest differences in the results from SME and  $Q\_base$  models can be seen for the greatest floods, while the calculation results are relatively reliable for the medium and small depth runoffs. The largest floods are best described by single parameter models NRCS- $CN_{cal}$ . Assuming the criteria presented by Moriasi *et al.* (2007) for calibration, MS model shall be deemed unsatisfactory ( $EF < 0.50$ ), NRCS- $CNPW_{emp}$ , SME, Sahu 1-p, Sahu 3-p are satisfactory ( $0.50 < EF \leq 0.65$ ), and  $Q\_base$  and NRCS- $CN_{cal}$  models are very good ( $EF > 0.75$ ). Figure 5 shows the fitting of the analyzed models to the observations in the case of verification. The best fitting was obtained for the SME and Sahu 1-p models. It can be concluded that for low values of observed runoff, the theoretical runoff yielded from the models is

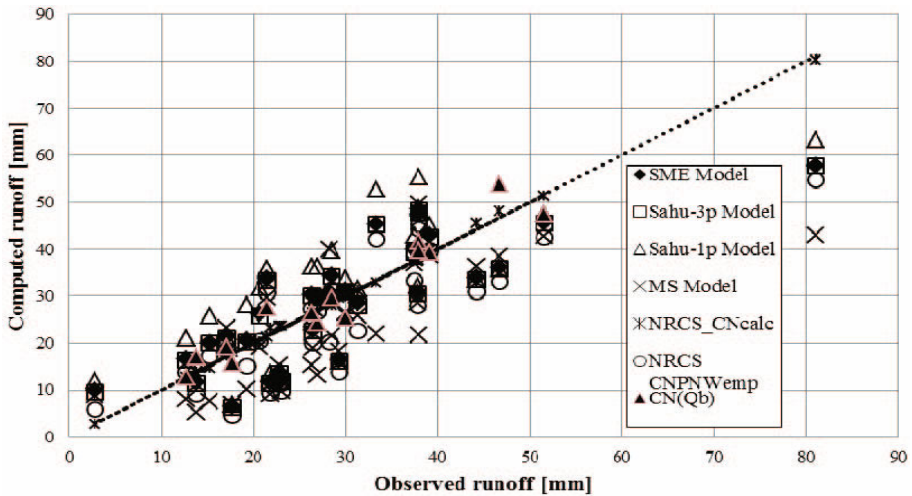


Fig. 4. Fitting of the original NRCS CN method and the modified models to the Kamiienica catchment for calibration.

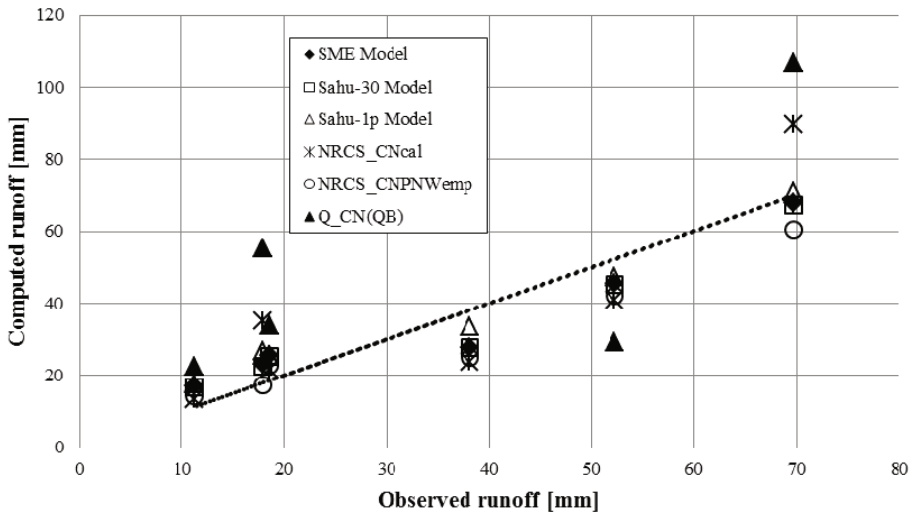


Fig. 5. Fitting of the original NRCS CN method and the modified models to the Kamiienica catchment for the verification.

slightly overestimated, and for higher observed runoffs it is underestimated. In the case of verification, NRCS-CN<sub>cal</sub> is satisfactory, the MS model is good ( $0.65 < EF \leq 0.75$ ), and the other models are very good.

Figure 5 and Table 4 show the significance of differences between the direct runoff values estimated using a variety of methods. Calculations showed

Table 4

Results of F test for the significance of differences  
between mean values of reduction coefficients in the analyzed methods

Method	SS	MS	F	$p$ [%]
	1355.60	271.10	1.53	0.18

**Explanations:** SS – sum of squares between groups, MS – mean squares between groups, F – F test value,  $p$  – probability level (at  $p < 0.05$  significant values).

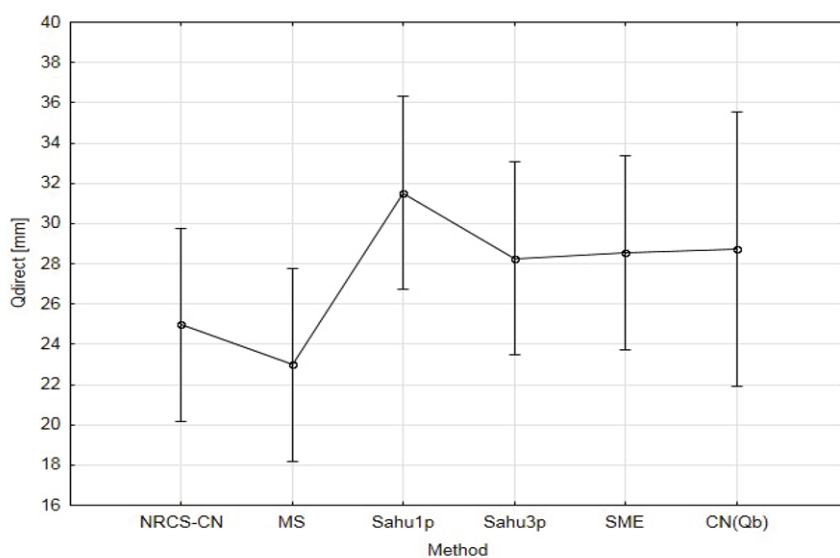


Fig. 6. Means and deviations of the direct runoff values determined for various methods.

that F was equal to 1.53, and was greater than the critical value, which indicated a lack of significant differences between the average runoffs estimated by means of different methods. The highest average runoff was calculated using Sahu 1-p method, and the lowest using MS model (Fig. 6).

Its values were very similar in SME, Sahu 3-p and CN(QB) models. Student's t test was used to evaluate the average value of  $CN_{cal}$  in relation to empirical values of  $CN_{emp}$  for three AMC levels. Calculations showed that in the case of  $CN_{emp}$  corresponding to AMCI, there were no reasons to reject the null hypothesis  $H_0: CN_{cal} = CN_{emp\_PNWIII}$  at a significance level  $\alpha = 0.05$ .

The results of Student's t test were as follows:  $t = -0.718$ ,  $p = 0.477$ . For the remaining AMC levels, there was no basis for accepting the null hypothesis  $H_0: CN_{cal} = CN_{emp\_PNWI}$  and  $CN_{cal} = CN_{emp\_PNWII}$ . As a result,

the alternative hypothesis  $H_A$  was accepted:  $CN_{cal} \neq CN_{emp\_AMCI}$ ,  $CN_{cal} \neq CN_{emp\_AMCII}$ . The results of Student's t test were as follows: for the hypothesis  $CN_{cal} \neq CN_{emp\_AMCI}$   $t = 21.549$ ,  $p = 0.00$ , and for the hypothesis  $CN_{cal} \neq CN_{emp\_AMCII}$   $t = 8.62$ ,  $p = 0.00$ . The presented results indicated that when calculating the effective rainfall with NRCS method in uncontrolled catchments with similar characteristics as the analyzed one,  $CN_{emp}$  value should correspond to AMCIII.

## 5. DISCUSSION

The conducted analyses showed significant differences between the runoff volumes calculated using the proposed model and based on the actual values. These results confirm the reports of other authors (Banasik and Woodward 2010), claiming that in normal conditions the empirically determined CN is significantly higher than the calculated CN. This means that, in the case of the investigated catchment, the rainfall reached already moist soil. The catchment soil moisture level was determined not only by the precipitation, but also by high level of ground water table that could be maintained after the winter period, leading to reduced catchment retention capacity, as well as poorly permeable soils that made precipitation infiltration more difficult. In practice, when modeling floods and estimating the depth of the effective precipitation according to the original NRCS-CN method, it is recommended to assume the moisture level typical for normal conditions (*e.g.*, MHP 2005). The results presented in this article suggest that this approach should be changed in the case of mountain catchments. As it is impossible to compare the calculation results with actual flows in uncontrolled catchments, it is recommended to assume the third level of catchment soil moisture when determining CN parameter, in order to ensure greater security of flood protection facilities. One should of course remember that the value of CN parameter needs to be verified in the catchments located in different climatic conditions and of different character than those for which this method was developed (*e.g.*, Krzanowski *et al.* 2013, Miler 2012). Therefore, a key issue while using the NRCS-CN method is to determine the catchment moisture conditions before a specific flood occurs. This made us attempt to verify other models for estimating the effective precipitation, in which the soil moisture level can be treated in a different way. The presented calculations indicate that in the case of MS and Sahu 1-p model it is also necessary to assume a specific moisture level. According to Sahu *et al.* (2012), MS method advantageously eliminates sudden jumps in CNs, and hence in computing runoff, through incorporation of the expression of  $M$  (Eq. 8), replacing the three AMCs. However, it does not reveal an explicit dependency of  $I_a$  on  $M$ . Furthermore, in this method,  $S$  is optimized as a parameter, which is, in fact, a varying quan-

tity depending on  $M$  for a given catchment. Hence, it is not clear which moisture level/condition the optimized  $S$  would correspond to. A similar situation occurs in the case of Sahu 1-p model. Analysis of calibration and verification results indicates that SME and Sahu 3-p models provide the most accurate values of the direct runoff. In the investigated models, the absolute maximum retention capacity  $S_0$  was replaced by a potential maximum retention  $S$ , determined for specific  $\text{PNW}_{\text{emp}}$  and CN. This modification was made to enable a direct application of these models in uncontrolled catchments, where there is no possibility of parameter calibration. While making this assumption, a hypothesis was adopted saying that in a mountain catchment with poorly permeable ground, the absolute maximum retention capacity  $S_0$  may be similar to the potential maximum retention  $S$ . This hypothesis was supported by the fact that the simulations performed for calibrated values of  $S_0$  based on the original method yielded very inadequate results. The resulting model quality in the analyzed catchment was similar or even slightly better than reported by, *e.g.*, Sahu *et al.* (2007, 2010). It is worth emphasizing that the proposed models were applied in a forest-agricultural mountain catchment with the area of over  $60 \text{ km}^2$ , while previous studies mainly focused on agricultural catchments with low slope and area up to 72 hectares. Our analyses of the  $Q_{\text{base}}$  model showed that using the base flow as a measure of soil moisture in a mountain catchment to calculate CN parameter was justified, and Eq. 25 is recommended in this case. However, for large  $Q_b$ , the calculated CN and direct runoff may be unrealistically high. This is due to the very low share of high base flows in the analyzed sample, which causes considerable errors in the calculation regarding the upper part of the regression curve. To verify this hypothesis, it is necessary to carry out further research, based on greater amount of observational data. When using the proposed method, a designer is obviously faced with a serious problem of determining the base flow. It can be determined for monitored water indicators with continuous flow measurements or for periodic stations. Further research should be aimed at generalization of the developed relationships, so that the method could be used in uncontrolled catchments.

## 6. CONCLUSIONS

Based on our study, the following conclusions may be drawn:

□ The values of CN parameter, determined empirically based on recorded rainfall-runoff episodes, differ significantly from the theoretical values, calculated according to NRCS. This indicates the need to verify the value of CN parameter for local conditions accounting for the course of flood formation in a given catchment.

- The values of CN parameter greatly depend on a catchment moisture level prior to the analyzed flood. Using the NRCS recommended criteria for determining the catchment moisture level can result in considerable inaccuracy in determining CN parameter and calculating the effective precipitation.
- Direct runoff values calculated according to Sahu 3-p and SME models are the most similar to the actually recorded ones. Therefore, these models may constitute an alternative for other methods used for calculating this parameter. Their unquestionable advantage is making the direct runoff independent of variable moisture levels, as proposed in the original NRCS-CN method.
- Knowledge of the base flow value can be useful when calculating CN parameter. The base flow may characterize the catchment moisture level, as it describes in a more comprehensive manner the hydraulic relations between groundwater and surface waters and, to some extent, the catchment retention capacity.

#### References

- Banasik, K., and D.E. Woodward (2010), Empirical determination of runoff curve number for a small agricultural watershed in Poland. **In:** *2nd Joint Federal Interagency Conference, 27 June – 1 July 2010, Las Vegas, USA*.
- Caviedes-Voullième, D., P. García-Navarro, and J. Murillo (2012), Influence of mesh structure on 2D full shallow water equations and SCS Curve Number simulation of rainfall/runoff events, *J. Hydrol.* **448-449**, 39-59, DOI: 10.1016/j.jhydrol.2012.04.006.
- Chauhan, M.S., V. Kumar, and A.K. Rahul (2013), Modelling and quantifying water use efficiency for irrigation project and water supply at large scale, *Int. J. Adv. Sci. Tech. Res.* **3**, 5, 617-639.
- Cunha, L.K., W.F. Krajewski, R. Mantilla, and L. Cunha (2011), A framework for flood risk assessment under nonstationary conditions or in the absence of historical data, *J. Flood Risk Manag.* **4**, 3-22, DOI: 10.1111/j.1753-318X.2010.01085.x.
- Deshmukh, D.S., U.C. Chaube, A.E. Hailu, D.A. Gudeta, and M.T. Kassa (2013), Estimation and comparison of curve numbers based on dynamic land use land cover change, observed rainfall-runoff data and land slope, *J. Hydrol.* **492**, 89-101, DOI: 10.1016/j.jhydrol.2013.04.001.
- Ebrahimian, M., A.A.B. Nuruddin, M.A.B.M. Soom, A.M. Sood, and L.J. Neng (2012), Runoff estimation in steep slope watershed with standard and slope-adjusted curve number methods, *Pol. J. Environ. Stud.* **21**, 5, 1191-1202.
- Efstratiadis, A., A.D. Koussis, D. Koutsoyiannis, and N. Mamassis (2014), Flood design recipes vs. reality: can predictions for ungauged basins be trusted?

- Nat. Hazards Earth Syst. Sci.* **14**, 1417-1428, DOI: 10.5194/nhess-14-1417-2014.
- Fan, F., Y. Deng, X. Hu, and Q. Weng (2013), Estimating composite curve number using an improved SCS-CN method with remotely sensed variables in Guangzhou, China, *Remote Sens.* **5**, 3, 1425-1438, DOI: 10.3390/rs5031425.
- Garen, D.C., and D.S. Moore (2005), Curve number hydrology in water quality modeling: uses, abuses, and future directions, *J. Am. Water Resour. Assoc.* **41**, 2, 377-388, DOI: 10.1111/j.1752-1688.2005.tb03742.x.
- Geetha, K., S.K. Mishra, T.I. Eldho, A.K. Rastogi, and R.P. Pandey (2007), Modifications to SCS-CN method for long-term hydrologic simulation, *J. Irrig. Drain. Eng.* **133**, 5, 475-486, DOI: 10.1061/(ASCE)0733-9437(2007)133:5(475).
- Grimaldi, S., A. Petroselli, and N. Romano (2013), Green-Ampt Curve-Number mixed procedure as an empirical tool for rainfall-runoff modelling in small and ungauged basins, *Hydrol. Process.* **27**, 8, 1253-1264, DOI: 10.1002/hyp.9303.
- Hawkins, R.H., A.T. Hjelmfelt Jr., and A.W. Zevenbergen (1985), Runoff probability, storm depth, and curve numbers, *J. Irrig. Drain. Eng.* **111**, 4, 330-340, DOI: 10.1061/(ASCE)0733-9437(1985)111:4(330).
- Hong, Y., and R.F. Adler (2008), Estimation of global SCS curve numbers using satellite remote sensing and geospatial data, *Int. J. Remote Sens.* **29**, 2, 471-477, DOI: 10.1080/01431160701264292.
- Kabiri, R., A. Chan, and R. Bai (2013), Comparison of SCS and Green-Ampt methods in surface runoff-flooding simulation for Klang watershed in Malaysia, *Open J. Modern Hydrol.* **3**, 3, 102-114, DOI: 10.4236/ojmh.2013.33014.
- Krzanowski, S., A.T. Miler, and A. Wałęga (2013), The effect of moisture conditions on estimation of the CN parameter value in the mountain catchment, *Infrastruc. Ecol. Rural Areas* **3**, 4, 105-117 (in Polish).
- Maidment, D.R. (1993), *Handbook of Hydrology*, McGraw-Hill, New York, 1424 pp.
- McCuen, R.H. (2003), *Modeling Hydrologic Change: Statistical Methods*, Lewis Publishers/CRC Press, Boca Raton.
- Merz, R., and G. Blöschl (2009), A regional analysis of event runoff coefficients with respect to climate and catchment characteristics in Austria, *Water Resour. Res.* **45**, 1, W01405, DOI: 10.1029/2008WR007163.
- MHP (2005), *Application of Hydrologic Methods in Maryland. Report*, Maryland Hydrology Panel, The Maryland State Highway Administration and The Maryland Department of the Environment, Baltimore, USA.
- Michel, C., V. Andréassian, and C. Perrin (2005), Soil conservation service curve number method: How to mend a wrong soil moisture accounting procedure, *Water Resour. Res.* **41**, 2, 1-6, W02011, DOI: 10.1029/2004WR003191.

- Miler, A.T. (2012), Influence of land use changes to flood outflows from areas with large afforestation of the Roztocze Środkowe, *Infrastruc. Ecol. Rural Areas* **2**, 1, 173-182 (in Polish).
- Mishra, S.K., and V.P. Singh (2002), SCS-CN-based hydrologic simulation package. **In:** V.P. Singh and D.K. Frevert (eds.), *Mathematical Models of Small Watershed Hydrology and Applications*, Water Resources Publ., LLC, Highlands Ranch, 391-464.
- Mishra, S.K., and V.P. Singh (2003a), *Soil Conservation Service Curve Number (SCS-CN) Methodology*, Kluwer Academic Publ., Dordrecht.
- Mishra, S.K., and V.P. Singh (2003b), Derivation of the SCS-CN parameter S from linearized Fokker-Planck equation, *Acta Geophys. Pol.* **51**, 2, 179-202.
- Mishra, S.K., M.K. Jain, P.K. Bhunya, and V.P. Singh (2005), Field applicability of the SCS-CN-based Mishra–Singh general model and its variants, *Water Resour. Manag.* **19**, 1, 37-62, DOI: 10.1007/s11269-005-1076-3.
- Mishra, S.K., S. Gajbhiye, and A. Pandey (2013), Estimation of design runoff curve numbers for Narmada watersheds (India), *J. Appl. Water Eng. Res.* **1**, 1, 69-79, DOI: 10.1080/23249676.2013.831583.
- Moriassi, D.N., J.G. Arnold, M.W. van Liew, R.L. Bingner, R.D. Harmel, and T.L. Veith (2007), Model evaluation guidelines for systematic quantification of accuracy in watershed simulations, *Trans. Am. Soc. Agricult. Biol. Eng.* **50**, 3, 885-900.
- Nash, J.E., and J.V. Sutcliffe (1970), River flow forecasting through conceptual models: Part I – A discussion of principles, *J. Hydrol.* **10**, 3, 282-290, DOI: 10.1016/0022-1694(70)90255-6.
- Petroselli, A., S. Grimaldi, and N. Romano (2013), Curve-Number/Green–Ampt mixed procedure for net rainfall estimation: A case study of the Mignone watershed, IT, *Procedia Environ. Sci.* **19**, 113-121, DOI: 10.1016/j.proenv.2013.06.013.
- Ponce, V.M. (1989), *Engineering Hydrology: Principles and Practices*, Prentice Hall, Englewood Cliffs.
- Ponce, V.M., and R.H. Hawkins (1996), Runoff curve number: Has it reached maturity? *J. Hydrol. Eng.* **1**, 1, 11-19, DOI: 10.1061/(ASCE)1084-0699(1996)1:1(11).
- Sahu, R.K., S.K. Mishra, T.I. Eldho, and M.K. Jain (2007), An advanced soil moisture accounting procedure for SCS curve number method, *Hydrol. Process.* **21**, 21, 2872-2881, DOI: 10.1002/hyp.6503.
- Sahu, R.K., S.K. Mishra, and T.I. Eldho (2010), An improved AMC-coupled runoff curve number model, *Hydrol. Process.* **24**, 20, 2834-2839, DOI: 10.1002/hyp.7695.
- Sahu, R.K., S.K. Mishra, and T.I. Eldho (2012), Performance evaluation of modified versions of SCS curve number method for two watersheds of Maharashtra,

- India, *ISH J. Hydraul. Eng.* **18**, 1, 27-36, DOI: 10.1080/09715010.2012.662425.
- SCS (1956), *SCS National Engineering Handbook. Section 4. Hydrology. Supplement A*, Chp. 10, Soil Conservation Service, US Dept. of Agriculture, Washington, USA.
- Smith, R.E., and J.R. Williams (1980), Simulation of the surface water hydrology. **In:** W.G. Knisel (ed.), *CREAMS: A Field-scale Model for Chemicals, Run-off, and Erosion from Agricultural Management Systems*, Conservation Research Report No. 26, US Dept. of Agriculture, Washington, USA, 165-192.
- Váňová, V., and J. Langhammer (2011), Modelling the impact of land cover changes on flood mitigation in the upper Lužnice basin, *J. Hydrol. Hydromech.* **59**, 4, 262-274, DOI: 10.2478/v10098-011-0022-8.
- Wałęga, A., A. Cupak, and W. Miernik (2011), Influence of entrance parameters on maximum flow quantity receive from NRCS-UH model, *Infrastruc. Ecol. Rural Areas* **7**, 85-95 (in Polish).
- Wałęga, A., E. Drożdzał, M. Piórecki, and R. Radoń (2012), Some problems of hydrology modelling of outflow from ungauged catchments with aspects of flood maps design, *Acta Scient. Polon. Format. Circum.* **11**, 3, 57-68 (in Polish).
- Woodward, D.E., C.C. Hoefl, R.H. Hawkins, J. van Mullem, and T.J. Ward (2010), Discussion of “Modifications to SCS-CN method for long-term hydrologic simulation” by K. Geetha, S.K. Mishra, T.I. Eldho, A.K. Rastogi, and R.P. Pandey, *J. Irrig. Drain. Eng.* **136**, 6, 444-446, DOI: 10.1061/(ASCE)IR.1943-4774.0000231.

Received 15 April 2014

Received in revised form 22 October 2014

Accepted 19 January 2015



## Remote Sensing Data Binary Classification Using Boosting with Simple Classifiers

Artur NOWAKOWSKI

Space Research Centre, Polish Academy of Sciences, Warszawa, Poland  
e-mail: anowakowski@cbk.waw.pl

### Abstract

Boosting is a classification method which has been proven useful in non-satellite image processing while it is still new to satellite remote sensing. It is a meta-algorithm, which builds a strong classifier from many weak ones in iterative way. We adapt the AdaBoost.M1 boosting algorithm in a new land cover classification scenario based on utilization of very simple threshold classifiers employing spectral and contextual information. Thresholds for the classifiers are automatically calculated adaptively to data statistics.

The proposed method is employed for the exemplary problem of artificial area identification. Classification of IKONOS multispectral data results in short computational time and overall accuracy of 94.4% comparing to 94.0% obtained by using AdaBoost.M1 with trees and 93.8% achieved using Random Forest. The influence of a manipulation of the final threshold of the strong classifier on classification results is reported.

**Key words:** land cover classification, boosting, artificial area, IKONOS.

## 1. INTRODUCTION

Contemporary commonly used methods of satellite image supervised classification are usually based on neural networks, decision trees or support vector machine (SVM) (Brito and Quintanilha 2012). The need for high accuracy of results leads to search for new approaches. One of them is boosting (Quinlan 1996), which has been proven useful in other applications, especially in biometrics. It is a technique which builds a strong classifier from many weak ones and is an example of ensemble classification.

Boosting was employed in a wide range of applications in computer vision for non-satellite imaging. For example, it was successfully applied in face detection (Viola and Jones 2004), license plate localization (Dlagnekov 2004), and biomedical datasets classification (Cerquides *et al.* 2006).

The technique has been already partially exploited in satellite image classification for the pixel-oriented approach. As for weak classifiers can be chosen any of contemporary classification methods (*e.g.*, thresholding spectral values, nearest-neighbourhood, neural network, decision trees, support vector machine, Bayesian methods, *etc.*), the vast majority of satellite image studies employ boosting with decision trees methods (Schneider *et al.* 2010, Chan and Paelinckx, 2008, Lawrence *et al.* 2004, Friedl *et al.* 1999, 2002; McIver and Friedl 2001). They are mostly based on C4.5/C5.0 algorithms and tools implemented in C/C++ (or J4.8 – their Java version) developed by Quinlan (1996). Only few studies are related to utilization of boosting with weak classifiers other than decision trees. Briem *et al.* (2002) and then Benediktsson *et al.* (2007) compared performance of different classification methods including simple one-feature algorithm 1R (Holte 1993), decision table and decision tree to their ensemble versions, where these methods were used as weak classifiers. They used three ensemble methods: boosting, bagging, and consensus theory. In the comparison, authors also included other popular classifiers like minimum Euclidean distance, Gaussian maximum likelihood, and neural network. Performance results on two multisource remote sensing and geographic datasets indicate that boosting classifiers outperforms other ones: for the first datasets the highest overall and average test accuracies were obtained for boosting with simple one-feature 1R classifiers while for the second dataset boosting with decision trees was the best.

In this paper we investigate a novel scenario for land cover classification for pixel-oriented approach, where as weak classifiers for boosting we use simple threshold classifiers based not only on spectral values of the pixel, but also on statistical and contextual information. The weak classifiers are defined adaptively to training data. The method can be applied for any land cover binary classification problem, but in order to prove its high performance we tested the method on non-trivial exemplary classification problem.

As the example we selected artificial area identification on IKONOS multi-spectral data.

## 2. BOOSTING IDEA

The idea of creating a strong classifier from many weak ones has been investigated since the mid-1980s (Valiant 1984, Kearns 1988). The first algorithm of boosting classification, which became popular because of its reliability, was developed by Y. Freund and R. Schapire in 1995 and called AdaBoost (Freund and Shapire 1996). Since then, some variants of that method have been introduced as well as many other boosting algorithms have been proposed (Matas and Sochman 2001).

Boosting is a supervised method and it assumes availability of a set of training samples. It has two phases of processing: training and testing. During training procedure, a strong classifier is built based on training data. Testing serves for classification of all image pixels using obtained strong classifier.

The common approach to the training stage of boosting methods is to build a strong classifier from iteratively selected weak classifiers. In each iteration, every weak classifier is evaluated on weighted training data and a classification error is provided. The weak classifier which produces the smallest error is added to the resulting strong classifier with computed weight. In the same iteration, weight of every training sample which has been wrongly classified by the selected weak classifier is increased, while the weights of other samples are decreased. This operation allows to concentrate the algorithm on problematic samples in next iteration. The response of the resulting strong classifier  $K$  is a weighted linear combination of responses of selected weak classifiers  $k_i$ ,  $i = 1, \dots, N$ :

$$K = \omega_1 k_1 + \omega_2 k_2 + \omega_3 k_3, \quad (1)$$

where  $\omega_i \in R: (0,1]$  denotes weights. This strong classifier is directly used in the testing stage.

Adaptation of the boosting algorithm to a classification problem requires: (i) selection of a feature space, (ii) construction of a set of weak classifiers, (iii) definition of a classification error measure, and (iv) selection of training samples.

## 3. FEATURE SPACE

Spectral information is the most frequently selected feature for pixel-oriented classification in decision trees with boosting solutions (Schneider *et al.* 2010, Chan and Paelinckx 2008, Lawrence *et al.* 2004) and other approaches (Brito and Quintanilha 2012). Other features like textural, geomet-

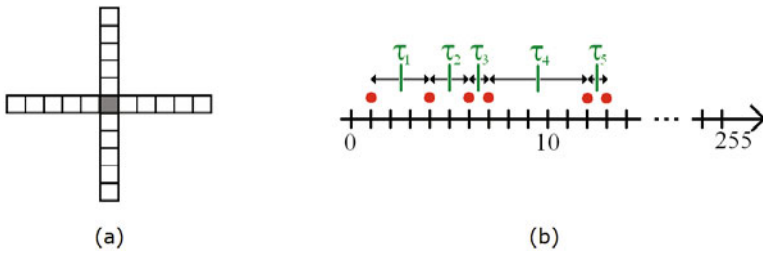


Fig. 1. Neighbourhood window for the actual pixel (localized in the middle) (a), and threshold selection in a binary histogram, where circle denotes that a certain value exists in training data and  $\tau_i$  are necessary thresholds (b).

tric or topologic information are used rarely. They are applied mainly in object-oriented classification (Brito and Quintanilha 2012).

In our method devoted to land cover classification we propose to utilize all available spectral bands and create one additional band containing mean value of all image band values. Current trends show that besides spectral values of the pixel, spatial information could help in classification (Benediktsson *et al.* 2007). Therefore, we include a few basic statistics in the neighbouring window of each considered pixel for each spectral band:

- mean value,
- variance,
- maximal spectral difference (the difference between maximum and minimum).

The shape of the neighbouring window is designed to meet the opposite criteria: minimal size and simplicity (to limit computing time), and maximum information about the neighbourhood (to maximize accuracy). In order to fulfil these, we resigned from using classical square window and left only these neighbouring pixels from it which contained information in four main directions, obtaining the cross-shaped window (Fig. 1a). All the resulting statistic values are scaled linearly to the same discrete range as spectral values to unify the codomain and to reduce computation cost. The size of the window has been set to 11 pixels in horizontal and vertical directions. For dealing with the edge pixels we chose mirroring approach, however other methods could also be applied.

The total number of features amounts to  $4 * (N_b + 1)$ , where  $N_b$  denotes the number of bands in an imagery.

#### 4. WEAK CLASSIFIERS

For each selected feature we consider a set of all possible threshold classifiers. For a single feature with  $N$  possible discrete values there exist  $N - 1$  possible values for the threshold, and therefore  $N - 1$  different threshold

classifiers can be defined. Considering all of the features leads to very large total number of weak classifiers. For example, for IKONOS 4-band 8-bit imagery we get 20 features and therefore obtain  $20 \times 255 = 5100$  possible thresholds assuming that every non-spectral feature has a range of 8 bits.

Each threshold is a base to define two classifiers: one determining whether a particular class has values equal or less than the threshold, the second determining whether this class has values above it. Therefore, the number of weak classifiers is equal to double the number of thresholds. For considered example, we achieved over  $10^4$  weak classifiers.

However, it is probable that real data does not contain all of the theoretically possible values. Therefore, in order to reduce the total number of weak classifiers, only the thresholds necessary in the analysed case are considered (Fig. 1b). For every feature, the algorithm builds a binary histogram which has a positive value for those theoretical feature values which exist in data, and a zero value in opposite case. Subsequently, the thresholds are defined as mean values of two neighbouring non-zero values in the histogram.

A set of all found classifiers based on feature of one kind (among spectral values, mean values in window, variances in window or maximal difference in window) is hereinafter called a family of weak classifiers. Defined families of weak classifiers are used by boosting algorithm in order to build one strong classifier.

## 5. CLASSIFICATION METHOD

The method assumes availability of a training set of pixels classified into two classes. During the whole process, manual work is needed only for the creation of the training set. Training and testing phases are fully automatic.

### 5.1 Training

In the first step, for each training point, the features described in Section 3 are computed and the set of necessary thresholds for each feature is calculated according to Section 4. The list of determined thresholds is an input to the second step which applies the boosting algorithm. We chose AdaBoost.M1 algorithm due to its simplicity and reliability (Freund and Schapire 1996). Among few possible implementations we choose the classical one of Viola and Jones (2001). It assumes that positive training samples are classified as 1 while the negative training samples as 0. The algorithm starts with the initialization of sample weights according to their positive or negative type ( $w_{p,i}$  or  $w_{n,j}$ ):

$$w_{p,i} = \frac{1}{2N_p}, \quad i = 1, \dots, N_p, \quad (2)$$

$$w_{n,j} = \frac{1}{2N_n} \quad j = 1, \dots, N_n, \quad (3)$$

where  $N_p$  and  $N_n$  denote the number of positive and negative samples, respectively.

Next, the main boosting loop begins. In each iteration a number of steps are executed and sample weights are normalized by division by the sum of all weights (including weights of positive and negative samples). After this operation all the weights sum up to 1 and can be interpreted as probability distribution. Subsequently, all weak classifiers (defined using input thresholds) in all families are consecutively tested on weighted training data. For each feature and each of its thresholds  $\tau_k^f$ ,  $k = 1, \dots, K^f$ ,  $f = 1, \dots, F$  ( $K^f$  denotes the number of thresholds for feature  $f$ ,  $F$  denotes number of features) two classification errors,  $e_0(k, f)$  and  $e_1(k, f)$ , are computed. The first one is devoted for the weak classifier where the first class is considered to be below the threshold, the latter one being dedicated for the opposite case. They are calculated as a sum of weights of misclassified training samples  $w_i$ :

$$e_{k0}(k, f) = \sum_{i=1}^n w_i, \quad i = 1, \dots, N_k^f, \quad (4)$$

$$e_{k1}(k, f) = 1 - e_{k0}, \quad (5)$$

where  $N_k^f$  denotes the number of misclassified pixels using the weak classifier of feature  $f$  and threshold  $k$  and the first class is considered to have values below the threshold.

As we need to select the best weak classifier, minimal error  $e_{\min}$  is found in a set of values  $e_{k0}$  and  $e_{k1}$  for all thresholds for all features:

$$e_{\min} = \min_{k=1, \dots, K^f, f=1, \dots, F} \{e_{k0}(k, f), e_{k1}(k, f)\}. \quad (6)$$

During consecutive evaluations we preserve only the value of the smallest error already computed, related feature number, threshold value and binary information whether this is  $e_{k0}$  or  $e_{k1}$ .

Next, we update the weights of training samples which were correctly classified by the corresponding classifier:

$$w_i' = \frac{e_{\min}}{1 - e_{\min}} w_i. \quad (7)$$

We do not modify the weights of wrongly classified samples directly, but in fact they are increased in the next loop because of the normalization step. In the last step of the loop, the found best weak classifier  $k_j$  is added to the resultant strong classifier with the calculated weight  $\omega_j$ :

TRAINING	<p><b>Inputs:</b></p> <ol style="list-style-type: none"> <li>1) <math>I_L</math> - an image with L channels,</li> <li>2) <math>p_i \in \mathbb{N}^2</math>, <math>i=1, \dots, N_p</math>, <math>n_i \in \mathbb{N}^2</math>, <math>i=1, \dots, N_n</math> - localisations of positive (valued as 1) and negative (valued as 0) samples</li> <li>3) <math>N_s</math> - maximum number of steps,</li> <li>4) <math>e_m</math> - maximum classification error</li> </ol> <p><b>Method</b></p> <p><b>I. Compute features:</b></p> <ol style="list-style-type: none"> <li>1) For each pixel <math>i \in I_L</math> for each spectral value and the mean of all of them compute the following additive features: mean value, variance, maximal spectral difference.</li> <li>2) For every feature <math>f</math> normalise values for all training samples into range <math>[0, 255]</math>.</li> </ol> <p><b>II. Select classification thresholds</b> For each feature <math>f</math>:</p> <ol style="list-style-type: none"> <li>1) compute binary histogram of values,</li> <li>2) select thresholds <math>\tau_k^f</math>, <math>k=1, \dots, K^f</math></li> </ol> <p><b>III. Classify data using AdaBoost.M1:</b></p> <ol style="list-style-type: none"> <li>1) Initialize weights of samples:  <math display="block">w_{p,i} = \frac{1}{2N_p}, i = 1, \dots, N_p, \quad w_{n,j} = \frac{1}{2N_n}, j = 1, \dots, N_n</math> </li> <li>2) For <math>s=1, \dots, N_s</math> do: <ol style="list-style-type: none"> <li>a) normalize weights of samples: <math>w_{p,i} = \frac{w_{p,i}}{\sum_{j=1}^{N_p} w_{p,j} + \sum_{j=1}^{N_n} w_{n,j}}</math></li> <li><math display="block">w_{n,i} = \frac{w_{n,i}}{\sum_{j=1}^{N_p} w_{p,j} + \sum_{j=1}^{N_n} w_{n,j}}</math></li> <li>b) for each feature <math>f</math> and each of its thresholds <math>\tau_k^f</math>, compute two classification errors <math>e_0(k, f)</math> and <math>e_1(k, f)</math> on weighted samples,</li> <li>c) select the classifier <math>k_s</math> resulting in the smallest value <math>e_{min}</math> and add it to the strong classifier with the weight:  <math display="block">\omega_j = \log \frac{1 - e_{min}}{e_{min}}</math> </li> <li>d) if <math>e_{min} &lt; e_s</math> then break,</li> <li>e) update the weight of correctly classified samples by <math>k_s</math>:  <math display="block">w'_i = \frac{e_{min}}{1 - e_{min}} w_i, 3</math> </li> </ol> </li> </ol> <p><b>IV. Normalize the strong classifier:</b></p> <ol style="list-style-type: none"> <li>1) For each weak classifier normalise its weight:  <math display="block">\omega_j = \frac{\omega_j}{\sum_{j=1}^J \omega_j}</math> </li> </ol> <p><b>V. Shorten the strong classifier</b></p> <p><b>Output:</b> Normalised strong classifier: <math>K = \omega_1 k_1 + \omega_2 k_2 + \dots + \omega_s k_s</math></p>
TESTING	<p><b>Inputs:</b></p> <ol style="list-style-type: none"> <li>1) <math>I_L</math> - an image with L channels,</li> <li>2) <math>K</math> - normalised final strong classifier</li> </ol> <p><b>Method</b></p> <p><b>For every pixel <math>i \in I_L</math>:</b></p> <ol style="list-style-type: none"> <li>1) For each spectral value and the mean of all of them compute the following additive features: mean value, variance, maximal spectral difference.</li> <li>2) Classify pixel using <math>K</math>:  if <math>K(i) = \sum_{j=1}^J \omega_j k_j(i) \geq 0.5</math> then mark pixel as positive (1)  else mark as negative (0)</li> </ol> <p><b>Output:</b> Classified image <math>I_L</math></p>

Fig. 2. Pseudocode of the proposed classification method.

$$\omega_j = \log \frac{1 - e_{\min}}{e_{\min}} . \quad (8)$$

The loop of the algorithm is continued and in each iteration the best weak classifier is selected. The process stops if the classification error  $e_{\min}$  is less than a set value or the number of iteration exceeds assumed level. The resultant strong classifier is a weighted sum of all the selected weak classifiers according to Eq. 1. The last step is a normalization of weak classifiers' weights:

$$\omega_j = \frac{\omega_j}{\sum_{j=1}^J \omega_j} . \quad (9)$$

The rate of the convergence in iterations of the method to minimal classification error strongly depends on data and employed types of weak classifiers and is difficult to predict. In general, the rate should increase with dimensionality of the feature space and with the use of more accurate weak classifiers. On the other hand, our experiments have shown that in some cases, after the algorithm converged to the minimum classification error, the error could start to slowly increase in next iterations. Therefore, if the method stopped because the number of iteration exceeded the assumed level, the strong classifier is shortened according to the loop for which the minimal error was achieved.

The training phase of the method is summarized in pseudocode in Fig. 2.

## 5.2 Testing

Assuming that a weak classifier denotes pixel belonging to the first class as 1, and the rest of pixels as 0, pixel's class is based on determination if the response of the strong classifier is below or above the half of the sum of all weights of the weak classifier. The sum of all weights is equal to 1 because of normalization step (Eq. 9). According to Eq. 1, a pixel  $p$  can be classified as belonging to the first class if the following condition is true:

$$K(p) = \sum_{j=1}^J \omega_j k_j(p) > 0.5 . \quad (10)$$

Elsewhere, the pixel  $p$  is considered to be a member of the second class. The testing phase of the method is summarized in pseudocode in Fig. 2.

## 6. IMPLEMENTATION

Implementations of basic boosting algorithms could be found in some statistical tools or programming libraries. However, in order to have an operational implementation allowing full insight into the process with a possibility to modify it and to access partial results, we implemented the method in

C++. All the processing steps of the method are done automatically for both training and testing phases. We employed GDAL library (<http://www.gdal.org>) for handling the input and output. It allows us to work with many different image file formats.

## 7. EXPERIMENTS

### 7.1 Classification problem

In order to show that the introduced method can be successfully used for satellite data classification it is tested for a problem of artificial area identification on multispectral IKONOS imagery. For such data, precise classification of artificial areas is a challenge due to spectral diversity of the class. Target areas include roads, pavements, buildings, car parks, *etc.* They could be in size of few or even sub-pixel. In order to achieve high level of information about details and to not omit any target areas we focus on one pixel accuracy of classification. In the case of larger minimal mapping unit, it is possible to use existing methods of aggregation in postprocessing of the results obtained with the method described here.

### 7.2 Test data

We defined a fragment of 8-bit multispectral IKONOS imagery with spatial resolution of 4 m, sized  $1100 \times 600$  pixels, as an experimental area which depicts southern part of the City of Warsaw (Fig. 3a). It includes a variety of types of artificial areas: sparse and dense, high-rises and low-rises with big and small roof areas, regular and irregular shapes and different roof cover, different kinds of roads, car parks, pavements, construction sites, cemeteries, *etc.* On the other hand, the test image contains examples of various types of other classes: water, forests, bushes, grasslands, meadows, green parks, bare soil, *etc.* By visual inspection we prepared 1643 training pixels selected as single ones or in polygons of which 767 pixels belong to the artificial area class (positive samples) and 876 pixels to the non-artificial area class (negative samples).

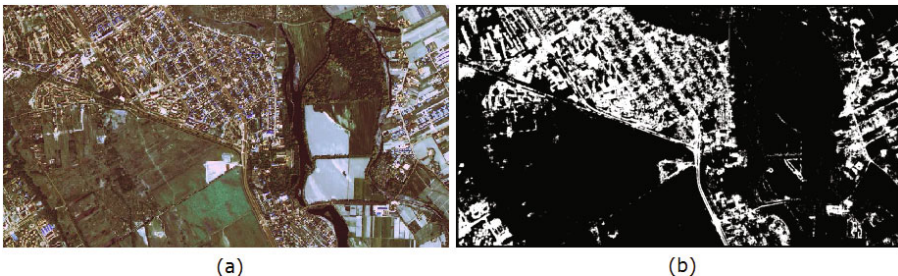


Fig. 3. Artificial area identification: (a) original IKONOS data, and (b) classification results.

### 7.3 Classification results

For the training phase an important issue is the speed of convergency of the method to the minimum classification error. Figure 4 shows how the classification error decreases in consecutive iterations of a boosting loop for the training data. As we defined that this error cannot exceed 0.003, the boosting method stopped because of the second stop criterion – the maximal number of iterations (set to 200). This number should not be too high in comparison to number of training pixels in order to avoid overfitting. The whole training process on middle class PC (Intel Core2Quad CPU Q9300, 2.5GHz, 4MB) took 6 s.

Results of the testing phase (classification of the whole test area) are presented in Fig. 3b (computational time was about 1 min). The method shortened a strong classifier to 197 weak classifiers, for which the classification error on the training data achieved the smallest value of 0.0067.

Generally, the achieved results should be marked as very good considering that the image was classified into only two heterogenic classes. Visual analysis highlighted two main misclassification problems. Firstly, borders of some wetland were detected as artificial areas. Secondly, few bare soil areas were detected also as artificial, which is probably connected to the fact that some examples of construction sites included in artificial areas training set were during ground works.

In order to obtain authoritative assessment of the classification results, the validation procedure was applied. We used a set of 2000 validation pixels, different from the training ones, selected by visual inspection including analysis of data from other imageries. Their localization was chosen randomly using standard uniform distribution over the whole test data. As we aimed at pixel level accuracy, we were confronted with the problem of classification of pixels which are not unimodal (contain both classes) or pixel repre-

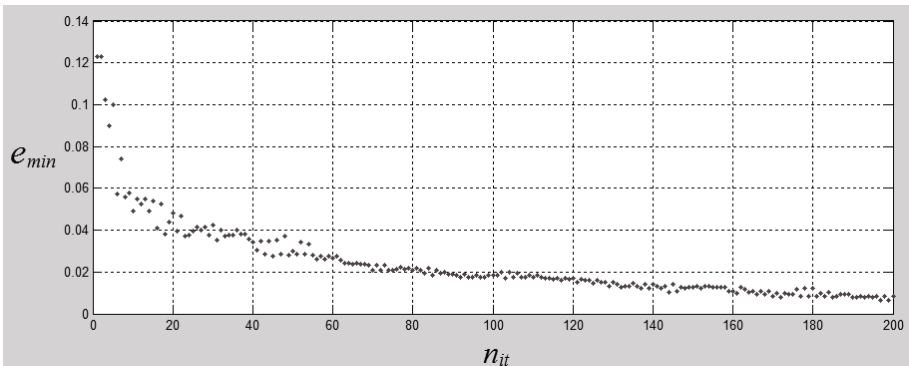


Fig. 4. Classification error ( $e_{min}$ ) versus number of boosting loop iterations ( $n_{it}$ ).

senting undetermined land cover. Therefore, we defined 3 classes that a pixel could represent: 1 – pure artificial area, 2 – non-classified or mixed, 3 – pure non-artificial area. Statistics of the validation set are presented in Table 1.

Table 1  
Validation classes and statistics

Class no.	Class description	Number of pixels
1	Pure artificial	283
2	Non-classified or mixed	424
3	Pure non-artificial	1293
Total:		2000

The overall accuracy achieved 94.4%. Such high accuracy is due to spatial dominance of non-artificial areas in the image. Nevertheless, producer and user accuracies for artificial area class are still high (see details in Table 2).

Table 2  
Validation results

Accuracy	Pure artificial [%]	Pure non-artificial [%]
User	82.3	97.1
Producer	86.0	96.2
Overall	94.4	

Using the same training and validation data and the same features we computed classification accuracies for two other ensemble methods: AdaBoost.M1 with decision trees as weak classifiers and Breiman's Random Forest' algorithm (we used implementation of the methods from Statistics Toolbox in Matlab R2012a). For both methods we prepared classification for different numbers of weak classifiers. The obtained overall accuracies in comparison to results of the proposed method are presented in Fig. 5. Computations for the proposed method stopped for the number of 354 weak classifiers when the training error achieved 0 value. Therefore setting up more steps resulted in the same accuracy, which was the best one. Other two methods achieved slightly worse maximums of accuracies equal to 94.0% (AdaBoost with trees) and 93.8% (Random Forest). On the other hand, differences in computational efforts are very significant. Considering only the

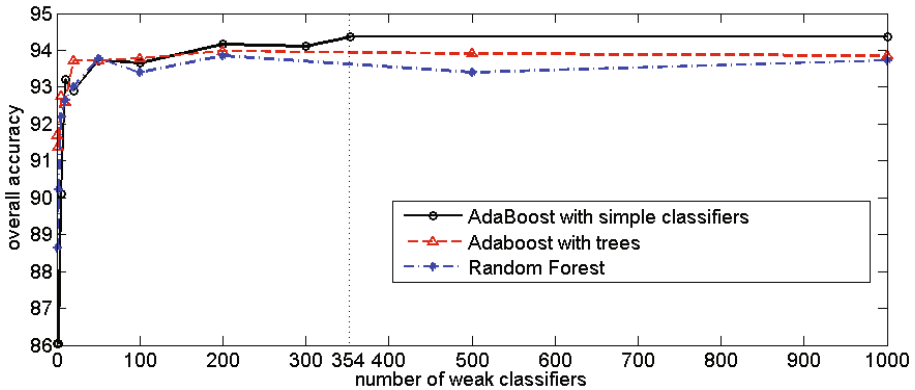


Fig. 5. Overall accuracy on validation set *versus* number of weak classifiers.

testing phase of the classification, when the minimisation of the efforts is critical due to the necessity of processing all pixels in an imagery, the proposed method needs only one threshold comparison for each weak classifier. AdaBoost.M1 employing trees and Random Forest need as much threshold comparisons as the number of internal nodes is in each decision tree. For the results presented in Fig. 5, the AdaBoost employing trees produced trees with mean number of internal nodes equal to 57, while for Random Forest this number is 63. Thus, the difference in needed comparisons is several dozen. Moreover, storing, managing and even interpretation of strong classifier is much easier in the proposed method, because the structure of proposed strong classifier is less complex.

#### 7.4 Final threshold manipulations

In the boosting method the final classification decision is done using a threshold 0.5 (Eq. 10). In theory, this coefficient is utilized in order to minimize the error (*e.g.*, misclassification rate). However, the coefficient can also be seen as a parameter which can be changed in order to manipulate classification accuracies. According to Eq. 10:

$$K(p) = \sum_{i=1}^J \omega_j k_j(p) > T, \quad T \in (0,1) . \quad (11)$$

In Figure 6 we present the results of such a manipulation for the considered problem after validation. Although we expected to achieve the highest overall accuracy for  $T_1 = 0.50$ , it was obtained for  $T_2 \approx 0.51$  (Fig. 6a). This difference, almost negligible, improves the overall accuracy by only about 0.3% to 94.7%.

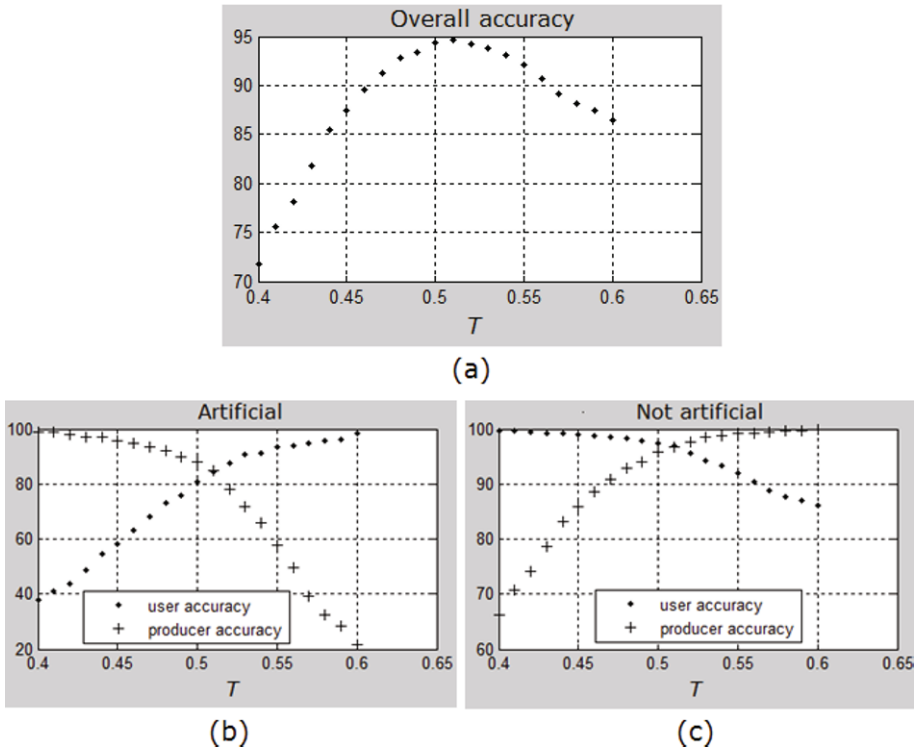


Fig. 6. Classification accuracy *versus* final threshold of the method: overall accuracy (a), user and producer accuracies for artificial (b) and non-artificial (c) surfaces.

Nevertheless, the manipulation of  $T$  can be useful to change the compromise between user and producer accuracies for a certain class (Fig. 6b-c). Depending on an application of the classification it is sometimes desired to prefer one kind of these accuracies over another. For the classification error computation employed here (sum of weights of misclassified training samples) it is clear that user and producer accuracy for both artificial and non-artificial surfaces are equal when the maximum of overall accuracy is achieved at  $T_2$ . At that time, the accuracy for artificial surfaces amounted to 84.5% while for non-artificial ones it was 96.8%.

## 8. DISCUSSION AND CONCLUSIONS

We introduced a novel satellite image classification method which is based on the boosting classification. Simple threshold classifiers are used as weak ones instead of popular decision trees. We chose all possible threshold classifiers based on spectral values of pixels and basic statistics of pixel cross-

shaped neighbourhood. The numbers of threshold classifiers are minimized based on data histograms.

The method is a supervised technique and requires a training set. However, training and testing are fully automatic, once the two parameters for stop criteria are defined. It could also be used in a semi-automatic way for the case when user is not interested in maximizing the overall, but only user or producer accuracy. In that case, the final threshold of the method could be manipulated in order to meet user's needs.

The method was implemented as stand-alone independent software and obtained computational time was short for both training and testing.

The performance was tested on a difficult problem of artificial area identification on IKONOS multispectral imagery. The obtained classification accuracy is 94.4%, which is slightly better than accuracies obtained by using other two state-of-the-art ensemble methods: AdaBoost.M1 with decision trees and Random Forest. Achieved results together with evaluations introduced with Briem *et al.* (2002) and then Benediktsson *et al.* (2007) prove the thesis that there is no need to use advanced weak classifiers to obtain high accuracy of classification results.

As the boosting scenario which is based on advanced weak classifiers has already been partially exploited in satellite image analysis, the scenario with very simple classifiers is a novel one and need further investigations, in particular in the area of performance with other types of features and classifiers, and in adaptation to other practical classification problems.

**Acknowledgments.** This work was supported by ESA under the framework of PECS, project No. 4000105537/12/NL/KML: Implementation of remote sensing data and models in optimizing the localisation of renewable energy sources on the example of biofuel crops with respect to ecological constraints.

## References

- Benediktsson, J.A., J. Chanussot, and M. Fauvel (2007), Multiple classifier systems in remote sensing: from basics to recent developments. **In:** M. Haindl, J. Kittler, and F. Roli (eds.), *Multiple Classifier Systems*, Lecture Notes in Computer Science, Vol. 4472, Springer, Berlin Heidelberg, 501-512, DOI: 10.1007/978-3-540-72523-7\_50.
- Briem, G.J., J.A. Benediktsson, and J.R. Sveinsson (2002), Multiple classifiers applied to multisource remote sensing data, *IEEE Trans. Geosci. Remote Sens.* **40**, 10, 2291-2299, DOI: 10.1109/TGRS.2002.802476.

- Brito, P.L., and J.A. Quintanilha (2012), A literature review, 2001-2008, of classification methods and inner urban characteristics identified in multispectral remote sensing images. **In:** *Proc. 4th GEOBIA, 7-9 May 2012, Rio de Janeiro, Brazil*, 586-591.
- Cerquides, J., M. López-Sánchez, S. Ontañón, E. Puertas, A. Puig, O. Pujol, and D. Tost (2006), Classification algorithms for biomedical volume datasets. **In:** R. Marin, E. Onaindia, A. Bugarin, and J. Santos (eds.), *Current Topics in Artificial Intelligence*, Springer, Berlin Heidelberg, 143-152, DOI: 10.1007/11881216\_16.
- Chan, J.C.W., and D. Paelinckx (2008), Evaluation of Random Forest and AdaBoost tree-based ensemble classification and spectral band selection for ecotope mapping using airborne hyperspectral imagery, *Remote Sens. Environ.* **112**, 6, 2999-3011, DOI: 10.1016/j.rse.2008.02.011.
- Dlagnekov, L. (2004), License Plate Detection using AdaBoost, Computer Science and Engineering Department, University of California, San Diego, USA.
- Freund, Y., and R.E. Schapire (1996), Experiments with a new boosting algorithm. **In:** *Proc. 13th Int. Conf. Machine Learning, 3-6 July 1996, Bari, Italy*, 148-156.
- Friedl, M.A., C.E. Brodley, and A.H. Strahler (1999), Maximizing land cover classification accuracies produced by decision trees at continental to global scales, *IEEE Trans. Geosci. Remote Sens.* **37**, 2, 969-977, DOI: 10.1109/36.752215.
- Friedl, M.A., D.K. McIver, J.C.F. Hodges, X.Y. Zhang, D. Muchoney, A.H. Strahler, C.E. Woodcock, S. Gopal, A. Schneider, A. Cooper, A. Baccini, F. Gao, and C. Schaaf (2002), Global land cover mapping from MODIS: algorithms and early results, *Remote Sens. Environ.* **83**, 1-2, 287-302, DOI: 10.1016/S0034-4257(02)00078-0.
- Holte, R.C. (1993), Very simple classification rules perform well on most commonly used datasets, *Mach. Learn.* **11**, 1, 63-91, DOI: 10.1023/A:1022631118932.
- Kearns, M. (1988), Thoughts on hypothesis boosting, University of Pennsylvania, Machine Learning class project, 105 pp. (unpublished).
- Lawrence, R., A. Bunn, S. Powell, and M. Zambon (2004), Classification of remotely sensed imagery using stochastic gradient boosting as a refinement of classification tree analysis, *Remote Sens. Environ.* **90**, 3, 331-336, DOI: 10.1016/j.rse.2004.01.007.
- Matas, J., and J. Sochman (2001), Adaboost. Center for Machine Perception, Czech Technical University, Prague, Czech Republic.
- McIver, D.K., and M.A. Friedl (2001), Estimating pixel-scale land cover classification confidence using nonparametric machine learning methods, *IEEE Trans. Geosci. Remote Sens.* **39**, 9, 1959-1968, DOI: 10.1109/36.951086.
- Quinlan, J.R. (1996), Bagging, boosting, and C4.5. **In:** *Proc. 13th National Conference on Artificial Intelligence, 12-17 February 1996, Phoenix, USA*, Vol. 1, 725-730.

- Schneider, A., M.A. Friedl, and D. Potere (2010), Mapping global urban areas using MODIS 500-m data: New methods and datasets based on ‘urban ecoregions’, *Remote Sens. Environ.* **114**, 8, 1733-1746, DOI: 10.1016/j.rse.2010.03.003.
- Valiant, L.G. (1984), A theory of the learnable, *Commun. ACM* **27**, 11, 1134-1142, DOI: 10.1145/1968.1972.
- Viola, P., and M. Jones (2001), Rapid object detection using a boosted cascade of simple features. **In:** *Computer Vision and Pattern Recognition CVPR 2001*, Vol. 1, I-511–I-518, DOI: 10.1109/CVPR.2001.990517.
- Viola, P., and M.J. Jones (2004), Robust real-time face detection, *Int. J. Comput. Vision* **57**, 2, 137-154, DOI: 10.1023/B:VISI.0000013087.49260.fb.

Received 26 June 2014

Received in revised form 27 November 2014

Accepted 5 January 2015